Fall 2022

A Study of Ship Airwakes Using Dual Plane Stereoscopic PIV

Guillermo Mazzilli
Embry-Riddle Aeronautical University, mazzillg@my.erau.edu

By

A Thesis Submitted to the Faculty of Embry-Riddle Aeronautical University

In Partial Fulfillment of the Requirements for the Degree of

Master of Science in Aerospace Engineering

Embry-Riddle Aeronautical University

Daytona Beach, Florida

By

THESIS COMMITTEE

Graduate Program Coordinator, Dr. Hever Moncayo	Date
Dean of the College of Engineering, Dr. James W. Gregory	Date
Associate Provost of Academic Support, Dr. Christopher Grant	Date

ACKNOWLEDGMENTS

I could not have undertaken this journey without the help of my advisor and mentor, Professor Ebenezer P. Gnanamanickam, who granted me the opportunity to pursue a graduate degree under his guidance at Embry-Riddle Aeronautical University. It has been a little over a year since Dr. Gnanamanickam afforded me the opportunity to join the research team under the U.S. Vertical Lift Research Center of Excellence (VLRCOE) program, where I have grown as a student, scientist, and most importantly, as a person. Since day one, I have been inspired by Dr. Gnanamanickam's creativity and I look forward to the day I can think outside the box like he does. I very much look forward to pursuing my doctoral studies under his guidance and keep learning from his dedication and passion for his work.

I would also like to thank Dr. J. Gordon Leishman, who agreed with Dr. Gnanamanickam and allowed me to join the VLRCOE research team. Dr. Leishman provided valuable suggestions and answered many of my questions along the process. I am also thankful to Dr. Anastasios Lyrintzis, whose ideas helped me expand my horizons of knowledge. I would also like to extend my gratitude to Dr. Zheng Zhang, who taught me how to properly use wind tunnel equipment and provided smart suggestions to improve the experimental PIV setup. I must also acknowledge the contributions of Mr. Joel Mills, who was always willing to help install Cowdrey rods and also provided suggestions based on his vast experience working with wind tunnel models. I also want to thank Ms. Cynethia Goodwyn and Dr. Pamela Daniels for always being available to answer questions regarding the tedious but necessary administrative work.

I am extremely grateful to my labmates Nicholas Zhu and Kaijus Palm, who patiently taught me about PIV systems and shared their research studies to help me undertake this journey. Additionally, the majority of the experimental setup had already been planned and developed by them when I started this study, which saved me a considerable amount of time and allowed me to shift my focus toward the results and data analysis. Thank you to Dr. Dhuree Seth, whose doctoral work included the experimental setup for the simulated

atmospheric boundary layer that was made available for the current research. I also want to thank Michael Wannemacher, who helped me run most of the experiments in record time.

Many thanks to Professor A. J. McGahran, who provided guidance through my undergraduate studies and allowed me to be part of his chemistry laboratory practices as a teaching assistant before I joined the VLRCOE research team. I would also like to acknowledge Paul Winner, Greeshma Daniel, Pratik Deshpande, Vaishak Thiruvenkitam, Miriam Theobald-Deschine and Patricio Garzon for supporting me through this journey.

I would also like to extend my gratitude to my friends outside of school - Ryan Groel, Maricarin Minnock, Mason Anderson, Connor Smith, and David Cueva - who unconditionally supported me even when they did not fully understood what this research entailed.

I am forever grateful to my parents and my sister, whose unconditional support help me overcome obstacles and keep a positive attitude in life. I want to extend a special thanks to my mother, whose strength and humility inspire me from thousands of miles away. I hope I make her proud.

Lastly, I would like to thank the U.S. Army/Navy/NASA Vertical Lift Research Center of Excellence at Penn State University and Georgia Tech for the support received. This research was partially funded by the Government under Cooperative Agreement No. W911 W6-17-2-0003, as well as Agreement No. W911W6-21-2-0001. The U.S. Government is authorized to reproduce and distribute reprints for Government purposes notwithstanding any copyright notation thereon. The views and conclusions contained in this document are those of the authors and should not be interpreted as representing the official policies or position, either expressed or implied, of the U.S. Army Combat Capabilities Development Command (DEVCOM), Aviation & Missile Center (AvMC), or the U.S. Government.

ABSTRACT

The airwake of a model Simple Frigate Shape 2 (SFS2) was studied in a low-speed wind tunnel. This airwake was measured using a novel time-dependent, dual plane, stereoscopic particle image velocimetry approach. Two flow planes over the flight deck, one parallel and one perpendicular to the free-stream were simultaneously measured. Measurements were carried out over four such pairs of streamwise-spanwise plane combinations. Additionally, the airwake with and without a simulated atmospheric boundary layer (sABL) was studied. The synchronicity of the measurements were taken advantage of to carry out conditional averages of the flow field to isolate and study certain flow events (and its footprint) within the airwake. Those flow events that are likely relevant to rotorcraft operations in the vicinity of ships were chosen to carry out this conditional analysis.

Conditionally averaged statistics of the large vertical fluctuations in the shear layer over the flight deck revealed sharp velocity gradients as well as large-scale flow features above and over large portions of the deck. The fields conditioned on large positive vertical fluctuations were opposite in sign (or the mirror) of those with large negative vertical fluctuations, pointing to a temporal symmetry associated with the oscillation of the shear layer. The flow scenario with the sABL showed similar turbulence levels with almost identical flow structures. An examination of the two stable flow states of the hangar door wake, based on conditional statistics, revealed that each state influenced nearly the entire flow field. Additionally, the mean temporal and spatial evolution of the airwake as the flow transitions between these two states was established. In the case of the flow with the sABL, both flow states persisted for shorter time periods. Overall this study strengthened the growing body of evidence that points to the airwake being a flow field that is a coupled or encapsulating flow structures that are interacting.

TABLE OF CONTENTS

LIST OF FIGURES

Figure **Page**

LIST OF TABLES

Table **Page**

NOMENCLATURE

$\bar{t}$	Non-dimensional time
$\bar{u}, \bar{v}, \bar{w}$	Time-averaged components of velocities, $\mathrm{m\,s^{-1}}$
$\bar{u}_{unc}, \bar{v}_{unc}, \bar{w}_{unc}$	Time-averaged velocity uncertainty components, $\mathrm{m\,s^{-1}}$
Δt	Straddling time between frames, µs
ℓ_f	Flight deck length, ft
$\hat{u}, \hat{v}, \hat{w}$	Conditionally-averaged velocity components, $\mathrm{m\,s^{-1}}$
τ	Time delay between PIV systems, ms
$\tilde{u}, \tilde{v}, \tilde{w}$	Average velocity components in conditional region, $\mathrm{m\,s^{-1}}$
F_s	Sampling frequency, Hz
h_s	Ship height, ft
k	Turbulent kinetic energy, $\mathrm{m^2\ s^{-1}}$
k_u, k_v, k_w	Velocity thresholds to isolate flow events, $\mathrm{m\,s^{-1}}$
l_s	Ship length, ft
n	Number of transitions between bistable states within a dataset
t_0	Time instance of transition between bistable states
T_s	Sampling period, s
u', v', w'	Fluctuating components of velocities, $\mathrm{m\,s^{-1}}$
u, v, w	Streamwise, spanwise, and wall-normal velocities, $\mathrm{m\,s^{-1}}$
U_{ref}	Reference velocity, $\mathrm{m\,s^{-1}}$

U_∞	Free-stream velocity, $\mathrm{m\,s^{-1}}$
$u_{RMS}, v_{RMS}, w_{RMS}$	Root mean square values of velocity components, $\mathrm{m\,s^{-1}}$
V	Combined flow speed
w_b	Ship width, ft
x, y, z	Streamwise, spanwise, and wall-normal positions, ft
3D	Three-dimensional
Re	Reynolds number
CFD	Computational Fluid Dynamics
DES	Detached-Eddy Simulations
DI	Dynamic Interface
DP-sPIV	Dual-Plane stereoscopic Particle Image Velocimetry
ERAU	Embry-Riddle Aeronautical University
FOCFT	First of Class Flight Trials
FOV	Field of View
HWA	Hot Wire Anemometry
LDA	Laser Doppler Anemometry
LES	Large-Eddy Simulations
LSWT	Low-Speed Wind Tunnel
M	Mach number
MILES	Monotone Integrated Large Eddy Simulation

Nd:YLF	Neodymium-doped Yttrium Lithium Fluoride
PDF	Probability Density Function
PIV	Particle Image Velocimetry
PTU	Programmable Timing Unit
RANS	Reynolds Average Navier-Stokes
ROI	Region of Interest
sABL	Simulated Atmospheric Boundary Layer
SFS2	Simple Frigate Shape No. 2
SHOL	Ship-Helicopter Operational Limits
SP	Spanwise plane
SW	Streamwise plane
T23	Royal Navy Type 23 Frigate
TI	Turbulence Intensity
TKE	Turbulent Kinetic Energy
WOD	Wind Over Deck

1 Introduction

The present work is devoted to improving the overall understanding of the airwake/rotor dynamic interface (DI). In this context, the primary objective of this thesis is to analyze the highly unsteady three-dimensional (3D) flow structures of the ship airwake. This complex flow field is the result of the interaction between the atmospheric boundary layer developing over the sea and the bluff, unstreamlined shapes of ships. Specifically this thesis deals with a class of ships that are of interest to the Navy. This chapter presents the primary motivation behind this work along with a chronological review of relevant previous studies, leading to a description of the objectives and an outline of the thesis.

1.1 The Ship Airwake and the Dynamic Interface Problem

Many Naval operations of helicopters and other aircraft involve taking off and landing from the flight deck, which is usually located near the stern of ships, as shown in Fig. 1.1. The ship airwake is one fundamental contributor to the so-call dynamic interface (DI), which is defined as the environment between the ship and such aircraft in the vicinity of the ship. The unstreamlined shape of naval ships are known to create complex three-dimensional separated flows with embedded turbulence. Specifically, airwakes tend to produce localized zones of high upwash and downwash over the flight deck [18]. These highly turbulent flow features coupled with the rotor downwash tend to produce highly unsteady airloads on rotorcraft. Specifically, rotorcraft flying in a ship airwake experience unsteady loading on both the rotor and the fuselage due to the inherent shear layers and high flow vorticity present within the airwake. This results in degrading rotorcraft handling qualities, which requires an increase in pilot control activity during near-ship operations [19]. Previous airwake studies [2, 10, 14] identified large-scale turbulent structures over the flight deck that contribute to the complexity of the ship airwake. As shown in Figure 1.2, the bow of the ship generates upstream turbulence. In addition, the funnel structure generates a shedding wake as well as a horsehoe vortex that extends downstream. Further, a flow recirculation region forms behind each backward-facing step (the flight hangar forming one such step) and additional flight

deck vortices are generated. These structures are highly three-dimensional and unsteady in nature [2, 14]. Moreover, the downwash of the rotor and associated ground effects coupled with these unsteady flow features of the airwake further increase the complexity of the DI. The ship's motion, which is influenced by sea conditions, adds another layer of complexity to the DI. For example, ships can roll, pitch, yaw, heave, surge, and sway [13] complicating landing or takeoff operations for pilots and onboard personnel.

Figure 1.1 A helicopter landing on the flight deck of a frigate [1].

The primary motivating factor for understanding the ship airwake is personnel, ship, and aircraft safety [12]. To determine the safety and limitations of helicopter-ship operations, Ship-Helicopter Operational Limits (SHOL) are used. Here, SHOL is a safety envelope constructed based on first-of-class flight trials (FOCFTs), for every combination of in-service helicopter and ship [20]. These SHOL diagrams show relative wind-over-deck (WOD) directions and speeds at which the aircraft can operate. The FOCFTs are conducted at sea to determine the boundaries of this envelope. They are usually performed over a relatively short period of time and are at the mercy of the weather. Consequently, it is not possible to obtain test points at every desired WOD limit, resulting in conservative SHOLs that are often limited by schedule and meteorological constraints rather than pilot capabilities

[3]. Figure 1.3 shows an example of a SHOL diagram. It provides WOD angles around the circumference and WOD speeds. The thick black lines denote the SHOL boundaries that enclose the safety envelope within which rotorcraft-ship operations can be safely conducted [3].

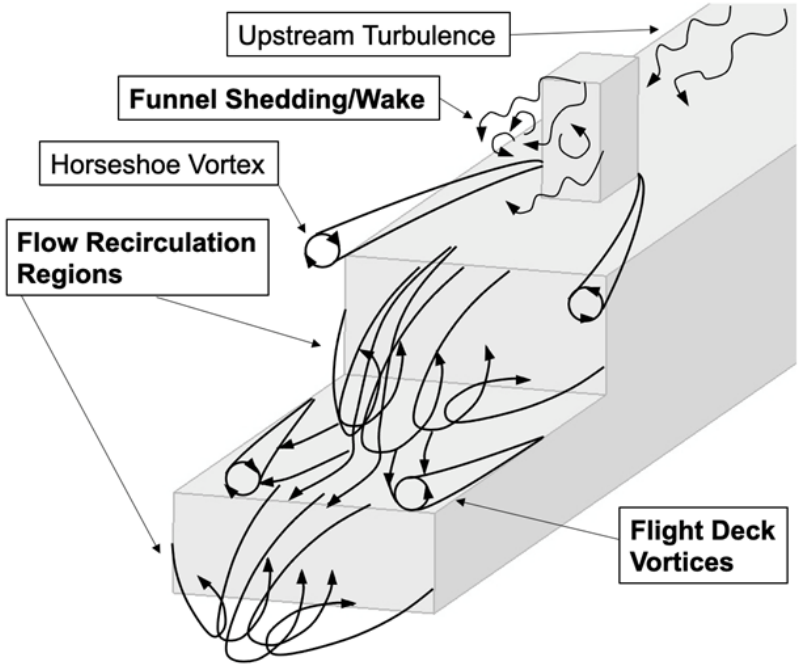

Figure 1.2 Large-scale turbulent structures over the flight deck [2].

While at-sea trials are expensive and time consuming, flight simulators offer a safer and cheaper way to train pilots in these operations [4]. Thus, a model that represents the airwake accurately for use in flight simulators is important to improve pilot training and operational limits in a more effective manner than sea trials [21]. Other potential benefits of high-fidelity DI models include expanding the safety envelope of SHOLs along with possible improvements in ship design [19]. Hence, from various perspectives a better understanding of the physics of the DI is needed. This has been the long-term goal of most, if not all, aerodynamic studies of the ship airwake found in the literature. Such studies included computational and/or experimental approaches. In this regard, the literature survey presented in this thesis provides a detailed examination of previous research using computational simulations

as well as different experimental techniques. This literature review also highlights the current gaps in understanding the three-dimensional behavior of the ship airwake, which motivated the present work.

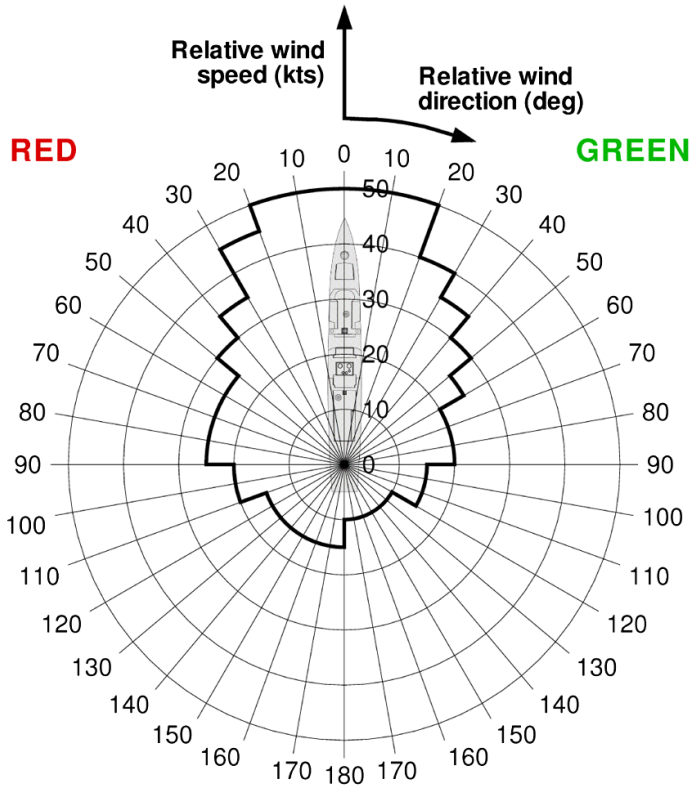

Figure 1.3 A typical SHOL diagram [3].

1.2 Literature Review

This section provides a review of the relevant work on ship airwakes. Both computational and experimental approaches are considered. Particularly, experimental studies that used the particle image velocimetry (PIV) approach are reviewed in detail as it is the approach used in the current study. Additionally, the importance of properly representing the atmospheric boundary layer in experimental studies is discussed.

1.2.1 Computational Airwake Modeling

The increased computational power and availability of appropriate computational fluid dynamics (CFD) codes have led to rapid progress in computational airwake modeling. Numerical efforts at simulating the airwake began in the early 2000s [22]. These computational

approaches can be distinguished based on the fidelity of the solvers and turbulent models used. They are categorized into the following broad - Euler (inviscid) solvers, Reynolds Averaged Navier Stokes (RANS) solvers, Detached-Eddy Simulations (DES), and Large-Eddy Simulations (LES).

In the early 2000s, Euler (inviscid) solvers were used by Bogstad et al. [23] and Sezer-Uzol et al. [24] to construct an aerodynamic database for ship-specific simulators. These authors argued that inviscid CFD simulations offered a cost-effective alternative to solvers that account for viscous effects. However, inviscid solvers inherently present results with limited validity because of the overlooked viscous effects. Some of the shortcomings of this approach were highlighted by Sezer-Uzol et al. [24], who observed that the simulated wake over the flight deck occupied a smaller spatial region and presented less axial asymmetry when compared to experimental results.

Technological advancements allowed for the use of more sophisticated turbulent models to simulate the airwake with higher degrees of fidelity. The RANS method numerically solves the averaged quantities of the flow field using time-averaged Navier-Stokes equations [25]. In contrast to LES and DES, this method is computationally less expensive. However, all RANS models have limitations due to the modelling assumptions used to derive the mathematical formulation of the model [26]. Hence, these models have to be validated against experimental data for better accuracy and reliability [27].

More recent studies used Large-Eddy Simulations (LES), where only the subgrid small scales were modelled. However, due to its high computational cost, it is also common to encounter airwake simulations that used a hybrid approach called Detached-Eddy Simulations (DES). This approach combines LES and Reynolds Average Navier-Stokes (RANS) modeling. This approach offers the accuracy benefits of LES modeling while retaining the efficiency of RANS models, which results in reduced computational costs compared to a full fledged LES approach [26].

Forrest and Owen [4] carried out DES simulations of the ship airwake using unstructured

grids at several WOD angles. The Simple Frigate Shape No. 2 (SFS2) and a Royal Navy Type 23 Frigate (T23) were studied. Figure 1.4a shows the time-averaged and instantaneous velocity contours corresponding to the headwind case on the SFS2 model. The results clearly showed the distinctive flow features of the ship airwake such as the recirculation regions behind each step, the wake behind the funnel, and the flow reattachment region further downstream over the flight deck. *In-situ* and wind tunnel measurements were used to validate computational results on the T23 and SFS2 models, respectively. The mean velocity showed fairly good agreement with experimental data for the headwind case, as shown in Fig. 1.4b and Fig. 1.4c. However, some differences between computational and experimental results existed for the oblique WOD case (e.g., wind at 45° from starboard). Figure 1.4d shows that although the qualitative trends of all three mean velocity components were captured, the CFD results underestimated the magnitudes of the streamwise and spanwise mean velocities and overestimated the mean wall-normal velocity. Similarly, the turbulence intensity (shown in Fig. 1.4e) presented higher degrees of disagreement in the case of the oblique WOD case when compared to the headwind case. These authors concluded that DES was suitable for ship airwake modeling because of its ability to capture smaller-scale turbulent structures in the flow. However, some fundamental limitations of this approach, particularly at the higher WOD angles, were observed.

Polsky [22] investigated the suitability of using a Monotone Integrated Large Eddy Simulation (MILES) in conjunction with a $k-\omega$ turbulence modeling approach to study the ship airwake. MILES is a non-classical Large Eddy Simulation (LES) approach based on using the unfiltered Navier Stokes equations [28]. The author concluded that steady-state CFD calculations were unable to accurately model the ship airwake. Yet, the time-accurate calculations showed good agreement with experimental data. The author also observed that using coarse grids in regions of flow separation (e.g, recirculation bubble) resulted in large discrepancies in flow velocities when compared with wind tunnel data, highlighting the importance of grid quality in computational airwake simulations.

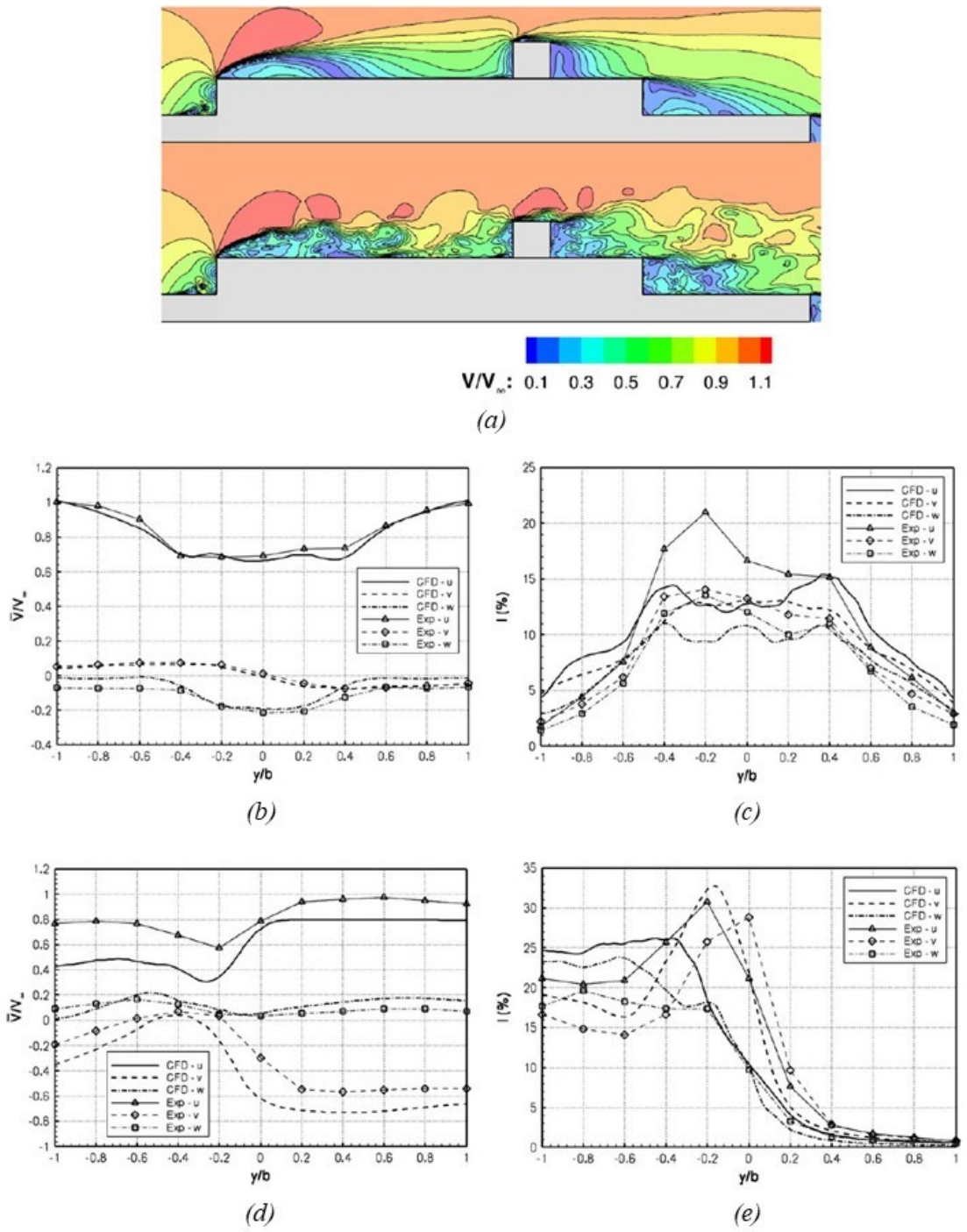

Figure 1.4 (a) Mean and instantaneous velocity contours for the headwind case on the SFS2 model. (b) through (e) show comparisons between computational and experimental data: (b) headwind mean velocity comparison (c) headwind turbulence intensity (d) mean velocity for wind at 45° from starboard (e) turbulence intensity for wind at 45° from starboard. All turbulence intensity values were normalized by V_∞ at 50% deck length. [4].

Later on, Snyder and Kang [5] carried out a computational analysis of the ship airwake using Cobalt, a commercial parallel processing Navier-Stokes solver on an unstructured tetrahedral grid [29]. This study also used a MILES flow model. Figure 1.5 and 1.6 show the time-averaged flow velocity compared with those from experiments for the ship in a 7-knot headwind. Figure 1.5 highlights the plane along the ship centerline. In this figure, the white arrows represent the CFD results and the black arrows represent *in-situ* scaled measurements. Figure 1.6 shows the comparison of the computational results with wind tunnel point measurements. This study showed reasonable agreement with experimental measurements, with better agreement in velocity direction than in magnitude. However, vector comparison at only certain locations in the flow provided limited insight into the spatial structure of the airwake. Moreover, each plane was interpreted separately, completely omitting the correlation between centerline and horizontal planes. Thus, the three-dimensional aspects of the airwake were overlooked.

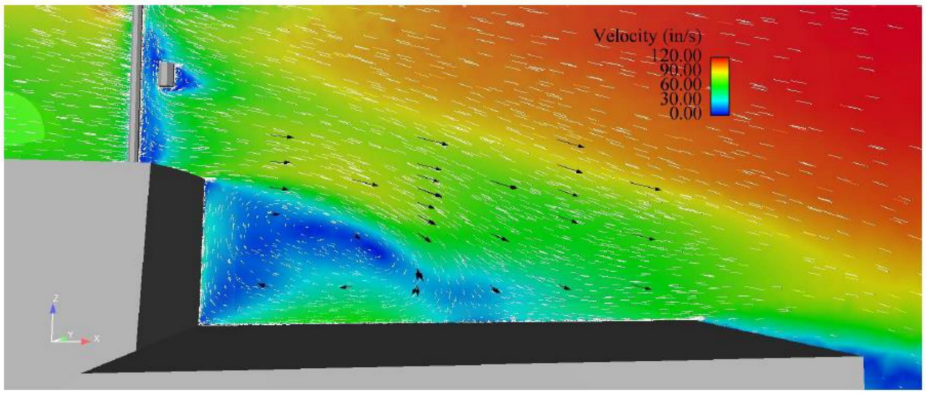

Figure 1.5 CFD results by Snyder and Kang [5] depicted in white arrows and color contours. They were compared to *in-situ* scaled data (black arrows) for a 7-knot (141 in s^{-1}) headwind case.

Other airwake studies that utilized an LES approach include those by Rao et al. [6] and Zhang et al. [30]. These studies were carried out to predict the flow past the SFS2. The main focus of these studies was on capturing the asymmetric flow phenomena of simplified frigate shapes previously investigated by Syms [31] and Herry et al. [8]. These studies highlighted

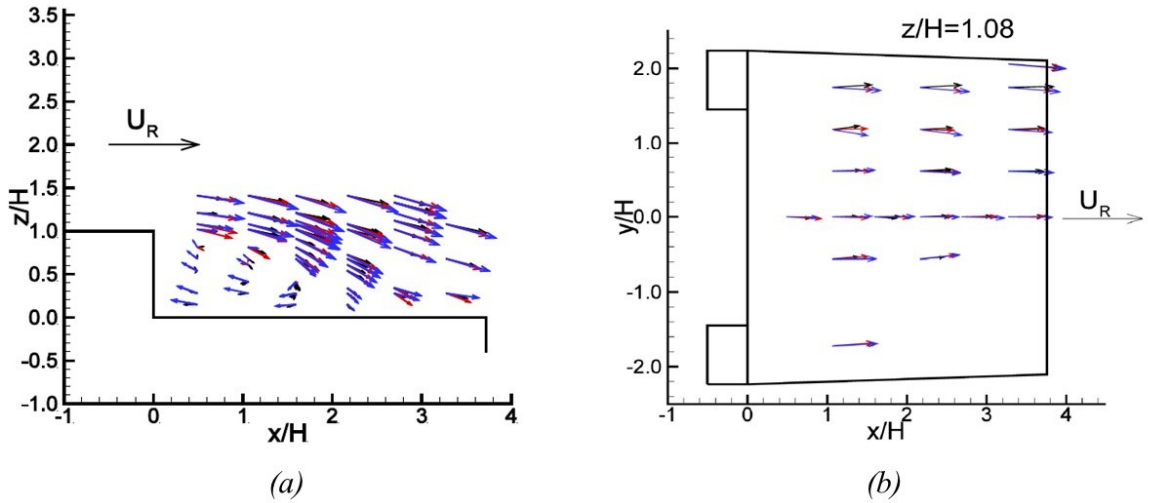

Figure 1.6 CFD results from Snyder and Kang [5] in blue arrows. They were compared to *in-situ* measurements (black arrows) and wind tunnel measurements (red arrows) for a 7-knot headwind case. (a) Ship centerline vertical plane. (b) Horizontal plane parallel to the flight deck [5].

the presence of two stable flow configurations behind each backward-facing step of the SFS2. Each state featured two distinct vortices: one located on one side, whereas the other, narrower and stretched, was seen on the opposite side with respect to the ship midplane. This flow configuration was observed to switch between stable states intermittently.

Figure 1.7 shows the time-averaged vorticity overlaid with streamlines. These results showed that each state featured two characteristic vortices: a larger vortex on one side of the ship behind the step and a smaller vortex on the opposite side with respect to the ship centerline, located above the step. Additionally, the authors observed that in each of the two flow states, the larger vortex behind the step persisted further downstream as compared to its counterpart across the vertical midplane. Rao et al. [6] concluded that the unequal strength of streamwise vortices close to the lateral edges of the ship provoked either bistable flow states. Nevertheless, neither study investigated the temporal behavior of this bistable phenomenon.

Even though computational simulations have proved to be useful in investigating ship airwakes, there exist clear limitations. Simulations require fine computational grid in re-

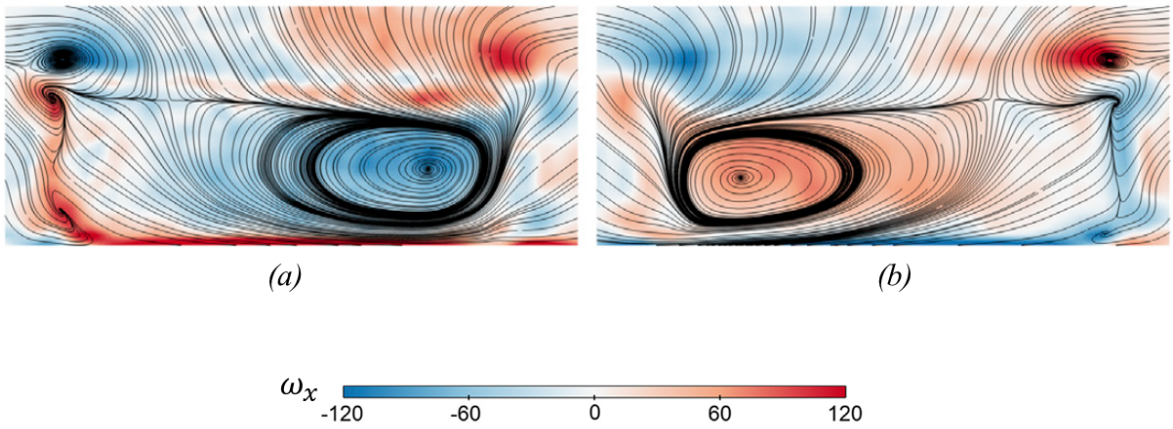

Figure 1.7 Contours of the time-averaged streamwise vorticity overlaid with streamlines in the wake of the ship model showing (a) state 1 and (b) state 2. The plane is located directly downstream of the ship, looking upstream [6].

gions of flow separation as well as precise schemes to accurately model the spatio-temporal characteristics of the ship airwake. This is because of its highly unsteady and turbulent nature. More modern turbulent models such as DES have proven to be insightful. Nevertheless, discrepancies with experimental measurements were observed in some cases. This is perhaps because of the high dissipation levels of the turbulent scales in the airwake, which pose many challenges for most CFD simulations [14]. Finally, computational studies that used LES approaches provided limited insight in the airwake physics because of the lack of suitable validation data and/or overlooked spatio-temporal characteristics of the flow. Consequently, the predictive capabilities of CFD airwake simulations still remain uncertain.

1.2.2 Experimental Airwake Studies

For many years, various experimental techniques have been used to study the flow field around ships. Particularly, recent technological developments in experimental equipment and data processing tools have allowed in-depth studies of the airwake physics using image-based experimental approaches. This section discusses previous airwake research that used an experimental approach. First, *in-situ* measurement techniques such as sonic and ultra-sonic anemometry are presented. Then, studies that involved model-scale testing in wind tunnels such as flow visualization approaches, hot wire anemometry (HWA), multi-hole probes,

Laser Doppler anemometry (LDA), and particle image velocimetry (PIV) based studies are discussed. An emphasis is made on PIV techniques since it is the approach used for the current study.

The airflow over the flight deck of ships has been measured with the goal of improving physical understanding as well as model and simulation validation. Sea trials included the use of different types of anemometers to measure the ship airwake at different locations on ship decks. Unfortunately, this approach presented many challenges and limitations such as the dependence on weather conditions, safety concerns with respect to installation of experimental equipment on ships, time constrains, and high costs. Additionally, much at-sea airwake measurements have limited reliability due to contamination from high levels of electromagnetic interference from ship systems and instruments [21].

Snyder and Kang [5] used ultrasonic, three-velocity component anemometers on the flight deck of a U. S. Naval Academy Yard Patrol vessel to validate CFD simulations. While the data was adequate for validation purposes, the mean velocity direction and magnitude from point measurements did not provide a complete picture of the airflow over the ship deck because very few locations were sampled at a time. Similarly, Luznik et al. [32] performed turbulence measurements at various spatial locations over the flight deck of a 32-meter-long U.S. Navy training vessel using sonic anemometers as well as thermometers. Once again, the data allowed the analysis of mean flow and turbulence statistics but were insufficient for detailed analysis of the airwake due to operational and instrumentation factors such as varying wind direction, inconsistent vessel speed, unequal measurement periods and sparse spacing of anemometers on the flight deck. Overall, *in-situ* measurements are highly dependent on operational and environmental factors. Therefore, most of the data currently used for both physical studies as well as CFD validation are obtained from wind tunnel experiments. The controlled environment in wind tunnels offers the advantage of maintaining constant upstream conditions such as free-stream velocity, pressure, temperature, and Reynolds number (Re) as well as allowing easier access to install measurement equipment,

thus providing reliable measurements at a lower cost.

A few experimental studies of the ship airwake included wind tunnel flow visualization studies. For example, Mora [7] used this technique to study the aerodynamics of the SFS2 model by identifying the three-dimensional flow structures that formed on the flight deck surface. Figure 1.8 shows a top view of the model's flight deck and the flow patterns on the surface as a result of this simple but effective technique. They showed the formation of two foci behind the backward-facing step as well as a flow reattachment region downstream of the recirculation bubble, which were in agreement with the turbulent structures previously identified (see Fig. 1.2 for reference).

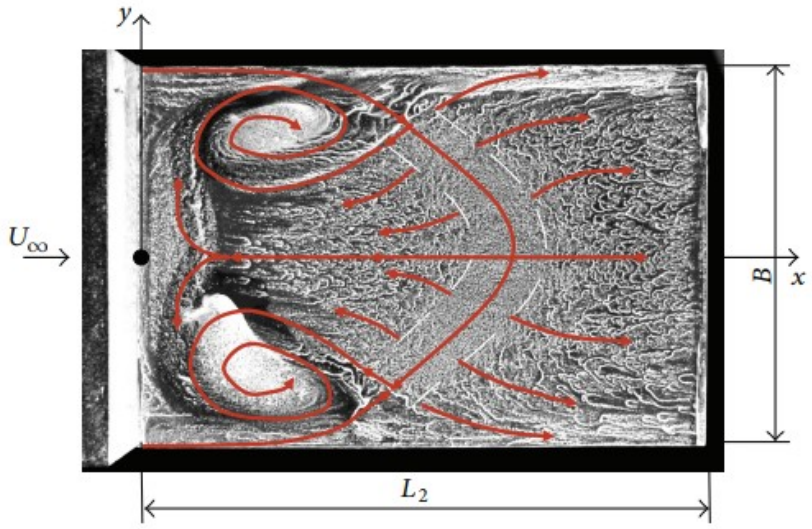

Figure 1.8 Flow pattern on the SFS flight deck surface at zero-angle WOD [7].

Another experimental technique used to study the ship airwake included pressure probes. Specifically, White and Chaddock [33] used multi-hole probes to gather wind speed and turbulence data at various locations over the flight deck of a model Navy frigate and compared them with sea trial measurements. They concluded that the model flow field was not an identical replica of the full-scale field since the wind tunnel measurements underestimated the severity of the turbulence levels measured from sea trials.

Other flow measurement approaches such as hot wire anemometry (HWA) and pressure probes have also been used in ship airwake studies. In 1998, Zan et al. [34] used cross-wire

HWA to map out the flow field in the vicinity of the flight deck of a model frigate. The cross-wire HWA approach was used to measure the instantaneous streamwise and wall-normal velocities, providing two-dimensional flow measurements. The author highlighted that HWA had good resolution and fast response. However, it could not differentiate between forward and reversing flows, resulting in unreliable measurements in zones of potentially reversing flow such as the recirculation region. Another notable study involving HWA measurements was that by Healey [35]. The measurements included instantaneous velocities, turbulence intensities, and spectra at seventeen locations along a typical helicopter glide path over the deck. The gathered measurements provided a single-point database for simulations of helicopter flight in the airwake. However, they were not used to study the physics of airwakes. Overall, HWA has been proven to be suitable for CFD validation and establishing databases. However, it is not effective in mapping spatially correlated velocity fields because this approach yields point measurements at limited spatial locations over the deck, resulting in a limited physical insight into the correlated motions of the flow.

1.2.3 Particle Image Velocimetry (PIV) Approach

Recently, PIV techniques have been more commonly used in ship airwake studies. This non-intrusive technique uses optical methods to obtain instantaneous velocity fields, providing suitable data for physical analyses of the airwake. In 2004, Wadcock et al. [36] studied the aerodynamic interactions between a tandem-rotor helicopter and an amphibious assault ship using PIV measurements. This study used one laser sheet at a fixed streamwise location, perpendicular to the flow direction, to acquire three-component velocity field measurements. A combination of different ship yaw angles and helicopter landing sites were studied. The tunnel and model allowed the translation of the ship in the streamwise direction, which eliminated camera and laser sheet re-calibration for different trials, saving time and reducing uncertainties. It was noted, however, that a disadvantage of this approach was that the laser sheet was no longer parallel to the ship's longitudinal axis in the case of the yawed ship. Nevertheless, the PIV measurements showed the effects of ship yaw an-

gles on deck vortex strength and location. Additionally, measurements from the combined ship-helicopter configurations identified the locations on the deck where the helicopter wake convected, which contributed to the understanding of the DI. This work provided a benchmark for CFD validation and a wealth of information needed to further understand the ship-rotorcraft aerodynamic interactions.

Herry et al. [8] studied the effects of ship yaw angles on the bistable states of the wake behind a three-dimensional double backward facing steps (behavior also observed by Rao et al. [6] in computations). In this case, they used a single laser sheet positioned on the horizontal plane located at the step midheight (see Fig. 1.9). The time-averaged flow fields, viewed from above (see Fig. 1.10) showed clear flow asymmetries with respect to the ship centerline for different yaw angles. The authors concluded than in a headwind, the recirculation region showed two bistable states. However, the yawed ship resulted in biased flow which featured a larger vortex on the port and starboard sides for positive and negative ship yaw angles, respectively (see Fig. 1.10 for reference). Herry's work allowed for the study of coherent flow features in the airwake, which was possible thanks to the spatially correlated PIV measurements. Additionally, these measurements provided valuable information for computational validation. Nevertheless, this study only offered a two-dimensional perspective of the physics of the bistable states. This is because only one measurement plane was used. In order to further understand airwake flow features such as the one studied by Herry et al. [8], three-dimensional correlated measurements in more than one plane are needed. Particularly, these measurements are necessary to identify any interactions between these bistable states and other flow states.

More recently, Dooley et al. [9] combined PIV and LDA approaches to investigate the airwake of a model ship in a water tunnel. The single point measurements using LDA were at a location where a helicopter is expected to hover as it lands on the flight deck. Figure 1.11 shows the time-averaged streamwise and wall-normal velocities as well as the turbulence intensities, respectively. The gaps observed are due to blockage of the PIV cameras by a

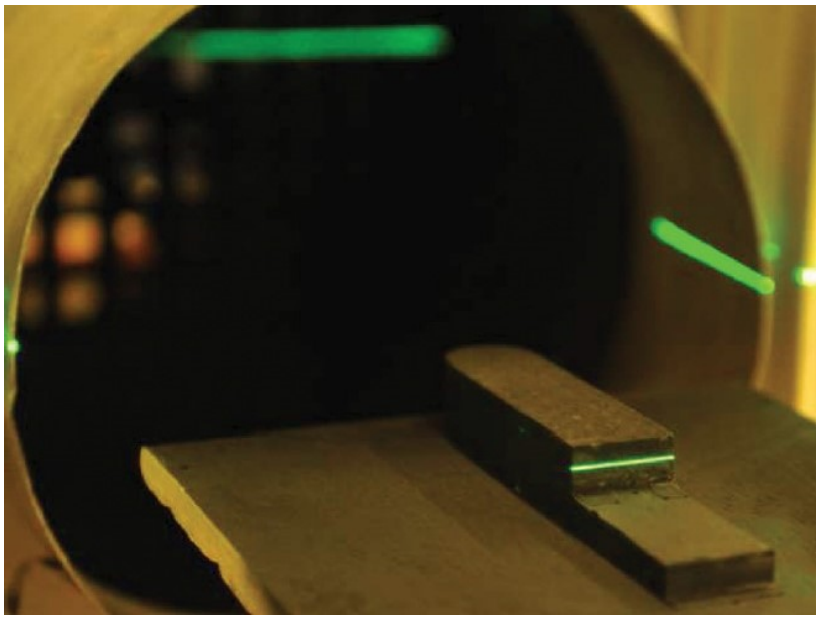

Figure 1.9 Single horizontal laser sheet located at the step midheight to study flow bistability with a three-dimensional double backward facing steps [8].

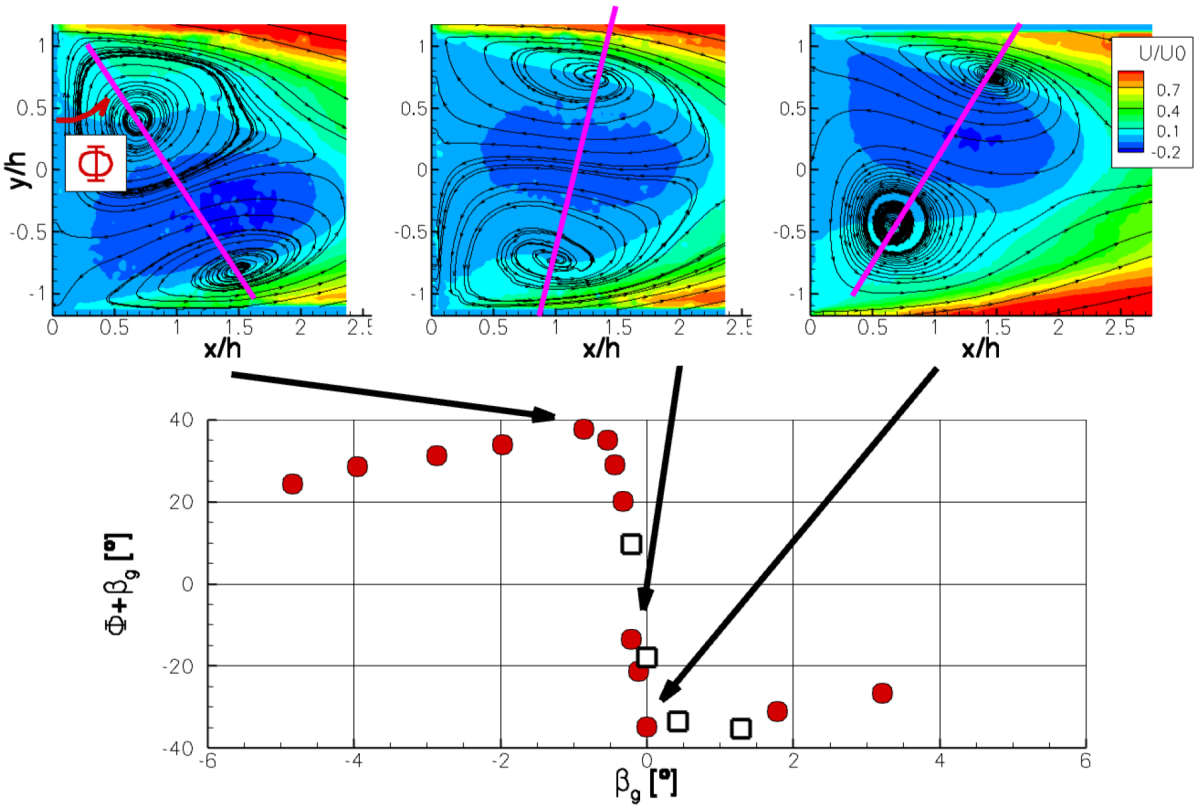

Figure 1.10 The yawed ship resulted in biased flow which featured a larger vortex on starboard and port sides for negative and positive ship yaw angles β_g, respectively. [8].

structural beam of the tunnel. Small discrepancies between the experimental and computational results were found in the shear layer area, where the LDA technique was used. On the other hand, turbulence intensities showed relatively high discrepancies as CFD consistently overpredicted turbulence intensity levels in multiple spatial regions when compared to the experimental data. Overall, this experimental approach presented an interesting alternative to the conventional PIV approach as the LDA point measurements were used to validate PIV measurements. The main focus of this study was computational validation rather than an in-depth study of the physics. Thus, a single laser sheet was sufficient. However, if a similar approach was desired to experimentally study three-dimensional coherent structures in the airwake, a combination of multiple PIV measurement planes and/or LDA measurements in various locations may be required.

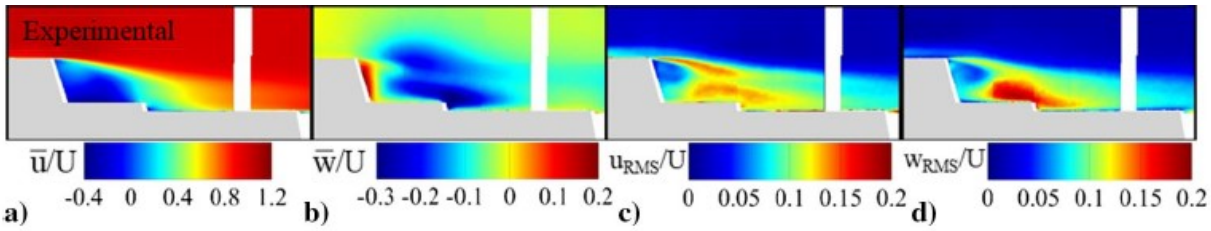

Figure 1.11 Time-averaged streamwise and wall-normal velocities $\bar{u}$ and $\bar{w}$ as well as the turbulent intensities u_{RMS} and w_{RMS}, respectively [9].

Some experimental studies have used two PIV measurement planes, measuring each plane independently and superposing the time-averaged results from the isolated planes to infer three-dimensional behavior. In 2009, Tinney and Ukeiley [10] investigated the flow over a three-dimensional double backward facing step using two PIV planes, measuring each plane independently. This study allowed quantitative measurements with these two planes along the streamwise and spanwise directions, (x, y) and (y, z) planes in Fig. 1.12, respectively. The laser sheet location used for the streamwise plane was varied between seven positions while that of the spanwise plane included twelve locations.

The mean velocity fields and stream traces in the streamwise plane (see Fig. 1.13) clearly showed the recirculation regions behind each step while the mean turbulence stress contours

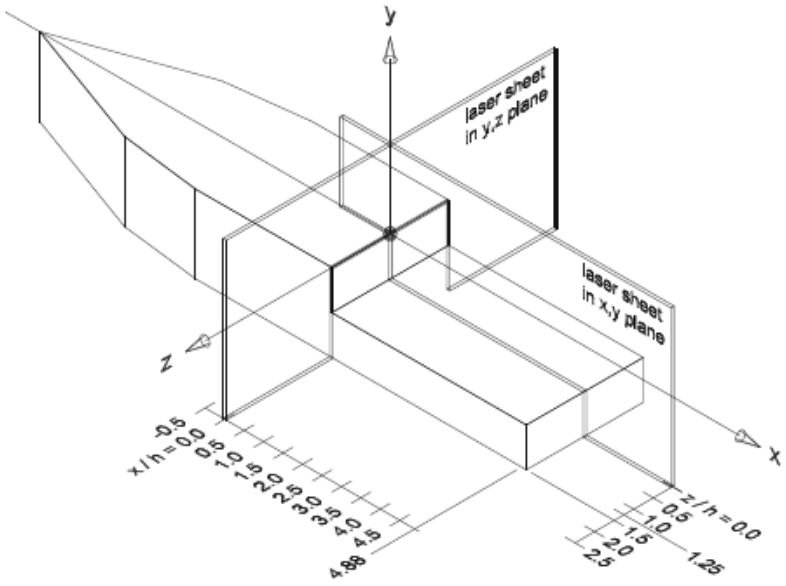

Figure 1.12 Schematic of the model ship and the two measurement planes used by Tinney and Ukeiley [10].

indicated separated shear layers over the flight deck. Measurements from snapshots in the spanwise plane revealed vortex sheets upstream of the steps over the top surface of the model and a horseshoe vortex behind the first step. Additionally, turbulent kinetic energy (TKE) levels in the spanwise planes before and after the flow reattachment region showed agreement with the TKE levels in the streamwise plane (see Fig. 1.14). This demonstrated that using multiple intersecting planes allows for the observation of three-dimensional time-averaged turbulent structures in the airwake. However, the planes under investigations were

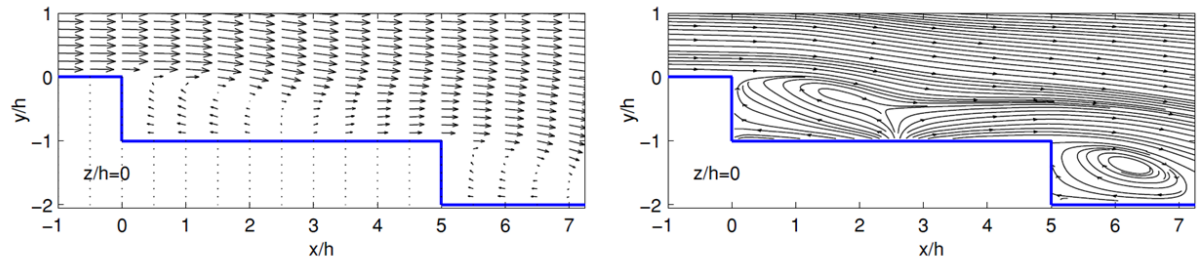

Figure 1.13 Time-averaged velocity fields and stream traces in the streamwise plane along the ship centerline. Study by Tinney and Ukeiley [10].

not temporally correlated with each other but rather measured and processed independently. Consequently, this approach did not allow a three-dimensional spatio-temporal analysis of the airwake, which is needed for a deeper understanding of the flow and ultimately representing the airwake in flight simulators.

Later on, Nacakli [11] used a similar approach while incorporating a helicopter rotor to

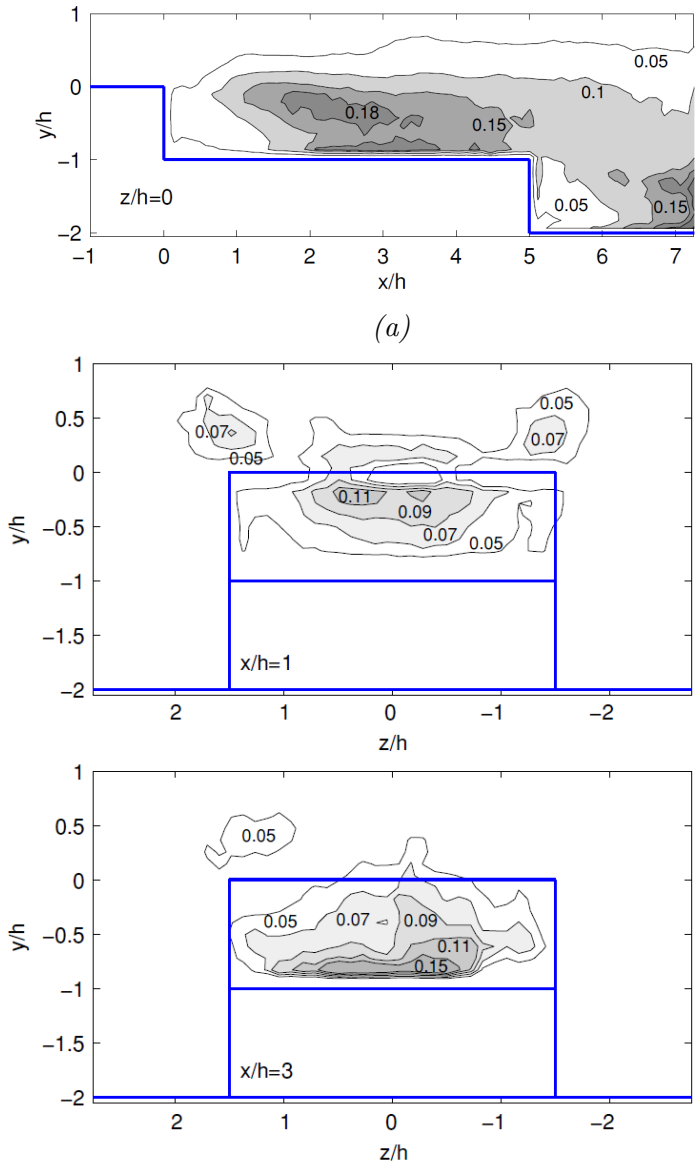

Figure 1.14 Turbulent kinetic energy contours of wall-normal fluctuations in the (a) streamwise and (b) two spanwise planes. Study by Tinney and Ukeiley [10].

analyze its effects on the airwake. PIV surveys included one plane along the ship centerline and one at the mid-deck location perpendicular to the ship centerline. Each plane was measured individually and mean statistics were compared. Additionally, rotor thrust measurements accompanied the PIV surveys. Figure 1.15 shows the flow velocity fields with the rotor on both planes. This study showed the time-averaged effects of the rotor downwash on the ship airwake and provided practical spatial resolution for mapping the thrust coefficient response along both planes. However, the lack of temporal correlation between the intersecting planes limited the three-dimensional applicability of this study, which is fundamental in understanding whole-field characteristics of the airwake/rotorcraft interface.

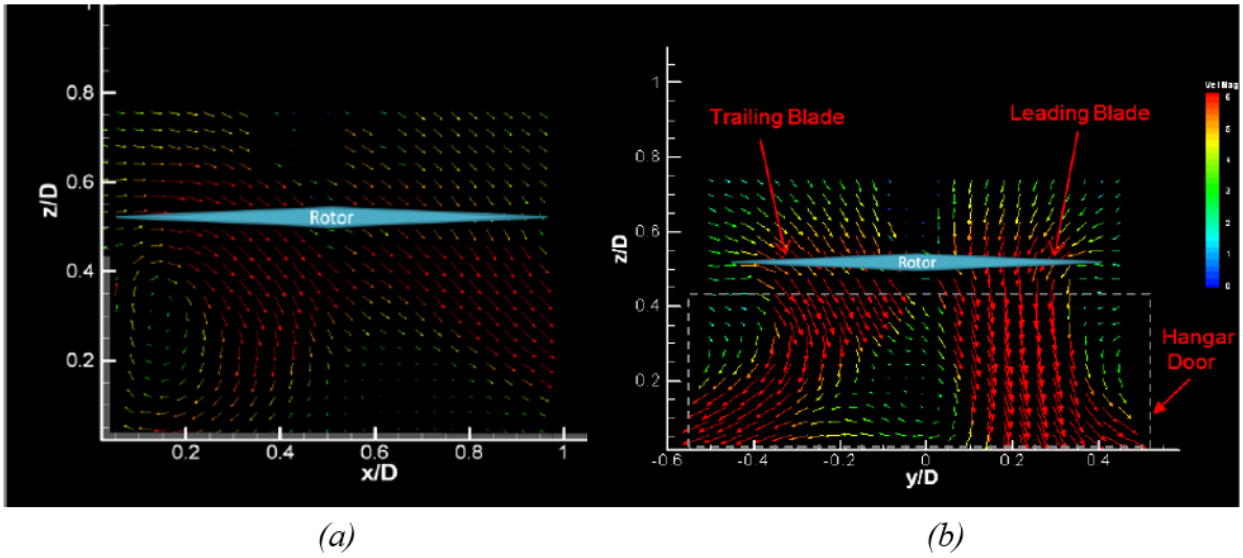

Figure 1.15 Mean flow velocity in (a) measurement plane along ship centerline and (b) measurement plane perpendicular to ship centerline. Both planes include the operating rotor [11].

Other PIV approaches involved measuring the plane along the ship centerline and an intersecting horizontal plane parallel to the flight deck surface. For example, Mora [7] used this approach on a SFS model using PIV complemented with LDA measurements at strategically selected locations within the flow field. Each plane was measured independently and mean flow contours were compared to analyze time-averaged flow features. These measurements showed the spanwise and streamwise extent of the recirculation bubble. However, only

mean flow velocity maps were analyzed, overlooking the temporal behavior of the airwake. Additionally, only 50 instantaneous frames were used, which may limit the reliability of the study due to the possible lack of convergence of the turbulence statistics.

Gallas et al. [12] measured the flow fields over identical planes on a simplified frigate model to study the effects of active flow control on the ship airwake. In this case, the laser sheet was directed through the model and reflected using a mirror, allowing it to be transmitted through the hangar door and illuminate a plane parallel to the flight deck (see Fig. 1.16).

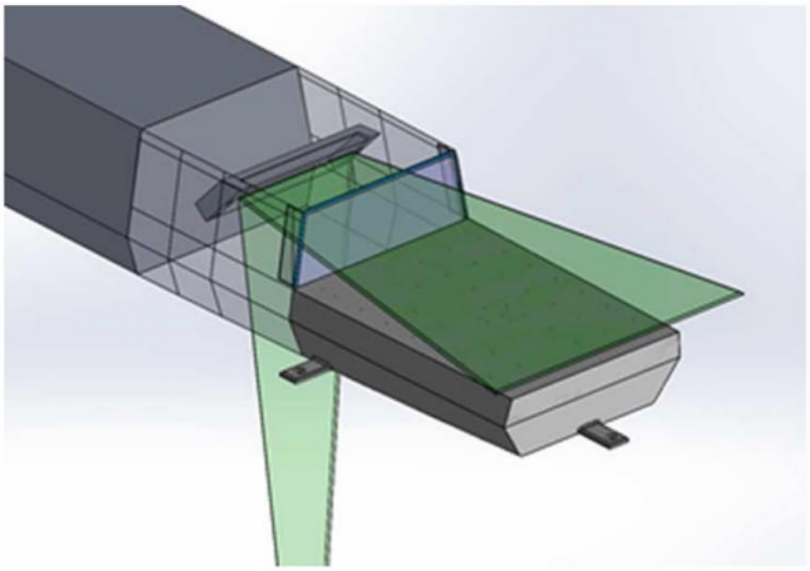

Figure 1.16 Experimental schematic of Gallas et al. [12], which featured a horizontal measurement plane parallel to the flight deck.

The mean flow structure was obtained by superposing the time-averaged results from the two planes. An illustrative map is shown in Fig. 1.17, which displays the magnitude of the streamwise velocity field without active flow control. While this approach is valid for an average flow analysis, three-dimensional, unsteady flow effects could not be analyzed because the measurement planes were again not temporally correlated.

At ERAU, experimental airwake studies were conducted by Palm [13], Seth [14], and Zhu [15]. In 2020, Seth [14] used a combination of HWA and PIV measurements supported by surface oil flow visualization to better characterize the unsteady aerodynamics of the airwake

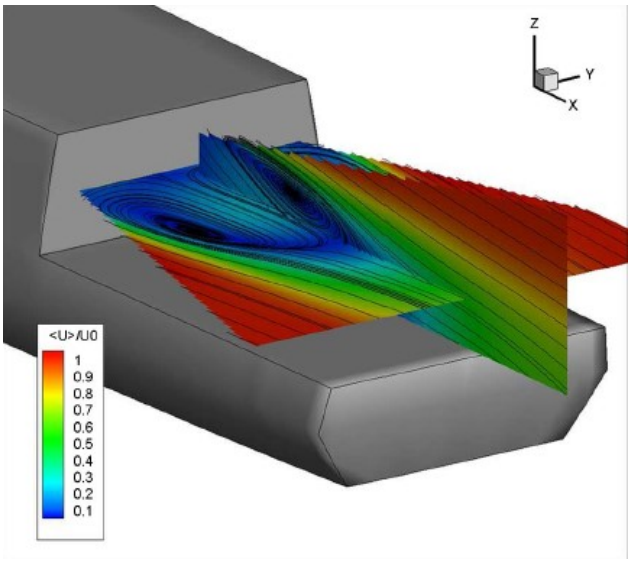

Figure 1.17 Mean velocity contours from superposed measurement planes by Gallas et al. [12].

of the model SFS2. This study involved measuring five streamwise planes (parallel to the ship centerline) and three spanwise planes (perpendicular to ship centerline) independently. The measurements revealed that the airwake comprised large regions of unsteady flow separation and vortical flows over the flight deck. These structures were presumably caused, in part, by the upstream funnel and superstructure of the ship. Additionally, it was suggested that synchronous flow measurements (i.e., measurements from planes that were obtained at the same instants in time) were necessary to study the correlation between the time dynamics of different coherent structures within the airwake.

Later on, Zhu [15] further investigated the SFS2 airwake using PIV measurements and surface oil flow visualization techniques. This study also used velocity fields from independent streamwise and spanwise measurement planes. Modal decomposition was used on the PIV measurements which allowed an inspection of the individual scales of the flow field. This approach was used to carry out a spatiotemporal analysis of the airwake. The reduced order models (ROM) obtained in this study helped understand the dynamics of the large-scale features of the airwake. This study also contributed toward a quantitative, spatiotemporal comparison of complex fluid flows, not just limited to the ship airwake.

In 2022, Palm [13] measured the ship airwake in quartering wind conditions of 10° and 20°. This study used various PIV approaches to measure the flow on planes that were parallel and perpendicular to the ship centerline. The author observed that the recirculation region changed in size and became asymmetric for both quartering wind cases, as shown in Fig. 1.18. Furthermore, a spectral analysis concluded that the streamwise fluctuations contained more energy for the quartering wind cases in the funnel wake region. The author also investigated the effects of Reynolds number on the ship airwake and concluded that the SFS2 airwake was not affected significantly by changes in the Reynolds number range considered i.e., $Re \in [3.2, 6.4] \times 10^6$.

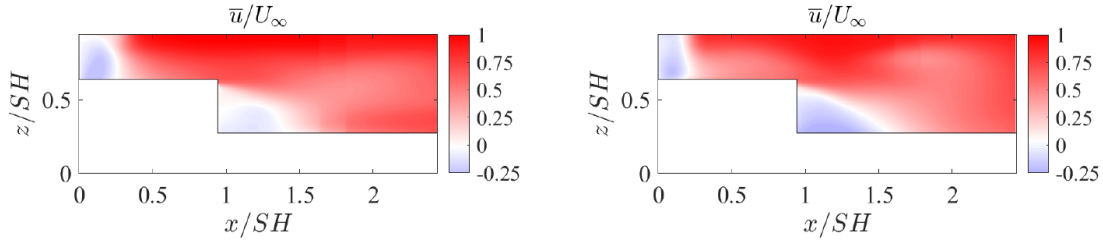

(a) $\psi = 10°$. *(b)* $\psi = 20°$.

Figure 1.18 Streamwise velocity fields at different quartering wind angles. The measurement plane covered the ship centerline [13].

In summary, previous studies that used PIV based approaches have yielded temporally and/or spatially correlated results. However, conventional PIV measurements usually, if not always, used individual measurement planes. As shown in this section, most of the airwake analysis featuring multiple planes were performed by relating predominantly time-averaged features of the flow to infer three-dimensional, whole-field characteristics. However, the turbulent structures in the airwake occupy a certain (sometimes substantial) three-dimensional spatial region with an associated temporal evolution. Hence, to truly understand the physics of the airwake and ultimately understand its interaction with a rotor, temporally and spatially correlated measurements over a three-dimensional domain are required. Further, these kind of measurements are also required for faithful representation of the airwake using reduced order models.

1.2.4 Simulation of the Atmospheric Boundary Layer

The proper simulation of the atmospheric boundary layer in a wind tunnel environment is essential to analyze the ship airwake and it has been treated by many scientists as a prerequisite in previous experimental work [14]. However, modeling the velocity profile, gradients and the turbulence content in the boundary layer poses a challenge. In the past, different approaches have been taken to simulate the atmospheric boundary layer in a wind tunnel environment with varying degrees of success. This section summarizes previous work on these efforts. Furthermore, studies that investigated the effects of the atmospheric boundary layer on ship airwakes are briefly discussed. This is relevant to the current work as a simulated atmospheric boundary layer (sABL) was used to study its effects on ship airwakes.

Methods that have been used to properly simulate the atmospheric boundary layer include the use of elliptical wedge generators, triangular spires, grids, and rods [37]. In 1967, Cowdrey [38] used circular rods that were positioned parallel to the tunnel floor to produce a velocity and momentum deficit in the flow to simulate a boundary layer that conformed closely to the 1/7-th power law [14]. This method has been adapted by other scientists such as Rosenfeld et al. [39], who measured wind load coefficients on a scaled model ship. They concluded that the measurements were found to be highly sensitive to the sABL profile, suggesting that the proper representation of the atmospheric boundary layer was necessary to accurately measure ship aerodynamics.

More recently, Seth [14] characterized the sABL by performing aerodynamic scaling of its thickness, velocity profile, and turbulence. The author's work employed the previously mentioned Cowdrey grid method using horizontal rods and turbulence screens. Figure 1.19 shows a schematic of the experimental setup for this study. This method allowed *apriori* calculations of the initial rod position, diameter, and spacing because the desired velocity profile was based on a theoretical rationale. The author highlighted that the effects of the sABL were important in determining the details of the flow over the deck, but overall the airwake flows with and without the sABL were qualitatively very similar.

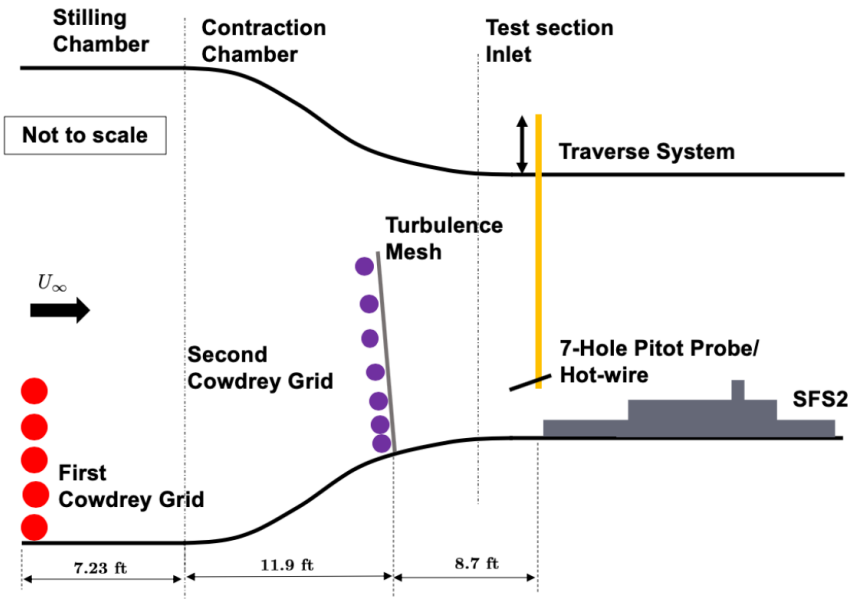

Figure 1.19 Experimental setup by Seth [14]. The Cowdrey grids were used to simulate the atmospheric boundary layer.

Studies by Zhu [15] included experiments with and without the sABL to understand its effects on the airwake structure. This study showed that the energy of the funnel wake and flight deck vortices at low-frequency were significantly affected by the sABL. However, the large-scale organized motions within the airwake seemed relatively unaffected. Furthermore, the author concluded that the structure of the recirculation region was largely unaffected by the presence of the sABL. However, the intensity of the fluctuations seemed to be higher for cases with the sABL, as shown in Fig. 1.20.

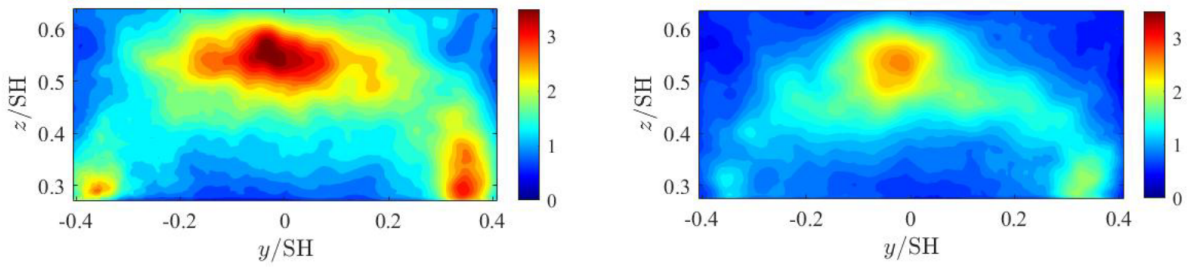

Figure 1.20 TKE of reduced order model (ROM) resolving 90% of energy [15].

Palm [13] also studied the effects of the sABL on the ship airwake with quartering wind conditions. The comparison between cases with and without the sABL revealed that the

greatest effects of the sABL were seen at quartering wind angles of 20°. In this case, some of the vortical structures present in the flow field without the sABL were not present in the cases with the sABL. A closer inspection suggested that the vortical system was shifted outside of the measurement plane, indicating a shift away from the flight deck of the ship due to the added upstream turbulence. The velocity fluctuation and TKE contours provided some insight into the turbulent behavior of the airwake with the sABL. However, the author concluded that different tools were required to consider the more detailed changes in turbulence produced by the sABL.

The review presented in this section strengthens the growing body of evidence that the proper simulation of the atmospheric boundary layer is fundamental in studying the ship airwake problem. The set of Cowdrey grids designed by Seth [14] and previously used by Palm [13] and Zhu [15] were used in the present work. Therefore, cases with and without the Cowdrey grid were measured and compared as part of the current study.

1.3 Thesis Objectives and Outline

After a review of prior research on ship airwakes, it is clear that a three-dimensional physical insight is needed to understand the physics of the complex airwake phenomenon. Although several computational and experimental studies have characterized the mean flow features of the ship airwake, much of its combined spatio-temporal behavior, in general, has not been characterized and so the overall physics are still poorly understood. Understanding the three-dimensional and coupled physics of the airwake requires synchronous spatial and temporal measurements at high resolution. Therefore, with the focus on truly capturing the three-dimensionality of the flow and its turbulent characteristics, the following objectives of this thesis are presented.

1. *High-resolution spatially and temporally synchronous measurements:* A novel measurement technique called time-dependent, dual-plane, stereoscopic PIV (DP-sPIV) allows high-resolution spatially and temporally synchronous measurements. This approach requires the use of two lasers, temporally synchronized with each other, used to il-

luminate two planes, one parallel and one perpendicular to the free-stream. While the streamwise plane is fixed, the spanwise plane is varied. In this manner, a three-dimensional description of the flow is constructed.

2. *Study the temporal and spatial behavior of coherent turbulent structures using conditional averaging:* The spatially and temporally synchronous measurements obtained using the current experimental approach allows for the extraction of the three-dimensional structure of flow features, particularly of large scales, as they are relevant to the DI. Both the temporal and spatial evolution of these large scales are studied using a statistical tool called conditional averaging. This tool is used to isolate and identify specific and/or extreme flow events that can potentially interact with rotorcraft flying over the flight deck. The following flow events are studied:

   (a) *Extreme vertical flow events in the shear layer:* It was suggested that the superstructure shear layer over the flight deck induces unsteady airloads, and is thus relevant to the safety of rotorcraft during near-ship operations. A three-dimensional spatio-temporal perspective of extreme vertical flow events in the shear layer over the flight deck will be identified.

   (b) *Bistable behavior of the hangar door wake:* Conditional averaging applied to the synchronous measurements can isolate each bistable flow state of the hangar door wake. This technique also allows the study of the footprint of each state both upstream and downstream of the wake. In this case, the condition is applied on the spatial field.

   (c) *The transition between the bistable states of the hangar door wake:* A temporal understanding of the flow is needed to study the transition between the two stable flow states of the hangar door wake. A temporal analysis will be used to characterize possible interactions between flow structures in the airwake that could influence the transition between states.

(d) For the events listed above, the flow fields with and without the simulated atmospheric boundary layer (sABL) are measured, analyzed and compared. This allows for the study of the influence of upstream conditions on the ship airwake. Specifically during the events of interest.

Chapter 1 introduces the current work with a brief motivation. Additionally, this chapter includes a literature review on computational airwake simulations, experimental airwake measurements, previous wind tunnel experiments that used the PIV measurement approach for airwake analysis and the importance of using the sABL in airwake studies. Finally, the objectives of this thesis are presented. Chapter 2 documents the experimental approach as well as the tools used for data processing and analysis. A description of the experimental setup used to carry out the necessary spatially and temporally synchronous measurements is provided. Then, details of the stereoscopic PIV (sPIV) measurements and processing are presented. The latter part of this chapter contains a detailed description of the conditional averaging method and its applicability to study the ship airwake. Chapter 3 presents the results obtained using the proposed experimental approach and data processing tools. First, time-averaged results such as mean velocity, turbulence intensity and kinetic energy are shown and discussed. Then, the results of the conditional averaging analysis are presented. Chapter 4 concludes the present research with a summary of the key results and conclusions as well as suggestions for future research work.

2 Methodology

The present chapter presents a detailed description of the experimental approach and the data analysis techniques used to better understand the three-dimensional nature of the ship airwake. Measurements were carried out in the Embry-Riddle Aeronautical University (ERAU) low-speed wind tunnel (LSWT) facility, a closed-return wind tunnel with a closed test section. A 1:90 scale Simple Frigate Shape No. 2 (SFS2) model was investigated using a novel, dual-plane, stereoscopic particle image velocimetry (DP-sPIV) approach. This approach simultaneously measured two flow planes, parallel and perpendicular to the free-stream, over the flight deck. The flow parallel plane was fixed for all measurement sets and the spanwise plane was varied over different measurement sets. The selection of these plane combinations was informed by the characteristic flow structures identified by previous studies on ship airwakes [13–15]. All measurement sets were then repeated when the airwake developed in the presence of a simulated atmospheric boundary layer (sABL).

The instantaneous velocity fields obtained from the DP-sPIV measurements were analyzed using different approaches. First, a more traditional evaluation of the airwake examined the time-averaged velocity fields, turbulence intensity (TI) and kinetic energy (TKE). Then, a conditional averaging approach was used to isolate and study three-dimensional flow events that are likely relevant to rotorcraft operations. The latter part of this chapter describes these data analysis methods in detail.

2.1 Low-Speed Wind Tunnel Facility

The experiments were performed in the Embry-Riddle Aeronautical University (ERAU) low-speed wind tunnel (LSWT) facility, shown in Fig. 2.1. This state-of-the-art wind tunnel is a closed-return tunnel. The closed test section has a height of 1.2 m (4 ft), width of 1.8 m (6 ft) and length of 3.7 m (12 ft). The test section is equipped with corner fillets to minimize the streamwise pressure gradient. This tunnel is capable of reaching speeds up to M = 0.38 (130 $\mathrm{m\,s^{-1}}$ or 425 $\mathrm{ft\,s^{-1}}$). Within the test section, the measured turbulence intensities were $< 0.1\%$ for flow speeds below 45.7 $\mathrm{m\,s^{-1}}$ (150 $\mathrm{ft\,s^{-1}}$), and $< 0.25\%$ for flow speeds between

107 $\mathrm{m\,s^{-1}}$ (350 $\mathrm{ft\,s^{-1}}$) and 45.7 $\mathrm{m\,s^{-1}}$ (150 $\mathrm{ft\,s^{-1}}$).

Figure 2.1 The Embry-Riddle Aeronautical University (ERAU) low-speed wind tunnel (LSWT) facility at the MicaPlex Research Park.

A significant portion of the test section (65% by area) is covered by non-reflective optical-grade glass. This allows for many configurations in terms of laser and camera positioning which provides optimal flexibility and accessibility for non-intrusive measurements. This wind tunnel is also equipped with a heat exchanger to maintain the flow temperature within a tight range and thus holds a constant Reynolds number. Additionally, it has vents used to inject smoke into the tunnel along with a purge system, used to eject the smoke as needed. In this manner the volumetric density of the seeding can be controlled using these venting features. Finally, the extended length of the test section allows for the proper development of the wake of the ship before entering the high-speed diffuser section, a concern with many previously published ship airwake measurements [14]. Together these features make this facility well-suited for high-quality flow measurements of the ship airwake.

2.2 Simple Frigate Shape (SFS2)

The current study investigated a 1:90 scale Simple Frigate Shape No. 2 or SFS2 model, a geometrically simplified but representative Navy frigate developed under the auspices of an international collaborative research program with the U.S. Navy [40]. The SFS2 features sharp angular geometries, which were designed to minimize efforts required to generate computational grids for CFD studies [41]. Despite their relative simplicity, the observed flow features are comparable to full-scale models, making them valuable for fundamental studies [15].

Figure 2.2a shows a schematic of the SFS2 model highlighting its key features. This shape has been widely used for both computational and experimental studies of the airwake. The wind tunnel model used as part of the present effort was previously used by Seth [14], Palm [13], and Zhu [15] for ship airwake studies. Palm [13] refurbished it by applying a new low-reflective matte black finish as part of his studies. The equivalent surface roughness of the model, previously established by Seth [14], is between 600 and 800 grit. Table 2.1 gives the primary dimensions (ship height h_s, width b_w, length l_s, and flight deck length ℓ_f) of the SFS2 ship model at 1:90 and full (1:1) scales. Figure 2.2b also shows the dimensions in feet of the 1:90 scale.

Table 2.1 Dimensions of the SFS2 ship geometry at 1:90 and full scales.

Scale (ft)	h_s (ft)	w_b (ft)	l_s (ft)	ℓ_f (ft)
1:1	55.0	45.0	455.0	90
1:90	0.61	0.5	5.05	1.0

The origin of the coordinate system was at the ship centerline where the superstructure and the flight deck intersect (see Fig. 2.2a). The streamwise coordinate is x, spanwise is y, and wall-normal is z. The instantaneous velocities corresponding to the streamwise, spanwise, and wall-normal directions are u, v, and w, respectively. Additionally, the primary reference length used in this work for non-denationalization is the ship height (h_s), measured from the bottom of the ship to the top surface of the funnel, which is 0.186 m (0.61 ft). The

primary reference length used to calculate Reynolds number (Re) was the ship length l_s, which is 1.539 m (5.05 ft).

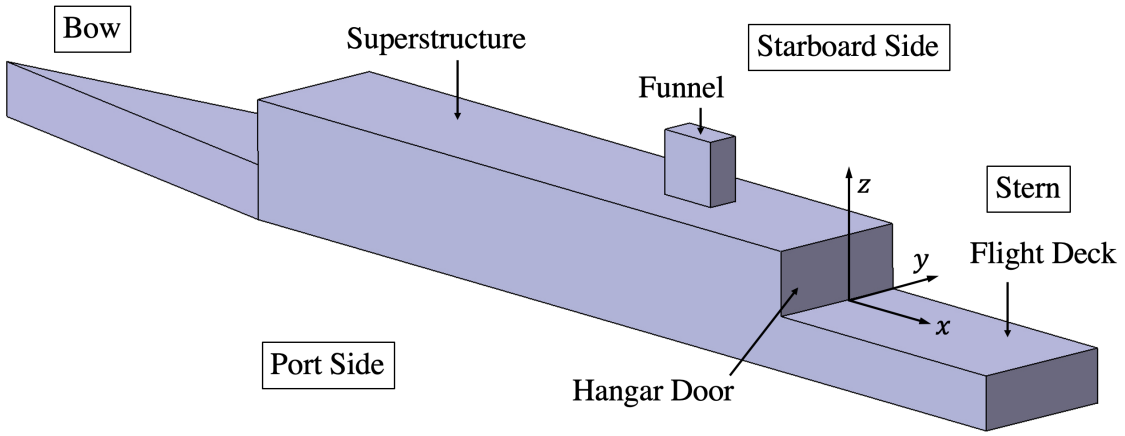

(a) The geometric shape and the terminology used with respect to the SFS2 model [2].

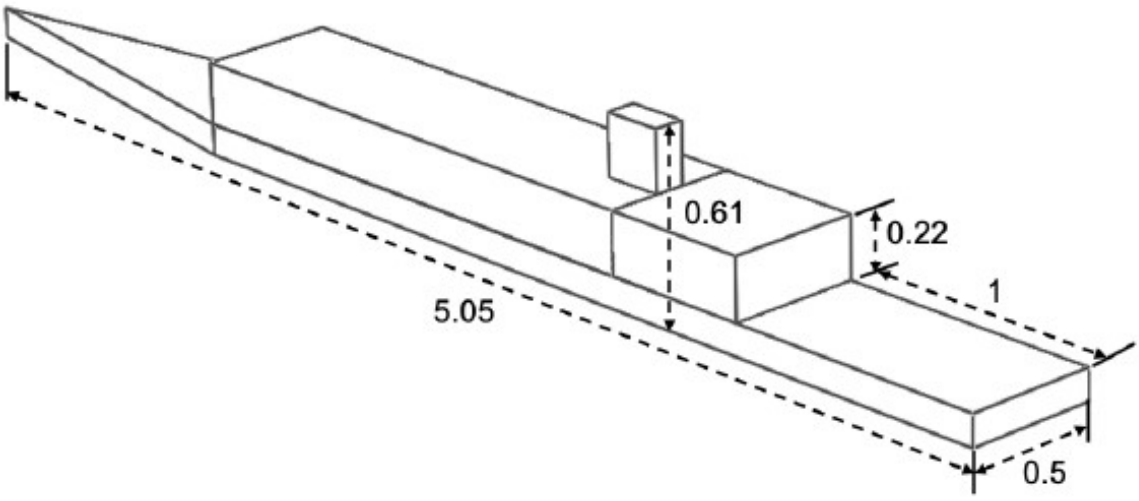

(b) Geometry of the scaled model SFS2 . Dimension are in feet (ft) [14].

Figure 2.2 Schematics of the SFS2 model highlighting its key features and dimensions.

2.3 Simulated Atmospheric Boundary Layer (sABL)

The literature review presented in the previous chapter emphasized the importance of properly simulating the atmospheric boundary layer for ship airwake studies. Winds constantly blow over the sea, so it is essential to take into account the turbulence intensity and velocity profile (or gradient) of the atmospheric boundary layer to properly analyze its effects on the flow over the ships' decks. Previous work by Seth [14, 37, 42] established the scaling

of the sABL for the LSWT facility used in the present research. One of the objectives of Seth's work was to achieve a mean sABL velocity profile that matched the 1/7-th power law along with a representative peak turbulence of about 10% of the free-stream velocity in the wall region. To achieve this, Seth used two sets of Cowdrey grids, comprised of horizontal rods [38]. The first set was located upstream in the settling chamber of the LSWT and had five rods stacked near the floor with a separation of 0.05 m (2 in) between them. Each rod was 4.39 m (14.4 ft) long and 0.11m (4.5 in) in diameter, as shown in Fig. 2.3. The second Cowdrey grid was located further downstream at the end of the contraction section of the LSWT and consisted of seven smaller rods of 1.52 m (60 in) in length and 0.027 m (1.05 in) in diameter. This Cowdrey grid also had a turbulence screen to homogenize the flow as shown in Fig. 2.3. This same set of Cowdrey grids designed by Seth [14] and previously used by Zhu [15] and Palm [13] were used in the present work.

Figure 2.3 Two sets of Cowdrey grids in the LSWT facility used in the present study [14].

Figure 2.4a shows the resulting mean velocity profile compared to the 1/7-th power law and the logarithmic law model, indicating sufficient development of a turbulent boundary layer in the test section. Figure 2.4b shows the resulting turbulence intensity in the test section using the sABL as well as a comparison to previous experimental atmospheric boundary simulations found in the literature [43–45]. The turbulence intensity of the sABL is important for ship airwake measurements as it influences the large turbulent structures under

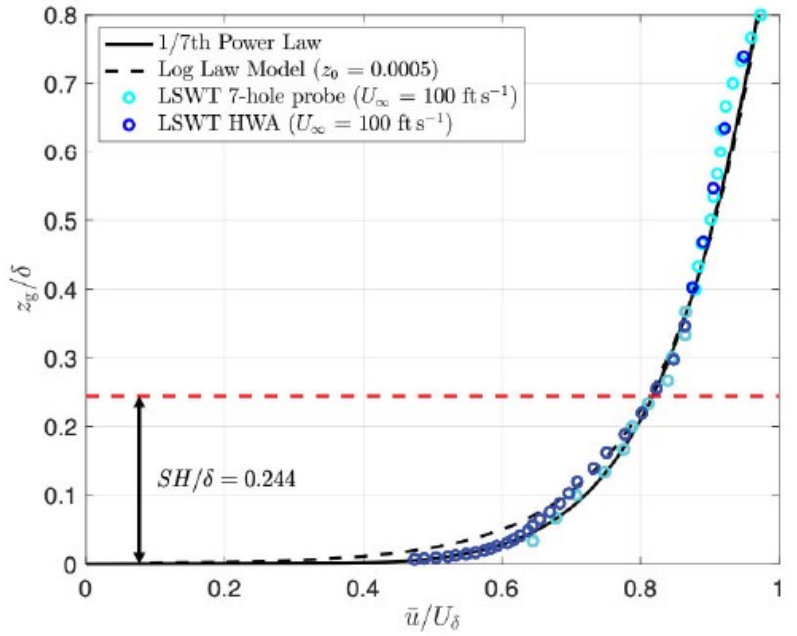

(a)

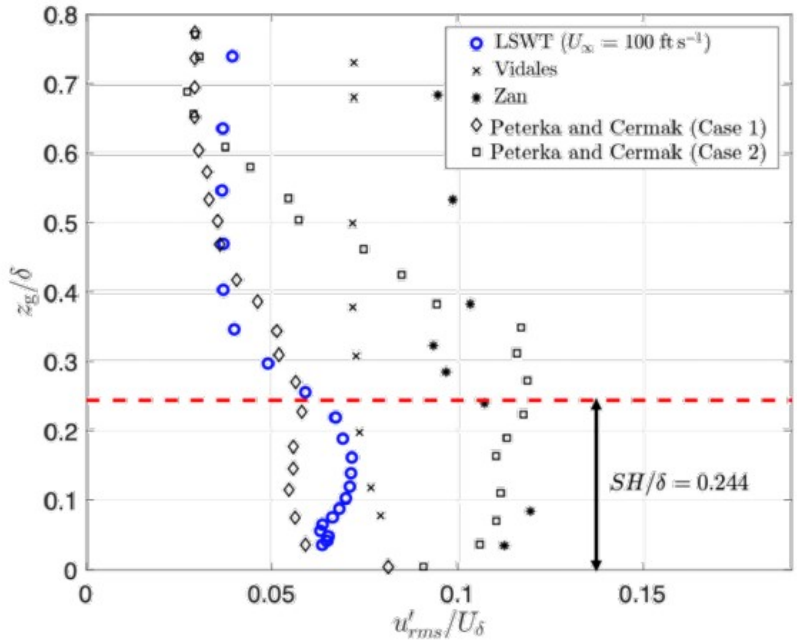

(b)

Figure 2.4 (a) Resulting mean velocity profile of the sABL compared to the 1/7-th power law and the logarithmic law model. (b) Resulting turbulence intensity of the sABL compared to measurements in the literature [14].

investigation. Overall, the resulting velocity profile and turbulence intensity are representative of an atmospheric boundary layer and will enrich the current work by providing a more accurate environment to study the ship airwake.

2.4 Dual Plane Stereoscopic Particle Image Velocimetry (DP-sPIV)

This section describes in detail the experimental approach used to measure the ship airwake over the flight deck region, which is primarily where the rotorcraft operates and where a deeper physical insight of the airwake is necessary. The non-intrusive optical technique called particle image velocimetry (PIV) was used to obtain instantaneous velocity fields. This approach involves capturing images of micro-sized aerosol particles illuminated by a laser sheet. High-speed lasers are used to illuminate these aerosol particles within the desired field of view (FOV) while high-speed cameras simultaneously record images of these particles. Image processing algorithms are then used to reconstruct a time-history of velocity fields [15].

PIV approaches may be stereoscopic or planar. The primary difference is in the number of velocity components resolved [13]. Planar PIV requires at least one camera positioned perpendicular to the laser sheet. This PIV technique can resolve two velocity components within the plane of interest. Stereoscopic PIV is based on the principle of stereoscopic imaging, which requires at least two cameras to image the illuminated flow particles from different perspectives, while focusing on a single plane. To do so, Scheimpflug mounts are used to adjust the relative angles between the image, lens, and object planes of each camera such that the planes converge on a single point (see Fig. 2.5) [17]. The combination of both camera projections allows the reconstruction of a third velocity component (out of plane component) within the measurement plane [16]. This third component is in addition to the two components resolved using a planar PIV approach. Figure 2.5 shows the different arrangements of the cameras for planar and stereoscopic PIV.

The present work utilized a novel method called dual plane stereoscopic particle image velocimetry (DP-sPIV), in which two flow planes, one parallel and one perpendicular to

the free-stream, were measured simultaneously using the stereoscopic PIV approach. Each measurement plane required the use of one high-speed laser and two high-speed 4 Megapixel cameras. This allowed for stereoscopic measurements at high sampling frequencies.

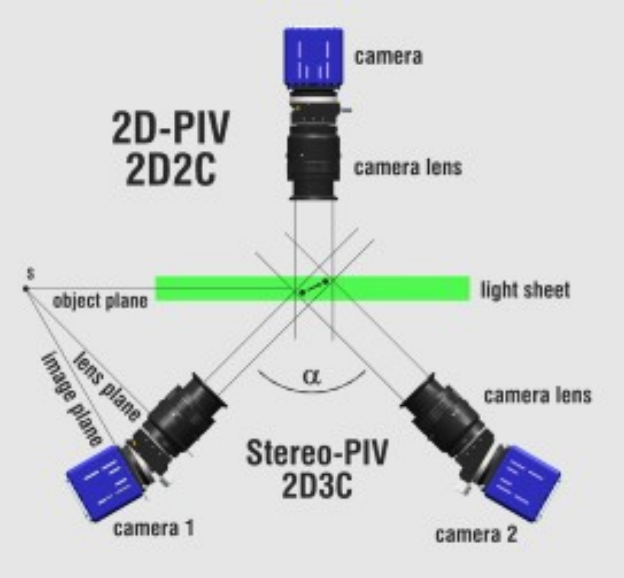

Figure 2.5 The planar (top) and stereoscopic (bottom) PIV approaches [16].

A schematic of the experimental setup is shown in Fig. 2.6. As previously discussed, the Cowdrey grids were located upstream of the wind tunnel test section to appropriately simulate the atmospheric boundary layer. The model SFS2 was mounted on the test section floor. The high-speed cameras measuring the streamwise plane (in blue) were placed infield of the tunnel while the spanwise plane cameras were located one on each side of the tunnel (one infield and one outfield). The high-speed lasers, whose laser beams were spread into thin sheets by appropriate optics, were located directly above the test section, allowing both the streamwise and spanwise planes to be illuminated in the desired manner. Note that the optics and lasers have been omitted from this schematic for clarity. The seeder, located infield near the settling chamber, injected smoke, which was then circulated through the tunnel until the aerosol was homogeneously mixed. For trials without the sABL, the Cowdrey rods were removed to allow turbulence-free airflow in the test section. However, the camera and laser configurations remained unchanged.

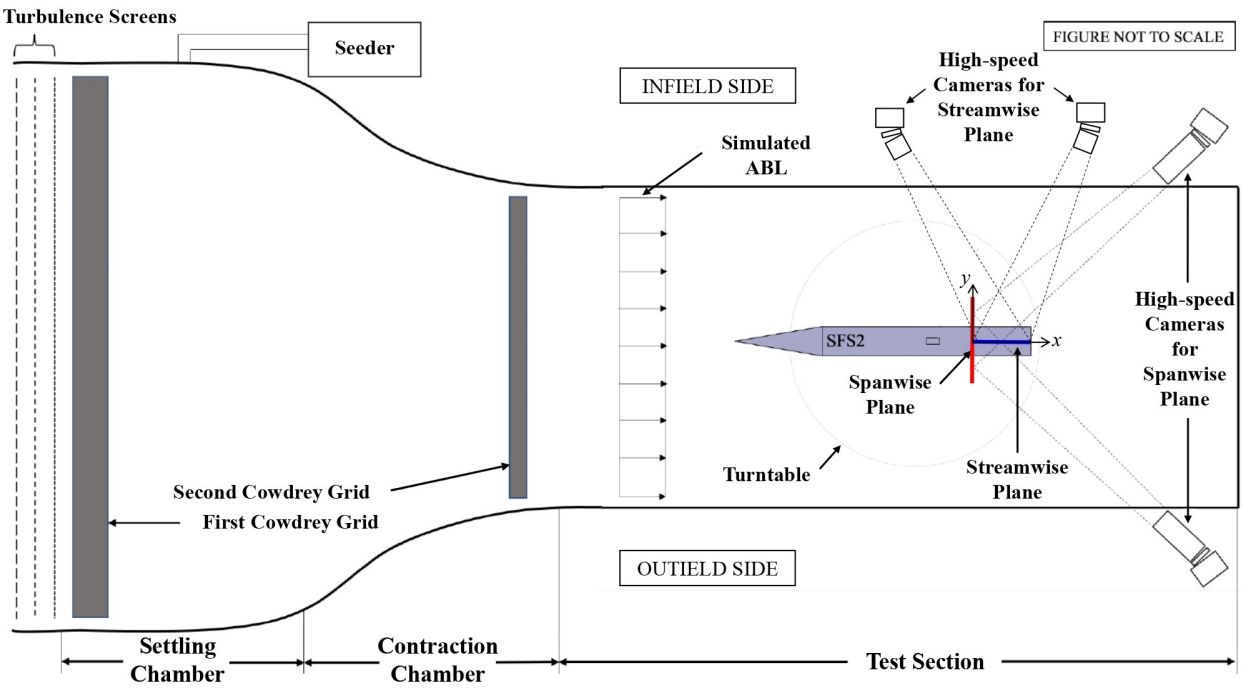

Figure 2.6 A schematic of the overall experimental instrumentation.

The DP-sPIV approach essentially used two independent stereoscopic PIV systems. As illustrated in Fig. 2.7a, each system comprised one high-speed laser and two high-speed cameras. System 1 (in blue) and system 2 (in red) were used for the streamwise and spanwise plane measurements, respectively. The timing of each system was controlled using a high-speed synchronizer. Figure 2.7b displays the oblique angles of the high-speed cameras necessary to carry out stereoscopic PIV measurements. The streamwise camera angle θ_1 was limited to 30° while the spanwise cameras allowed an angle θ_2 between 45° and 55°. These angles were limited by the availability of space on either side of the tunnel. However, they were consistent with previous PIV airwake studies [13–15].

The streamwise cameras (system 1) were fitted with microlenses of 105 mm (f-stop 2.8) focal length, and the spanwise cameras used ones with 200 mm (f-stop 4) focal length. A Scheimpflug mount was used on each camera to ensure uniform focus (see Fig. 2.5 for reference). Figure 2.8 shows the test section configuration for the present experiment with both lasers firing simultaneously.

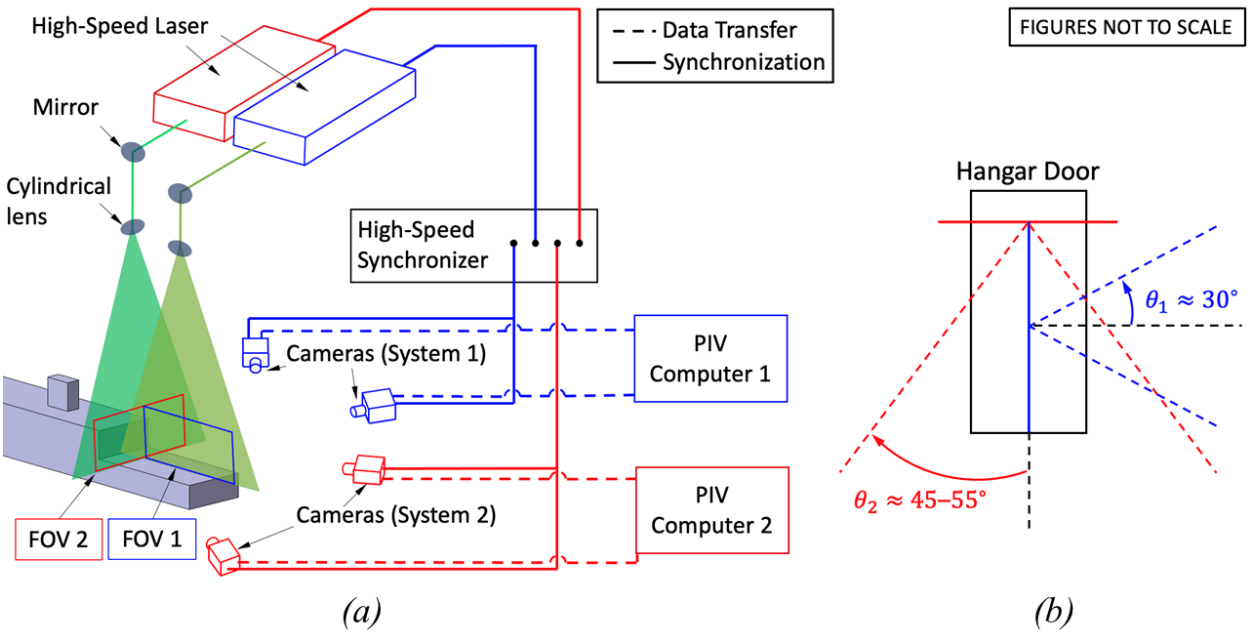

Figure 2.7 (a) Schematic of the experimental configuration for the dual-plane PIV system. (b) Top-down view of the oblique angles at which the cameras were positioned.

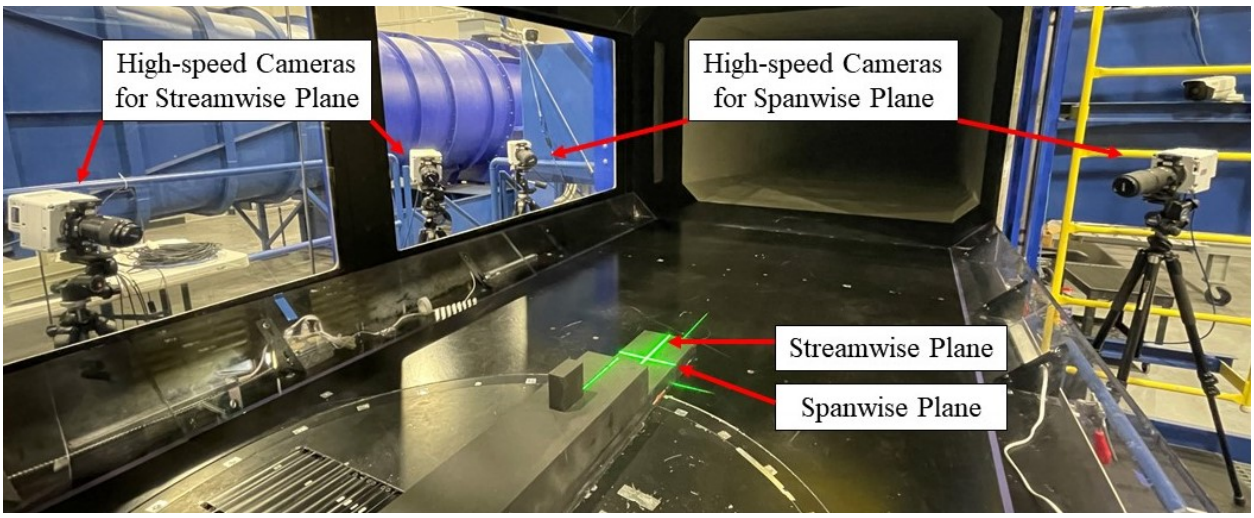

Figure 2.8 Test section configuration with both lasers firing simultaneously.

Each 30 mJ/pulse, Nd:YLF laser system consisted of a laser head, power supply, and a cooling unit. The emitted laser beams were passed through collimators and spread into a sheet by cylindrical lenses, as shown in Fig. 2.9. The cylindrical lenses had focal lengths of 25 mm and 50 mm for the streamwise and spanwise measurement planes, respectively. This resulted in the streamwise laser sheet being wider than the spanwise laser sheet, which was

desirable due to the larger dimension of the field of view parallel to the free-stream. The thicknesses of the laser sheets were 3 mm for both stereoscopic measurement planes as a compromise between laser brightness and the ability to capture out-of-plane motion.

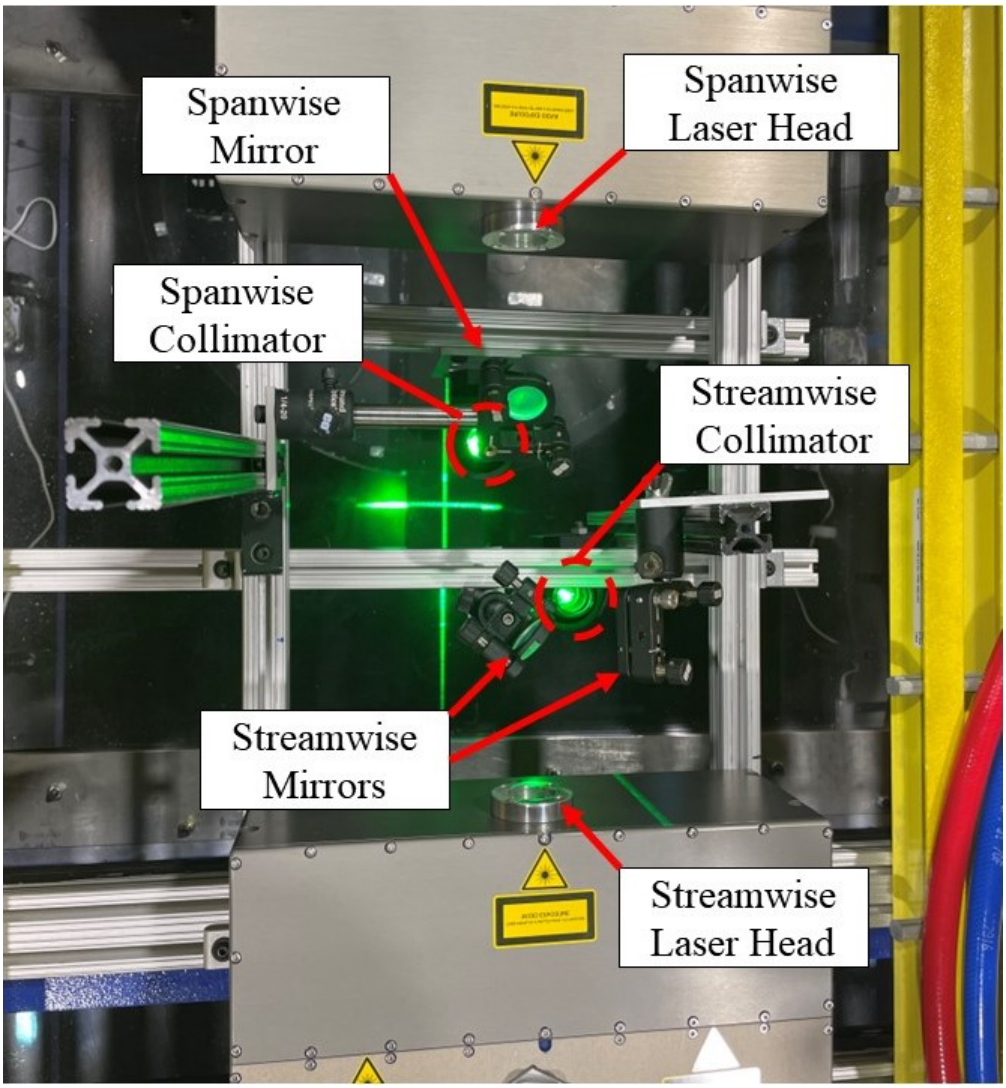

Figure 2.9 Top view of the experimental configuration with both lasers firing simultaneously.

A ViCount Compact 5000 smoke generator was used to generate seeding aerosol. According to the manufacturer [46], the mineral oil-based particles were consistently between 0.2 and 0.3 µm in diameter. The aerosol was injected from the infield side of the settling chamber (see Fig. 2.5 for reference) at low speeds (3.05 $\mathrm{m\,s^{-1}}$ / 10 $\mathrm{ft\,s^{-1}}$). The aerosol was then circulated in the tunnel until it was homogeneously mixed, uniformly seeding the

test section. Embry-Riddle's state-of-the-art LSWT facility allowed purging of the aerosol through a PIV venting system if it became excessive, allowing optimal control of the seeding density in the tunnel.

To optically isolate each one of the two PIV systems, a delay was introduced into the timing of both systems as shown in Fig. 2.10. In this figure, the first two rows correspond to PIV system 1, and the latter two rows to PIV system 2. For either system, the first pulse of the laser was fired at the end of the first frame, and the second pulse of the laser was fired at the beginning of the second frame. The duration between the first and second pulses is referred to as the straddling time Δt. The straddling time of system 1 was $\Delta t_{sw} = 32$ µs and $\Delta t_{sw} = 26$ µs for cases with and without the sABL, respectively. Similarly, the straddling time of system 2 was $\Delta t_{sp} = 20$ µs and $\Delta t_{sp} = 18$ µs for cases with and without the sABL, respectively. A shorter Δt_{sp} was required because the out-of-plane velocity for all spanwise planes was greater compared to the streamwise plane, so, the particles left the image plane more rapidly. On the contrary, a longer Δt_{sw} and Δt_{sp} were needed for trials with the sABL because the free-stream velocity was significantly lower, which required a longer time between captured frames for the algorithm to identify enough particle movement and accurately reconstruct the velocity fields.

The two PIV systems were staggered in time, and a constant (i.e., invariant with sampling frequency) offset of $\tau = 1.6$ ms existed between the two systems (see Fig. 2.10). Previous experimental airwake studies by Seth [14], Palm [13], and Zhu [15] used a programmable timing unit (PTU) to synchronize the high-speed lasers and cameras. However, a PTU does not allow synchronization of two systems working simultaneously. Thus, a signal generator triggered by a MATLAB script was used to provide the timing signals necessary to control the two systems as shown in Fig. 2.10. The Reynolds-number independence of the present flow field was highlighted in the literature [13, 14]. Hence, both experiments with and without the sABL were carried out at a single free-stream velocity U_∞ of 30.5 $\mathrm{m\,s^{-1}}$ (100 $\mathrm{ft\,s^{-1}}$). Using the SFS2 model length l_s as reference, this yielded a Reynolds number of 3.21 x10^6.

The sampling size of each measurement configuration was 7500 image pairs. The first dataset used a sampling rate of $F_s = 25$ Hz to obtain well-converged turbulence statistics. The second dataset used $F_s = 300$ Hz to examine the temporal evolution of the flow structures and their spectral characteristics. Thus, the total sample periods were $T_s = 300s$ (25 Hz) and $T_s = 25s$ (300 Hz), respectively. Table 2.2 shows a summary of all the experiment parameters for both measurement planes.

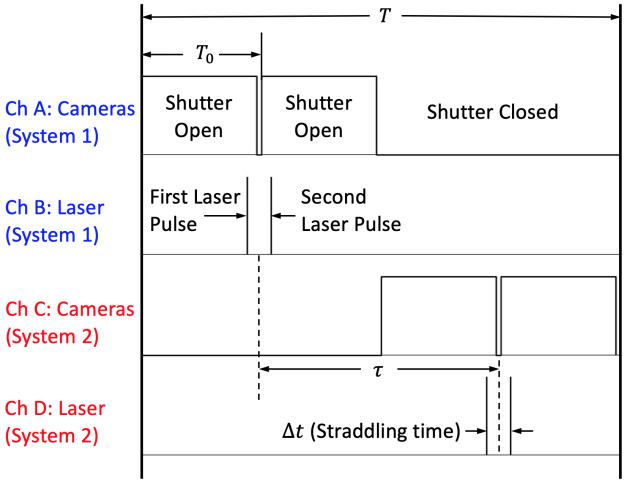

Figure 2.10 Timing diagram for the high-speed lasers and cameras. Channels A & B control PIV system 1 (blue), whereas C & D control PIV system 2 (red).

Table 2.2 DP-sPIV experiment parameters for streamwise and spanwise measurement planes.

U_∞ ($\mathrm{m\,s^{-1}}$/ $\mathrm{ft\,s^{-1}}$)	Re (10^6)	Δt_{sw} w/sABL (µs)	Δt_{sw} w/o sABL (µs)	Δt_{sp} w/sABL (µs)	Δt_{sp} w/o sABL (µs)	F_s (Hz)	T_s (s)
30.5/100	3.21	32	26	20	18	300	25
30.5/100	3.21	32	26	20	18	25	300

2.4.1 Regions of Interest (ROI)

Measurements were carried out on four spanwise-streamwise plane combinations as shown in Fig. 2.11. The planes in red denote the four spanwise measurement planes and the plane in blue the streamwise plane. This plane was fixed at the ship centerline and extended between spanwise plane 2 and 4 (SP2 and SP4).

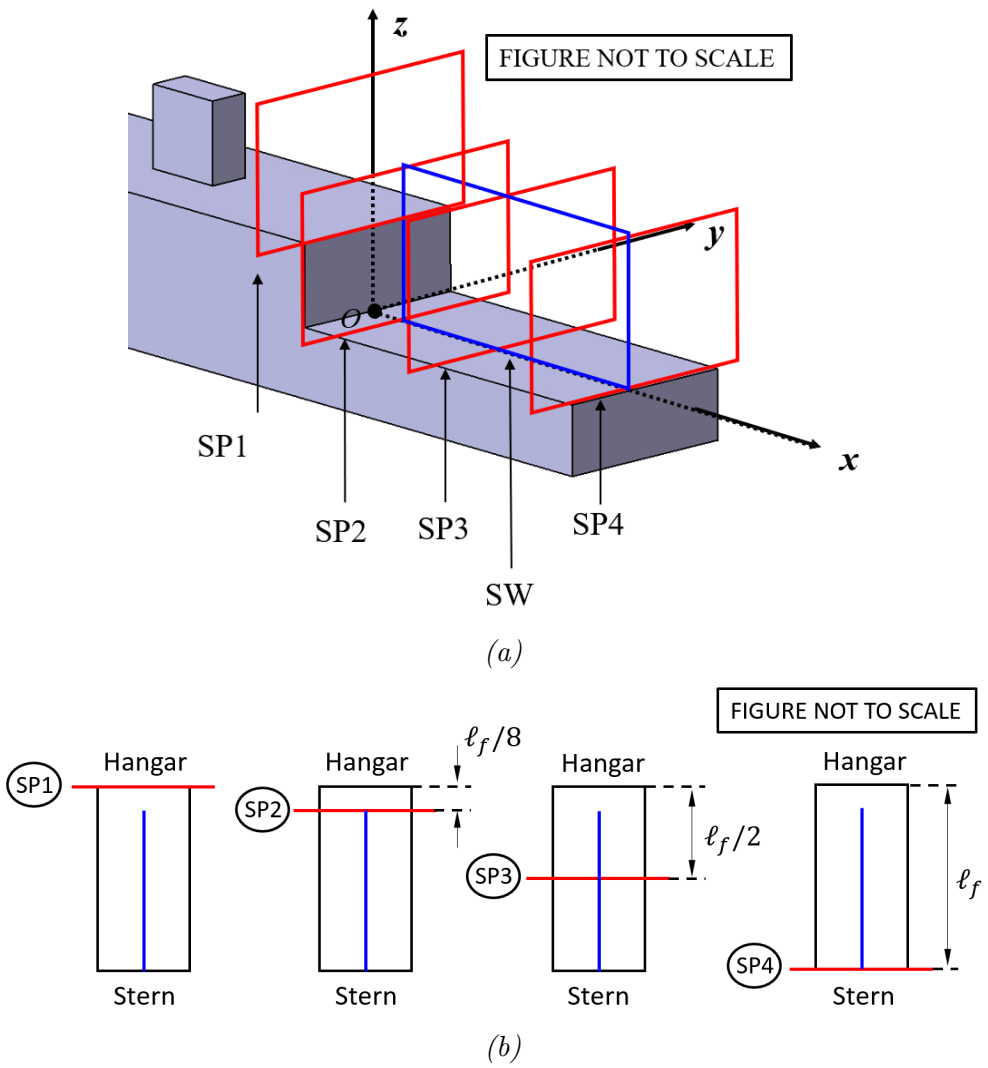

Figure 2.11 (a) Three-dimensional and (b) top-down view of the four streamwise-spanwise plane combinations investigated in the current study. The dimension ℓ_f is the length of the flight deck.

The regions of interest (ROI) were selected based on previous airwake studies [13–15]. The spanwise planes were located in flow areas where the signature of energetic flow structures that could have a significant impact on rotor systems were previously observed (see Fig. 1.2). The first ROI, investigated using spanwise plane 1 (SP1), was at the top edge of the hangar door, behind the funnel of the ship. According to the literature survey, this region contained vortices generated by the superstructure and also the structure of the funnel. The second ROI (SP2) was located 1/8-th of the flight deck length ℓ_f from the hangar door (see Fig. 2.11b).

This plane was chosen to capture the recirculation region behind the hangar door as well as its interaction with the upstream vortices generated by the superstructure. The downstream development of the funnel wake is also captured by this plane. The third ROI (SP3) was the mid-deck location. Most rotorcraft operations involve landing and taking off from the center of the flight deck, making this region a priority for ship airwake studies. Lastly, the fourth ROI (SP4) was selected to investigate the development of turbulent structures as they exit the flight deck. This provided a rear boundary to completely characterize the flow over the deck. The streamwise plane was chosen at the centerline of the ship to provide an anchor plane for the spanwise measurement planes.

The full resolution of each high-speed camera was 1600-by-2560 px. However, different resolutions were selected for each plane to keep the dimensions of the spanwise field of view (FOV) constant. The camera resolution was changed depending on the distance between each measurement plane and the cameras (whose position remained fixed) as well as the camera angles. For all spanwise and streamwise measurement planes, the vertical dimensions of the FOV were between 110–140 mm (4.3–5.5 in) and the horizontal dimensions were between 200–250 mm (7.9–9.8 in). A summary of the FOV dimensions as well as the camera and pixel resolutions is shown in Table 2.3.

Table 2.3 Dimensions of the FOV as well as camera and pixel resolutions for each measurement plane.

Plane	FOV Dimensions (mm^2)	Camera Resolution (px^2)	Pixel Resolution ($px^2/\mu m^2$)
SP1	120 X 230	1600 x 2480	75 x 116
SP2	130 X 200	1600 x 1920	85 x 105
SP3	120 X 220	1600 x 1920	75 x 115
SP4	110 X 240	1600 x 2480	69 x 117
SW	140 X 250	1440 x 2304	100 x 105

2.4.2 Measurement Errors and Uncertainty

In the case of stereoscopic PIV measurements, common sources of error include camera and laser sheet misalignment, excessive or insufficient seeding in the tunnel, incorrect camera

calibration, highly oblique camera angles, etc. The DP-sPIV approach adds another layer of complexity due to the staggering of two independent stereoscopic PIV systems. These additional error sources include laser and/or camera missfiring, system response lag and timing inconsistencies.

Rigorous error mitigation strategies were adopted. For instance, prior to carrying out each experimental run, an oscilloscope was used to ensure the signals generated by the synchronizer were timed appropriately, ensuring the time offset between PIV systems was constant as well as independent of the sampling frequency. Additionally, the brightness of each dataset was evaluated to ensure errors arising from issues such as laser missfiring and system response lag were eliminated. The algorithm computed the average brightness of each image (in units of pixel counts) and plotted it as a function of image number so any anomaly could be easily identified prior to processing the data. As an example, Figure 2.12 shows, in blue, the average brightness (in terms of pixel counts) of a 7500-frame dataset as a function of image number. Based on prior work [13–15], it was determined that if the average pixel count of any image varied by more than 30 pixels from the cumulative average, the laser and/or cameras had misfired and the dataset was no longer suitable for processing. The upper and lower brightness limits (red dotted lines) indicate the 30 pixel variation from the cumulative average (black dotted line).

The algorithm estimated measurement uncertainties based on the statistical analysis of Wieneke [47]. This method used the difference in intensity patterns between two frames and analyzed the effects of shifting the peak of the correlation function. This was used to obtain a standard deviation function, which was then converted into an uncertainty for the displacement vectors. The resulting time-averaged uncertainty was normalized by the time-averaged velocity at each spatial location to obtain a relative uncertainty. Figure 2.13a shows an example of the resulting uncertainty in the streamwise velocity $\bar{u}_{unc}$ normalized by the time-averaged streamwise velocity $\bar{u}$ in spanwise plane 1. Note the outline of the funnel was added to the figure. The maximum uncertainty was 1% of $\bar{u}$ in the funnel wake region.

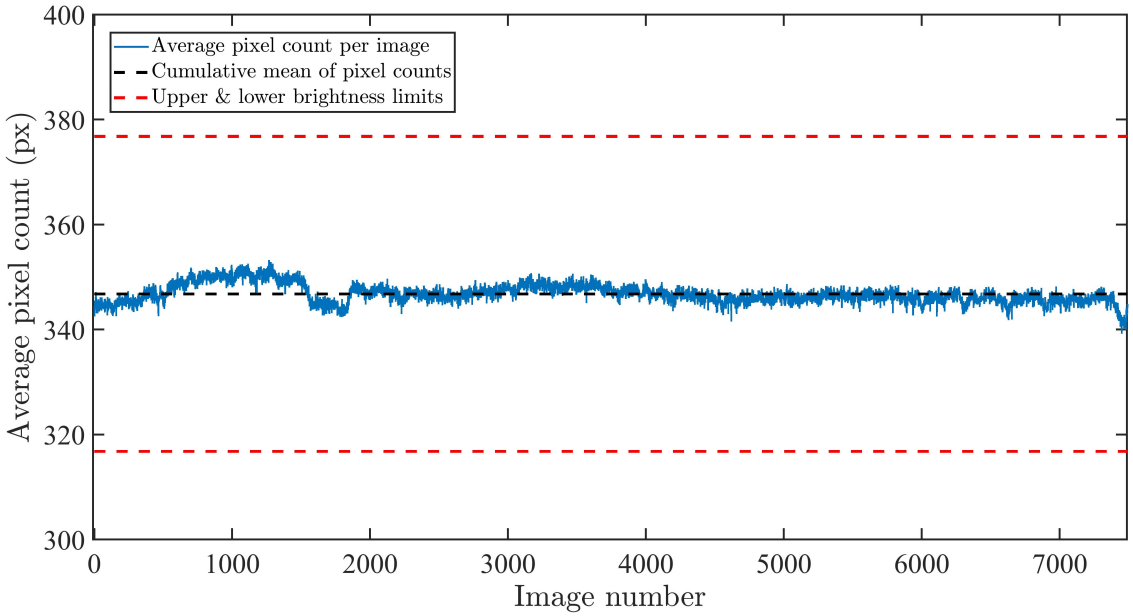

Figure 2.12 Average brightness in terms of pixel counts in the case of a 7500-frame dataset.

Similar uncertainties were also seen close to the bottom of the FOV, where uncertainty levels were expected to be higher due to laser reflection from the model surface.

To better understand how the uncertainties varied in the FOV, Fig. 2.13b shows the time-averaged streamwise velocity $\bar{u}$ and relative uncertainty $\bar{u}_{unc}$ (as error bars) along the ship centerline (blue line in Fig. 2.13a). Note that the uncertainties shown in the plot are not normalized by the time-averaged velocity. Therefore, as one moves up the blue line, the representative normalized uncertainties are reduced because $\bar{u}$ increases, especially above the funnel wake area, while $\bar{u}_{unc}$ remains constant.

Finally, an average of the normalized uncertainties at each spatial location was computed. This was carried out to obtain one relative uncertainty estimates for each measurement plane. The results are included in Appendix A. The spanwise planes presented relative uncertainties of 3% or lower. The streamwise plane presented a maximum uncertainty of 8% for the out-of-plane velocity component, which was expected considering the small pixel displacement in that direction. In summary, the error mitigation strategies ensured that the measurements were suitable for processing. Additionally, the low uncertainties of all measurement planes indicated that the obtained measurements were adequate for processing and analysis.

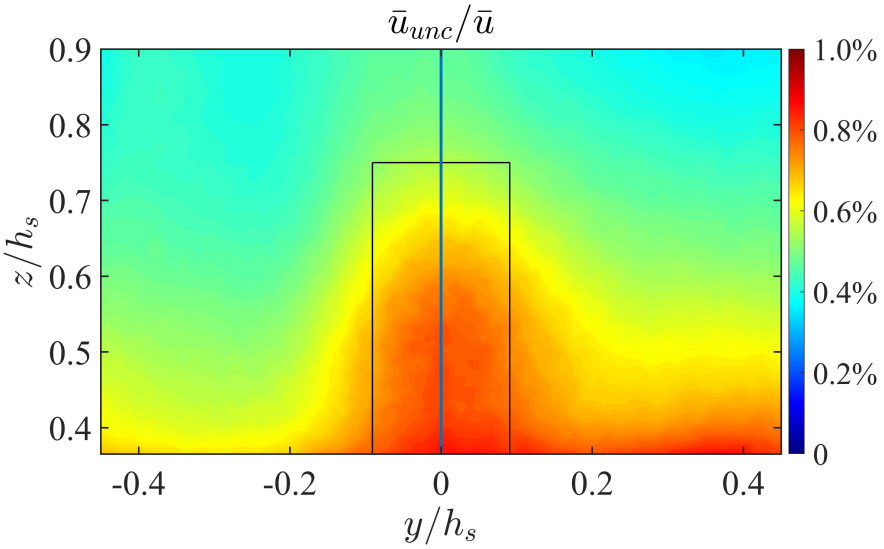

(a) Normalized uncertainty levels.

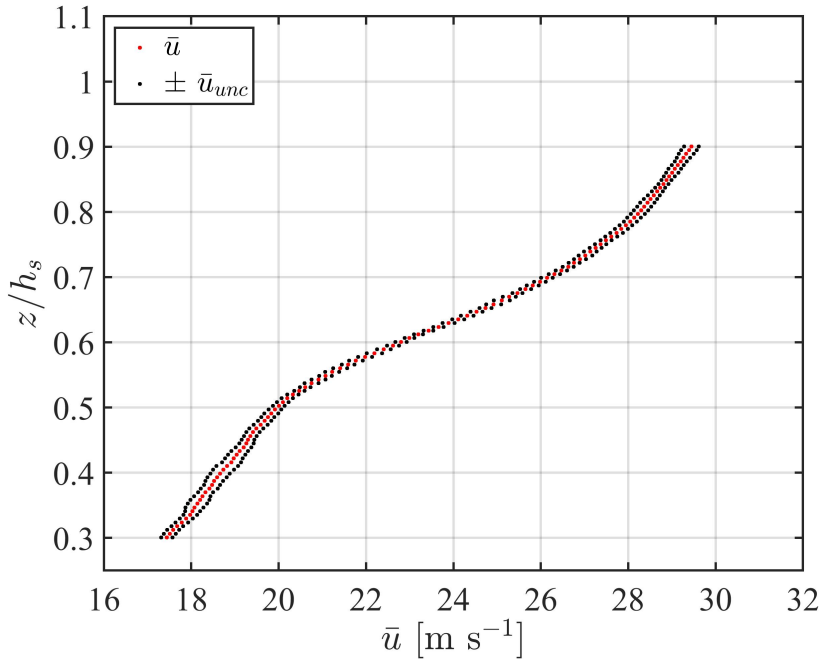

(b) Resulting uncertainties along the centerline shown in blue in Fig. 2.13a.

Figure 2.13 Distribution of uncertainties in spanwise plane SP1.

2.5 PIV and Data Processing

The current section describes the tools and methods used to analyze the instantaneous velocity fields to understand the structure of the ship airwake. First, a more traditional

evaluation of the airwake examined the time-averaged velocity fields, turbulence intensity (TI), and kinetic energy (TKE). Then, a conditional averaging approach was used to isolate and study three-dimensional flow events that are likely relevant to rotorcraft operations.

The commercial software DaVis, was used to process the raw images acquired by the high-speed cameras. A manual calibration for stereoscopic PIV measurements was performed prior to each trial using a calibration plate. An example of this type of plate is shown in Fig. 2.14a. The two-level, double-sided plate featured equally spaced white dots and a black background. The dots were 3 mm (0.12 in) in diameter and 15 mm (0.59 in) apart from each other. The plate had two levels that differed in depth by 3 mm (0.12 in). The calibration algorithm used a pinhole mapping function to identify the marks on the calibration plate. The algorithm distinguished each side of the calibration plate and recognized its orientation by detecting additional position marks [17]. Therefore, only one image of the calibration plate was necessary for calibration.

As shown in Fig. 2.14b, the calibration plate was positioned parallel to the laser sheet, such that the front face of the plate was in the path of the light-sheet plane. DaVis employed a fully empirical calibration method, which did not involve measuring physical angles or distances and had proven to be highly accurate and reliable [16].

Geometric masking was used to define the desired FOV in which the vectors would be calculated. The background camera noise was subtracted by applying a filter that removed the average intensity of all images from each dataset. A multi-pass (with decreasing window size) algorithm processed the raw images. Adaptive window shifting was used to compute the vectors. This method calculated the vector fields with an arbitrary number of iterations by successively decreasing the interrogation window size [17]. For all cases, the interrogation windows were 128-by-128 px^2 with 50% overlap for the initial pass and 48-by-48 px^2 with 75% overlap for the two final passes. The windows sizes were selected based on previous work by Palm [13] and Zhu [15]. After each pass, correlation peak ratios less than 1.5 were removed. The algorithm also computed outliers using the method of Westerweel and Scarano

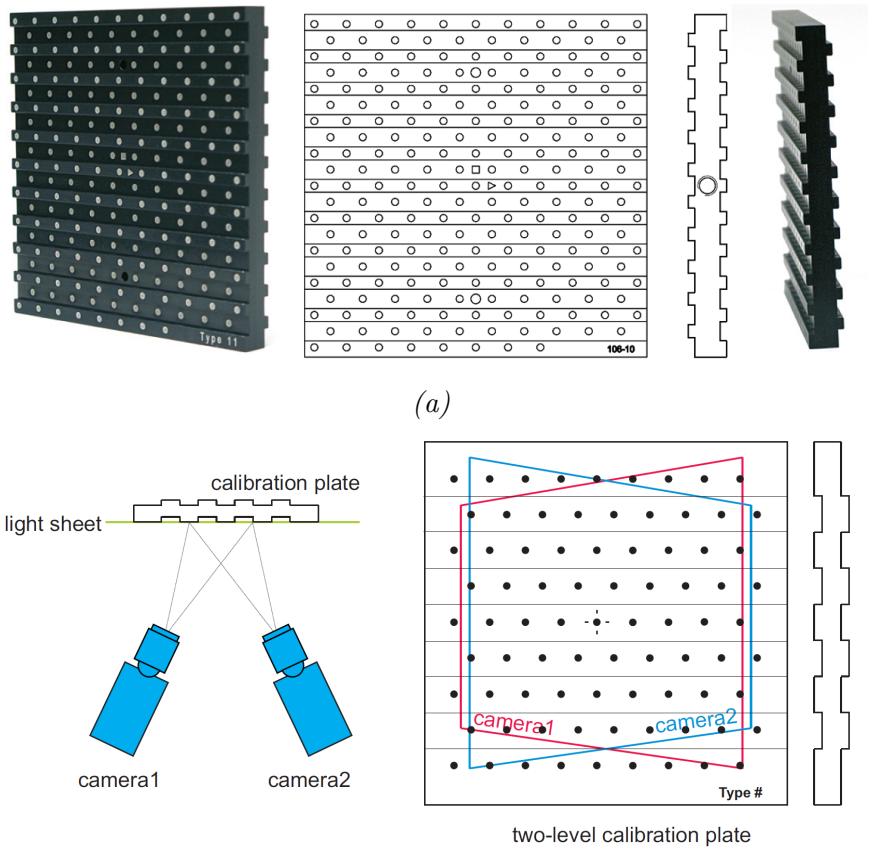

Figure 2.14 (a) Example of a two-level, double-sided calibration plate and (b) schematic of calibration of a stereoscopic PIV system using a two-level calibration plate [17].

[48]. The outliers where removed if residuals were greater than 2 and reinstated them if they were less than 3. The maximum pixel displacement was 8 pixels in the streamwise plane and 6 pixels in the spanwise plane. Lastly, the DaVis algorithm used interpolation to fill areas with missing vectors by using the average of the neighboring vectors if at least two out of four were available [17].

Various data analysis methods were used to understand the turbulent, three-dimensional physics of the ship airwake. First, the turbulence intensity (TI) and kinetic energy (TKE) as well as the mean velocity profiles were computed. Such analyses allow for the identification of energetic fluctuations within the flow, which are relevant to the present work as they affect rotorcraft operating near the flight deck. Following the kinetic energy equation, TKE per

unit mass, represented as k, is obtained using the mean-subtracted velocities (u', v', w').

$$k = \frac{1}{2}(\overline{u'u'} + \overline{v'v'} + \overline{w'w'}) \tag{2.1}$$

Another quantifiable metric used to study the turbulent behavior of flow fields is known as the turbulence intensity (TI), which is calculated by obtaining the root-mean-square of u', v', and w', and is non-demantionalized by a reference velocity. Both TI and TKE results were useful in identifying strategic regions in the airwake that were necessary to carry out conditional analyses, as explained in the following section.

2.5.1 Conditional Average Analysis

In order to identify flow events within the airwake that potentially impact rotor systems, a conditional averaging approach was used. Conditional averaging is an average computed using only certain occurrences, within a large number of occurrences, that meet one or more condition(s). Applying this statistical tool to DP-sPIV measurements allowed for the identification of three-dimensional, large-scale flow structures associated with events in the flow that may have a significant impact on the airloads of an incoming rotorcraft.

First, a small spatial region (< 40 mm^2) was strategically selected. Figure 2.15 shows an example of a region of interest. In this example, this region was selected to isolate flow events associated with vertical motions of the shear layer behind the hangar door. The average wall-normal fluctuations over that spatial region $\tilde{w}(t)$ were calculated for each PIV realization and hence were a function of time when considering the entire dataset. Then, a probability density function (PDF) of $\tilde{w}(t)$ was computed (see Fig. 2.16). In probability theory, a PDF is used to determine how likely it is for a random variable to be within certain bounds of a sample space. These functions are always positive and the integral of all possibilities is always equal to one [49].

Other statistical tools, such as the skewness and the kurtosis of the PDF, were used to characterize the probability distribution. The skewness is a measure of the symmetry of

distributions. A skewness value of 0 represents a symmetrical distribution (e.g., a Gaussian or normal distribution) [50]. On the other hand, kurtosis measures whether the data are heavy-tailed or light-tailed relative to a normal distribution. A kurtosis value of 3 represents a Gaussian, or normal distribution [50]. For the current study, kurtosis values that deviated from 3 represent biased flow velocity over the conditional region.

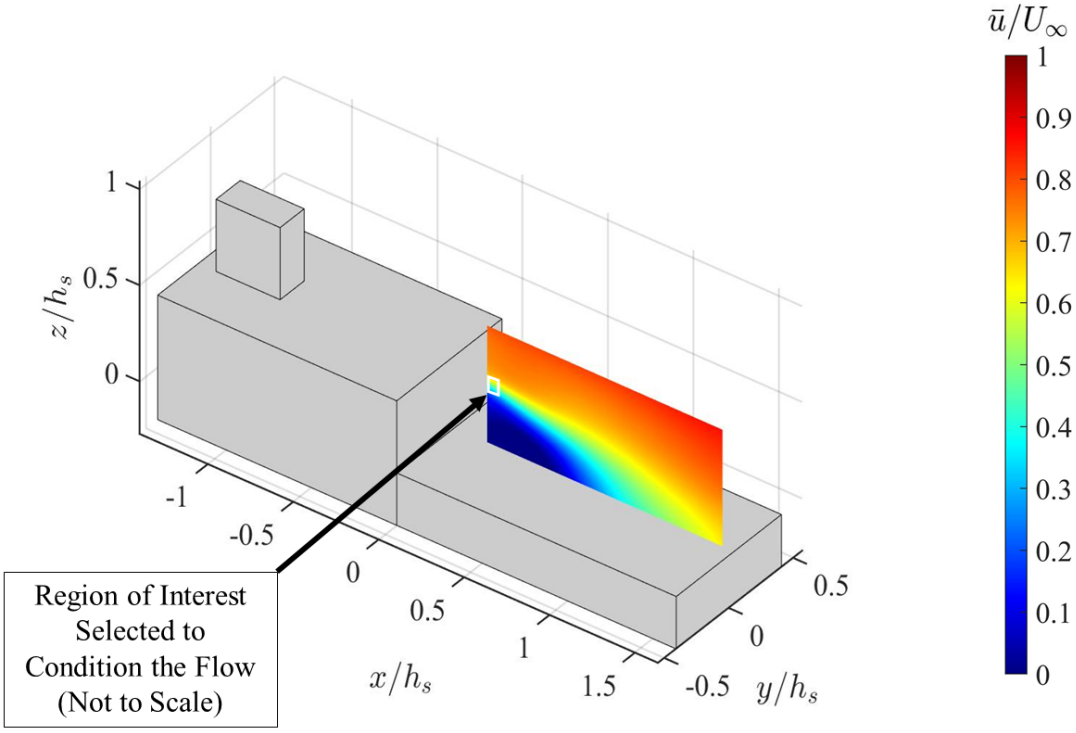

Figure 2.15 Example of a spatial region of interest (in white) in the streamwise plane used to study the vertical motions of the shear layer behind the hangar door.

A condition was chosen using the probability density function (PDF) to identify the flow event. In the case of the previous example, this would be all instances when the vertical velocity was greater than some threshold k_w, i.e., $\tilde{w}(t) > k_w$. The red bins in Fig. 2.16 show the realizations that satisfy this condition for some k_w. The average velocity fields were then calculated using only these realizations. It is emphasized that any structure in the flow that is inferred from conditional plots is an *average* flow structure when a certain criterion is satisfied. Hence, it is a statistical measure and does not necessarily imply that such a structure persisted in the flow instantaneously. This approach offers the possibility

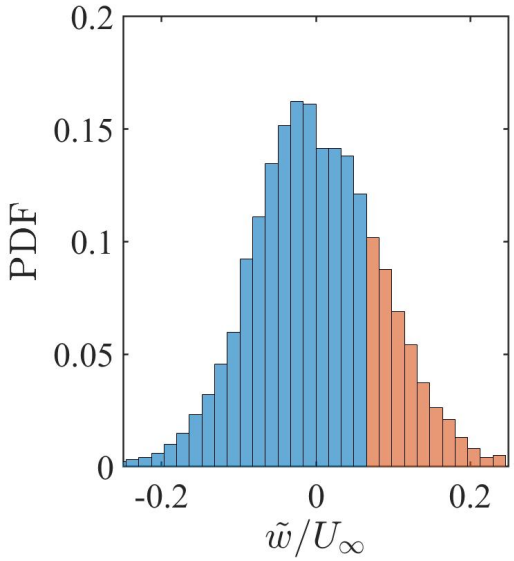

Figure 2.16 Probability density function (PDF) of $\tilde{w}(t)$. The red bins indicate the occurrences in which $\tilde{w}(t) > k_w$

of isolating flow features based on specific events. For instance, positioning the conditional region behind the hangar door, as shown in Figure 2.15 can help identify the footprint of the shear layer over the flight deck.

There is one fundamental limitation to this approach in the context of dual plane stereoscopic PIV. In order to obtain three-dimensional results, all conditional regions need to reside in the streamwise plane. This is because the streamwise plane is the *anchor* plane that is common to all measurement sets. Keeping this in consideration, the velocity fields of the streamwise plane from each trial were interpolated onto a single *master* streamwise plane grid to ensure that the location and coordinates of the conditional regions were the same for all measurement sets. Different flow events of interest such as extreme vertical motions of the shear layer and the two bistable flow states of the hangar door wake were studied using conditional averages. The results of this analysis are presented in the following chapter.

3 Results & Discussion

Results from the DP-sPIV measurements are presented in the current chapter. First, the time-averaged velocity fields over the flight deck are presented. This includes mean flow velocity, turbulence intensity (TI) and turbulent kinetic energy (TKE) contours. Then, the conditional flow analysis results are presented. Three important flow events in the airwake were isolated and studied: (i) extreme vertical (normal to the flight deck) large fluctuations in the shear layer, (ii) the two bistable flow configurations of the wake behind the hangar door and (iii) the temporal transition between the bistable states of the hangar door wake. All results in this chapter are shown in both two- and three-dimensional perspectives to better illustrate and interpret the behavior of the flow structures under investigation.

Figure 3.1 shows a three-dimensional view of all the measurement planes: spanwise planes 1 through 4 (SP1 through SP4) in red and the invariant streamwise plane (SW) in blue. All three-dimensional results in the current section are shown from this perspective. In addition, the two-dimensional views of the spanwise (SP) and streamwise (SW) planes are presented.

As previously discussed, the flow speeds under the influence of the sABL are significantly slower because of the resulting velocity profile upstream of the model ship. It is challenging to identify a clear free-stream velocity due to the significant mixing caused by the Cowdrey rods. Hence, for all the results with the sABL, the streamwise velocity at a point above the funnel structure ($z/h_s = 1, y/h_s = 0.4$) in SP1 was picked to use as U_∞. At this location, the flow is presumably less likely to interact with the ship and can be considered "free-stream." This value was 21.7 $\mathrm{m\,s^{-1}}$ (71.2 $\mathrm{ft\,s^{-1}}$). On the other hand, the wind tunnel flow velocity of 30.5 $\mathrm{m\,s^{-1}}$ (100 $\mathrm{ft\,s^{-1}}$) was used as the reference velocity for cases without the sABL.

3.1 Time-Averaged Statistics of the Ship Airwakes

The current section presents the time-averaged velocity, TI and TKE contours obtained using the DP-sPIV technique. Previous ship airwake studies [13–15] previously identified three notable large-scale flow structures from time-averaged statistics: (i) the recirculation region aft of the hangar door (ii) the shear layer that originates above the hangar door and

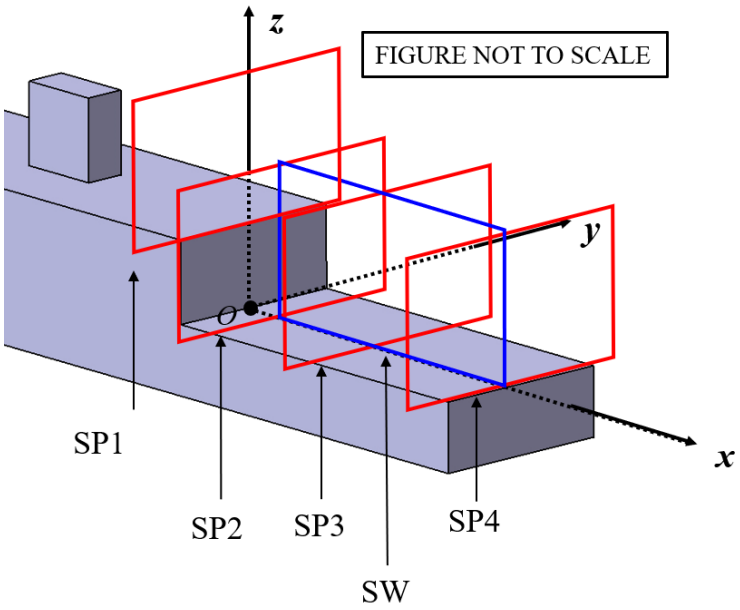

Figure 3.1 The three-dimensional results show the spanwise planes SP1 through SP4 and the invariant streamwise plane (SW).

propagates downstream over the flight deck (iii) symmetric funnel and flight deck vortices that extend downstream of the recirculation region, covering a significant spatial domain over the flight deck. Indeed, these flow structures were highly unsteady and often intermittent in nature, but the current work starts by identifying the three-dimensional, time-averaged, footprint of these flow features.

The time-averaged results are presented in the current study for multiple purposes: (i) to ensure that the large-scale turbulent structures within the airwake were in agreement with results from previous work (ii) to corroborate that the flow over the flight deck was symmetric with respect to the ship's centerline, thus proving that the ship model was not yawed during the experiment (iii) to verify that the streamwise and spanwise results showed agreement when superposed in a three-dimensional sense, highlighting the consistency of the measurements in a spatial sense when viewed from a three-dimensional perspective.

Figure 3.2 shows the time-averaged streamwise flow velocity $\bar{u}/U_\infty$ (without the sABL) over the flight deck of the SFS2 model. Figure 3.2a and 3.2b show the isolated spanwise and streamwise measurement planes, respectively while Fig. 3.2c shows the three-dimensional

contour slices. Most subsequent plots in this section follow an identical format i.e., the sub figure (a) shows the isolated spanwise planes, (b) shows the streamwise plane and (c) shows the three-dimensional perspective. In this figure, the blue region in the streamwise (SW) plane indicated negative streamwise velocity $\bar{u}$, which was characteristic of the recirculation region aft of the hangar door. This region of reverse flow extended along the entire width of the flight deck as shown in SP2 and SP3. The flow reattachment point (e.g., $\bar{u} = 0$) was identified at the approximate streamwise location $x/h_s = 1$.

The time-averaged results showed the large-scale turbulent structures that were consistent with those previously identified by experimental studies on ship airwakes. Additionally, these results verified the consistency between spanwise and streamwise planes as the sharp velocity gradients within the airwake showed agreement (in space) when superposed.

Streamlines were used to identify the funnel and flight deck vortices for both cases with and without the sABL. A two-dimensional perspective was more suitable to identify these structures. Therefore, the time-averaged spanwise $\bar{v}$ and wall-normal $\bar{w}$ velocity fields were combined into a contour of $\sqrt{\bar{v}^2 + \bar{w}^2}/U_\infty$ accompanied by the respective streamlines. Fig. 3.3 shows the four spanwise planes in the case without the sABL (Fig. 3.3a) and with the sABL (Fig. 3.3b). Both figures show the presence of these vortices. However, clear differences in the vortex structures existed between cases with and without the sABL.

Spanwise planes SP1 and SP2 showed the horseshoe vortex structure formed behind the funnel of the ship, while SP3 and SP4 highlighted the flight deck vortices that formed downstream of the hangar door. These flight deck vortices remained close to the flight deck surface along the entire deck length. Comparing the vortices in Fig. 3.3a and 3.3b, the cases with the sABL showed larger and more defined vortices as well as less drastic velocity gradients than the cases without the sABL. This may be accredited to the slower and more turbulent upstream flow conditions (generated by the sABL) interacting with the model ship. In contrast, the upstream flow without the sABL presented higher flow speeds and less turbulence, which resulted in smaller funnel horsehoe and flight deck vortices when compared

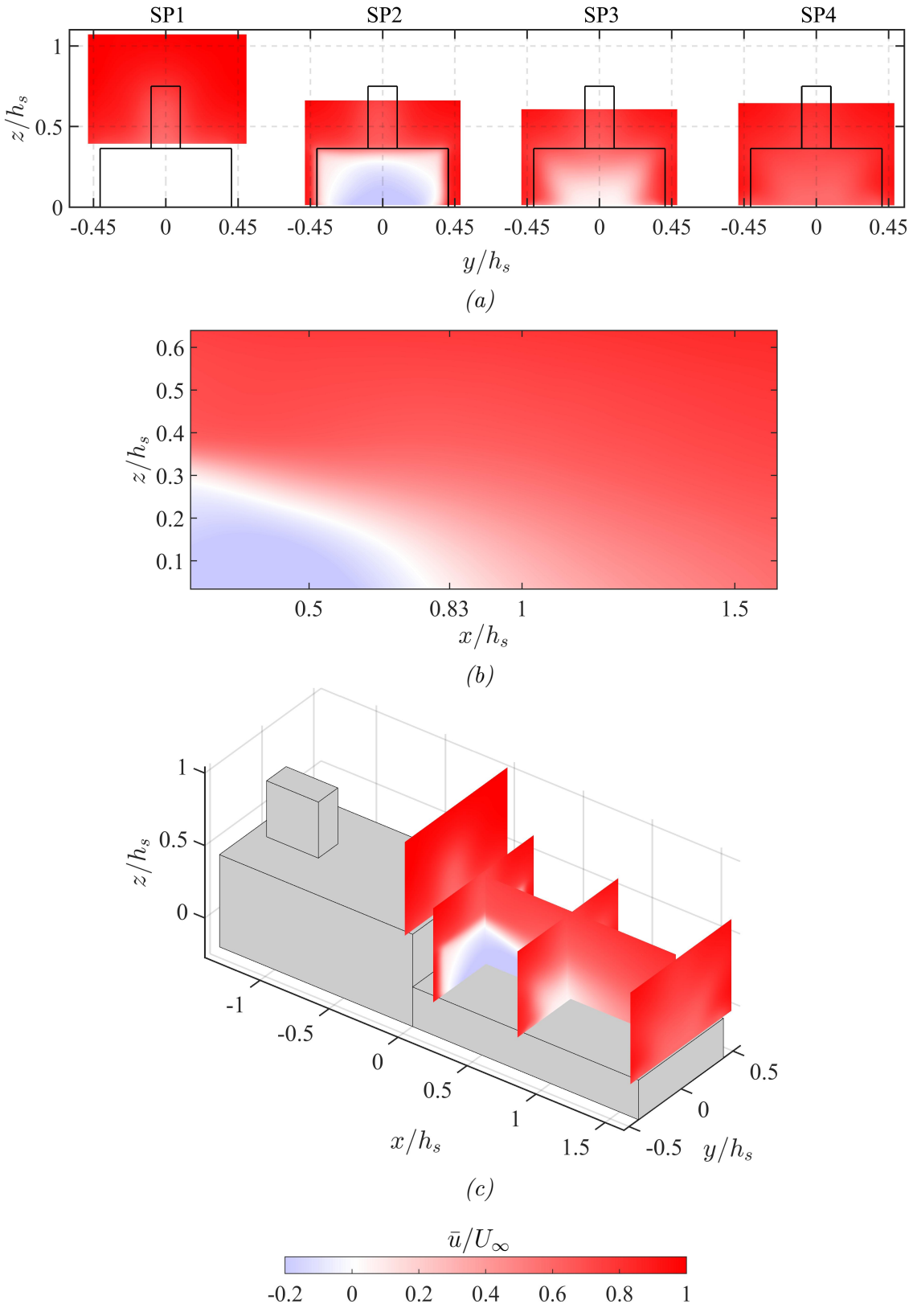

Figure 3.2 Time-averaged streamwise velocity $\bar{u}$ without the sABL. (a) the four spanwise planes, (b) the streamwise plane, and (c) the 3D perspective.

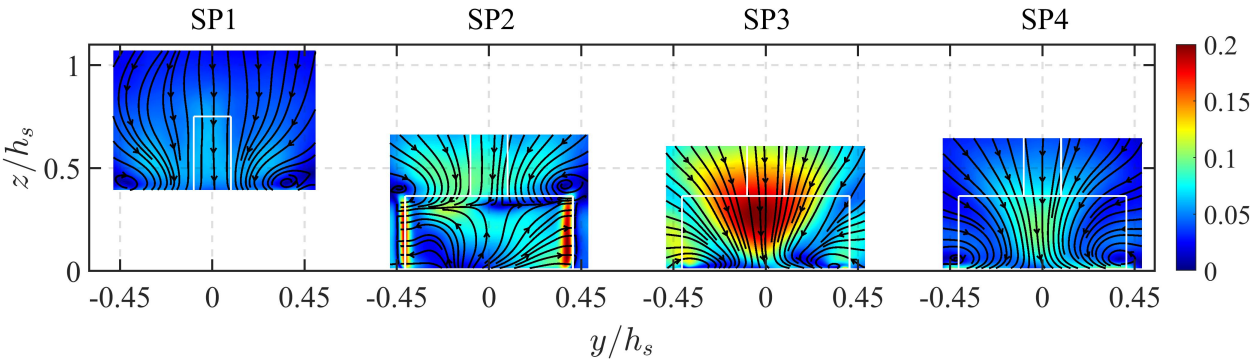

(a) $\sqrt{\bar{v}^2 + \bar{w}^2}/U_\infty$ - Case without the sABL.

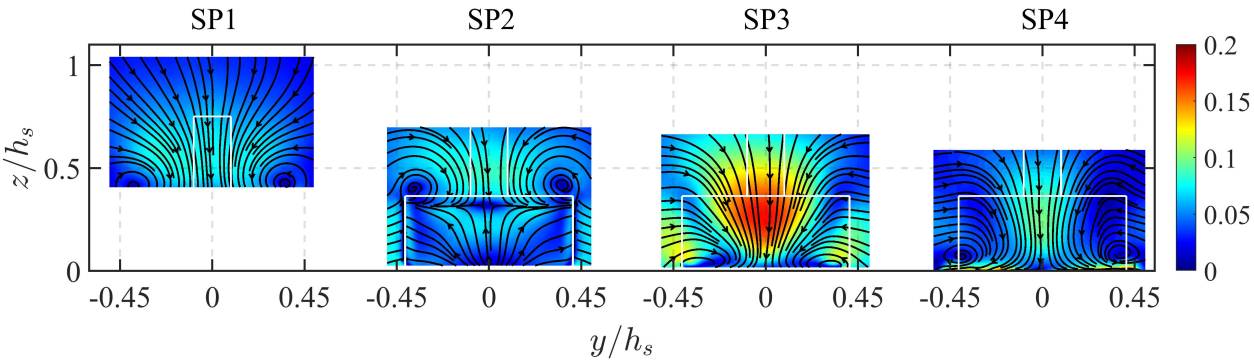

(b) $\sqrt{\bar{v}^2 + \bar{w}^2}/U_\infty$ - Case with the sABL.

Figure 3.3 Combined time-averaged spanwise and wall-normal velocity fields on all four spanwise planes.

to cases with the sABL.

The same analysis was carried out using the velocity fields in the streamwise (SW) plane. In this case, the time-averaged streamwise $\bar{u}$ and wall-normal $\bar{w}$ velocity fields were combined into a contour of $\sqrt{\bar{u}^2 + \bar{w}^2}/U_\infty$ accompanied by the respective streamlines. Figure 3.4 compares both cases with and without the SABL. The streamwise planes showed important flow features such as flow recirculation and reattachment regions and shear layers that extended over the flight deck. These mean flow structures appeared to be similar for both cases with and without the sABL.

Overall, the time-averaged velocity contours were useful to confirm the validity of the experimental approach used in the present research. First, these results showed large-scale turbulent structures that were consistent with those that have been identified in previous experimental airwake studies [13–15]. Additionally, the results confirmed the consistency be-

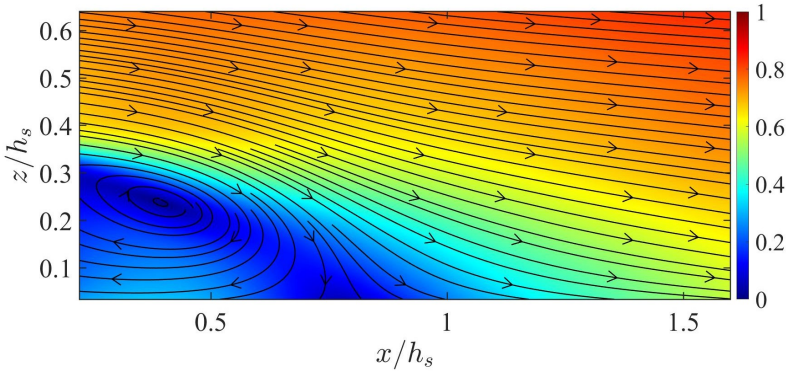

(a) $\sqrt{\bar{u}^2 + \bar{w}^2}/U_\infty$ - Case without the sABL.

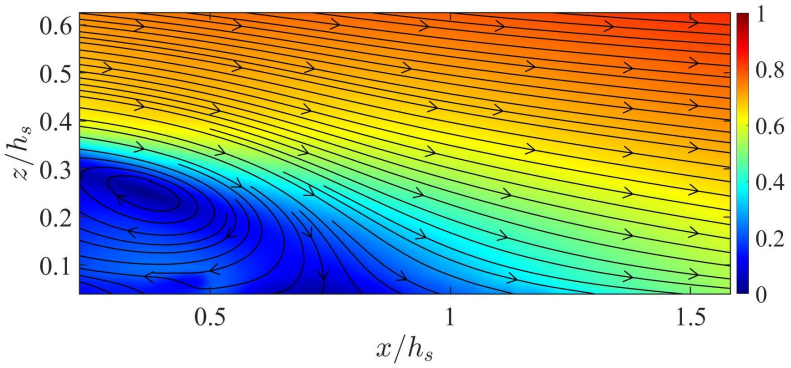

(b) $\sqrt{\bar{u}^2 + \bar{w}^2}/U_\infty$ - Case with the sABL.

Figure 3.4 Combined streamwise and wall-normal velocity fields in the streamwise plane showing cases with and without the sABL.

tween all spanwise and the streamwise planes by showing matching velocity contours when superposed to provide a three-dimensional perspective. Finally, two-dimensional planes further confirmed the time-averaged symmetry of the flow using streamlines and two-component ($\sqrt{\bar{v}^2 + \bar{w}^2}/U_\infty$ or $\sqrt{\bar{u}^2 + \bar{w}^2}/U_\infty$) velocity contours. While the results on the streamwise plane did not show major differences between the cases with and without the SABL, the spanwise planes revealed some differences in velocity gradients as well as vortex structure.

3.1.1 Turbulence Intensity (TI) Fields

The present section shows and discusses the three-dimensional extents of regions that presented high turbulence levels. These regions are relevant to near-ship operations as the high levels of turbulence potentially affect the aerodynamic performance of approaching

rotorcraft. In addition, the results presented in this section seek to contribute to the understanding of the three-dimensional turbulent behavior of the airwake by superposing TI contours from the streamwise and spanwise planes. The stereoscopic PIV measurements provided velocity components in all three axes. This allowed the use of u', v', and w' data from all spanwise and streamwise planes to carry out a three-dimensional analysis of turbulence statistics. The TI of the streamwise velocity fluctuations (u_{RMS}/U_∞) is presented in this section. The TI of the spanwise (v_{RMS}/U_∞) and wall-normal (w_{RMS}/U_∞) velocity fluctuations can be found in Appendix B.

Figures 3.5 and 3.6 show the TI of the streamwise velocity fluctuations (u_{RMS}/U_∞) for the cases without the sABL and with the sABL, respectively. Both cases showed similar regions of high TI over the flight deck. Specifically, the highest intensities were seen behind the hangar door, at the top of the reciruclation region, indicating the presence of intense shear and velocity gradients in this area. Additionally, high TI was seen throughout SP3 (in both cases with and without the sABL), which showed intense fluctuations on both the starboard and port sides, near the surface of the flight deck. These highly turbulent regions were symmetric with respect to the ship centerline. Spanwise plane SP3 captured the downstream end of the recirculation region and thus captured the flow reattachment area, which potentially caused the high TI in this plane. Moreover, the regions of high turbulence in SP3 also corresponded to the location of flight deck vortices found in close proximity to the deck surface (see Fig. 3.3 for reference). Thus, the flow in this region was highly three-dimensional since the large-scale regions of high TI extended in all three-dimensions over the flight deck. Finally, the fact that this highly three-dimensional activity occurred at the mid-deck location makes it relevant to rotorcraft safety as most take-off and landings usually occur at this location.

Some differences in TI between the cases with and without the sABL were observed by comparing the two-dimensional views of the spanwise planes in Figs. 3.5a and 3.6a. For example, the case without the sABL presented low and moderate levels of TI behind the ship

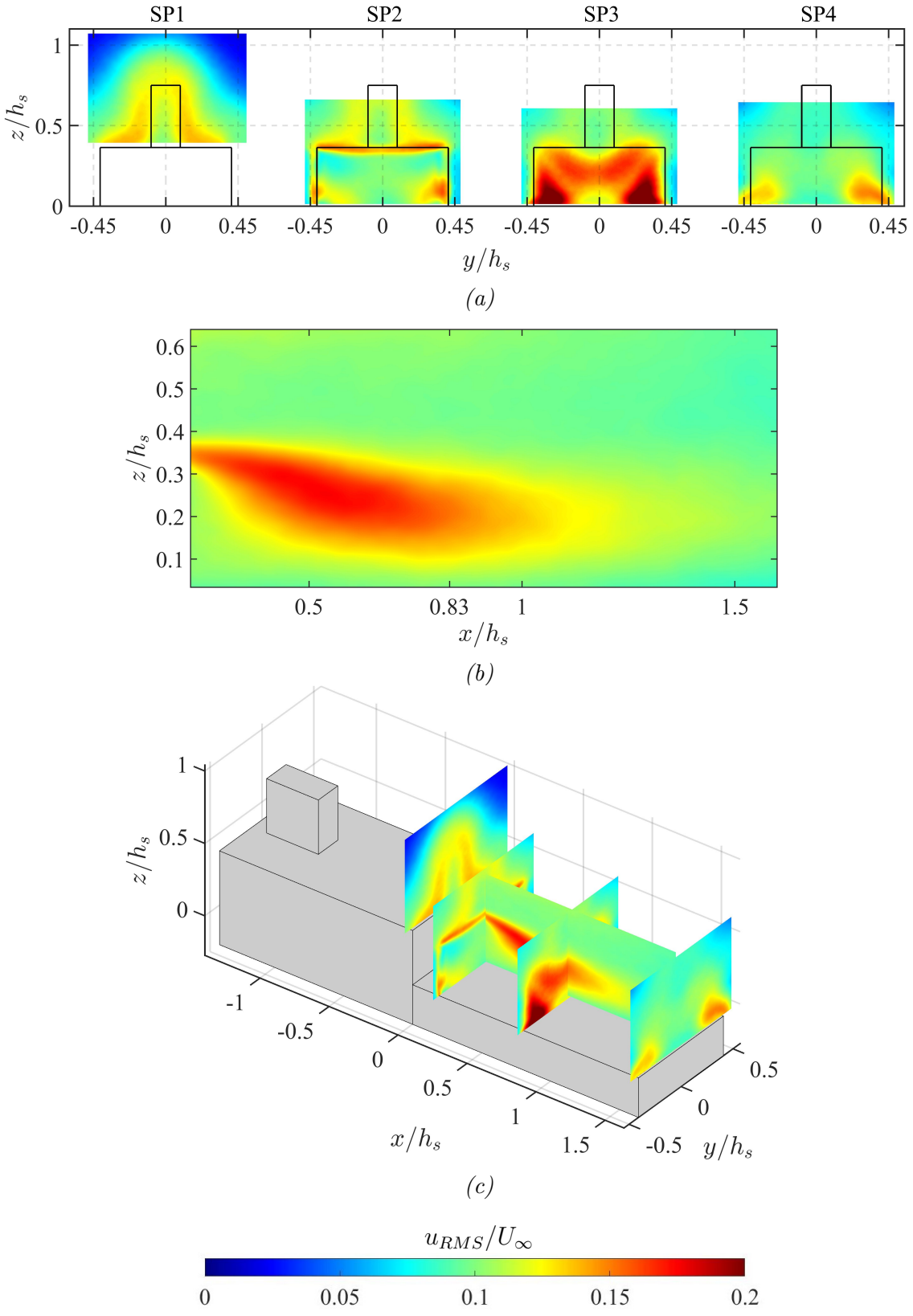

Figure 3.5 Turbulence intensity (TI) of the streamwise velocity in the case without the sABL. (a) the four spanwise planes, (b) the streamwise plane, and (c) the 3D perspective.

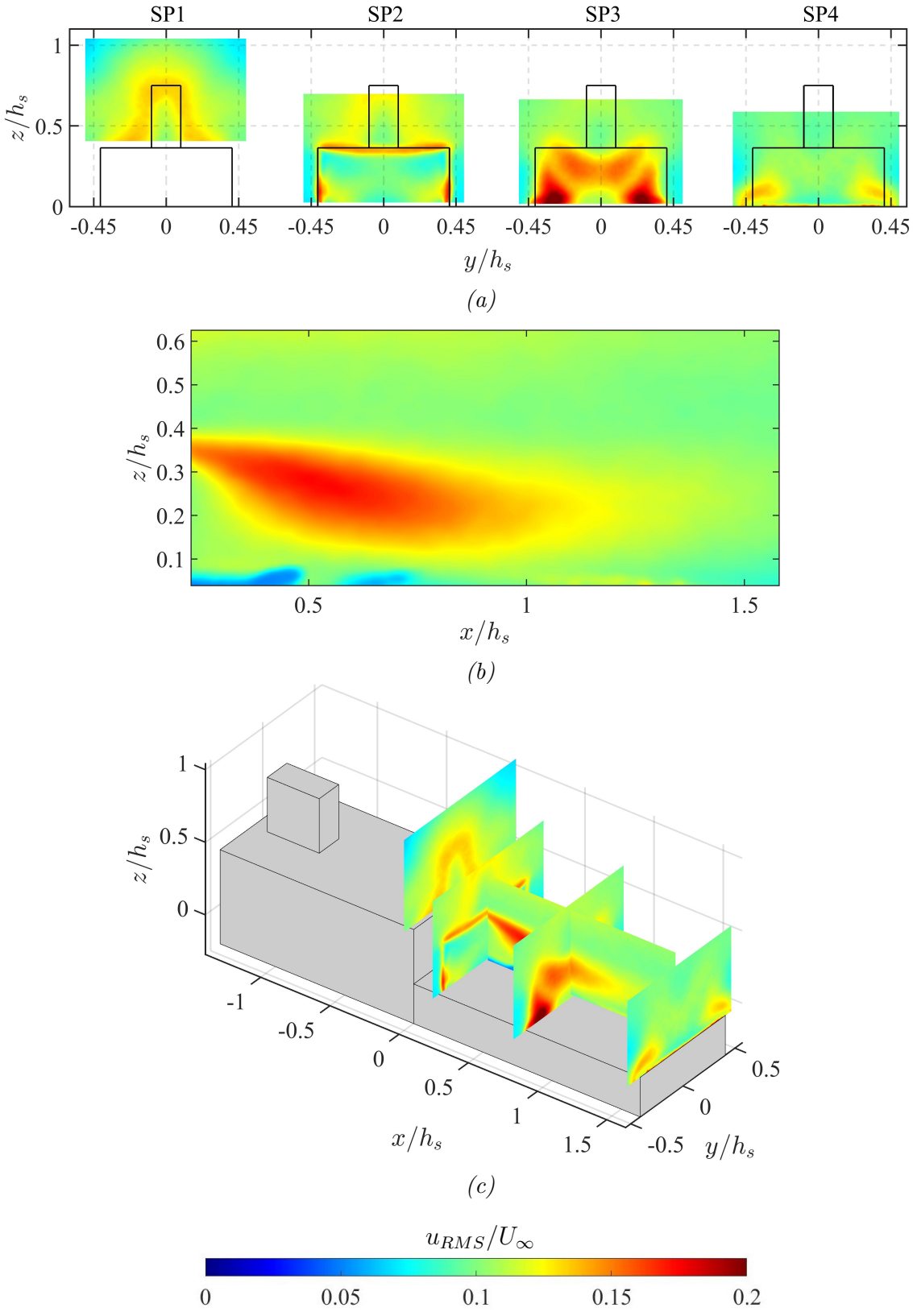

Figure 3.6 Turbulence intensity (TI) of the streamwise velocity in the case with the sABL. (a) the four spanwise planes, (b) the streamwise plane, and (c) the 3D perspective.

funnel but near-zero levels further away from the funnel. This indicates that the wake only extended directly behind the funnel structure while the flow around it was not perturbed. In contrast, the case with sABL showed higher levels of turbulence throughout the entire FOV, even around the funnel structure, while also showing moderate TI levels directly behind it. This appeared to be the result of the turbulent upstream conditions from the sABL interacting with the model ship. Another difference between cases with and without the sABL was seen when considering SP3. In the case with sABL, the highly turbulent regions on both the starboard and port side appeared more concentrated and were positioned closer to the flight deck surface. On the other hand, the case without the sABL showed larger areas of significantly high TI that further extended vertically.

To summarize, the resultant TI contours showed areas of high turbulence within the airwake. The streamwise plane showed that the upper portion of the recirculation region featured high levels of intensity generated by the detached flow behind the hangar door. Additionally, results from SP3 revealed a localized region of high turbulence potentially caused by the flow reattachment behavior combined with flight deck vortices.

3.1.2 Turbulent Kinetic Energy (TKE) Fields

The current section shows contours of the turbulent kinetic energy (TKE). These contours are often used to identify regions of high-energy flow fluctuations, offering an alternative tool from TI contours to analyze the turbulent characteristics of the airwake. The results shown in this section intend to be helpful in understanding these characteristics from a three-dimensional perspective.

Figure 3.7 shows the non-dimensional TKE levels for the case without the sABL. Considering Fig. 3.7a, the TKE contours in all spanwise planes showed a similar pattern to the previously shown streamwise TI contours (see Fig. 3.5 for reference). Specifically in SP3, where the fluctuations contained the highest levels of energy on both the starboard and port sides, closer to the flight deck surface. The contours in SP1 showed that the funnel airwake was energetic, although the TKE levels were low relative to the levels seen in SP3.

This outcome was also observed in the streamwise plane (see Fig. 3.7b), where high TKE levels extended vertically from the flight deck surface to the shear layer downstream of the hangar door. Additionally, this high-energy region appeared to extend downstream past the flow reattachment point. However, TKE levels decreased rapidly as the flow approached the stern. This reduction in TKE was also seen in the spanwise direction, as shown in SP4 in Fig. 3.7a.

Figure 3.8 shows the TKE contours when the airwake developed under the influence of the sABL. While the contours with and without the sABL showed similar turbulent characteristics, some differences were observed when the two cases were compared. For instance, for cases with the sABL, SP1 showed a greater extent of the funnel wake area in the spanwise direction as the bell-shape contour appeared to spread more in the spanwise direction. Additionally, the high-energy peaks in SP3 appeared to be concentrated closer to the flight deck surface. In contrast, SP4 showed a more uniform distribution of energy in the spanwise and vertical directions when compared to the case without the sABL. Finally, the streamwise plane shown in Figure 3.8b showed a more abrupt end of this high-energy region past the flow reattachment point.

In summary, the TKE contours presented in this section offered an alternative perspective of the energy content within the airwake. Both the TI and TKE contours were used to identify and isolate regions of interest for further study. For instance, the fluctuations in the shear layer resulted in highly energetic regions that extended throughout the entire length and span of the flight deck while also remaining close to the deck surface. These flow characteristics are likely relevant to the safety of rotorcraft operating near the flight deck due to the potential impact of unsteady, three-dimensional turbulent flow on rotor systems. These regions of interest were used to conduct a spatial and temporal study of the airwake using a conditional averaging approach, which was accomplished by leveraging the DP-sPIV measurements. These results are presented in the following section.

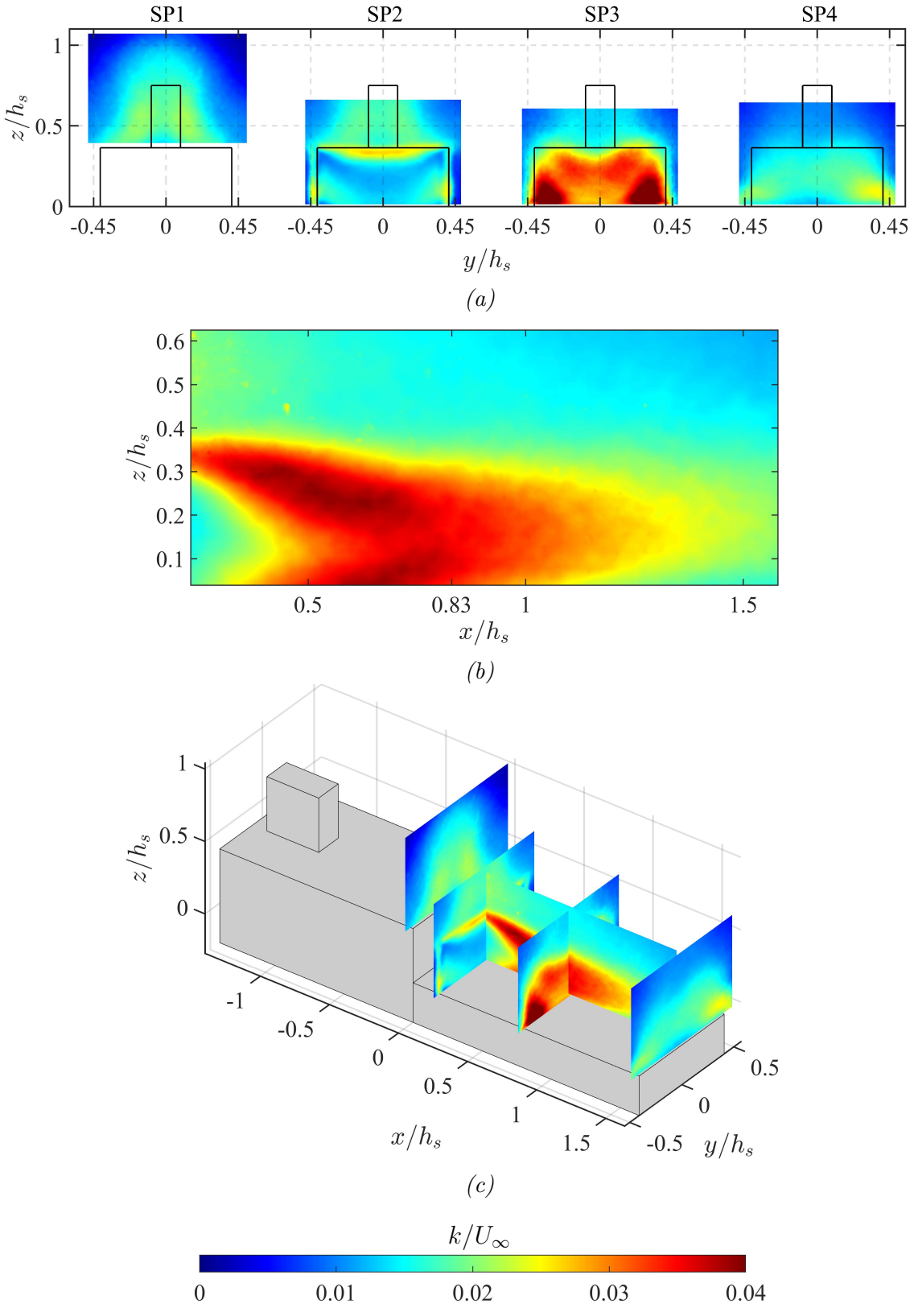

Figure 3.7 Turbulent kinetic energy (TKE) in the case without the sABL. (a) the four spanwise planes, (b) the streamwise plane, and (c) the 3D perspective.

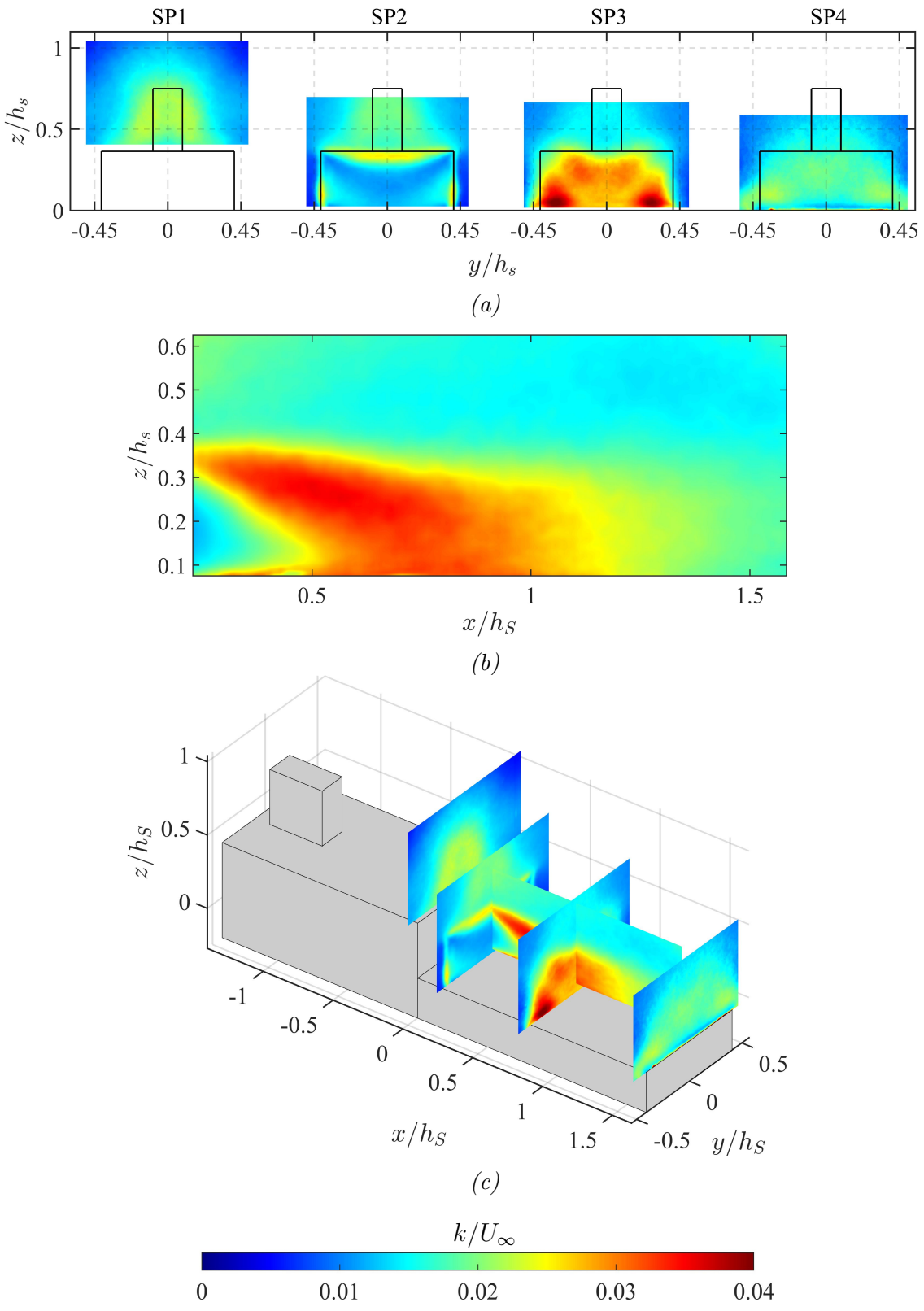

Figure 3.8 Turbulent kinetic energy (TKE) in the case with the sABL. (a) the four spanwise planes, (b) the streamwise plane, and (c) the 3D perspective.

3.2 Conditionally Averaged Flow Statistics

Conditionally averaged flow fields were used to isolate specific events that have a potential impact on the operations of rotorcraft in the vicinity of the flight deck. The temporally and spatially correlated measurements allowed for a three-dimensional, spatiotemporal analysis of these events of interest, which are presented in the current section. First, extreme vertical flow events in the shear layer are considered, followed by the bistability study of the wake behind the hangar door. For each event, its relevance to rotorcraft operations is discussed first. Then, a description of the identification and isolation process of the events using probability density functions (PDF) is provided, followed by the conditional flow statistics. Finally, it is emphasized that any structure in the flow that is inferred from conditional plots is an *average* flow structure when a certain criterion is satisfied. Hence, it is a statistical measure and does not necessarily imply that such a structure persisted in the flow instantaneously.

3.2.1 Extreme Vertical Flow Fluctuations

Both TI and TKE contours shown in the previous section presented a highly turbulent region behind the top edge of the hangar door. According to the literature [10, 14, 15], the flow detachment in this region results in a highly unsteady shear layer, which contains dramatic vertical flow motions as the shear layer "flaps" up and down. These vertical motions are important from a rotorcraft operational standpoint as they will likely have an impact on the airloads of an incoming rotorcraft.

The vertical motion of the shear layer was observed in instantaneous flow snapshots of the streamwise plane. For example, the flow speed $V(\sqrt{u^2+v^2+w^2})$ in Fig. 3.9 shows one flow instance in which the shear layer behind the hangar door "flapped" up and another in which it "flapped" down. The present approach allowed for the study of this behavior in a three-dimensional spatial and temporal sense thanks to the synchronous dual-plane measurements. The conditional results presented in this section were obtained using flow fields without the sABL. The corresponding conditional results with the sABL can be found in Appendix C.

The wall-normal TI was used to identify the spatial region in the shear layer in which the condition for significant vertical fluctuations was identified. Figure 3.10 shows the w_{RMS}/U_∞ contours in the streamwise plane as well as the selected region (in red) to condition the flow. This region was selected due to its high turbulent levels, which represented intense vertical fluctuations. It is also the region closest to the hangar door edge, where the shear layer was

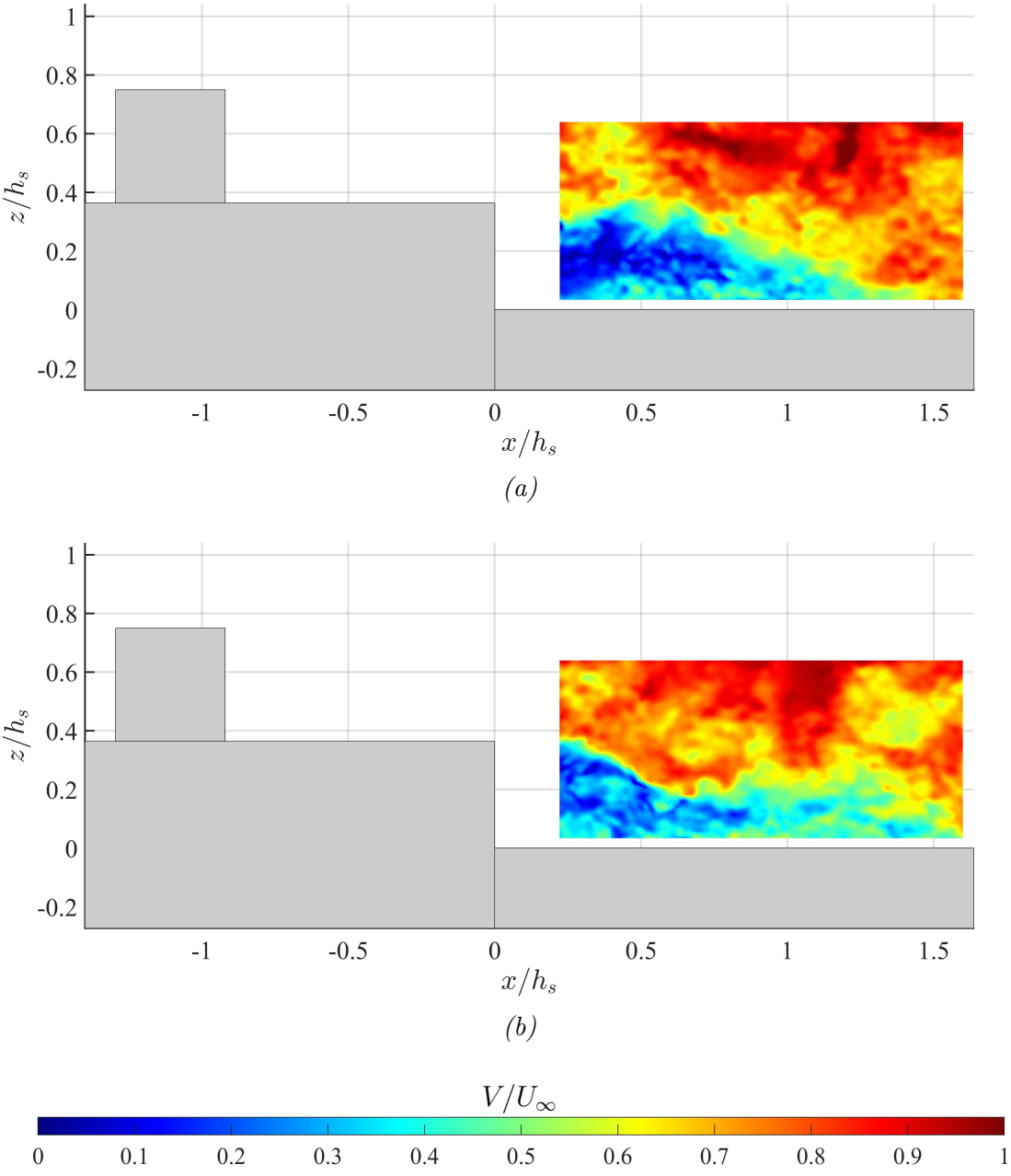

Figure 3.9 Two instantaneous snapshots showed the shear layer flapping (a) up and (b) down.

the predominant flow structure. Therefore, most, if not all, fluctuations could be attributed to it. The size of the region was 36 mm^2 $(0.032h_s)^2$ and a total of 25 flow vectors were included within this region.

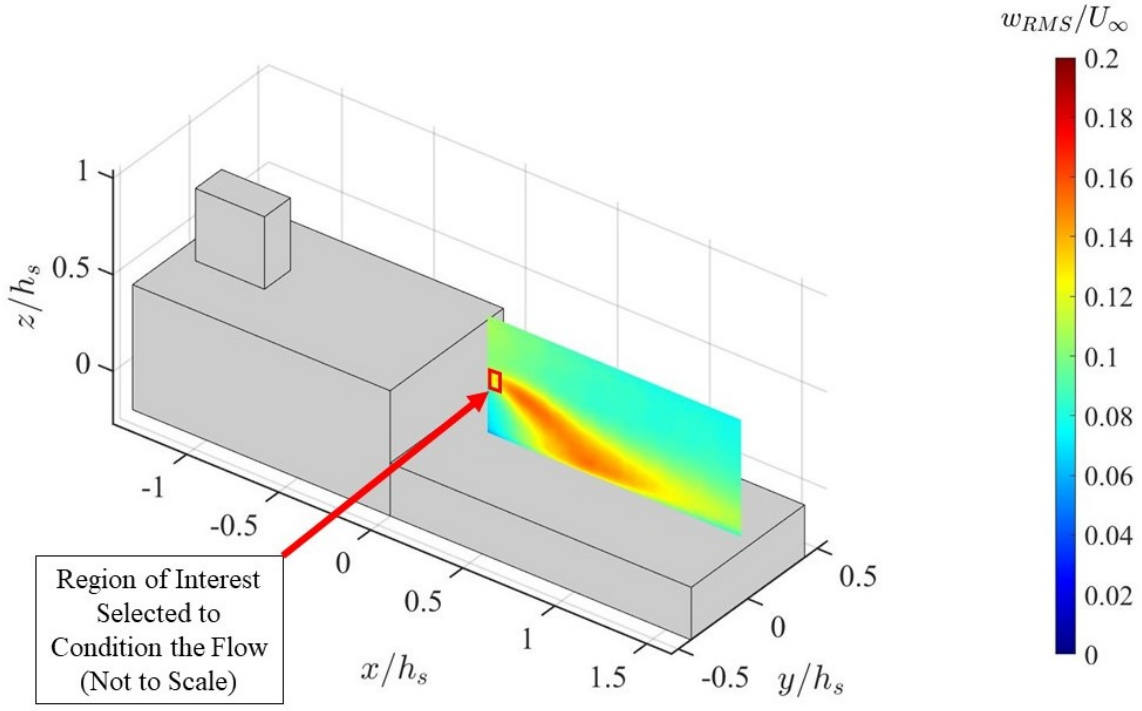

Figure 3.10 Spatial region selected to condition the flow based on w_{RMS}/U_∞ levels.

In order to accurately represent the fluctuating structures, a reference streamwise velocity U_{ref} was used to scale the conditionally-averaged velocity fields. The reference velocity was the average streamwise velocity over the spatial region shown in Fig. 3.11. This region had the same vertical dimension as the conditional region (see Fig. 3.10 for reference) but extended downstream, covering the entire length of the flight deck. This region clearly captured the downstream extent of the the shear layer as it "flapped" in the wall-normal direction. Hence, the average streamwise velocity in this region was considered a more suitable reference velocity, which was needed to accurately represent the intensity of the fluctuating structures shown in the current section. The reference velocity used in this section as well as in Appendix C was $U_{\text{ref}} = 0.58U_\infty$.

The average wall-normal fluctuations over the spatial region, denoted by $\tilde{w}(t)$, were

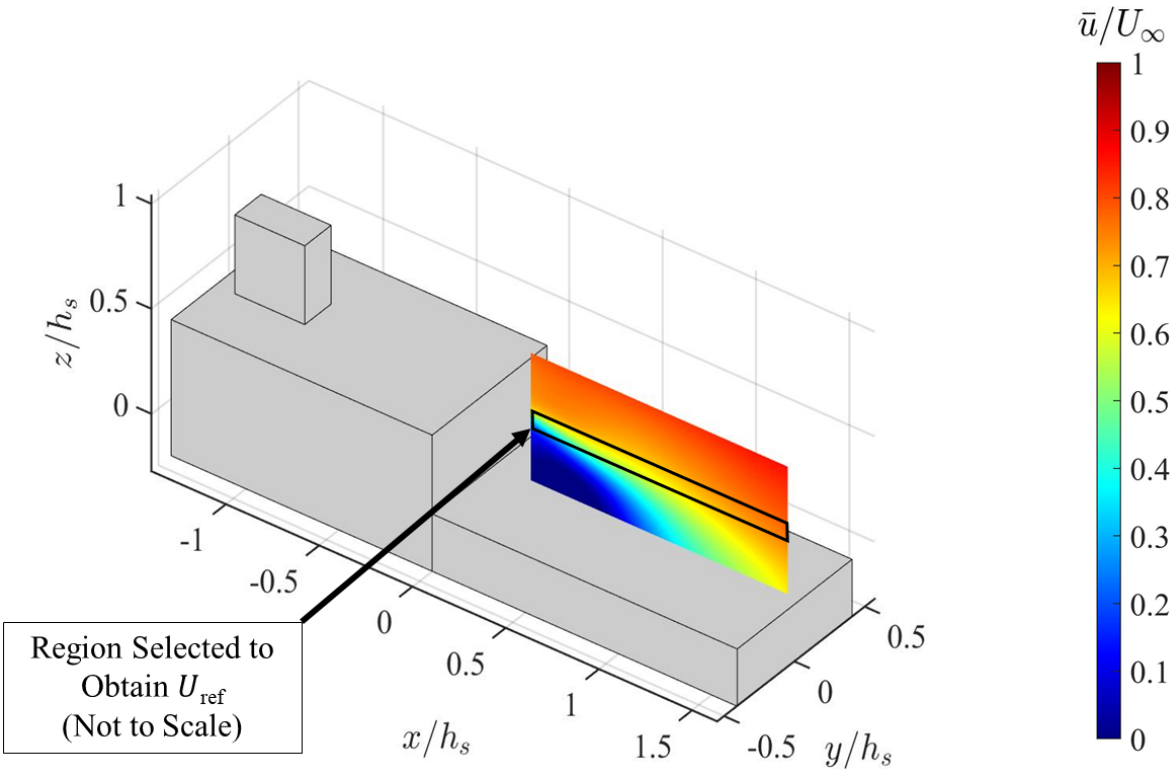

Figure 3.11 Spatial region selected to obtain the average streamwise velocity used as U_{ref} to accurately scale the intensity of the fluctuating structures. The reference velocity was $U_{\text{ref}} = 0.58U_\infty$.

calculated for each PIV realization. Therefore, this average velocity was a function of time over the entire data set. Figure 3.12 shows $\tilde{w}$ for a specific non-dimensional time period where $\bar{t} = tU_\infty/h_s$. As expected, $\tilde{w}$ fluctuated between positive and negative velocity peaks of up to $\pm 0.25U_\infty$ approximately. To further study these fluctuations, the probability density function (PDF) of $\tilde{w}$ in Fig. 3.13 was computed. The PDF distribution presented a skewness of 0.221 and a kurtosis of 3.144. This indicated that the PDF distribution was approximately a Gaussian (normal) distribution. This means that the likelihood of experiencing positive $\tilde{w}$ fluctuations was roughly the same as experiencing negative $\tilde{w}$ fluctuations in the selected region. The PDF was used to identify extreme vertical events by considering the $\tilde{w}$ values that fell above a standard deviation threshold k_w from the mean. These events were significantly greater in magnitude than the zero fluctuation value, and were considered extreme. First, the positive vertical fluctuations were considered using the threshold $k_w = 0.1U_\infty$ (3 m s^{-1}).

The red bins in Fig. 3.13 highlighted the instances when $\tilde{w}$ exceeded this threshold.

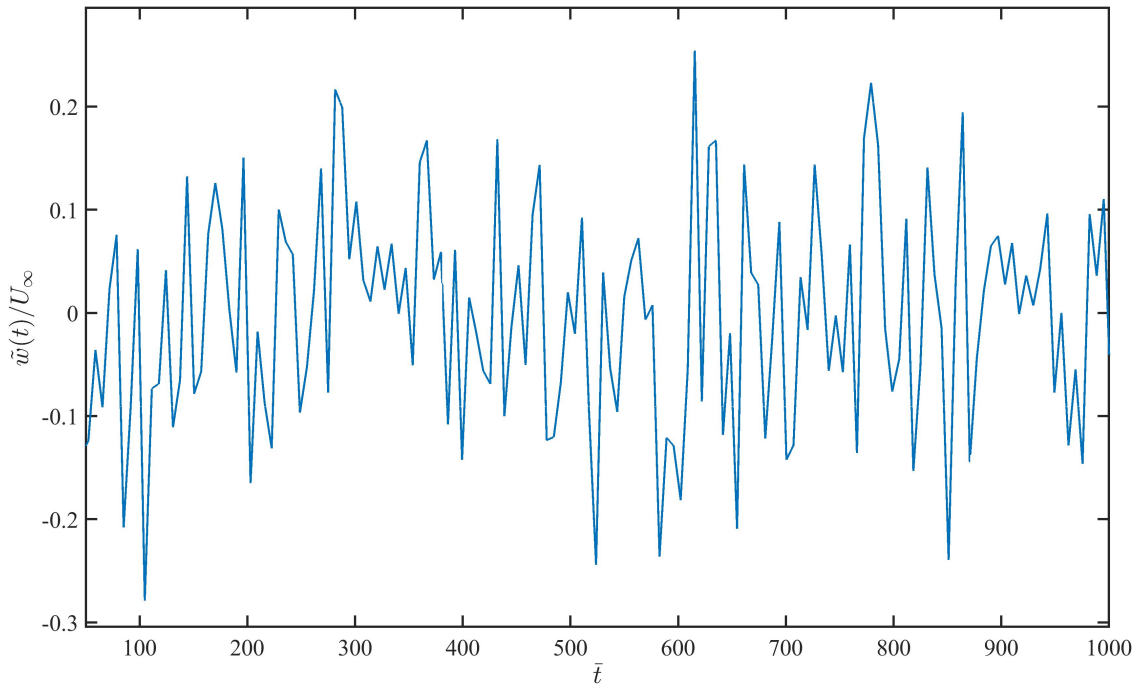

Figure 3.12 Average wall-normal fluctuations over the spatial region of interest $\tilde{w}$ for a specific time period.

This conditional analysis was carried out over all datasets, i.e, all four spanwise-streamwise plane configurations. As shown in Table 3.1, the number of instances in which $\tilde{w}(t)$ exceeded the threshold was approximately the same for each dataset. These instances were then used to obtain the conditionally averaged velocity fields, denoted as $\hat{u}$, $\hat{v}$ and $\hat{w}$. Note, these were derived mean subtracted velocity fields and thus the conditional average represented fluctuations about the mean. The conditionally averaged velocity fields are represented using the following notation: The conditional vertical velocity field $\hat{w}/U_{\text{ref}}$ when $\tilde{w} > k_w$ is denoted as $\hat{w}/U_{\text{ref}}|\tilde{w} > k_w$. The vertical $(\hat{w}/U_{\text{ref}}|\tilde{w} > 0.1U_\infty)$, streamwise $(\hat{u}/U_{\text{ref}}|\tilde{w} > 0.1U_\infty)$ and spanwise $(\hat{v}/U_{\text{ref}}|\tilde{w} > 0.1U_\infty)$ conditional velocity fields are shown in Figs. 3.14, 3.15 and 3.16, respectively.

First, the conditional vertical velocity field $\hat{w}/U_{\text{ref}}|\tilde{w} > 0.1U_\infty$ shown in Fig. 3.14 was considered. The streamwise plane showed that these fluctuations were associated with large vertical fluctuations $\hat{w}$ that spanned the entire measurement plane. Near the hangar door,

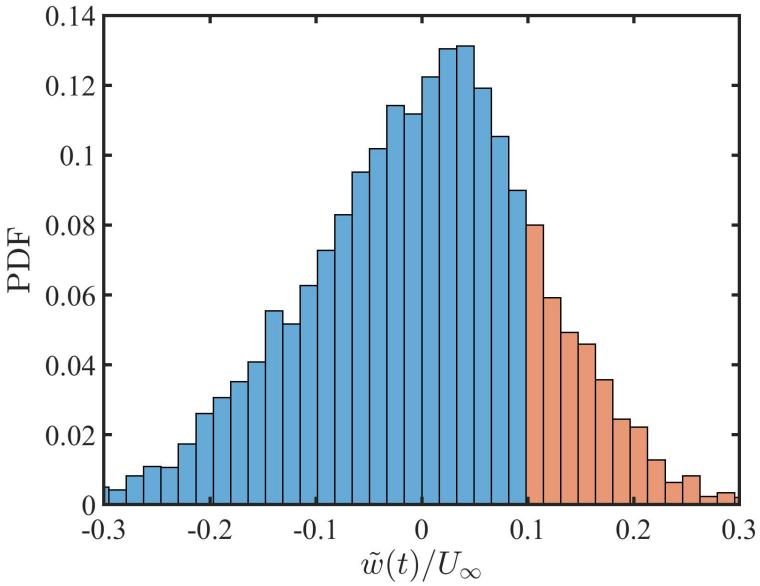

Figure 3.13 PDF of $\tilde{w}(t)$ used to identify the extreme vertical flow events. The red bins represented the positive flow fluctuations that exceeded the threshold $k_w = 0.1U_\infty$ ($3\ \mathrm{m\,s^{-1}}$).

Table 3.1 Number of instances in which $\tilde{w}(t) > 0.1U_\infty$ for each 7500-image dataset.

	SP#	SW#	No. Instances
Dataset 1	SP1	SW3	1381
Dataset 2	SP2	SW3	1328
Dataset 3	SP3	SW3	1375
Dataset 4	SP4	SW3	1334

these fluctuations were positive as required by the conditional criterion $\tilde{w}(t) > 0.1U_\infty$. Further downstream, a more complex pattern emerged with a region of negative $\hat{w}$ overlying a region of positive $\hat{w}$. This can be attributed to the oscillatory nature of the shear layer, in which a positive vertical flow variation was followed by a negative one. In this case, this resulted in the highly negative $\hat{w}$ region captured downstream. Furthermore, the positive $\hat{w}$ region closer to the flight deck surface appeared to be the result of a previous positive vertical fluctuation that was suppressed against the flight deck surface as the flow reattached. The proximity between these three $\hat{w}$ regions presented evidence of large-scale vortical motions containing sharp velocity gradients in an average sense.

The flow pattern within the streamwise plane was associated with flow features that

extended to the spanwise planes. For instance, SP2 showed that the positive $\hat{w}$ seen in the streamwise plane extended spanwise across the centerline. However, further away from the centerline, there were regions of negative $\hat{w}$ on both the port and starboard sides, indicating high levels of shear in the spanwise direction as well. At the mid-deck, the negative and positive layers of $\hat{w}$ remained closer to the centerline as they did not extend in the spanwise direction. Finally, positive $\hat{w}$ contours covered the majority of the spanwise plane at the stern of the ship. However, the flow intensity decreased significantly when compared to the levels seen upstream.

The streamwise conditional field $\hat{u}/U_{\text{ref}}|\tilde{w} > 0.1U_{\infty}$ is shown in Fig. 3.15. The streamwise plane showed that the flow over the entire region had negative $\hat{u}$ (low-speed) with an overlying flow that was mostly positive $\hat{u}$ (high-speed). Interestingly, the upper part of the negative $\hat{u}$ region had a wavy shape, indicating the influence of the previously discussed oscillatory behavior of the shear layer. This overlying high- and low-speed regions represented intense velocity gradients, and potentially abrupt changes in airloads, as a rotorcraft approaches the flight deck.

Considering SP2 (closest to the hangar), this low-speed region extended across the centerline. However, at the spanwise extremities of the flight deck, this low-speed region was flanked by high-speed regions ($\hat{u} > 0$) on both the port and starboard sides. This was a similar pattern observed in Fig. 3.14, where the regions at the spanwise extremities had equal magnitude but opposite orientation when compared to the region along the centerline. Additionally, these positive $\hat{u}$ regions were not symmetric with respect to the centerline as the region on the starboard side was significantly larger than the one on the port side.

Moving downstream to SP3, there was a high-speed region overlaying the low-speed region. It appeared that all the streamwise conditional velocity $\hat{u}$ regions on this plane were pushed against the flight deck surface as the flow reattached downstream. Finally, SP4 showed a single area of positive $\hat{u}$ on the starboard side of the ship closer to the deck surface while the rest of the FOV appeared to experience little to no fluctuations.

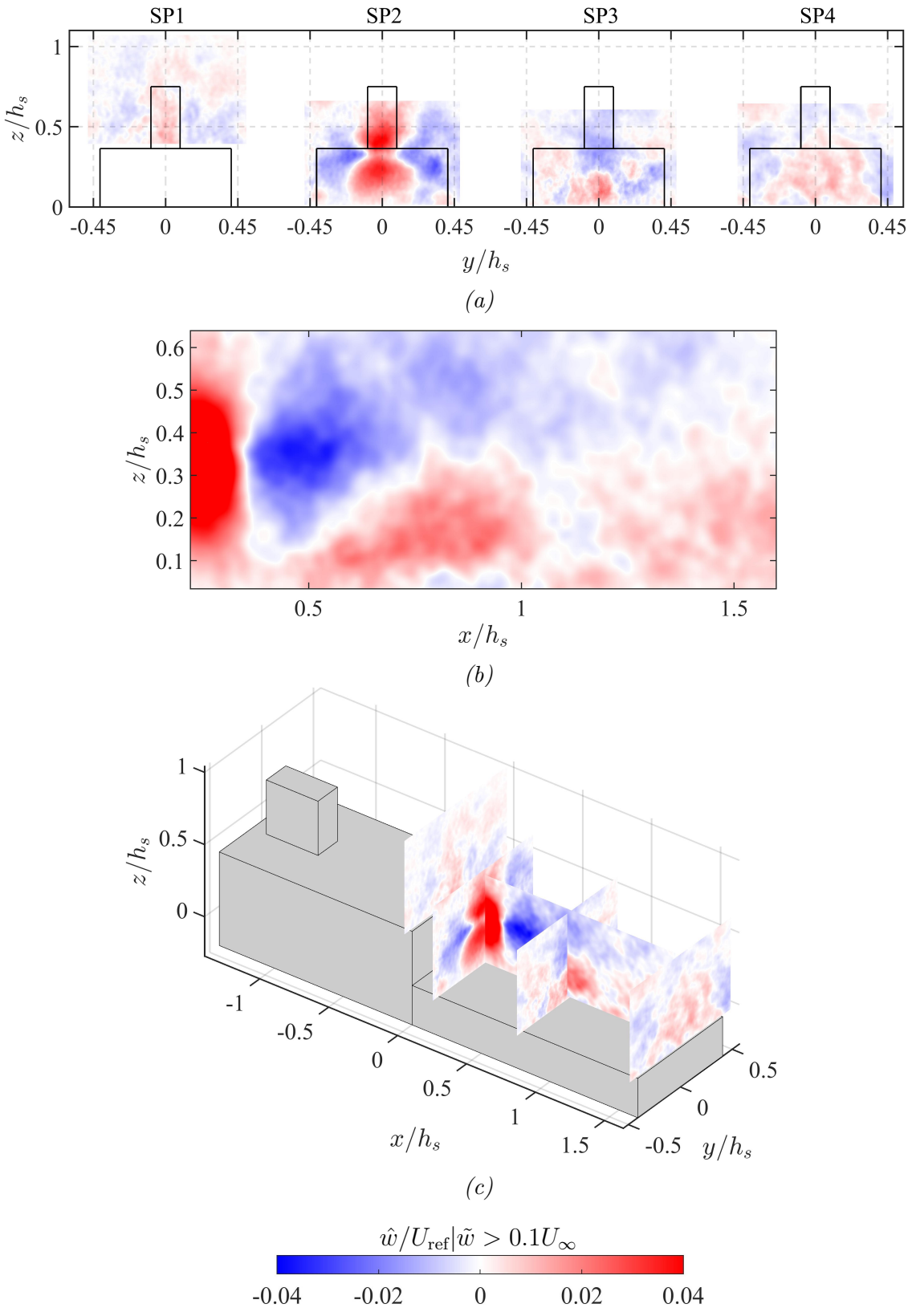

Figure 3.14 Wall-normal conditional velocity field $\hat{w}/U_{\mathrm{ref}}$ for positive fluctuations $\tilde{w} > 0.1U_\infty$.

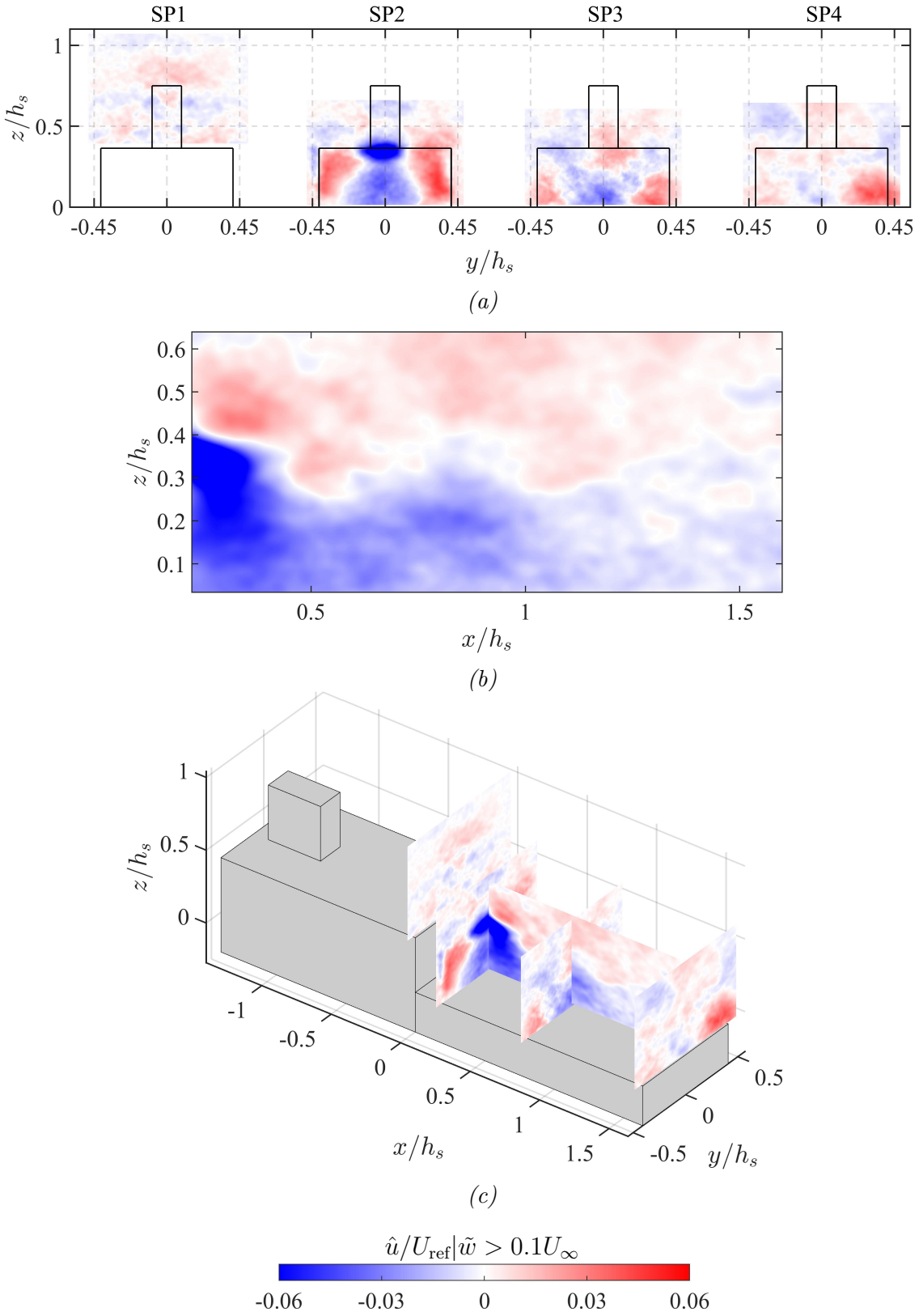

Figure 3.15 Streamwise conditional velocity field $\hat{u}/U_{\mathrm{ref}}$ for positive fluctuations $\tilde{w} > 0.1U_\infty$.

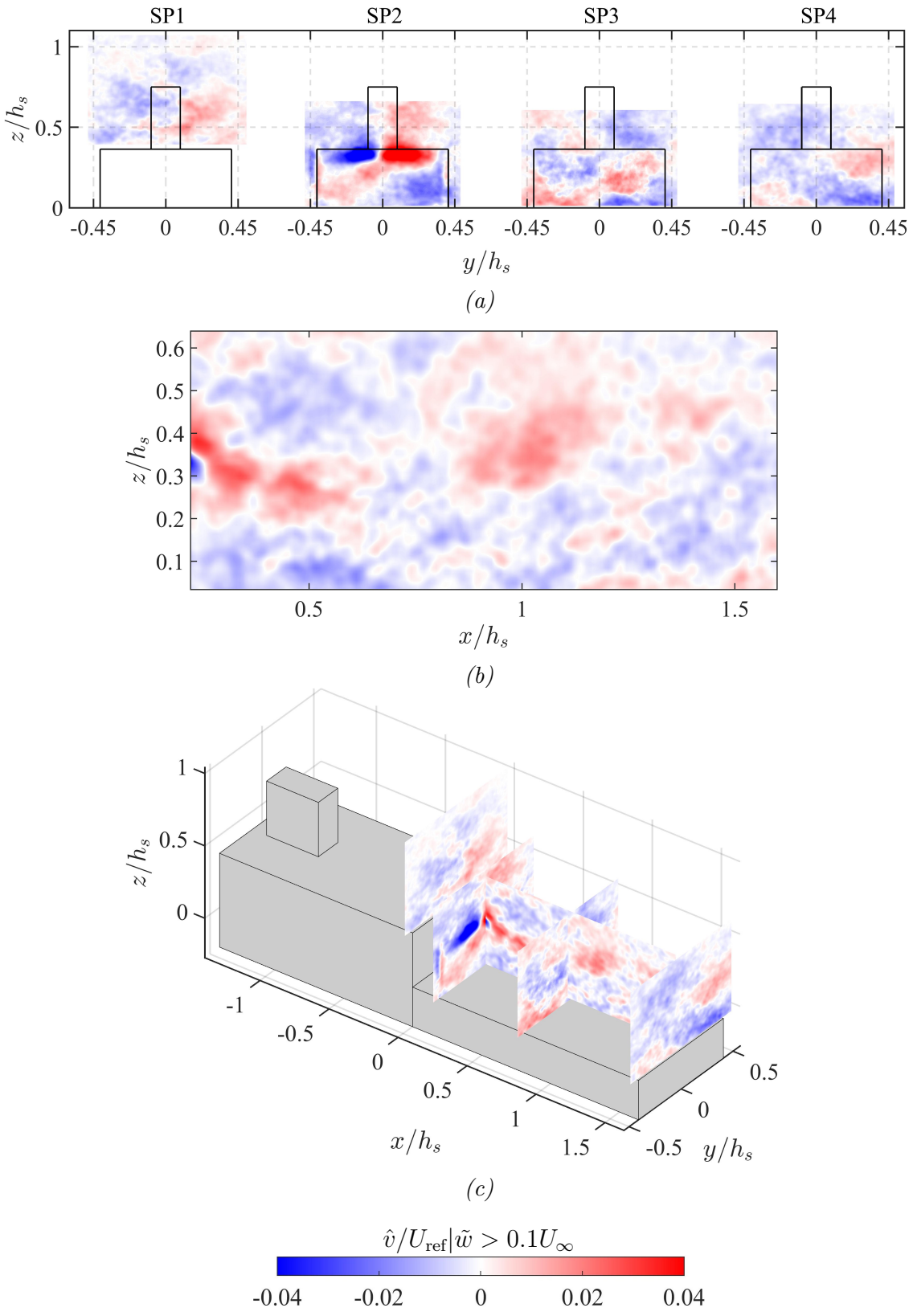

Figure 3.16 Spanwise conditional velocity field $\hat{v}/U_{\mathrm{ref}}$ for positive fluctuations $\tilde{w} > 0.1U_\infty$.

The spanwise conditional field $\hat{v}/U_{\text{ref}}|\tilde{w} > 0.1U_\infty$ in Fig. 3.16 resulted in a lower number of organized fluctuations compared to Figs. 3.14 and 3.15. In this case, however, an interesting pattern was seen upstream, closer to the hangar door. SP2 showed two defined regions - one highly positive and one highly negative, on the starboard and port sides, respectively. It appeared that the small, positive $\hat{v}$ region seen in the streamwise plane was the extension of the highly positive region from the starboard side. These two regions were (almost) symmetric across the ship centerline, resulting in intense velocity gradients at (or close to) the ship centerline. As for SP3 and SP4, the flow showed high asymmetry with respect to the centerline since positive and negative $\hat{v}$ regions were present but did not appear to form any large-scale organized structure.

Overall, the conditional fields obtained when the shear layer "flapped" up resulted in high velocity gradients, particularly in the wall-normal ($\hat{w}$) and streamwise ($\hat{u}$) velocities. The conditional velocity fields in the streamwise plane (Figs. 3.14 and 3.15) pointed to the oscillatory behavior of the shear layer, which appeared to influence the location of the positive and negative regions of intense fluctuations. Additionally, the conditional spanwise field in Fig. 3.16 showed a sharp spanwise gradient behind the top edge of the hangar door.

The conditional flow fields when there was a large negative vertical fluctuation right above the flight deck were considered next. As shown in Fig. 3.17, the negative fluctuations were identified using the identical PDF used to identify the positive vertical fluctuation. This time, the red bins highlighted the instances in which the fluctuations exceeded the negative threshold. Once again, the conditional method was applied to all four spanwise-streamwise plane configurations. As expected, the number of instances in which $\tilde{w}(t) < -0.1U_\infty$ were roughly the same as the positive case. Additionally, they were consistent among all four datasets, as shown in Table 3.2. The resulting conditional fields i.e., $\hat{w}/U_{\text{ref}}|\tilde{w} < -0.1U_\infty$, $\hat{u}/U_{\text{ref}}|\tilde{w} < -0.1U_\infty$ and $\hat{v}/U_{\text{ref}}|\tilde{w} < -0.1U_\infty$ are shown in Figs. 3.18, 3.19 and 3.20, respectively.

The conditional wall-normal velocity field $\hat{w}/U_{\text{ref}}|\tilde{w} < -0.1U_\infty$, shown in Fig. 3.18, re-

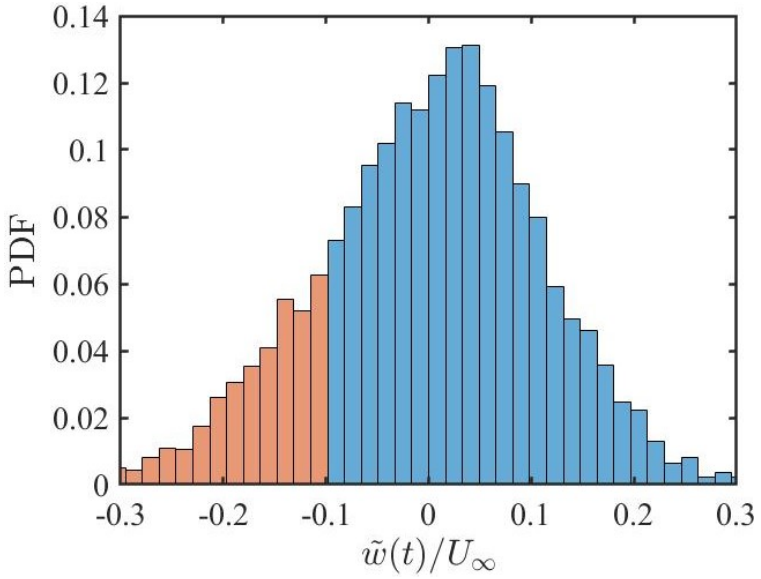

Figure 3.17 PDF of $\tilde{w}(t)$ used to identify the extreme vertical flow events. The red bins represented the negative flow fluctuations that exceeded the threshold $k_w = -0.1U_\infty$ (-3 $\mathrm{m\,s^{-1}}$).

Table 3.2 Number of instances in which $\tilde{w}(t) < -0.1U_\infty$ for each 7500-image dataset.

	SP#	SW#	No. Instances
Dataset 1	SP1	SW3	1401
Dataset 2	SP2	SW3	1394
Dataset 3	SP3	SW3	1420
Dataset 4	SP4	SW3	1377

vealed a similar pattern to the positive fluctuations case but with opposite orientation. This switch in sign and orientation of the $\hat{w}$ regions were likely due to the oscillatory behavior of the shear layer. In the spanwise planes, however, some small differences between the positive and negative fluctuating cases were observed. Starting with SP2, a narrower spanwise extension of the negative $\hat{w}$ region was present closer to the ship centerline. Similarly, the negative $\hat{w}$ regions at the spanwise extremities were significantly lower in magnitude. Additionally, SP3 did not show any defined structure in $\hat{w}$ but rather small fluctuations with significantly reduced magnitude when compared to the positive fluctuating case. Further downstream, SP4 showed the same area of less intense fluctuations close to the ship centerline as the positively conditioned plots.

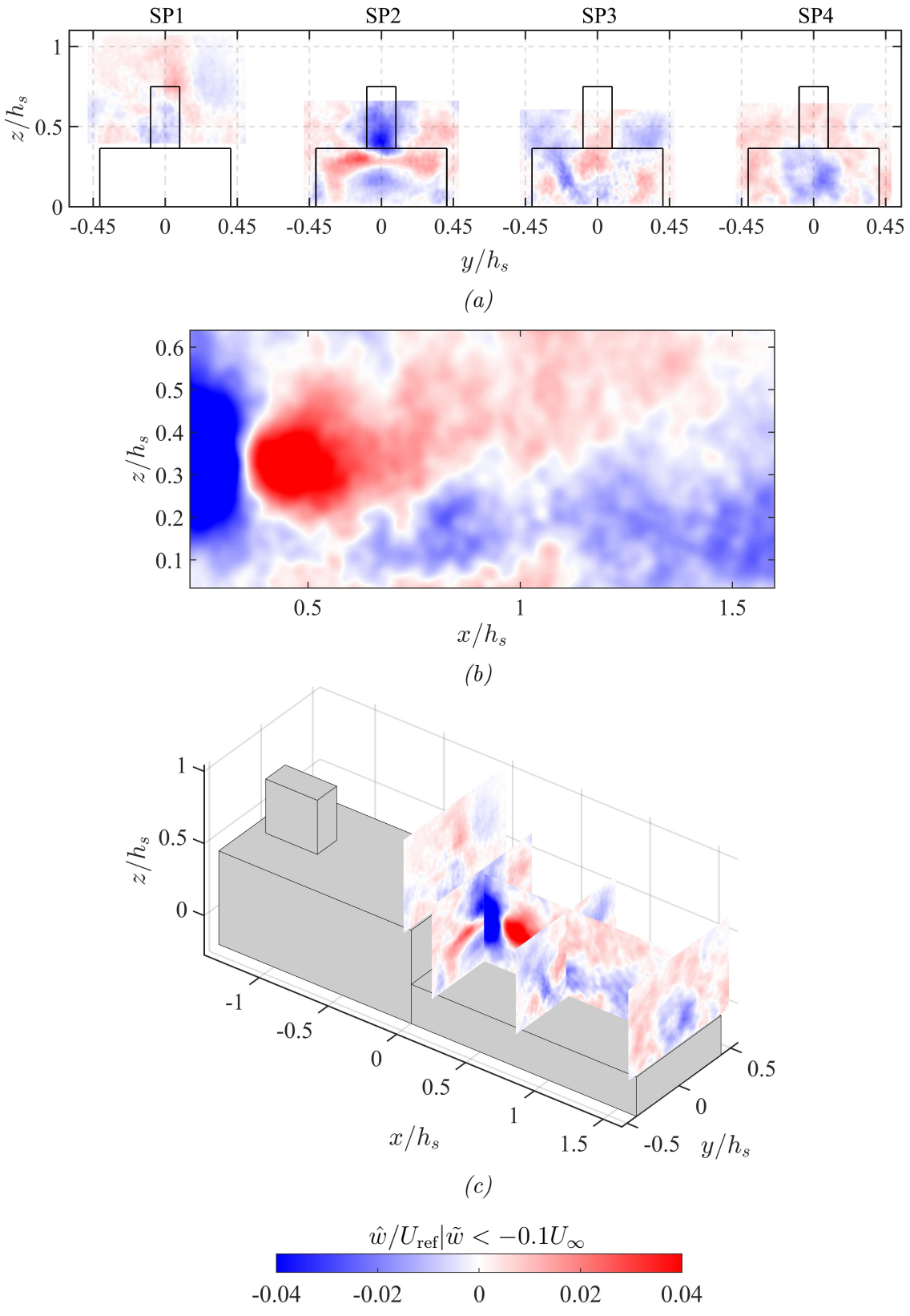

Figure 3.18 Wall-normal conditional velocity field $\hat{w}/U_{\mathrm{ref}}$ for negative fluctuations $\tilde{w} < -0.1U_\infty$.

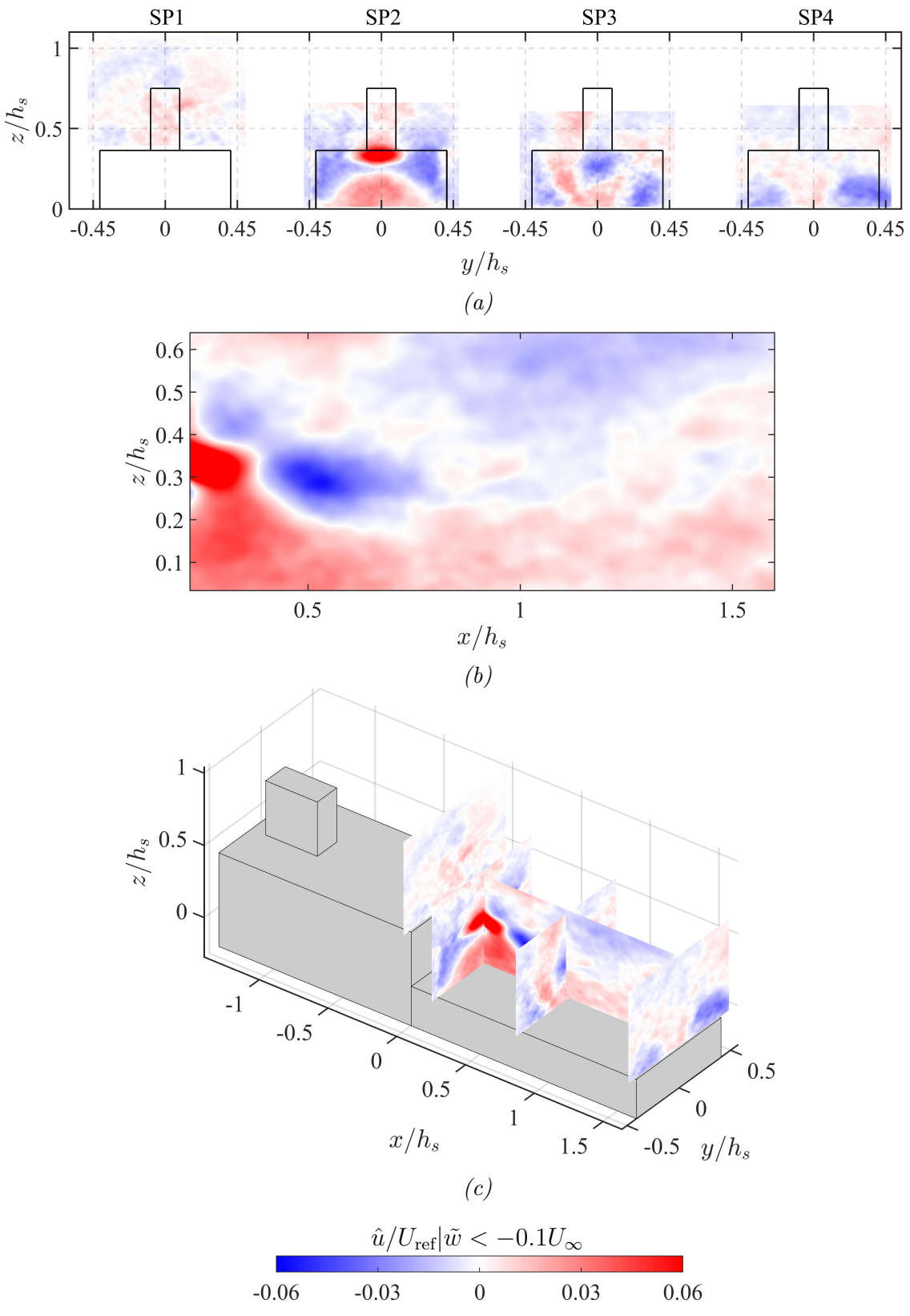

Figure 3.19 Streamwise conditional velocity field $\hat{u}/U_{\mathrm{ref}}$ for negative fluctuations $\tilde{w} < -0.1U_\infty$.

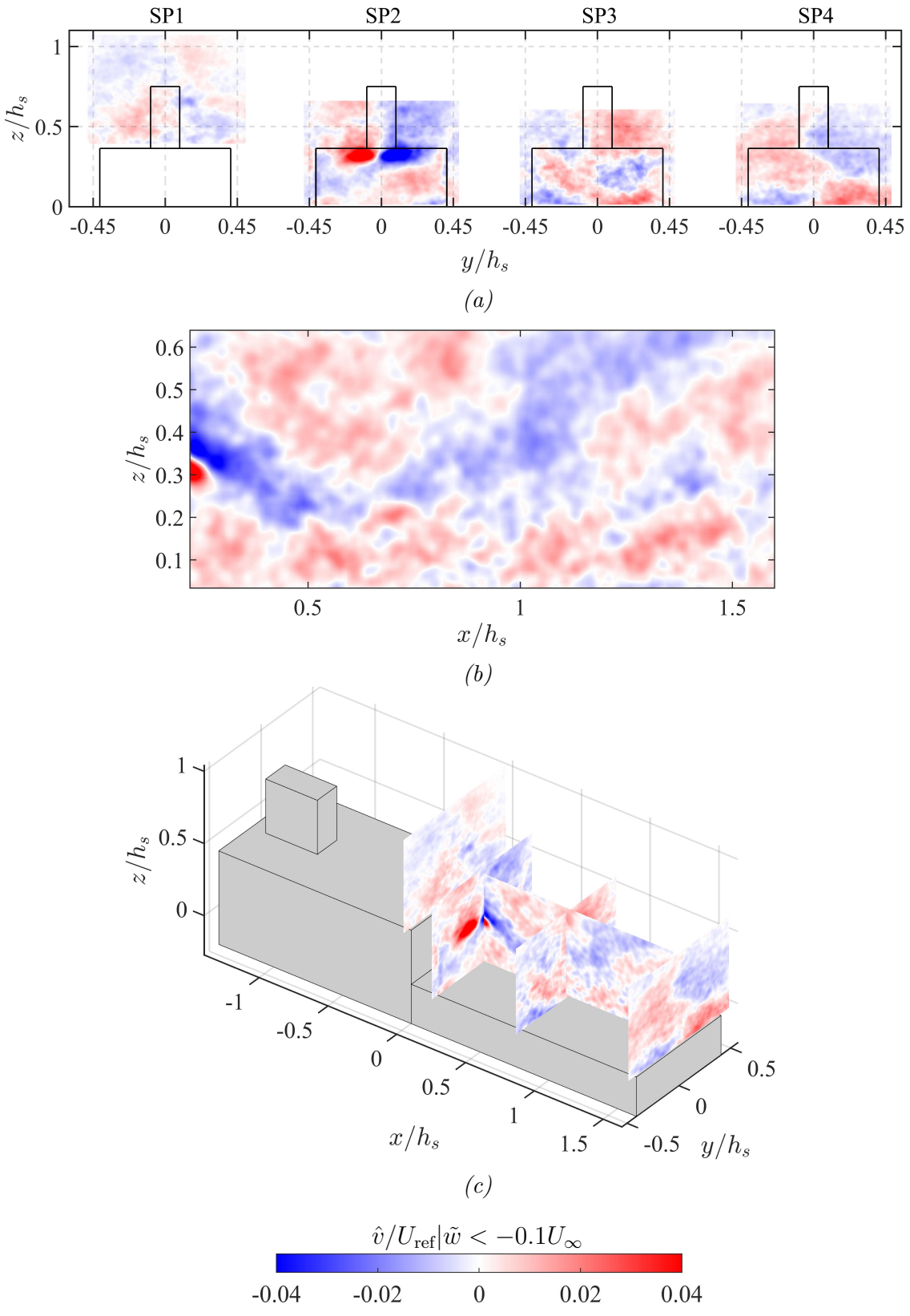

Figure 3.20 Spanwise conditional velocity field $\hat{v}/U_{\mathrm{ref}}$ for negative fluctuations $\tilde{w} < -0.1U_\infty$.

Looking at the streamwise conditional results $\hat{u}/U_{\text{ref}}|\tilde{w} < -0.1U_\infty$ shown in Fig. 3.19, the streamwise plane also indicated that this field was the opposite (in sign) counterpart of the cases conditioned upon positive fluctuations. However, some small differences were observed. For instance, SP2 showed symmetry across the centerline, while cases with positive fluctuations clearly showed an asymmetric behavior. SP3 and SP4 showed once again the mirror image of the positive fluctuations containing high- and low-speed regions closer to the flight deck, indicating intense velocity gradients and shear in an average sense.

Finally, the conditional spanwise velocity $\hat{v}/U_{\text{ref}}|\tilde{w} < -0.1U_\infty$ shown in Fig. 3.20 also presented lower fluctuation intensities when compared to $\hat{w}$ and $\hat{u}$. However, the two concentrated regions within SP2 observed when the shear layer "flapped" up were also present in this case. This time, the highly negative region was on the starboard side and the highly positive region was on the port side. The streamwise plane showed that the negative $\hat{v}$ region extended across this plane. Therefore, the axis of symmetry of these two regions was slightly shifted to the port side, which showed agreement with the results from positive fluctuations.

Figure 3.21 shows a side-by-side comparison of the resulting structures within the streamwise plane in cases that were conditioned upon positive and negative fluctuations. A closer look at these fields confirmed that the scale, orientation and arrangement of the fields conditioned in the case of negative fluctuations were (approximately) the mirror image of those with a large positive fluctuations. This suggested that the oscillations of the shear layer that resulted in $\tilde{w} > 0.1U_\infty$ and $\tilde{w} < -0.1U_\infty$ were temporally symmetric.

Fundamentally, it was evident from both sets of conditional fields that the vertical oscillatory motion of the shear layer was associated with large-scale flow features that spanned a large spatial area. This motion resulted in regions of intense gradients in all velocity components which have implications for safe rotorcraft operations. Thus, all conditional fields showed regions of correlated flow which have the potential to couple with an incoming or departing rotorcraft.

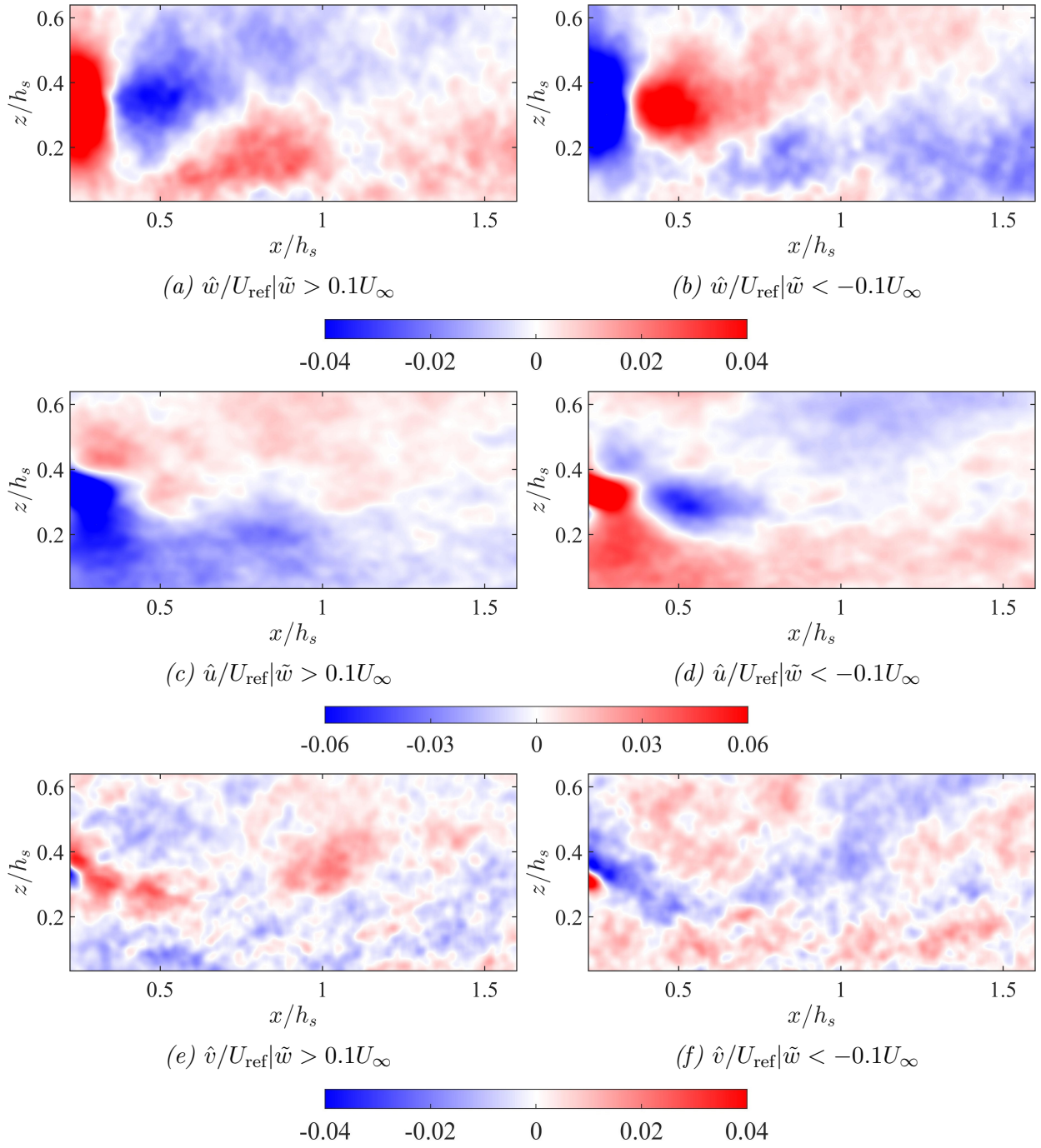

Figure 3.21 Side-by-side comparison of the streamwise plane showing fields conditioned upon positive (left) and negative (right) fluctuations in the shear layer.

3.2.2 Bistable Behavior of the Hangar Door Wake

Previous experimental and computational studies by Rao et al. [6], Herry et al. [8] and Zhang et al. [30] (among others) focused on the bistable flow features behind a backward-

facing, three-dimensional step. They concluded that each state showed a large vortex on one side while a smaller vortex was seen above the step on the opposite side with respect to the centerline. In order to study the bistable flow effects of the wake behind the hangar door, conditional averaging was used to isolate each stable state and study its effects on the airwake. The results presented in this section refer to the state in which $\tilde{v} < 0$ as state 1 and the state in which $\tilde{v} > 0$ as state 2 to maintain the same convention as that maintained by Rao et al. [6] (see Fig. 3.22). Cases with the sABL are presented in this section while the corresponding conditional results without the sABL can be found in Appendix C.

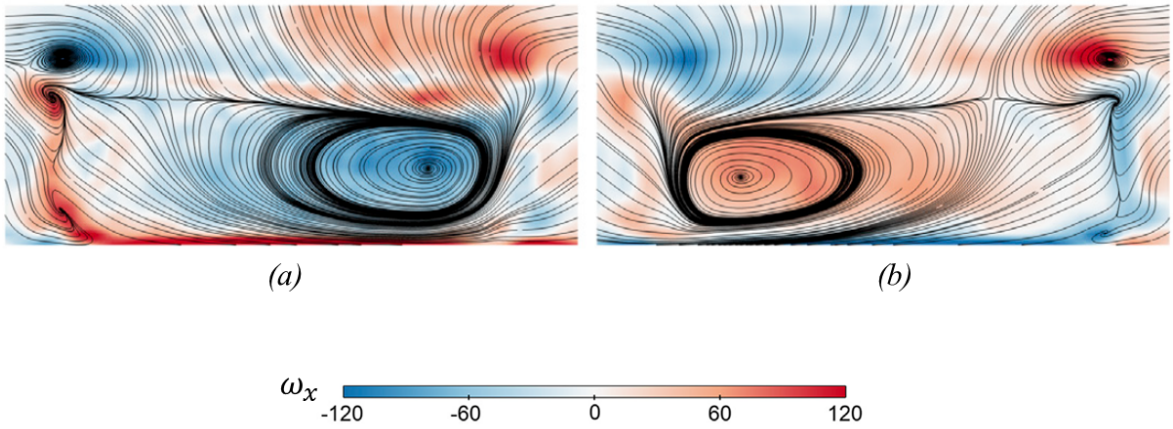

Figure 3.22 Two stable flow states behind a backward-facing, three-dimensional step. State 1 is shown in (a) and state 2 is shown in (b) [6].

The streamlines in Fig. 3.22 indicated that the spanwise velocity component v at the centerline closer to the deck surface was negative for state 1 and positive for state 2. Hence, conditional averaging was used to isolate each state based on the direction of v at this location. The region over which this condition was applied is shown in Fig. 3.23. This region was located closer to the flight deck surface because this area experienced clear changes in v for each state. Additionally, this region was selected as it was well within the wake of the hangar door. The size of the region was 36 mm^2 $(0.032h_s)^2$ and a total of 25 flow vectors were included within this region.

The spanwise velocity $\tilde{v}(t)$ over the spatial region was computed using the instantaneous

velocity v instead of the fluctuation v' because the bistable states were not related to flow fluctuations but rather to changes in the configuration of the wake i.e., the instantaneous flow velocity. Figure 3.24 shows $\tilde{v}(t)$ over a non-dimensional time period. The dotted black lines indicated the time intervals within which the peaks of $\tilde{v}(t)$ remained either positive or negative, which was used to identify each stable state.

The PDF of $\tilde{v}(t)$ is shown in Fig. 3.25. The skewness of the distribution was 0.023 and the kurtosis was 2.373. This implies that the PDF was approximately a Gaussian (normal) distribution. Hence, the probability of capturing one state (e.g., $\tilde{v} > 0$) at a certain time instance was roughly the same as the probability of capturing the other state (e.g., $\tilde{v} < 0$) as the skewness was close to zero. The red bins in Fig. 3.25 represented the instances when the wake configuration was categorized as state 1. The condition was applied to all four streamwise-spanwise plane combinations. The number of instances that met the criterion $\tilde{v} < 0$ are presented in Table 3.3.

First, the spanwise velocity fields conditioned to capture state 1 ($\hat{v}/U_\infty|\tilde{v} < 0$) were

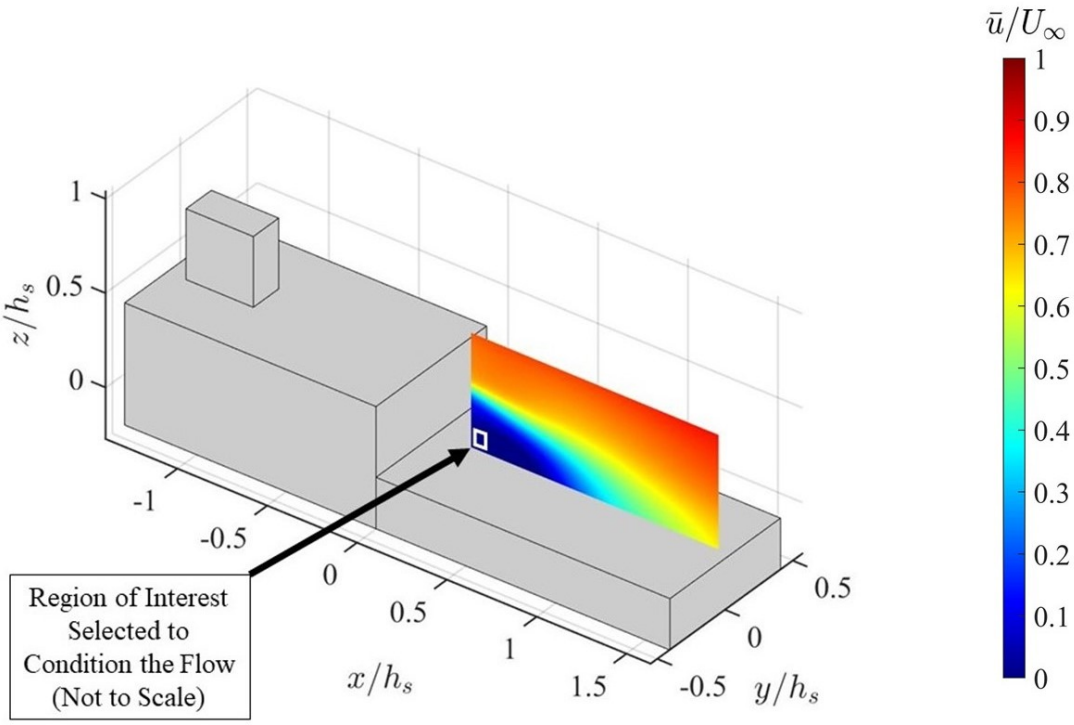

Figure 3.23 Conditional region selected to isolate each bistable state.

considered. In Fig. 3.26, SP1 showed unequal spanwise velocity $\hat{v}$ regions on either side of the ship. The positive $\hat{v}$ region on the port side appeared to be larger than the negative region on the starboard side, indicating potential asymmetric vortex structures with respect to the centerline. SP2 showed regions of negative $\hat{v}$ closer to the flight deck, as required to isolate state 1. Additionally, a highly positive $\hat{v}$ region behind the top edge of the hangar door was seen on the starboard side. Once again, the positive and negative $\hat{v}$ regions above the hangar door were unequal in size, which showed agreement with the behavior seen upstream in SP1.

Fig. 3.26b shows the streamwise extents of both the positive and negative $\hat{v}$ regions in

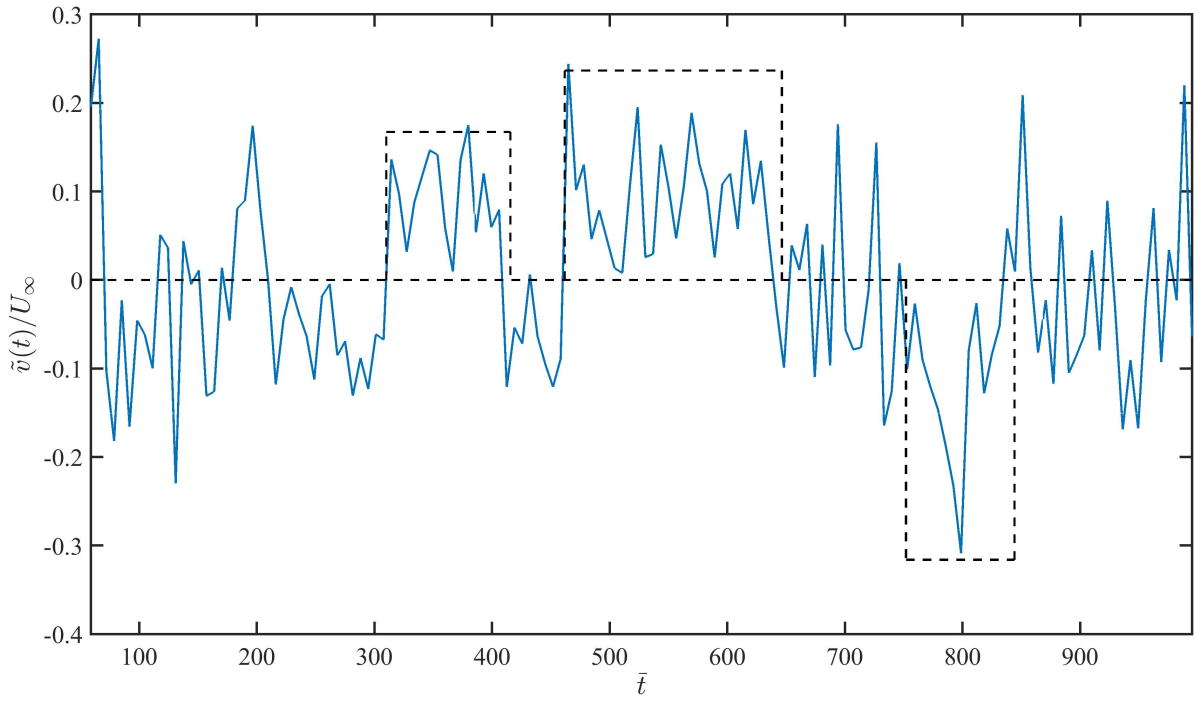

Figure 3.24 Average spanwise velocity over the spatial region of interest $\tilde{v}(t)$ over a non-dimensional time period. The dotted black lines helped identify each stable state.

Table 3.3 Number of instances in which $\tilde{v}(t) < 0$ for each 7500-image dataset.

	SP#	SW#	No. Instances
Dataset 1	SP1	SW3	3683
Dataset 2	SP2	SW3	3905
Dataset 3	SP3	SW3	4214
Dataset 4	SP4	SW3	3791

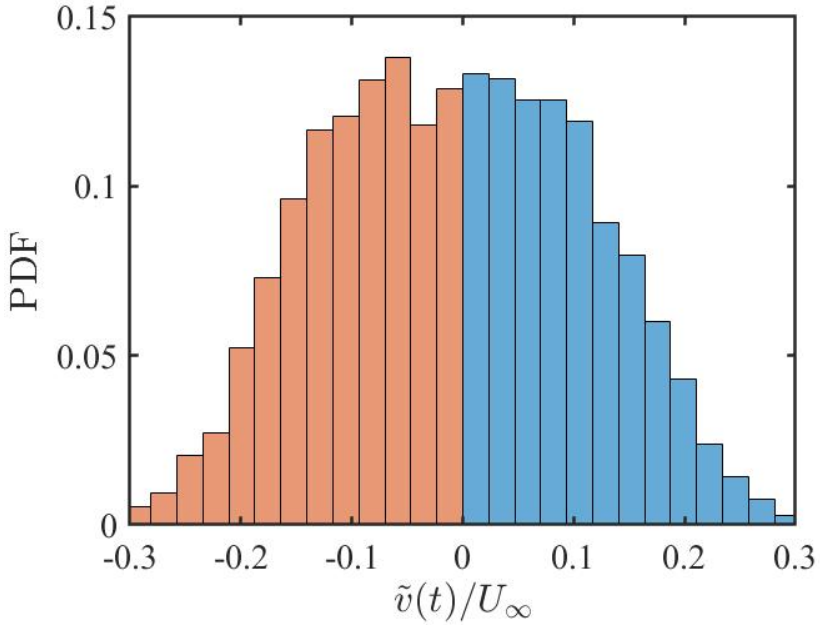

Figure 3.25 PDF used to identify each bistable state. The red bins represented the instances in which the wake configuration was categorized as state 1 ($\tilde{v} < 0$).

SP2. The larger negative $\hat{v}$ region in the streamwise plane covered the entirety of the flight deck length and remained in proximity to the deck surface. However, its intensity appeared to weaken as the flow developed downstream. On the other hand, the positive $\hat{v}$ region overlying the negative $\hat{v}$ region quickly dissipated. This region did not extend past the recirculation region and it appeared to be pushed against the deck by the effects of the flow reattaching over the deck. Moving downstream, spanwise plane 3 showed that the negative $\hat{v}$ contour region on the starboard side of this FOV extended across the ship centerline to the port side but only in the proximity of the deck surface. Finally, spanwise plane 4 showed less intense $\hat{v}$ gradients. However, higher $\hat{v}$ levels were identified on the port side of this FOV.

To further analyze the vortical structures in state 1, the conditional spanwise and wall-normal flow fields were combined. Figure 3.27 shows the contours of $\sqrt{\hat{v}^2 + \hat{w}^2}/U_\infty | \tilde{v} < 0$ with the respective pseudo-streamlines. The port side funnel vortex in SP1 was slightly larger than the one on the starboard side. The difference in funnel vortex size became more pronounced in SP2, where the vortex on the port side occupied a larger spatial domain

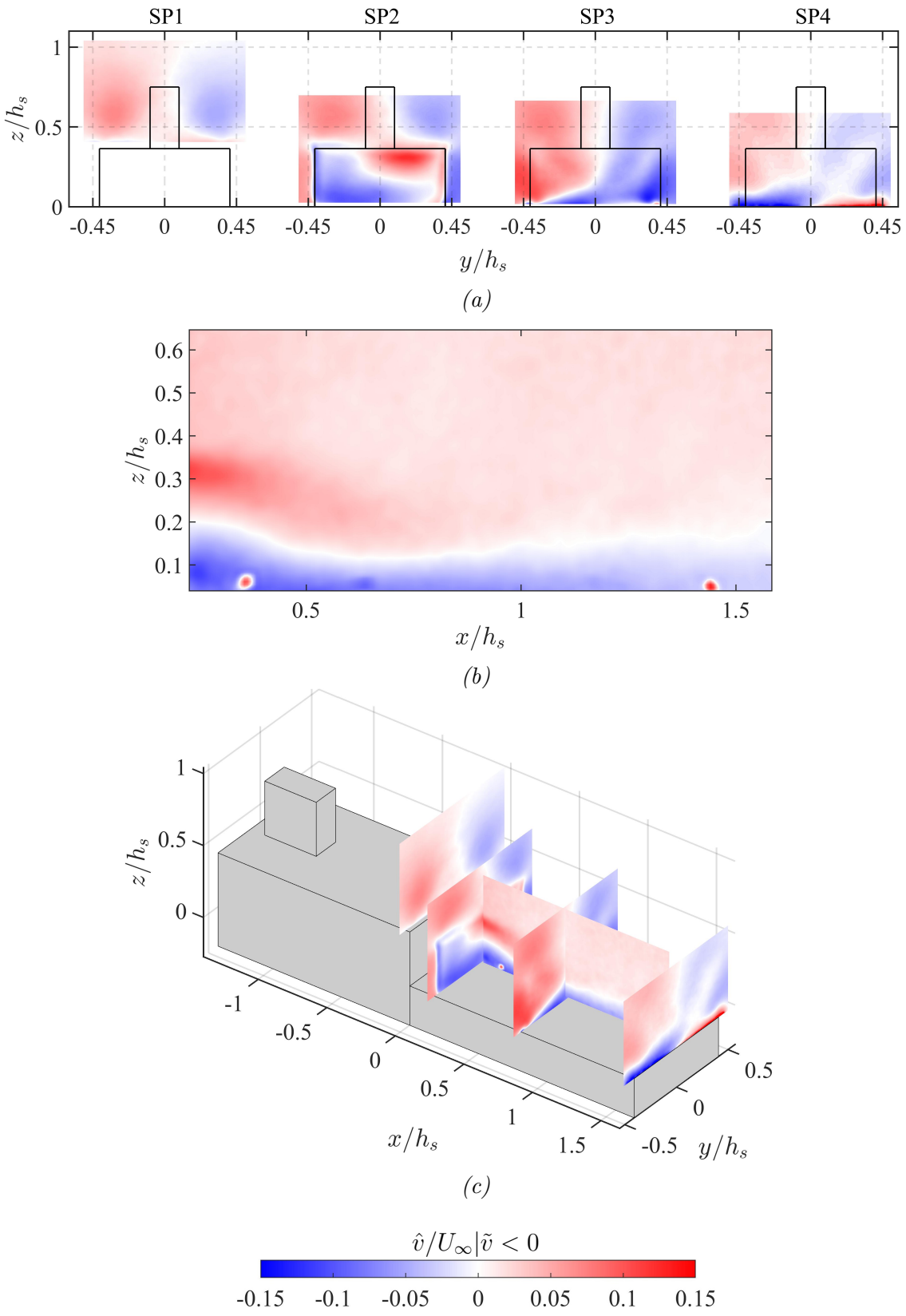

Figure 3.26 Conditional spanwise velocity field for state 1 ($\tilde{v} < 0$).

over the hangar door. Additionally, the characteristic vortex of state 1 was seen behind the hangar door rotating clockwise. These two vortical structures showed agreement with previous studies by Rao et al. [6] and Zhang et al. [30]. However, the smaller vortex on the starboard side appeared to be more defined when compared to their computational results.

Further downstream, the streamlines in SP3 clearly showed the effects of the negative $\hat{v}$ region moving towards the port side in proximity to the flight deck surface (previously seen in Fig. 3.26). This flow effect over the flight deck surface could potentially induce significant axial (spanwise) airloads on a rotorcraft operating at this location. Finally, SP4 showed a similar biased flow behavior closer to the flight deck, showing that this flow configuration remained fairly unchanged as the flow developed downstream. Figure 3.27b better showed the evolution of these structures along the flight deck. Note that the streamwise plane was omitted to better highlight the asymmetry along the centerline.

Overall, it was clear that state 1 influenced the flow structures both upstream and downstream of the hangar door wake. Spanwise planes 1, 3, and 4 showed biased flow potentially induced by this wake configuration. The flow downstream of the recirculation bubble featured high spanwise velocities close to the deck surface. This effect will likely induce significant axial airloads on rotor systems operating in the proximity of the deck.

State 2 was isolated using the condition $\tilde{v} > 0$, which was indicated by the red bins in Fig. 3.28. The instances that met this flow criterion were between 3500 and 3800 for each spanwise-streamwise configuration, as shown in Table 3.4. The spanwise conditional field $\hat{v}/U_\infty|\tilde{v} > 0$, shown in Fig. 3.29, was considered first. The spanwise plane 1 in Fig. 3.29a shows that the positive and negative spanwise conditional velocity $\hat{v}$ regions on the port and starboard side respectively appeared to be symmetric when compared to the contours conditioned to isolate state 1. Further downstream, spanwise plane 2 showed a highly positive $\hat{v}$ area that extended from starboard to port side and remained closer to the deck. The $\hat{v}$ region behind the top edge of the hangar door was negative and remained on the port side of the ship. Additionally, the wake funnel area above the hangar door appeared to show

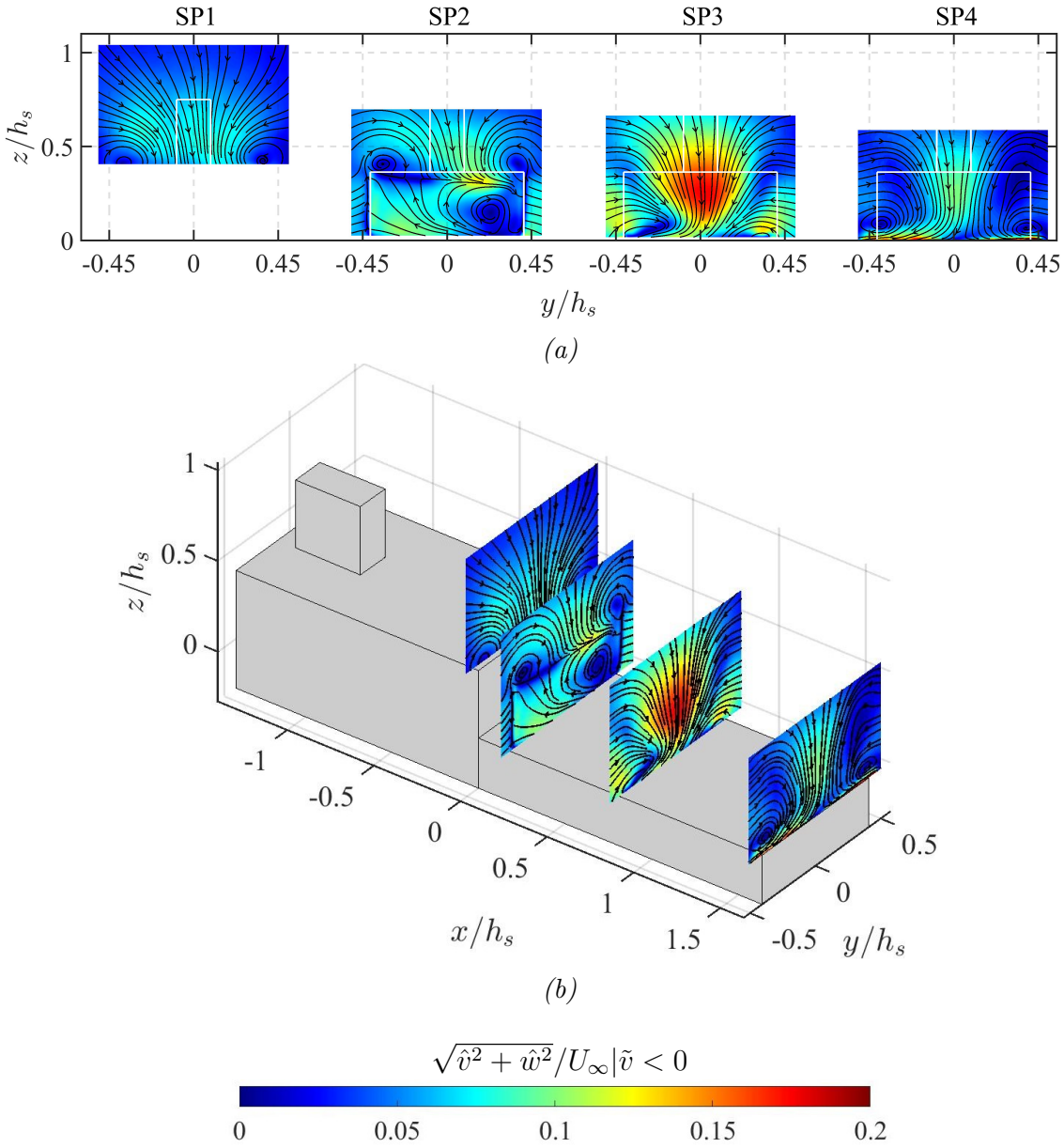

Figure 3.27 Combined spanwise and wall-normal conditional fields for state 1 ($\tilde{v} < 0$).

a semi-symmetric behavior as neither positive nor negative $\hat{v}$ regions extended across the centerline like it was observed in the flow conditioned to capture state 1. The mid-deck plane (SP3) showed the opposite trend compared to state 1 as the highly positive $\hat{v}$ region extended through the ship centerline from port to starboard while remaining close to the deck. Finally, spanwise plane 4 showed drastic $\hat{v}$ gradients only on the surface of the flight deck, showing a similar trend seen in state 1 but with flipped orientation.

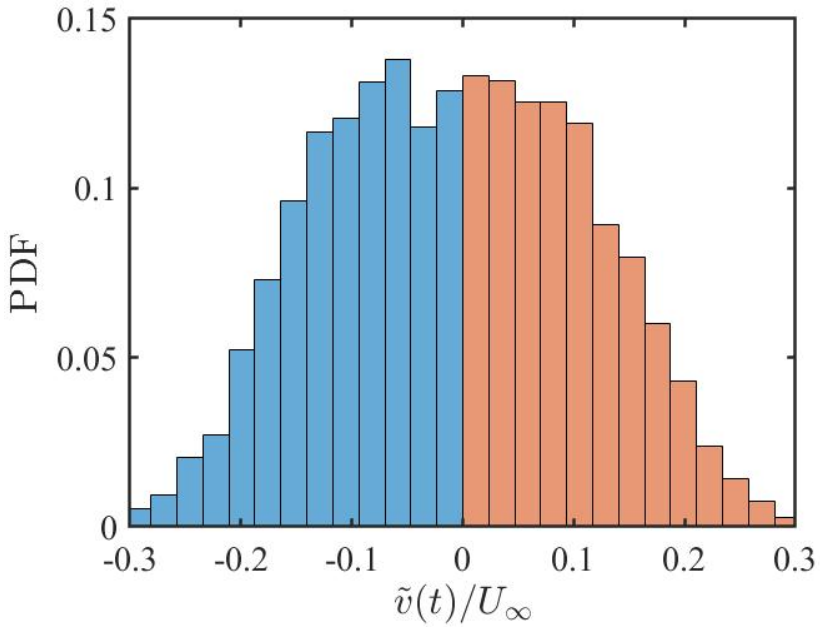

Figure 3.28 PDF used to identify each bistable state. The red bins represented the instances in which the wake configuration is categorized as state 2 ($\tilde{v} > 0$).

Table 3.4 Number of instances in which $\tilde{v}(t) > 0$ for each 7500-image dataset.

	SP#	SW#	No. Instances
Dataset 1	SP1	SW3	3817
Dataset 2	SP2	SW3	3595
Dataset 3	SP3	SW3	3286
Dataset 4	SP4	SW3	3709

The streamwise plane in Fig. 3.29b showed that the positive $\hat{v}$ region close to the flight deck surface extended along most of its length. However, the streamwise extent of the negative region in SP2 was not fully captured. Rather, a slightly negative region was seen at the upstream end of this plane, meaning this region only extended up to the ship centerline in the spanwise direction. This is shown in Fig. 3.29c. In addition, this three-dimensional perspective shows that the flow regions in state 2 were similar in size and location to the ones seen in state 1 but with flipped orientation. Therefore, the vortex structures and overall flow configuration induced by state 2 were the mirror image (about the ship centerline) of the structures seen in state 1.

The conditional spanwise and wall-normal velocity components were combined to better

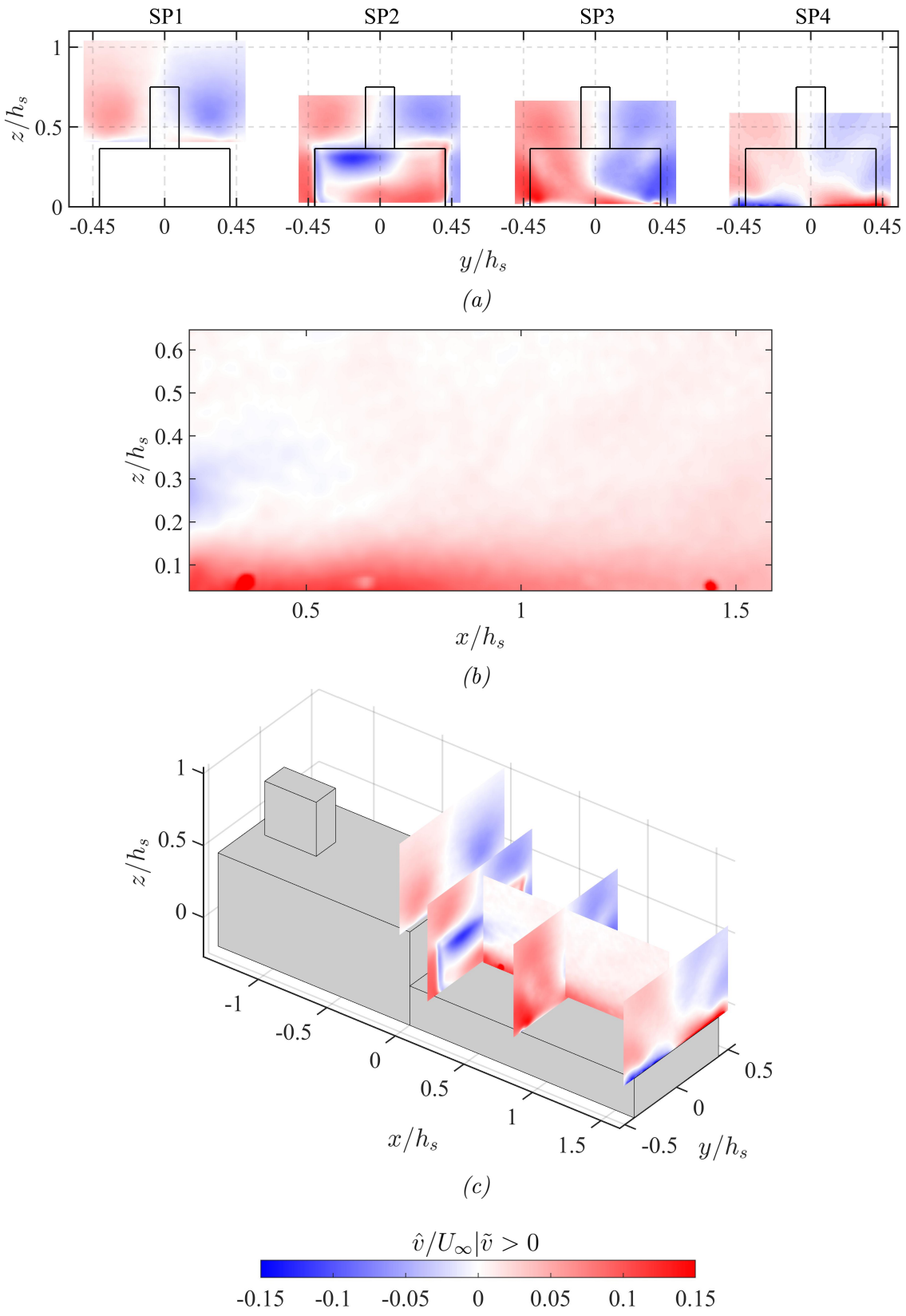

Figure 3.29 Conditional spanwise velocity field for state 2 ($\tilde{v} > 0$).

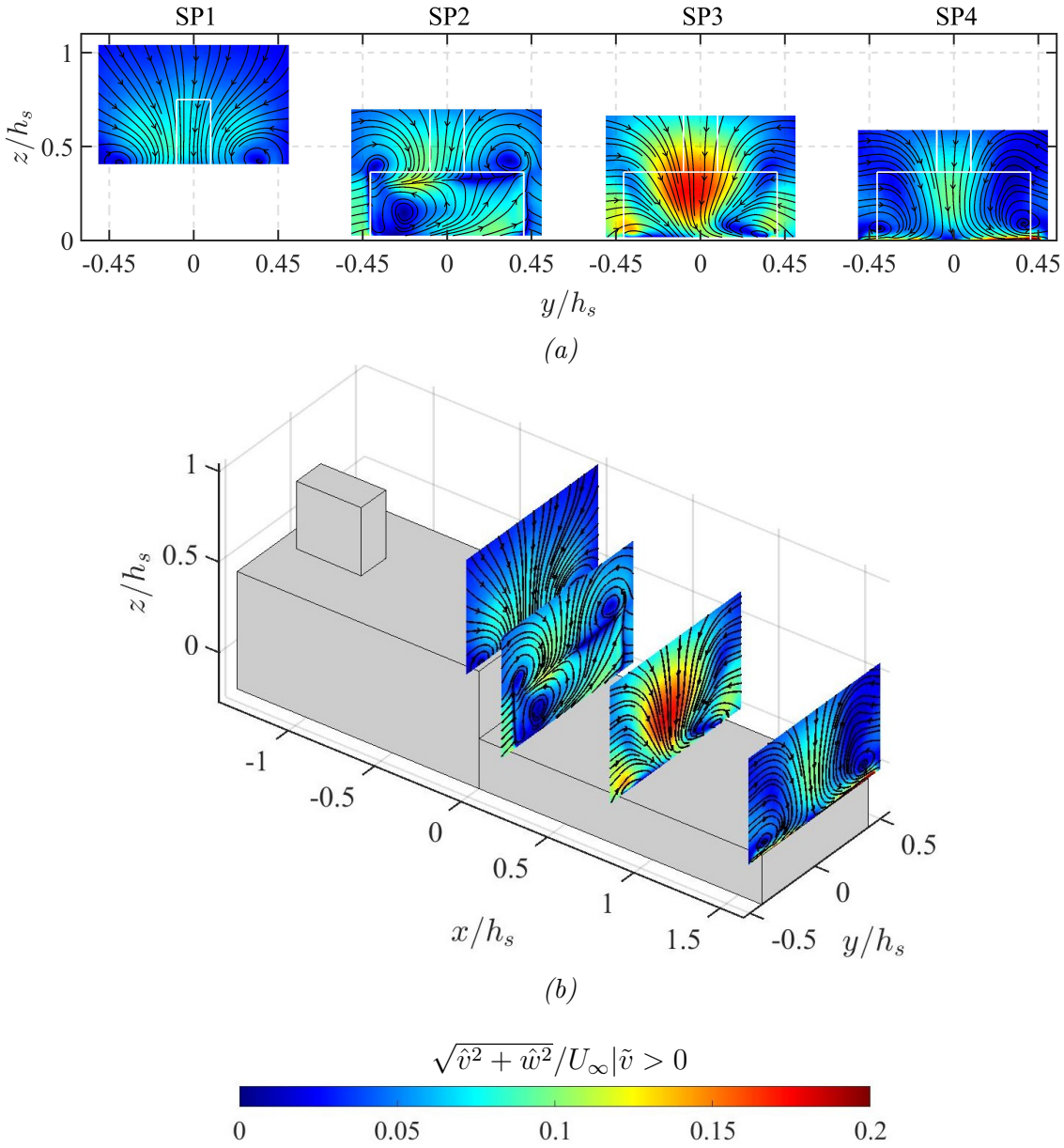

Figure 3.30 Combined spanwise and wall-normal conditional fields for state 2 ($\tilde{v} > 0$).

visualize the vortex structures present in state 2. Figure 3.30 shows the resulting vortices in two- and three-dimensional perspectives. First, SP1 showed a slightly larger funnel vortex on the starboard side of the ship, despite the equal size of the $\hat{v}$ regions seen in Fig. 3.29. The difference in vortex size became clearer in SP2, where the starboard vortex occupied a significant spatial domain above the hangar door while the port vortex was considerably small. Behind the hangar door, the characteristic vortex of the second state rotated coun-

terclockwise and was present on the port side of the ship. Downstream, the streamlines closer to the flight deck showed spanwise velocities biased towards the starboard side, which showed agreement with the contours in Fig. 3.29. Moreover, SP4 showed slightly larger flight deck vortices on the starboard side of the ship, which coincided with the trend initially seen upstream in the case of the funnel vortices.

In summary, the flow field conditioned to capture state 2 showed larger vortex structures on the starboard side in SP1, SP3, and SP4. The asymmetry in the funnel vortices observed behind the funnel structure became more pronounced as the flow detached past the hangar door. In the recirculation bubble, the characteristic vortex was present on the port side rotating counterclockwise. Downstream of the hangar door wake, high spanwise velocities towards the starboard side were observed closer to the flight deck, potentially inducing axial aerodynamic forces on any rotorcraft operating in the airwake.

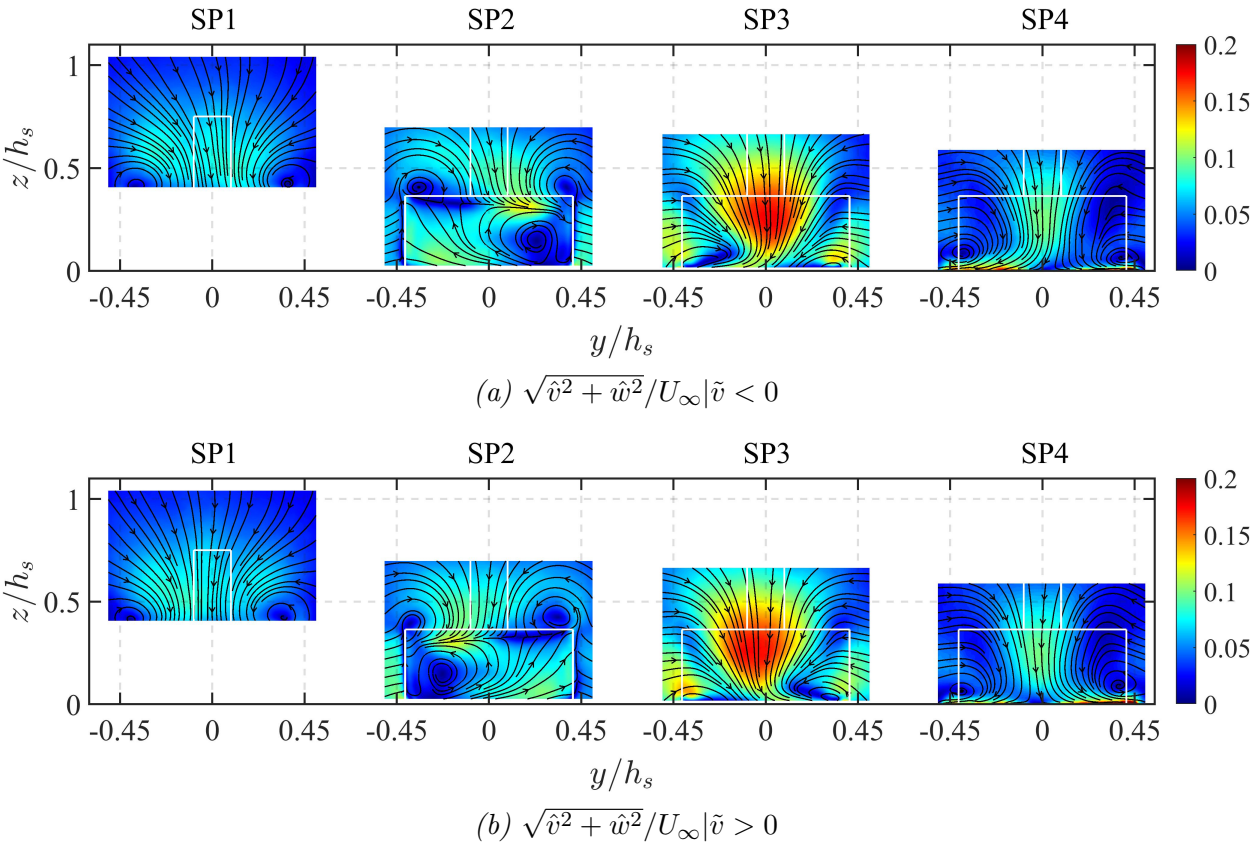

(a) $\sqrt{\hat{v}^2 + \hat{w}^2}/U_\infty | \tilde{v} < 0$

(b) $\sqrt{\hat{v}^2 + \hat{w}^2}/U_\infty | \tilde{v} > 0$

Figure 3.31 A direct comparison of each state. State 1 and 2 are shown in the top and bottom figures, respectively.

A direct comparison of each state is shown in Fig. 3.31, where the spanwise planes of state 1 and 2 are shown in the top and bottom figures, respectively. Comparing SP1 and SP2, the larger funnel vortex over the hangar door was on the port side when state 1 was captured and on the starboard side when state 2 was captured. The characteristic vortex behind the hangar door was also seen on opposite sides of the ship e.g., starboard side when state 1 was isolated and port side when state 2 was isolated. Moving downstream, the streamlines in SP3 showed opposite trends in the spanwise flow direction closer to the deck surface as states 1 and 2 showed negative $\hat{v}$ and positive $\hat{v}$ values respectively. Consequently, the flight deck vortices showed spatial asymmetry across the ship centerline.

3.2.3 Transition Between Bistable States of the Hangar Door Wake

The present section studies the transition between the two bistable states using conditional averages. According to the literature survey, there are three possibilities that cause the transition from one flow state to the other: Changes in the distribution of momentum on the model's lateral sides caused by upstream turbulence, separating shear layers on either side of the body triggered by turbulence changes and upstream flow perturbations [6, 30, 51]. All of these factors make the switch between stable states unpredictable. Nonetheless, it is possible to isolate transitions between the two states using conditional averages by applying the condition on a temporal basis. In the case of the current analysis, the instances before and after the formation of the characteristic vortex were considered for each bistable state. Thus, the flow structures during and after the transitional phase were captured. Additionally, the synchronous dual-plane measurements allowed for the study of the upstream and downstream effects of this transitional phase.

The convention for each state remained the same as the previous section: state 1 featured the characteristic vortex behind the hangar door on the starboard side while state 2 featured the same on the port side. If the conditional flow in SP2 featured neither, then it was considered part of the transitional phase. This analysis used the same conditional region and average spanwise velocity $\tilde{v}(t)$ over this region as used in Section 3.2.2. The corresponding

results presented in this section were obtained using flow fields with the sABL. The results using flow fields without the sABL are presented in Appendix C.

First, the transition to state 1 was studied. To identify the time instance t_0 at which transitions occurred, three temporal criteria had to be met: (i) $\tilde{v} < 0$ at t_0, (ii) $\tilde{v} > 0$ at the preceding time instance $t_0 - \Delta\bar{t}$ and (iii) $\tilde{v}(t) < 0$ for a minimum of five consecutive time instances following t_0 ($t_0 + \Delta\bar{t}$ to $t_0 + 5\Delta\bar{t}$). These criteria ensured that the instances used to compute the conditional average in fact captured the transition to state 1. In the case of this analysis, each state was identified using the sign convention of $v(t)$, e.g., if $v(t) > 0$, the sign of $v(t) = +1$ and if $v(t) < 0$, the sign of $v(t) = -1$. Figure 3.32 shows an example of a time instance that met these criteria and was considered to analyze the transition to state 1. Note that that $\bar{t} = tU_\infty/h_s$.

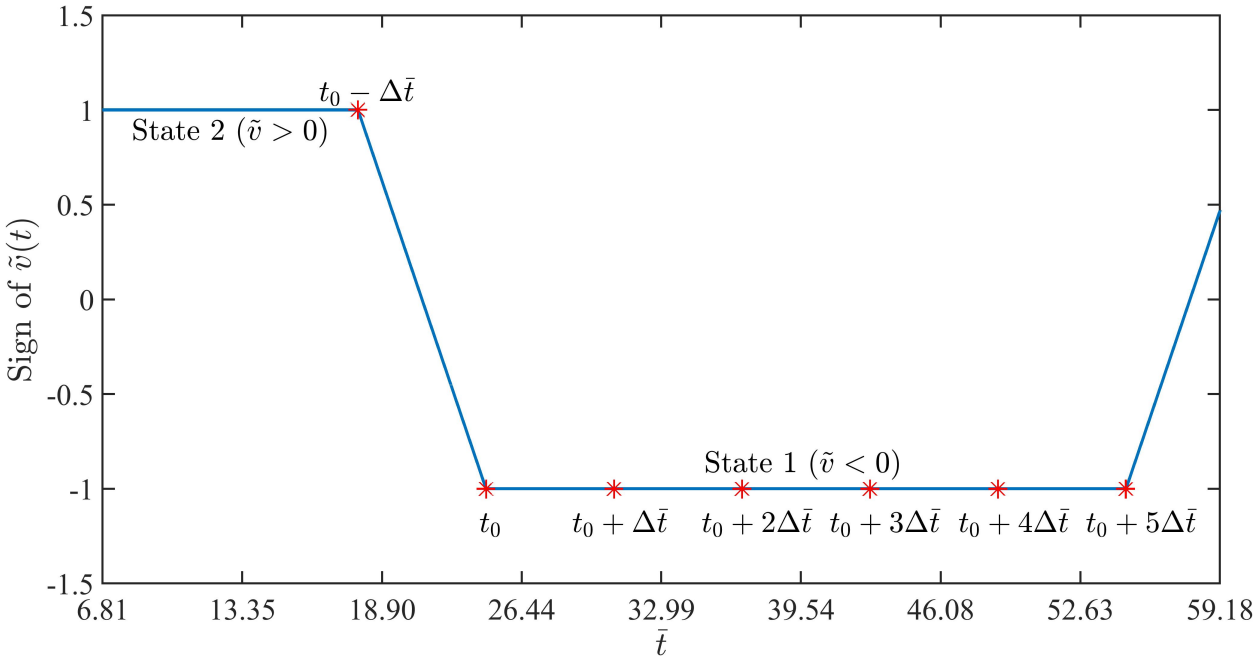

Figure 3.32 Example of time instance that met the flow criteria and was considered a transition to state 1.

This flow criteria was used to parse all 7500 instances in a dataset to isolate the instances in which a clear transitions to state 1 occurred. A total of 262 such transitions were identified. In the case of the current analysis, the transition number within the dataset is noted as n.

The ten instances before and after each transition were considered ($t_0 \pm 10\Delta t$) to obtain an average evolution of the transition in time. For example, consider the instantaneous velocity fields u, v, and w that were captured ten instances before the n^{th} transition to state 1. These instantaneous velocity fields were denoted as $u_{t_0-10\Delta\bar{t}}$, $v_{t_0-10\Delta\bar{t}}$, and $w_{t_0-10\Delta\bar{t}}$, respectively. Equation 3.1 illustrates the manner in which the temporally averaged streamwise velocity field $\bar{u}_{t_0-10\Delta\bar{t}}$ was obtained using the $t_0 - 10\Delta\bar{t}$ instances of each one of the 262 transitions ($N = 262$). Similarly, the conditionally averaged wall-normal and spanwise velocity fields were noted as $\bar{v}_{t_0-10\Delta\bar{t}}$ and $\bar{w}_{t_0-10\Delta\bar{t}}$, respectively. An identical temporal conditional average was obtained for all instances from $t_0-10\Delta t$ to $t_0+10\Delta t$, including the instance of transition t_0.

$$\bar{u}_{t_0-10\Delta\bar{t}} = \frac{\sum_{n=1}^{N} u_{t_0-10\Delta\bar{t}}(n)}{N} \tag{3.1}$$

Figure 3.33 shows the conditional development of the flow field at the instances preceding the transition. The comparison of the spanwise planes at each instance was useful to illustrate the conditional mean flow evolution of the transition to state 1. The instances from $t_0-10\Delta\bar{t}$ to $t_0 - 5\Delta\bar{t}$ are not included since the average flow structures did not change significantly during these occurrences. The conditionally averaged flow field captured at $t_0 - 4\Delta\bar{t}$ is shown in Fig. 3.33a. This was considered the beginning of the transition since it was the first instance that showed significantly biased flow structures corresponding to those seen in state 1. In this figure, the funnel vortices in SP1 remained symmetric with respect to the ship centerline. In SP2, the streamlines indicated that the flow moved from the starboard to the port side and up into the recirculation region. Further downstream, SP3 showed high spanwise velocities towards the port side over the flight deck. The same pattern was observed downstream in SP4, where the flow also moved towards the port side as it came close to the flight deck surface. These noticeable changes in flow structure are indicators of the flow beginning to transition to state 1.

Figure 3.33b shows the mean flow captured at $t_0 - 2\Delta\bar{t}$. The funnel vortices were sym-

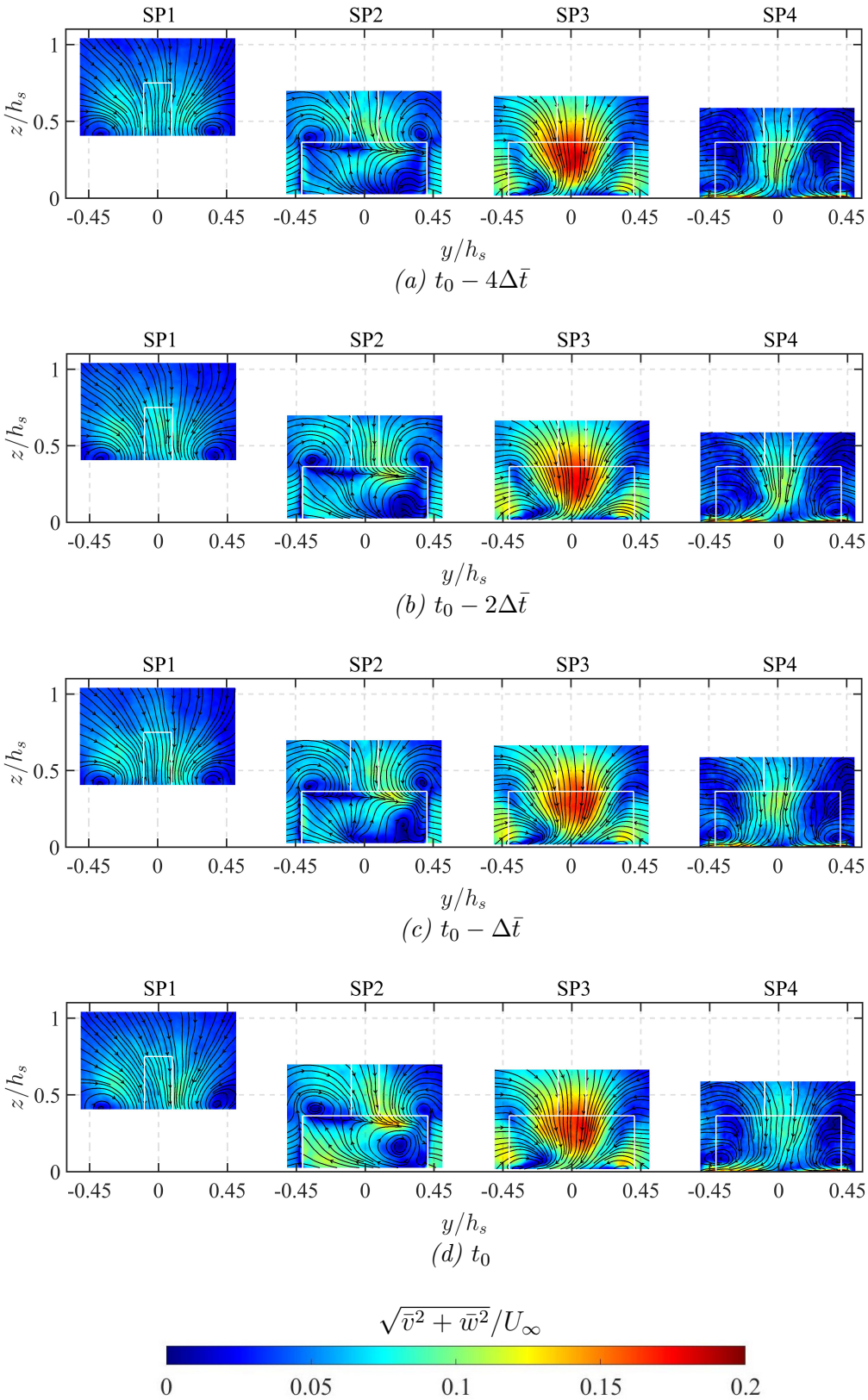

Figure 3.33 Temporal average obtained using the instants preceding the transition to state 1 in (a), (b), and (c) as well as at the instant of transition in (d).

metric with respect to the centerline within SP1. However, in SP2, the vortex on the port side appeared to be larger than the one on the starboard side. Additionally, the streamlines behind the hangar door showed the formation of a vortical structure on the starboard side of the ship. However, there was not a defined vortex at this time. Moving downstream, the streamlines in SP3 indicated a slightly higher spanwise velocity close to the deck. However, there were no major changes when compared to the contours obtained at $t_0 - 4\Delta\bar{t}$. The same pattern was observed in SP4, where the flow remained biased towards the port side of the ship.

The mean flow configuration before the transition ($t_0 - \Delta\bar{t}$) seen in Fig. 3.33c showed a more defined vortical structure on the starboard side behind the hangar door. Additionally, the funnel vortex on the port side was significantly larger than the one on starboard side. On the other hand, the flow configuration seen in SP1, SP3, and SP4 remained fairly unchanged when compared to the previous instances. This indicated that the upstream and downstream effects of state 1 were already noticeable prior to the formation of the characteristic vortex.

The conditionally averaged flow fields at the instant of transition are shown in Fig. 3.33d. Spanwise plane 1 showed a larger funnel vortex on the port side. In SP2, the funnel vortex asymmetry became more pronounced as the vortex on the port side was significantly larger. Finally, the characteristic vortex was formed behind the hangar door on the starboard side while the downstream flow seen in SP3 and SP4 did not change significantly when compared to the previous instances.

Overall, the main changes in time were seen within SP2, where the funnel vortex on the port side increased in size and the characteristic vortex behind the hangar door was on the starboard side. Even though the difference in funnel vortex size was not as pronounced within SP1, there existed an upstream bias that was captured at this plane. Downstream, SP3 and SP4 did not show significant changes in flow behavior since the flow showed high spanwise velocities towards the port side only in the proximity of the deck.

The instances after the transition were considered next. In this case, the flow configura-

tion remained fairly unchanged between the instance of transition t_0 and instance $t_0 + 7\Delta\bar{t}$, when the characteristic vortex behind the hangar door started to deform. This indicated the beginning of the transition out of state 1. Figure 3.34 shows the conditionally averaged flow during the transition as well as the flow captured at instances $t_0 + 4\Delta\bar{t}$, $t_0 + 7\Delta\bar{t}$, and $t_0 + 10\Delta\bar{t}$.

The flow structures shown in both Figs. 3.34a and 3.34b were similar. However, one notable difference in SP3 and SP4 existed between these two time instances. The magnitude of the biased flow over the flight deck surface was higher on both downstream planes in Fig. 3.34b. At this time instance, sate 1 was the predominant flow state for $4\Delta\bar{t}$. Thus, its persistence in time was likely responsible for the increase in biased flow velocity on these two downstream planes.

Figure 3.34c shows the conditionally averaged flow at $t_0 + 7\Delta\bar{t}$. In this case, the structure of the characteristic vortex in SP2 appeared to start to weaken. Additionally, the velocity contours behind the hangar door were lower in intensity when compared to Fig. 3.34b. Moving downstream, both SP3 and SP4 showed lower intensity levels over the flight deck when compared to the instance $t_0 + 4\Delta\bar{t}$. Finally, the conditionally averaged flow captured at $t_0 + 10\Delta\bar{t}$ is shown in Fig. 3.34d. In SP2, the characteristic vortex behind the hangar door weakened to the point where it no longer resembled a vortex. Additionally, the funnel vortex structures above the hangar door were of similar sizes within both SP1 and SP2. Downstream, the streamlines still showed biased flow in SP3. However, the streamwise velocities significantly reduced in magnitude. Spanwise plane 4 showed a mostly symmetric flow pattern, meaning that the spanwise velocities seen in SP3 did not propagate downstream.

In summary, the flow characteristics of state 1 were observed from the instant of transition t_0 to $t_0 + 10\Delta\bar{t}$, when the characteristic vortex started to deform. It can be observed that the characteristic vortex was present for ten time instances ($10\Delta t$). Note, this is an average behavior. Nevertheless, the downstream effects of state 1 were noticeable at the early transitional stages and prevailed even after the flow started transitioning out of this

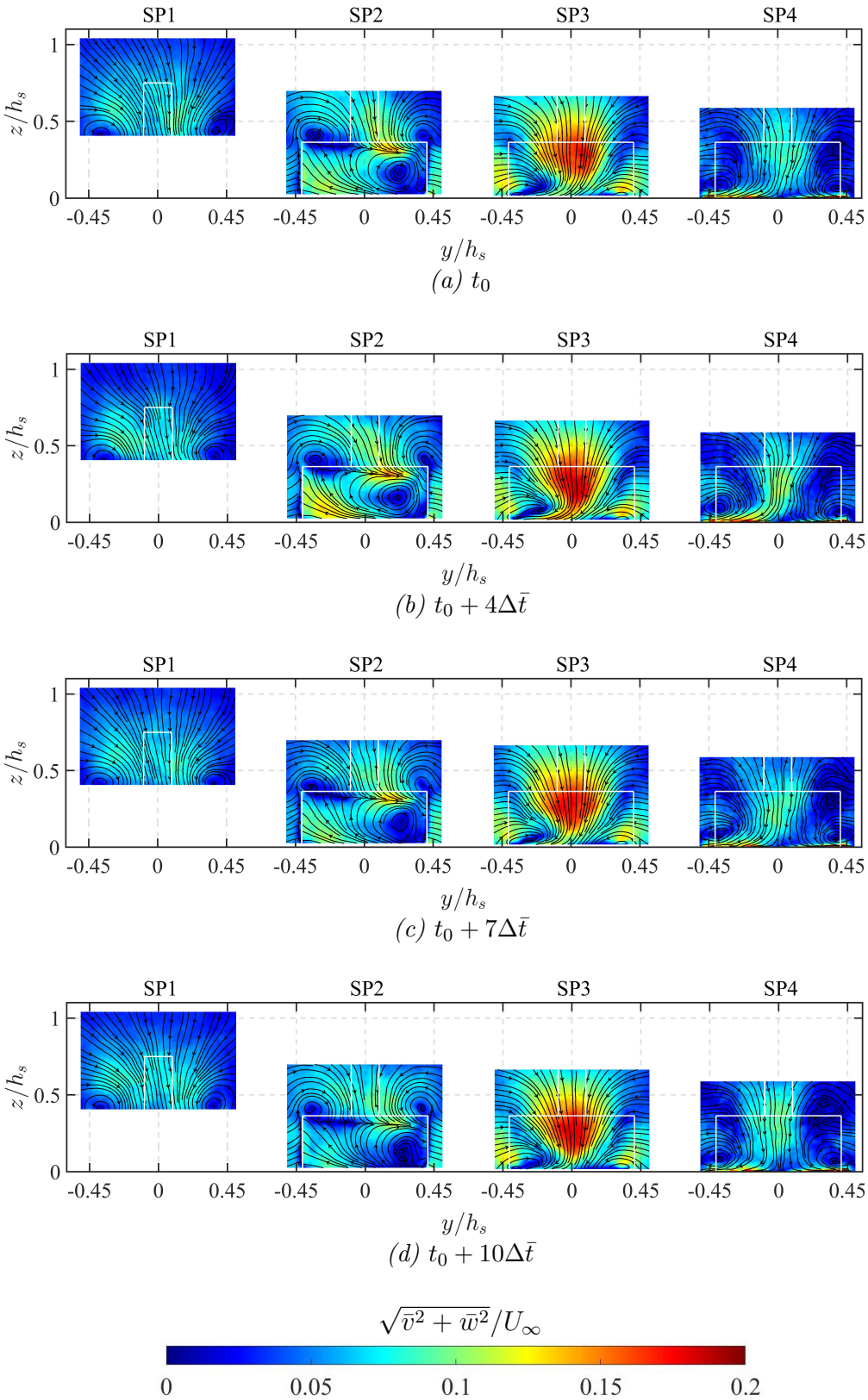

Figure 3.34 Temporal average obtained using the instant of transition to state 1 in (a) and using the instants after the transition in (b), (c), and (d).

state. Considering the instances in which the characteristic vortex was present, it was seen that the intensity of the flow contours increased in some regions as state 1 persisted through time. At $t_0 + 7\Delta\bar{t}$, the intensity of the contour levels were reduced and the characteristic vortex started weakening. This indicated the beginning of the transition out of state 1.

The same analysis was carried out to identify the transition into and out of state 2. In this case, state 2 is characterized by a positive sign of $\tilde{v}(t)$. Therefore, a transition was considered at a time instance t_0 when the following criteria were met: (i) $\tilde{v} > 0$ at t_0, (ii) $\tilde{v} < 0$ at the preceding time instance $t_0 - \Delta\bar{t}$ and (iii) $\tilde{v}(t) > 0$ for a minimum of five consecutive time instances following t_0 ($t_0 + \Delta\bar{t}$ to $t_0 + 5\Delta\bar{t}$). Using this criteria, 274 transitions to state 2 were identified. Figure 3.35 shows an example of a transition instance t_0 that met these requirements and was therefore considered for the current study.

The ten instances before and after the transition were considered to compute the conditionally averaged flow fields at each time step using the previously described process. The resulting mean evolution in time is shown in Fig. 3.36. A very similar temporal pattern to

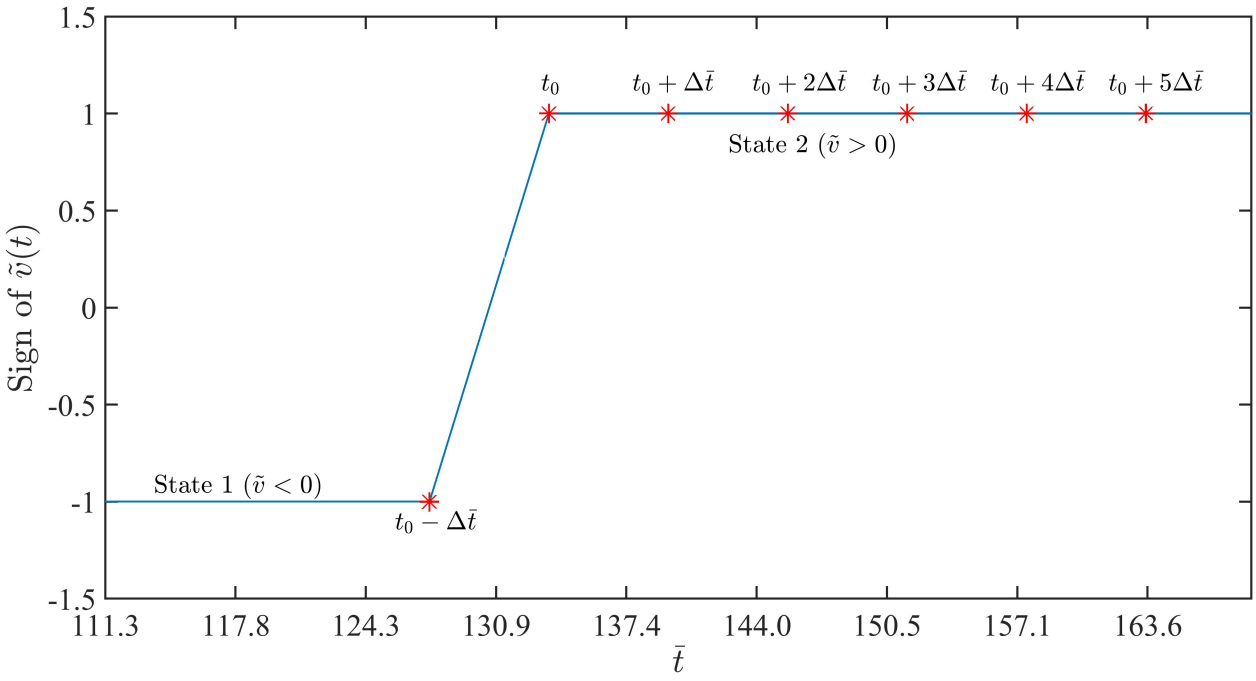

Figure 3.35 Example of time instance that met the temporal flow criteria and was considered a transition to state 2.

the transition into state 1 but with opposite orientation was observed. The mean flow from instances $t_0 - 10\Delta\bar{t}$ to $t_0 - 4\Delta\bar{t}$ did not show major changes in the flow structure. However, some changes were observed at $t_0 - 4\Delta\bar{t}$, which is shown in Fig. 3.36a. The structures of the funnel vortices within SP1 and SP2 were symmetric with respect to the ship centerline. However, the streamlines behind the hangar door showed biased flow within the recirculation bubble. Similarly, the streamlines in SP3 showed that the spanwise flow had the tendency to turn towards starboard side as it approached the flight deck surface. However, this effect did not prevail downstream because SP4 showed streamlines that indicated symmetric flow with respect to the ship centerline at the stern.

Moving to $t_0 - 2\Delta\bar{t}$ in Fig. 3.36b, the funnel vortices within SP1 showed asymmetry with respect to the ship centerline since the vortex on the port side was considerably smaller than the one on starboard side. This difference in size was also seen in SP2, where the starboard vortex covered a significant spatial domain above the hangar door. Additionally, the streamlines behind the hangar door depicted the beginning of the formation of the characteristic vortex of state 2 caused by a higher spanwise velocity from port to starboard as the flow moved up into the recirculation region. Within SP3, the spanwise velocity increased in magnitude closer to the deck. SP4 still showed unbiased streamlines, meaning the spanwise velocity seen in SP3 closer to the deck rapidly reduced in speed before reaching the stern of the ship. In Fig. 3.36c, the most significant change from the previous time step was seen behind the hangar door, where the streamlines showed a more defined vortical structure. However, this structure did not resemble the fully developed vortex that characterized state 2. Additionally, an increase in spanwise velocity was seen behind the top edge of the hangar door.

Considering the conditional fields at the transitional instances t_0 in Fig. 3.36d, a larger starboard vortex was observed within SP1. As for SP2, the port vortex appeared to be suppressed by the larger vortex to the point where it did not resemble a vortex. The characteristic vortex of state 2 was fully formed behind the hangar door. However, the downstream

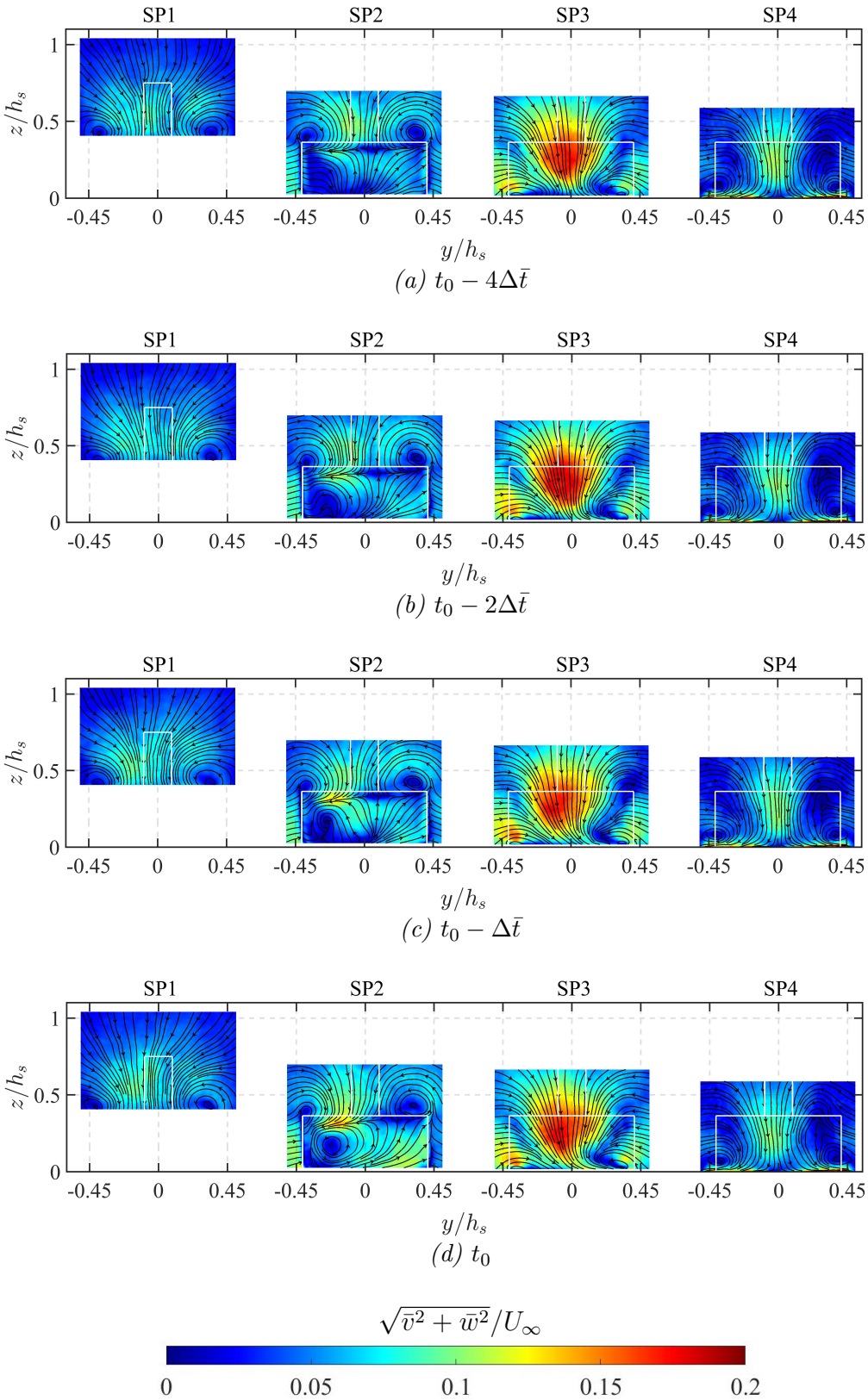

Figure 3.36 Temporal average obtained using the instances preceding the transition to state 2 in (a), (b), and (c) as well as at the instant of transition in (d).

effects on SP3 and SP4 remained unchanged. Unlike the transition to state 1, the flow at the stern of the ship remained unbiased during the transition to the second state.

Figure 3.37 shows the conditionally averaged flow captured after the transition to state 2. The flow structures remained fairly unchanged between t_0 and $t_0 + 7\Delta\bar{t}$. In order to highlight the flow in between these two instances, the conditional flow field at $t_0 - 4\Delta\bar{t}$ is shown in Fig. 3.37b. The only differences between instance t_0 and $t_0 + 4\Delta\bar{t}$ were in contour levels behind the hangar door and closer to the deck surface in SP4. The latter appeared to be strong enough to prevail downstream of SP4, which resulted in slightly higher spanwise velocities closer to the deck surface at the stern of the ship.

The beginning of the transition out of state 2 is shown in Fig. 3.37c, where the characteristic vortex in SP2 started to deform and the contour levels behind the top edge of the hangar door were lower in magnitude compared to those at $t_0 + 4\Delta\bar{t}$. Additionally, the funnel vortices above the hangar door were symmetric with respect to the ship centerline. The contours in SP3 showed lower velocity magnitudes closer the deck surface, indicating that the high spanwise velocities over the deck weakened in time. However, the downstream flow in SP4 remained unchanged. Finally, the conditional flow field at the instance $t_0 + 10\Delta\bar{t}$ in Fig. 3.37d no longer featured the characteristic vortex. However, the streamlines in SP2 still showed biased flow towards the port side. Moreover, symmetric funnel vortices were observed in both SP1 and SP2. Downstream, the streamlines in SP3 and SP4 showed symmetric flow with respect to the centerline over the deck.

In summary, the transition into and out of state 2 showed a similar pattern as state 1 with flipped orientation. Considering the transition of each state, significant changes in the flow that indicated the transition were observed only after $t_0 - 4\Delta\bar{t}$. Additionally, each state remained unchanged (on average) until the instance $t_0 + 7\Delta\bar{t}$. The transition out of each state was partially captured in the instances $t_0 + 7\Delta\bar{t}$ to $t_0 + 10\Delta\bar{t}$. However, the flow structure at instance $t_0 + 10\Delta\bar{t}$ still showed some biased flow for both states.

The temporal evolution of each transition showed significant changes in the following

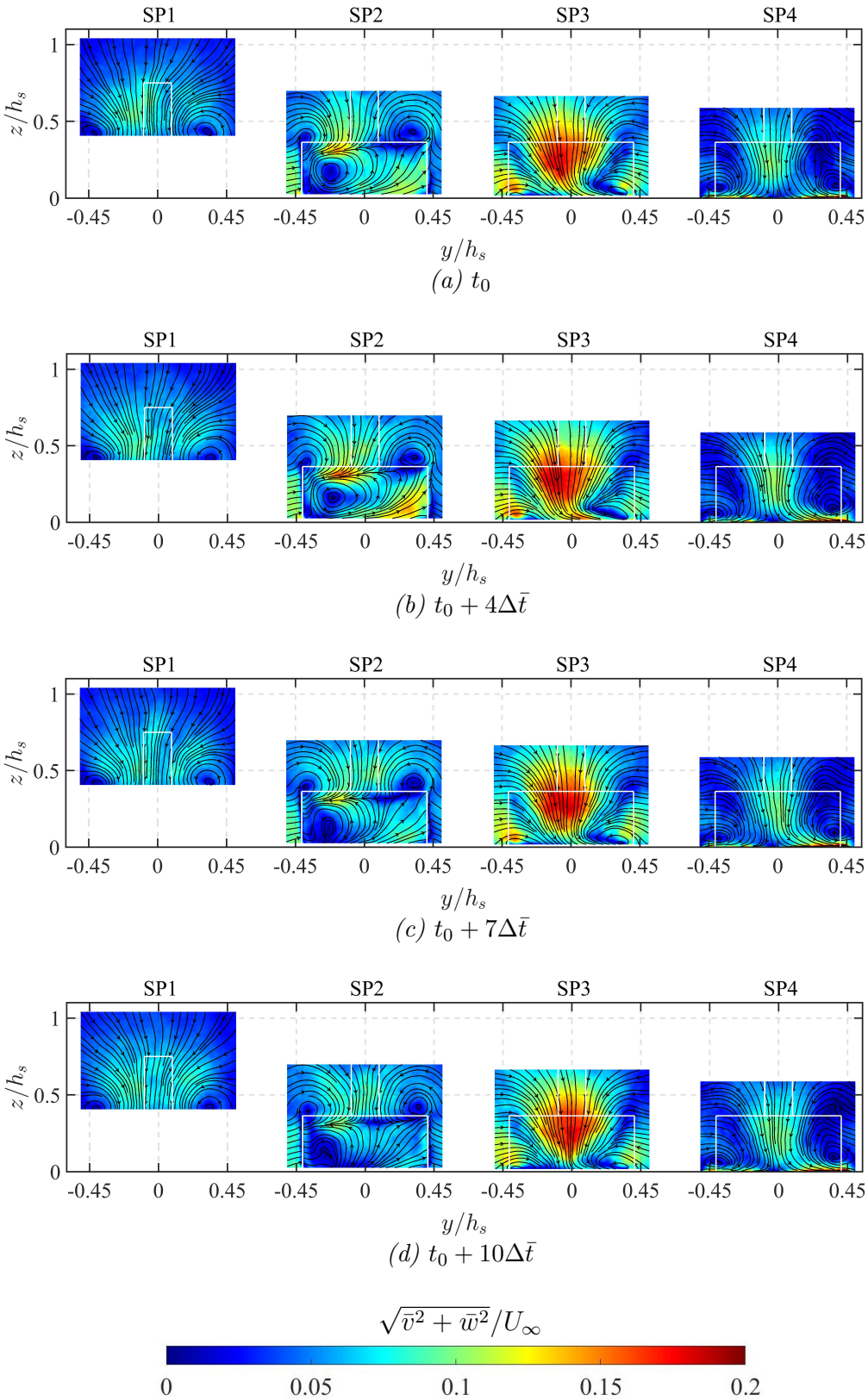

Figure 3.37 Temporal average obtained using the instant of transition to state 2 in (a) and using the instants after the transition in (b), (c), and (d).

coherent structures: (i) The funnel vortices, (ii) flow within the recirculation region behind the hangar door and (iii) spanwise velocities closer to the deck surface within SP3 and SP4. This adds to and strengthens the growing body of evidence that the entire flow field of the ship airwake is a coupled or interacting flow field. Finally, both upstream and downstream flow effects were noticeable several time instances before the characteristic vortex was formed behind the hangar door and they further strengthened after its formation. It can be then concluded that these premature changes in flow configuration could potentially induce unsteady airloads on operating rotorcraft even before the flow is fully stabilized as one state or the other.

4 Conclusions

Flow velocity fields within the airwake of a model Simple Frigate Shape No. 2 (SFS2) were measured using a novel, dual-plane, stereoscopic particle image velocimetry (DP-sPIV) approach. Two flow planes over the flight deck, parallel and perpendicular to the free-stream were simultaneously measured. The study was carried out at the ERAU low-speed wind tunnel facility. Such an approach allowed for spatially and temporally correlated measurements to capture the unsteady three-dimensional features of the airwake. These measurements were then used to carry out a conditional average of the flow statistics to isolate certain flow events within the airwake that are potentially relevant for rotorcraft operations. The flow events under investigation included extreme vertical flow events in the shear layer as well as the two bistable states of the wake behind the hangar door.

The conditional flow fields identified the three-dimensional structures that formed during the events under study. Additionally, the temporal analyses highlighted the evolution of these flow structures in time. Overall, this work provided a better understanding of the interaction between flow structures within the airwake during the events of interest. These flow interactions have the potential to induce unsteady airloads on rotor systems operating near the flight deck.

4.1 Summary of Conclusions

There were two primary thesis objectives outlined in Section 1.3. The key observations and primary conclusions of the present work are addressed in the same order below:

1. It was clear from the literature that one of the liming factors in experimental airwake studies was the lack of synchronous measurements of different measurement planes. The current research utilized a novel measurement approach called time-dependent, dual-plane, stereoscopic PIV (DP-sPIV). This approach allowed for high-resolution spatially and temporally synchronous measurements. Additionally, stereoscopic PIV allowed for the measurement of all three velocity components of the flow

within each plane. Two flow planes over the flight deck, one parallel and one perpendicular to the streamwise direction were simultaneously measured. Each experimental configuration measured one invariant streamwise plane along the ship centerline and one of the four spanwise planes, whose locations were strategically selected to capture important structures that were identified in previous airwake studies. The literature review also emphasized the need of properly simulating the atmospheric boundary layer in ship airwake studies. Thus, a simulated atmospheric boundary Layer (sABL) was used. Conditions with and without the sABL were measured and compared to study its effects on the spatiotemporal behavior of the airwake.

The DP-sPIV approach, which was described in Section 2.4, comprised two independent PIV systems, which resulted in the use of two high-speed lasers and a total of four high-speed cameras. A time delay was introduced in between PIV systems to avoid optical interference between measurement planes. This delay was independent of sampling frequency, which ensured that all spanwise and streamwise measurement planes were temporally correlated in a similar manner regardless of sampling frequency.

Staggering two independent PIV systems in time added another layer of complexity to the experimental trials. Therefore, new error mitigation strategies were developed to ensure that the measurements were optimal for spatiotemporal studies. These strategies included the use of oscilloscopes prior to performing the experiments to ensure the timing in between systems was correct. Additionally, the brightness and exposure of each image set was measured to confirm they were adequate for processing. This ensured that issues such as laser missfiring and system response lag during the experiments were discarded. Finally, the third party software used to process the images, DaVis, also estimated the measurement uncertainty using the method of Wieneke [47]. The normalized uncertainty within all measurement planes were less than 3% for all spanwise planes and 8% for the streamwise plane.

Before obtaining conditional averages, the mean flow contours were studied to corroborate that the resulting flow fields accurately captured the previously established features of the ship airwake. The time-averaged contours also corroborated that the flow over the flight deck was symmetric with respect to the ship's centerline, thus proving that the model ship was not yawed during the experiments. In addition, the resulting flow fields in the streamwise and spanwise planes showed agreement when superposed in a three-dimensional sense, confirming the consistency in results from the intersecting measurement planes.

Overall, this experimental approach was used to obtain measurements that were suitable to carry out both a temporal and spatial analysis of the airwake. The synchronous measurements allowed the correlation of all spanwise planes through the invariant streamwise plane, which were used to successfully capture the unsteady three-dimensional features of the airwake over the entire flight deck.

2. The synchronous measurements were used to calculate conditionally averaged flow statistics isolating events of interests. First, the turbulence intensity and kinetic energy contours were studied to identify the locations at which aircraft may experience significant time-varying airloads. The flow statistics at these locations were then used to obtain probability density functions (PDF), which helped determine the appropriate flow velocity criteria necessary to isolate each flow event. Finally, the flow field snapshots that met each criteria were used to obtain conditionally averaged structures. Three important flow events in the airwake were isolated and studied: (i) extreme vertical (normal to the flight deck) large fluctuations in the shear layer, (ii) the two bistable flow configurations of the wake behind the hangar door and (iii) the temporal transition between the bistable states of the hangar door wake.

   (a) The study analyzed cases of large positive and negative fluctuations in the shear layer above the flight deck. The conditional fields showed large-sale features

arising from the oscillatory motion of the shear layer, especially when considering the streamwise and wall-normal velocity components. The conditionally averaged flow structures occupied most of the deck length and width and also appeared to extend beyond the current fields of view.

(b) The conditional fields in the case of both positive and negative fluctuations showed consistent and persistent spatial asymmetries across the flight deck centerline within the two spanwise measurement planes closest to the stern. On the other hand, the spanwise plane behind the hangar door showed symmetric structures with respect to the ship centerline. This outcome indicated that the flow was symmetric within the upstream portion of the flight deck, where the shear layer formed. However, flow asymmetries developed as the flow evolved downstream.

The fields conditioned on large positive vertical fluctuations were opposite in sign (or the mirror) of those with large negative vertical fluctuations. This can be interpreted as a temporal symmetry. This temporal behavior combined with the persistent spatial asymmetries across the flight deck centerline would likely result in a challenging environment for operating rotorcraft.

Both cases with and without the sABL showed almost identical flow structures arising from both positive and negative oscillations in the shear layer. Additionally, the added upstream turbulence by the sABL did not have any significant effect on the intensity of the fluctuations observed in the conditional fields. Hence, it was concluded that the sABL did not have a major impact on the foot-print of the large-scale structures that were identified.

(c) Each of the bistable flow states of the hangar door wake were isolated and studied using a conditional averaging approach. The conditional fields showed that each bistable state featured a characteristic vortex behind the hangar door on one side of the ship well within the recirculation region and a smaller vortex on top

of the hangar door on the opposite side with respect to the ship centerline. These results agreed with previous computational and experimental studies [6, 8, 30, 51].

State 1 featured a characteristic vortex on the starboard side rotating clockwise while state 2 featured the same on the port side rotating counterclockwise. Upstream, the funnel vortices showed slight differences in symmetry across the deck centerline. For instance, a larger funnel vortex was seen on the port side in conditional fields corresponding to state 1 while the opposite trend was seen in the case of state 2. Similarly, the flow configuration downstream of the flow reattachment point featured high spanwise velocities close to the deck surface. In the case of state 1, the spanwise velocity was negative (toward the port side) and it was positive (toward the starboard side) in the case of state 2. The same flow pattern was seen at the stern of the deck but with weakened intensity. This effect will likely induce axial loads on the rotor and body of any rotorcraft operating close to the deck surface. Finally, the conditional fields obtained across all spanwise planes provided strong evidence of coupled flow interactions within the airwake since the footprint of each state was seen upstream and downstream of the hangar door wake.

Both cases with and without the sABL presented nearly identical flow configurations in each state. However, the spanwise velocities close to the deck surface were significantly higher in the cases without the sABL. This appeared to be the result of the higher upstream flow velocities interacting with the ship. Therefore, it was concluded that the downstream effects of each bistable state were more predominant without the sABL. Additionally, in the cases without sABL, a bias towards state 2 was observed since the resulting PDF showed that the probability of capturing state 2 was significantly higher than the probability of capturing state 1. Based on previous airwake studies [8, 14], this behavior is characteristic of the hangar door wake when the ship is slightly (in this case unintentionally)

yawed with respect to the free-stream.

(d) A temporal analysis was carried out to asses, on average, the transition from one stable state to the other. The time instances in which one state switched to the other were identified using a temporal conditional criteria. This allowed the study of the evolution of the flow structures (on average) as the flow evolved into each state. The spanwise planes both upstream and downstream of the hangar door revealed that the effects of each bistable state were noticeable several time instances before the characteristic vortex formed behind the hangar door. These effects were augmented once the characteristic vortex in the recirculation region was formed. The transition out of each state was also captured. In this case, the velocity contours in the recirculating region weakened and the characteristic vortex deformed. Even though the downstream effects of each state weakened, some of these effects remained noticeable even after the characteristic vortex in the recirculation bubble deformed.

The same flow configurations were observed in cases with and without the sABL. However, the flow field without the sABL was biased towards state 2, which appeared to remain for extended periods of time when compared to state 1. On the other hand, the flow fields with the sABL resulted in equal periods of time in which either flow configuration remained stable.

Based on this study, the resulting aerodynamic effects induced by each state on a rotorcraft would be noticeable even before the formation of the characteristic vortex. Additionally, the extremely quick transitions from one state to the other completely reverses the direction of the spanwise velocities closer to the flight deck. This will likely induce sudden changes in aerodynamic forces exerted on a rotor system. Overall, this analysis helped understand the average configuration of the flow during the transition to each state as well as its potential impact on operating rotorcraft.

Finally, the presented results highlighted the role that conditional statistics can play in analyzing complex flow fields such as the ship airwakes. Particularly the average footprint of specific events in the airwake were able to be isolated and characterized.

4.2 Recommendations for Future Work

The novel measurement approach presented in this thesis provided suitable data for three-dimensional spatiotemporal analyses of the ship airwake. The results obtained using conditional averaging helped providing new physical insight into the highly complex, unsteady, and turbulent airwake phenomenon. Nevertheless, some limitations in the experimental approach and data analysis techniques were observed. Additionally, the current effort focused on specific flow events within a highly complex flow field. Future work is needed to study other unexplored topics related to the dynamic interface (DI). Based on the results of the current work, the suggestions for future work are the following:

1. One of the major challenges in using PIV to measure the airwake is that each PIV system captures the flow field within a single plane. Due to the highly complex nature of the ship airwake, additional planes of interest can be considered in strategic locations over the flight deck. For example, using multiple spanwise planes in the recirculation region might offer a more detailed insight into the bistable flow states of the hangar door wake.

2. One of the main limitations in the use of conditional averages was that the region to condition the flow must be in the streamwise plane since it was used as the anchor plane to correlate all spanwise planes. In order to study events that are not necessarily captured by the streamwise plane but rather take place on one specific side of the ship, a horizontal measurement plane (parallel to the deck surface) may be used as the anchor plane to correlate the spanwise planes. A horizontal measurement plane may also reveal flow features that are not captured by the vertical planes.

3. Only the headwind case was considered in the current study. It is unlikely that full-scale

ships operate in a perfect headwind. So, different ship yaw angles should be considered. Existing studies of ship airwakes with quartering winds by Palm [13] suggested that a change in yaw angle had an effect on the overall flow field. Therefore, the dual-plane technique may be applied to different yaw angles to study these changes.

4. The influence of the sABL on the events of interests were challenging to interpret. Future research may seek to isolate flow events that are more likely to be affected by added upstream turbulence such as the funnel wake and the temporal behavior of the reattachment region.

5. Since the long-term goal of measuring the ship airwakes is to obtain a deeper understanding of the airwake/rotor interaction, future dual-plane PIV measurements should include a rotor in the proximity of the flight deck, allowing a three-dimensional analysis of the rotor wake interacting with the airwake. The obtained measurements can be used to study these interactions both spatially and temporally.

6. Even though the SFS2 model retains the quintessential features of Navy frigate ships, other frigate models should be considered to study the ship airwake. Conditional averages can be used to compare the flow events on different model ships to study the effects of the ship shapes on flow events that are likely relevant to rotor systems.

7. Current airwake studies by Zhu et al. [2] include the use of proper orthogonal decomposition (POD) to estimate the spanwise plane flow fields using the invariant streamwise plane. Conditional averages can be used in both estimated and measured fields as a tool to determine the accuracy of the flow estimations during specific flow events.

REFERENCES

[1] Wang, Y., Curran, J., Padfield, G. D., and Owen, I., "AirDyn: An Instrumented Model-Scale Helicopter for Measuring Unsteady Aerodynamic Loading in Airwakes," *Measurement Science and Technology*, Vol. 22, No. 4, 2011, p. 045901. https://doi.org/10.1088/0957-0233/22/4/045901.

[2] Zhu, N., Leishman, J. G., Gnanamanickam, E. P., and Zhang, Z., "Dynamics of Large-Scale Flow Structures in Ship Airwakes," *AIAA SciTech 2022 Forum*, San Diego, CA, 2022, pp. 1 – 23. https://doi.org/10.2514/6.2022-2532.

[3] Forrest, J. S., Owen, I., Padfield, G. D., and Hodge, S. J., "Ship-Helicopter Operating Limits Prediction Using Piloted Flight Simulation and Time-Accurate Airwakes," *Journal of aircraft*, Vol. 49, No. 4, 2012, pp. 1020–1031. https://doi.org/10.2514/1.C031525.

[4] Forrest, J. S., and Owen, I., "An Investigation of Ship Airwakes Using Detached-Eddy Simulation," *Computers & Fluids*, Vol. 39, No. 4, 2010, pp. 656–673. https://doi.org/10.1016/j.compfluid.2009.11.002.

[5] Snyder, M., and Kang, H. S., "Comparison of Experimental and Computational Ship Air Wakes for YP Class Patrol Craft," *AIAA Centennial of Naval Aviation Forum*, Virginia Beach, VA, 2011, pp. 1–18. https://doi.org/10.2514/6.2011-7045.

[6] Rao, A. N., Zhang, J., Minelli, G., Basara, B., and Krajnović, S., "Qualitative Assessment of the Bi-Stable States in the Wake of a Finite-Width Double Backward Facing Step," *Journal of Wind Engineering and Industrial Aerodynamics*, Vol. 186, 2019, pp. 241–249. https://doi.org/10.1016/j.jweia.2019.01.007.

[7] Mora, R. B., "Experimental Investigation of the Flow on a Simple Frigate Shape (SFS)," *The Scientific World*, Vol. 2014, 2014, pp. 818132–8. https://doi.org/10.1155/2014/818132.

[8] Herry, B. B., Keirsbulck, L., Labraga, L., and Paquet, J. B., "Flow Bistability Downstream of Three-Dimensional Double Backward Facing Steps at Zero-Degree Sideslip," *Journal of fluids engineering*, Vol. 133, No. 5, 2011. https://doi.org/10.1115/1.4004037.

[9] Dooley, G. M., Krebill, A. F., Martin, J. E., Buchholz, J. H., and Carrica, P. M., "Structure of a Ship Airwake at Multiple Scales," *AIAA journal*, Vol. 58, No. 5, 2020, pp. 2005–2013. https://doi.org/10.2514/1.J058994.

[10] Tinney, C. E., and Ukeiley, L. S., "A study of a 3-D double backward-facing step," *Experiments in Fluids*, Vol. 47, No. 3, 2009, pp. 427–438. https://doi.org/10.1007/s00348-009-0675-9.

[11] Nacakli, Y., "Analysis of Helicopter Downwash/Frigate Airwake Interaction Using Statistically Designed Experiments," Ph.D. thesis, Middle East Technical University, 2010.

[12] Gallas, Q., Lamoureux, M., Monnier, J. C., Gilliot, A., Verbeke, C., and Delva, J., "Experimental Flow Control on a Simplified Ship Helideck," *AIAA Journal*, Vol. 55, No. 10, 2017, pp. 3356–3370. https://doi.org/10.2514/1.J055902.

[13] Palm, K. H., "Time-Resolved PIV Measurements of Ship Airwakes with Quartering Winds," Master's thesis, Embry-Riddle Aeronautical University, 2022.

[14] Seth, D., "Contributions to the Understanding of Ship Airwakes Using Advanced Flow Diagnostic Techniques," Ph.D. thesis, Embry-Riddle Aeronautical University, 2020.

[15] Zhu, N., "Analysis of Ship Airwakes Using Model Decomposition," Master's thesis, Embry-Riddle Aeronautical University, 2021.

[16] LaVision, "2D & Stereo PIV," https://www.smart-piv.com/en/applications/fluid-mechanics/2d-stereo-piv/index.php, 2022. Accessed: 2022-07-23.

[17] LaVision, "Product Manual for DaVis 10.1," Computer software manual, 2020.

[18] Gnanamanickam, E. P., Zhang, Z., Seth, D., and Leishman, J. G., "Structure of the Ship Airwake in a Simulated Atmospheric Boundary Layer," *AIAA Aviation 2020 Forum*, 2020, pp. 1 – 16. https://doi.org/10.2514/6.2020-2702.

[19] Hodge, S. J., Zan, S. J., Roper, D. M., Padfield, G. D., and Owen, I., "Time-Accurate Ship Airwake and Unsteady Aerodynamic Loads Modeling for Maritime Helicopter Simulation," *Journal of the American Helicopter Society*, Vol. 54, No. 2, 2009, pp. 1 – 3. https://doi.org/10.4050/JAHS.54.022005.

[20] Memon, W. A., Owen, I., and White, M. D., "Motion Fidelity Requirements for Helicopter-Ship Operations in Maritime Rotorcraft Flight Simulators," *Journal of Aircraft*, Vol. 56, No. 6, 2019, pp. 2189–2209. https://doi.org/10.2514/1.C035521.

[21] Zan, S. J., "On Aerodynamic Modelling and Simulation of the Dynamic Interface," *Journal of Aerospace Engineering*, Vol. 219, No. 5, 2005, pp. 393–410. https://doi.org/10.1243/095441005X30315.

[22] Polsky, S., "A Computational Study of Unsteady Ship Airwake," *40th AIAA Aerospace Sciences Meeting & Exhibit*, Reno, NV, 2002, pp. 1–11. https://doi.org/10.2514/6.2002-1022.

[23] Bogstad, M. C., Habashi, W. G., Akel, I., Ait-Ali-Yahia, D., Giannias, N., and Longo, V., "Computational-Fluid-Dynamics Based Advanced Ship-Airwake Database for Helicopter Flight Simulators," *Journal of Aircraft*, Vol. 39, No. 5, 2002, pp. 830–838. https://doi.org/10.2514/2.3003.

[24] Sezer-Uzol, N., Sharma, A., and Long, L. N., "Computational Fluid Dynamics Simulations of Ship Airwake," *Proceedings of the Institution of Mechanical Engineers. Part G, Journal of Aerospace Engineering*, Vol. 219, No. 5, 2005, pp. 369–392. https://doi.org/10.1243/095441005X30306.

[25] Shukla, S., Singh, S., Sinha, S., and Vijayakumar, R., "Comparative Assessment of URANS, SAS and DES Turbulence Modeling in the Predictions of Massively Separated Ship Airwake Characteristics," *Ocean Engineering*, Vol. 229, 2021, p. 108954. https://doi.org/https://doi.org/10.1016/j.oceaneng.2021.108954.

[26] Ideal Simulations, "Turbulence models in CFD - RANS, DES, LES and DNS," https://www.idealsimulations.com/resources/turbulence-models-in-cfd/, 2022. Accessed: 2022-09-12.

[27] Shukla, S., Sinha, S. S., and Singh, S. N., "Ship-Helo Coupled Airwake Aerodynamics: A Comprehensive Review," *Progress in Aerospace Sciences*, Vol. 106, 2019, pp. 71–107. https://doi.org/https://doi.org/10.1016/j.paerosci.2019.02.002.

[28] Grinstein, F. F., and Fureby, C., *On Monotonically Integrated Large Eddy Simulation of Turbulent Flows Based on FCT Algorithms*, Springer Berlin Heidelberg, Berlin, Heidelberg, 2005. https://doi.org/10.1007/3-540-27206-2_3.

[29] William, S., Robert, T., and Matthew, G., "The Defining Methods of Cobalt-60 - A Parallel, Implicit, Unstructured Euler/Navier-Stokes Flow Solver," *37th Aerospace Sciences Meeting and Exhibit*, Wright Patterson AFB, OH, 1999, pp. 1–3. https://doi.org/10.2514/6.1999-786.

[30] Zhang, J., Minelli, G., Basara, B., Bensow, R., and Krajnović, S., "Yaw Effect on Bi-Stable Air-Wakes of a Generic Ship Using Large Eddy Simulation," *Ocean Engineering*, Vol. 219, 2021, p. 108164. https://doi.org/10.1016/j.oceaneng.2020.108164.

[31] Syms, G. F., "Simulation of Simplified-Frigate Airwakes Using a Lattice-Boltzmann Method," *Journal of Wind Engineering and Industrial Aerodynamics*, Vol. 96, No. 6, 2008, pp. 1197–1206. https://doi.org/https://doi.org/10.1016/j.jweia.2007.06.040.

[32] Luznik, L., Brownell, C., Snyder, M. R., and Kang, H. S., "Influence of the Atmospheric

Surface Layer on a Turbulent Flow Downstream of a Ship Superstructure," *Journal of Atmospheric and Oceanic Technology*, Vol. 30, No. 8, 2013, pp. 1803–1819.

[33] White, H. E., and Chaddock, D. R., "Comparison of Full Scale and Model Data of the Wind Velocity Over the CVS 16 Flight Deck," Tech. rep., Naval Ship Research and Development Center, Aerodynamics Lab, Washington D.C., 1967.

[34] Zan, S., Syms, J., and Cheney, B., "Analysis of Patrol Frigate Air Wakes," *In Proceedings of the NATO RTO-AVT Symposium on Fluid Dynamics Problems of Vehicles Operating Near or in the Air-sea Interface*, Amsterdam, The Netherlands, 1998, p. 05.

[35] Healey, J., "Establishing a Database for Flight in the Wakes of Structures," *Journal of Aircraft*, Vol. 29, No. 4, 1992, pp. 559–564. https://doi.org/10.2514/3.46202.

[36] Wadcock, A. J., Yamauchi, G. K., Heineck, J. T., Silva, M. J., and Long, K. R., "PIV Measurements of the Wake of a Tandem-Rotor Helicopter in Proximity to a Ship," *4th Decennial Specialist's Conference on Aeromechanics*, San Francisco, CA, 2004, pp. 1–24.

[37] Seth, D., Zhang, Z., Gnanamanickam, E. P., and Leishman, J. G., "Time-Resolved PIV Measurements of a Ship Airwake in a Simulated Atmospheric Boundary Layer," *AIAA Aviation 2020 Forum*, Virtual Event, 2020, p. 2701–2734. https://doi.org/10.2514/6.2020-2701.

[38] Cowdrey, C., "A Simple Method for the Design of Wind-Tunnel Velocity-Profile Grids," Tech. rep., NPL Aero Note 1055, National Physical Laboratory, Teddington, Middlesex, England, 1967.

[39] Rosenfeld, N., Kimmel, K., and Sydney, A. J., "Investigation of Ship Topside Modeling Practices for Wind Tunnel Experiments," *53rd AIAA Aerospace Sciences Meeting*, 2015, pp. 1–22. https://doi.org/10.2514/6.2015-0245.

[40] Wilkinson, C. H., Zan, A. J., Gilbert, N. E., and Funk, J. D., "Modeling and Simulation of Ship Air Wakes for Helicopter Operations: A Collaborative Venture," *In Proceedings of the NATO RTO-AVT Symposium on Fluid Dynamics Problems of Vehicles Operating Near or in the Air-sea Interface*, Amsterdam, The Netherlands, 1998, p. 8–12.

[41] Zan, S., "Surface Flow Topology for a Simple Frigate Shape," *Canadian Aeronautics and Space Journal*, Vol. 47, 2001, p. 33–43.

[42] Seth, D., Leishman, J. G., Gnanamanickam, E. P., and Zhang, Z., "Time-Resolved PIV Measurements of a Ship Airwake in a Simulated Atmospheric Boundary Layer," *AIAA Journal of Aircraft*, 2020, pp. 624–649. https://doi.org/10.2514/1.C035886.

[43] Rius-Vidales, A., "Air-Wake Flow Dynamics on a Simplified Frigate Shape," Ph.D. thesis, 12 2016. https://doi.org/10.13140/RG.2.2.20488.03849.

[44] Zan, S., and Garry, E., "Wind Tunnel Measurements of the Airwake Behind a Model of a Generic Frigate," *National Research Council of Canada, NRC-IAR-LTR-AA-13*, 1994.

[45] Peterka, J. A., and Cermak, J. E., "Simulation of Atmospheric Flows in Short Wind Tunnel Test Sections," TR 73/74-32, Colorado State University, Fort Collins, CO, 1974.

[46] Pea Soup Smoke Machines, "Pea Soup ViCount Compact Oil Based Smoke System," https://www.pea-soup.com/rocket.shtml, 2022. Accessed: 2022-08-01.

[47] Wieneke, B., "PIV Uncertainty Quantification From Correlation Statistics," *Measurement Science and Technology*, Vol. 26, No. 7, 2015, p. 074002. https://doi.org/10.1088/0957-0233/26/7/074002.

[48] Westerweel, J., and Scarano, F., "Universal Outlier Detection for PIV Data," *Experiments in Fluids: Experimental Methods and Their Applications to Fluid Flow*, Vol. 39, No. 6, 2005. https://doi.org/https://doi.org/10.1007/s00348-005-0016-6.

[49] Feller, W., *An Introduction to Probability Theory and Its Applications*, Vol. 1, Wiley, 1968.

[50] Oric, D., Nikolic-Doric, V., E.and Jevremovic, and Malisic, J., "On Measuring Skewness and Kurtosis," *Quality & Quantity*, Vol. 43, No. 3, 2009, pp. 481–493. https://doi.org/10.1007/s11135-007-9128-9.

[51] Burton, D., Wang, S., Smith, T. D., Scott, H. N., Crouch, T. N., and Thompson, M. C., "The Influence of Background Turbulence on Ahmed-Body Wake Bistability," *Journal of Fluid Mechanics*, Vol. 926, 2021, pp. 1–15. https://doi.org/https://doi.org/10.1017/jfm.2021.706.

PUBLICATIONS

Mazzilli, G. A., Zhu, N., Gnanamanickam, E., and Leishman, J. G., "A Study of Extreme Vertical Flow Fluctuations of the Ship Airwake," *AIAA Scitech 2023 Forum*, National Harbor, MD, 2023 (Accepted)

A Measurement Uncertainties

The uncertainties of the stereoscopic PIV measurements were calculated to examine the validity of the current study. Section 2.4.2 describes how the uncertainties related to the streamwise velocity component were calculated. This appendix covers the uncertainties related to the spanwise and wall-normal velocity components.

As previously mentioned in Section 2.4.2, the measurement uncertainties were calculated by DaVis, which used a method by Wieneke [47] to compute uncertainty values at every measurement point on the plane. The time-averaged velocities and uncertainties along the ship centerline (shown in Fig. 2.13a) were plotted. The time-averaged velocities and uncertainties in the spanwise and wall-normal directions along the ship centerline are shown in Fig. A.1 and Fig. A.2, respectively. The red dots represent the time-averaged velocities and the black dots represent the uncertainties as error bars. The spanwise velocity component in Fig. A.1 showed constant uncertainties of approximately ± 0.1 m s^{-1} while the wall-normal uncertainties in Fig. A.2 were higher (approximately ± 0.2 m s^{-1}).

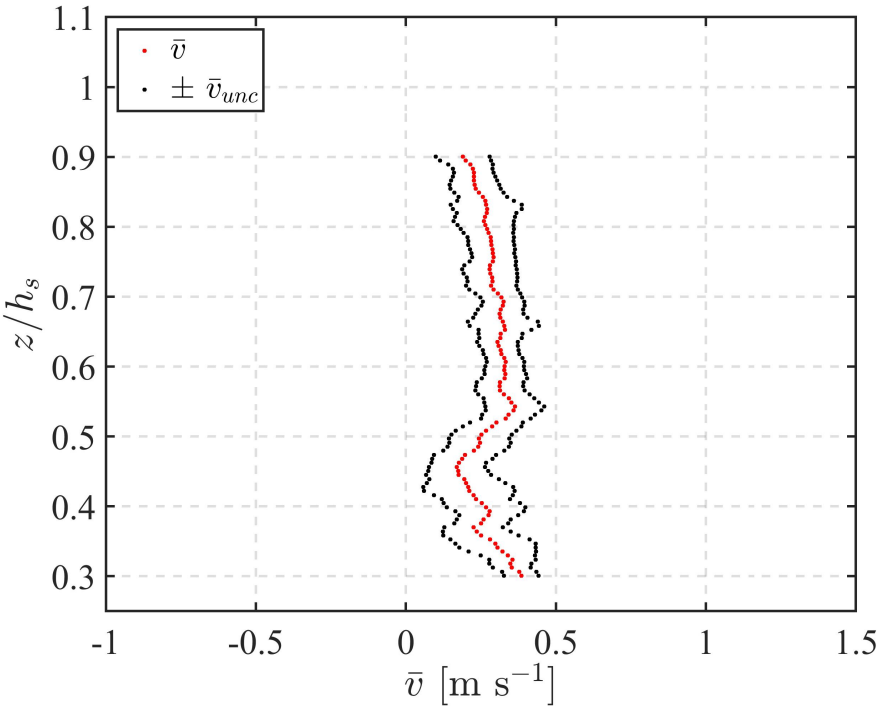

Figure A.1 Time-averaged spanwise velocities and uncertainties along the ship centerline.

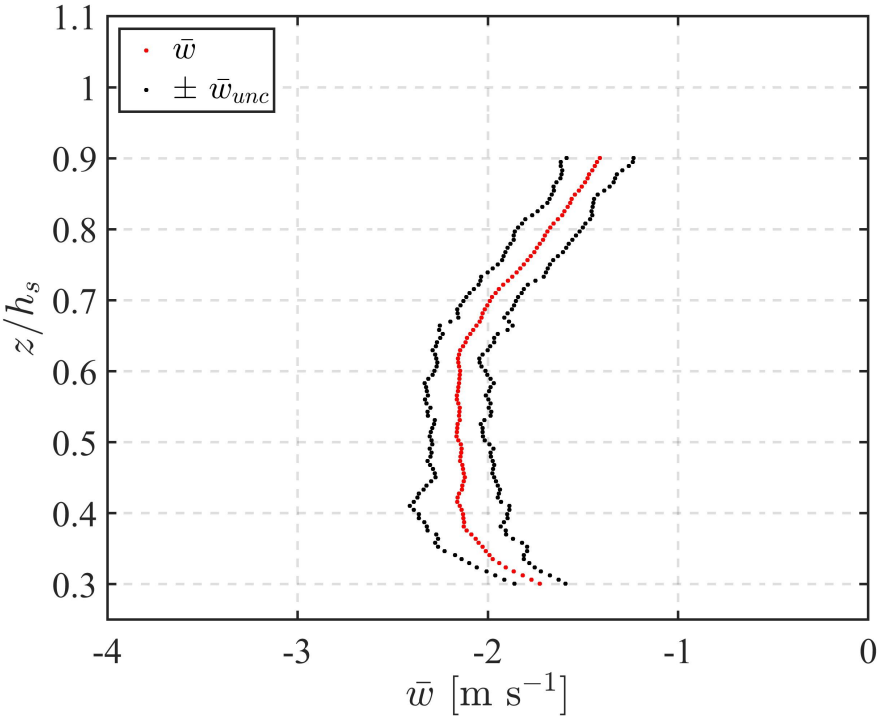

Figure A.2 Time-averaged wall-normal velocities and uncertainties along the ship centerline.

The representative uncertainties were obtained by normalizing the time-averaged uncertainty by the time-averaged velocity at each spatial location. This allowed the examination of the validity of the PIV measurements as a whole on each plane. Tables A.1 and A.2 show the representative uncertainties for cases with and without the sABL, respectively. In both tables, the spanwise plane uncertainties were all less than 8%; note that the most downstream plane (SP Plane 4) had the largest oblique angles, which led to higher uncertainties. For the streamwise plane, the large uncertainties in v were likely because it was the out-of-plane velocity component and its pixel displacement was relatively small.

Overall, the low uncertainties on all measurement planes indicate that the obtained PIV

Table A.1 Representative measurement uncertainties for trials with the sABL.

	SP1	SP2	SP3	SP4	SW
$\bar{u}_{unc}/\lvert\bar{u}\rvert$ (%)	0.48	0.74	0.98	0.99	0.90
$\bar{v}_{unc}/\lvert\bar{v}\rvert$ (%)	1.67	2.17	1.45	1.24	7.22
$\bar{w}_{unc}/\lvert\bar{w}\rvert$ (%)	7.02	1.66	1.85	1.99	1.41

results were representative of the flow within the studied Simple Frigate Shape No. 2 airwake. The uncertainties are attributed to oblique camera angles, non-uniform particle reflection, background noise, etc.

Table A.2 Representative measurement uncertainties for trials without the sABL.

	SP1	SP2	SP3	SP4	SW
$\bar{u}_{unc}/\lvert\bar{u}\rvert$ (%)	0.31	0.52	0.52	0.31	0.29
$\bar{v}_{unc}/\lvert\bar{v}\rvert$ (%)	3.08	2.12	1.79	3.08	5.40
$\bar{w}_{unc}/\lvert\bar{w}\rvert$ (%)	6.12	4.98	3.30	6.12	1.43

B Time-Averaged Results

The time-averaged streamwise velocity and turbulence intensity (TI) for cases without the sABL are shown in Section 3.1. However, time-averaged results were obtained for all three velocity components. The remaining velocity components that were not included in Chapter 3 are presented in this Appendix.

The time-averaged flow fields for both cases with and without the sABL are shown below. Fig. B.1 and Fig. B.2 show the spanwise and wall-normal velocity contours without the sABL, respectively. Similarly, the mean streamwise, spanwise, and wall-normal flow fields under the influence of the sABL are shown in Fig. B.3, B.4, and B.5, respectively. Comparing these results, it appeared that the large-scale turbulent structures remained unchanged when the sABL was added. However, some subtle differences in the mean flow features were observed. The mean spanwsie velocity $\bar{v}$ in the case with the sABL showed a more symmetric structure with respect to the ship centerline since both positive and negative $\bar{v}$ regions appeared to be symmetrically spaced with respect to the ship centerline. Moreover, the entirety of the streamwise plane showed unbiased spanwise flow (e.g, $\bar{v} = 0$). On the other hand, cases without the sABL resulted in asymmetric $\bar{v}$ regions, shown in the spanwise planes in Fig. B.1. The asymmetric $\bar{v}$ flow fields agreed with the bistability behavior observed in the cases without the sABL, in which one state was more likely to be present than the other. Finally, the streamwise plane also showed regions of biased flow (i.e., $\bar{v} \neq 0$) closer to the flight deck surface.

The spanwise TI in the cases without the sABL is shown in Fig. B.6. Additionally, the spanwise and wall-normal TI results in the cases with the sABL are shown in Fig. B.7 and B.8, respectively. Some subtle differences between cases with and without the sABL existed when comparing the TI contours. For instance, in SP1, lower v_{RMS} levels were observed in the "free-stream" region in cases without the sABL. The recirculation region also resulted in lower v_{RMS} with the sABL since a larger region of low TI was present behind the hangar door. Nevertheless, both cases showed areas of high v_{RMS} close to the deck surface.

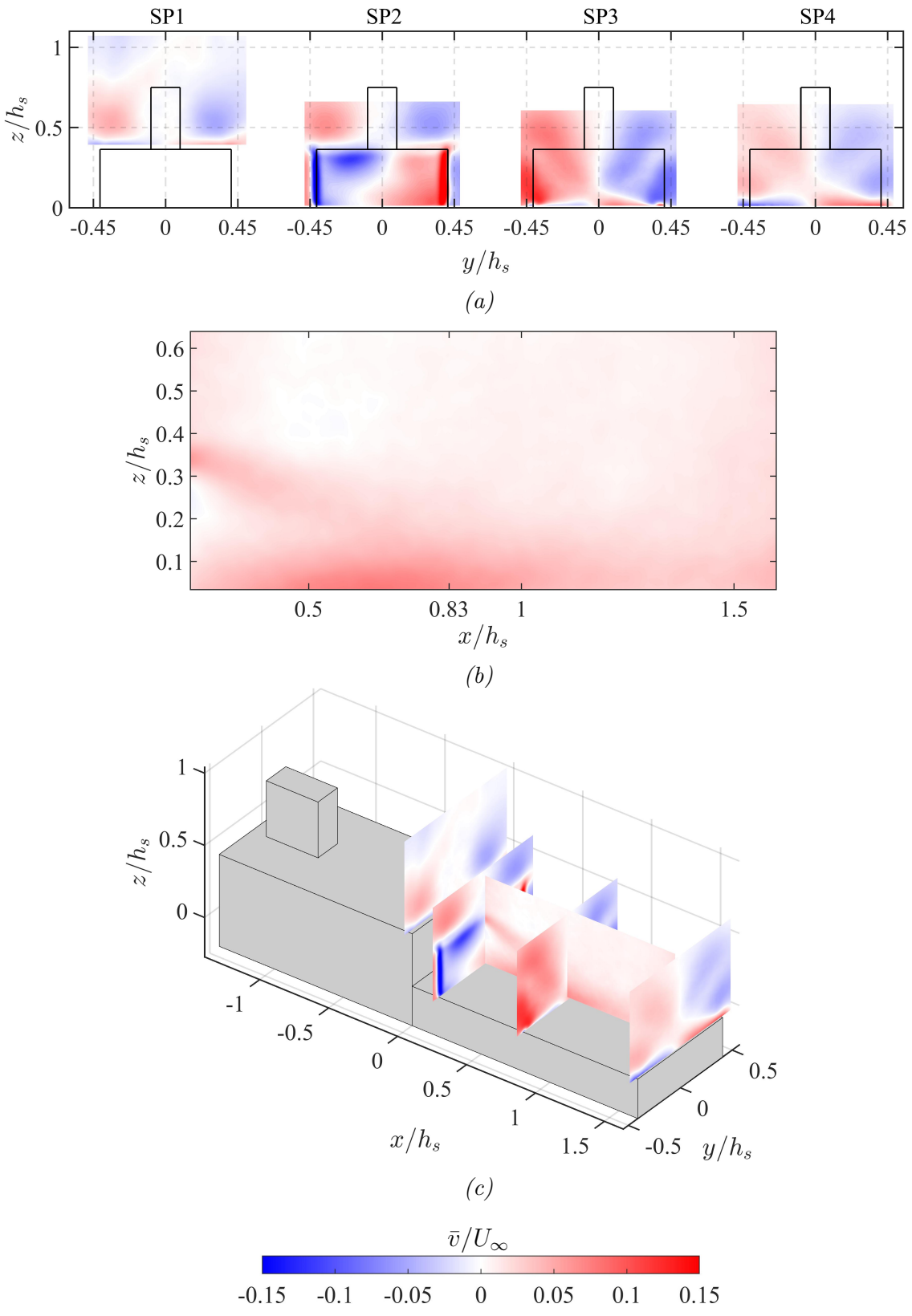

Figure B.1 Time-averaged spanwise velocity without the sABL. (a) the four spanwise planes, (b) the streamwise plane, and (c) 3D perspective.

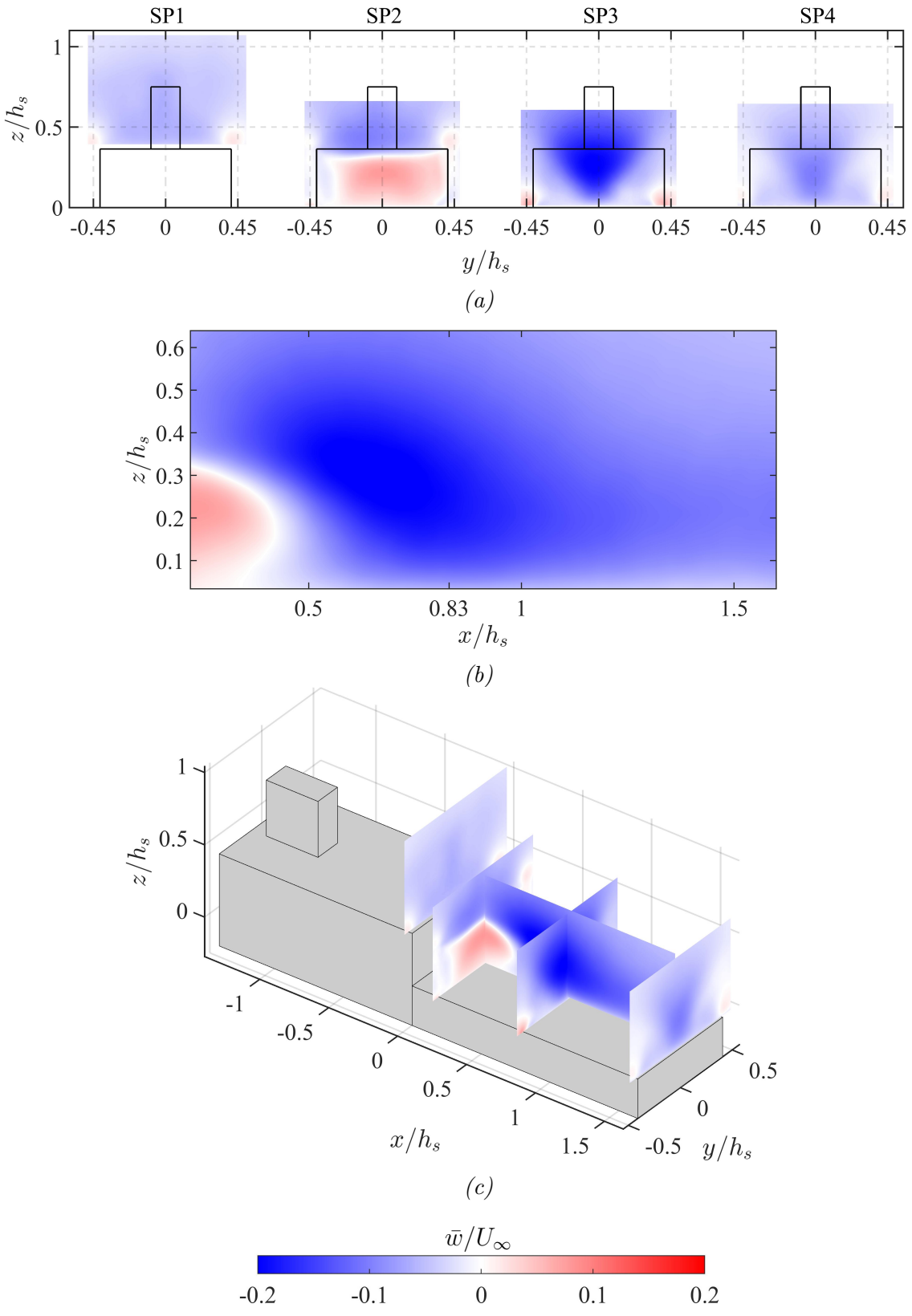

Figure B.2 Time-averaged wall-normal velocity without the sABL. (a) the four spanwise planes, (b) the streamwise plane, and (c) 3D perspective.

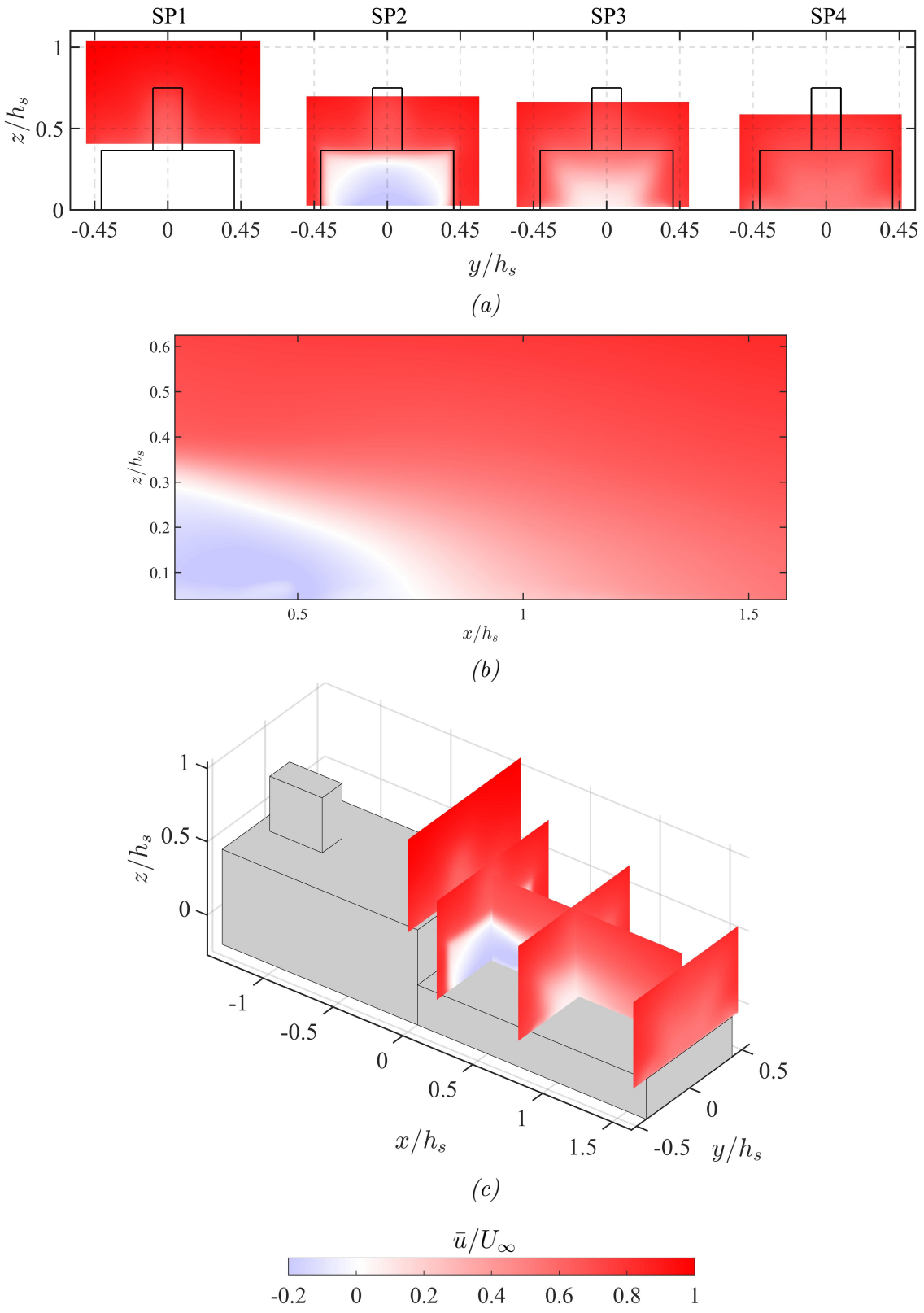

Figure B.3 Time-averaged streamwise velocity under the influence of the sABL. (a) the four spanwise planes, (b) the streamwise plane, and (c) 3D perspective.

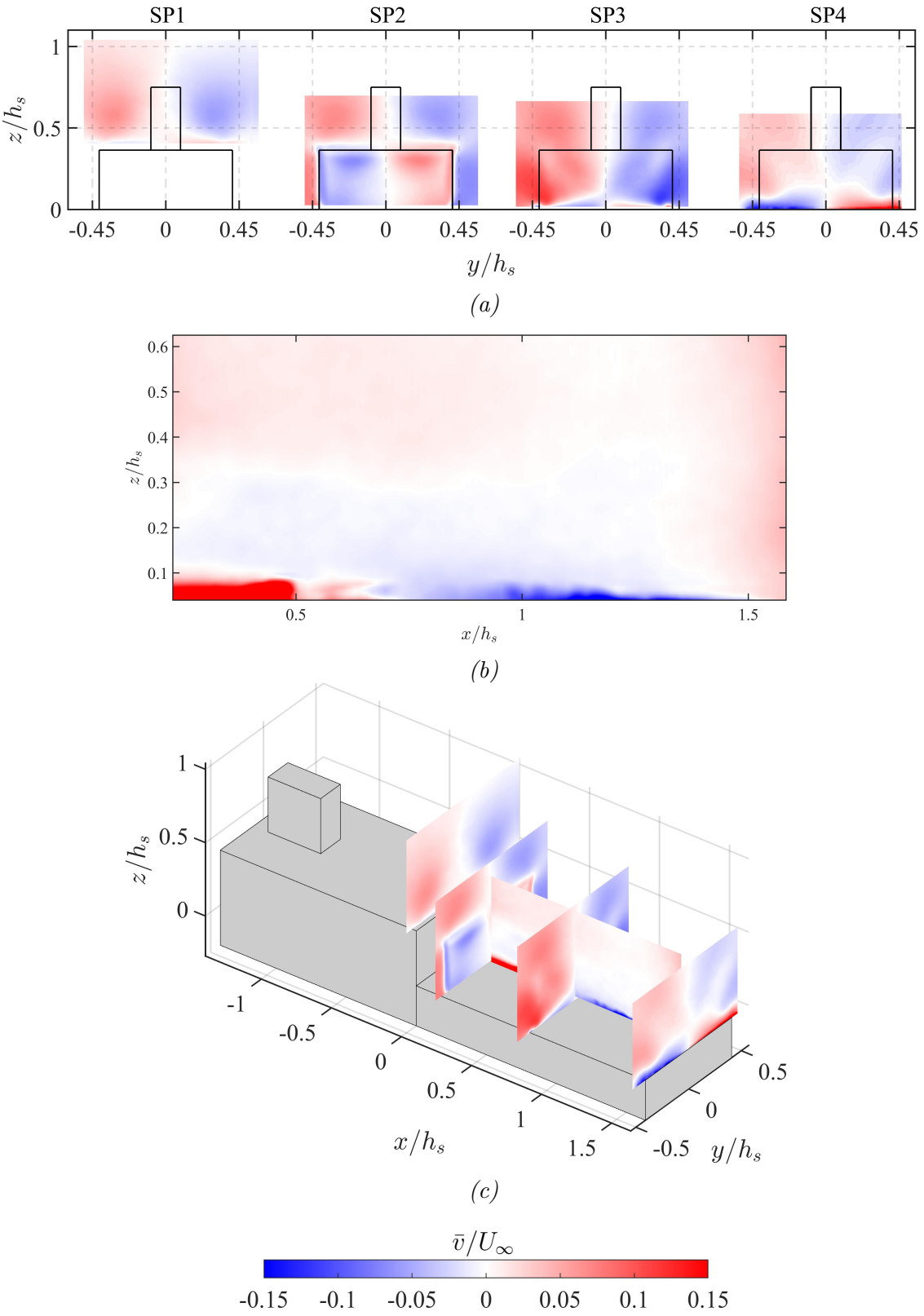

Figure B.4 Time-averaged spanwise velocity under the influence of the sABL. (a) the four spanwise planes, (b) the streamwise plane, and (c) 3D perspective.

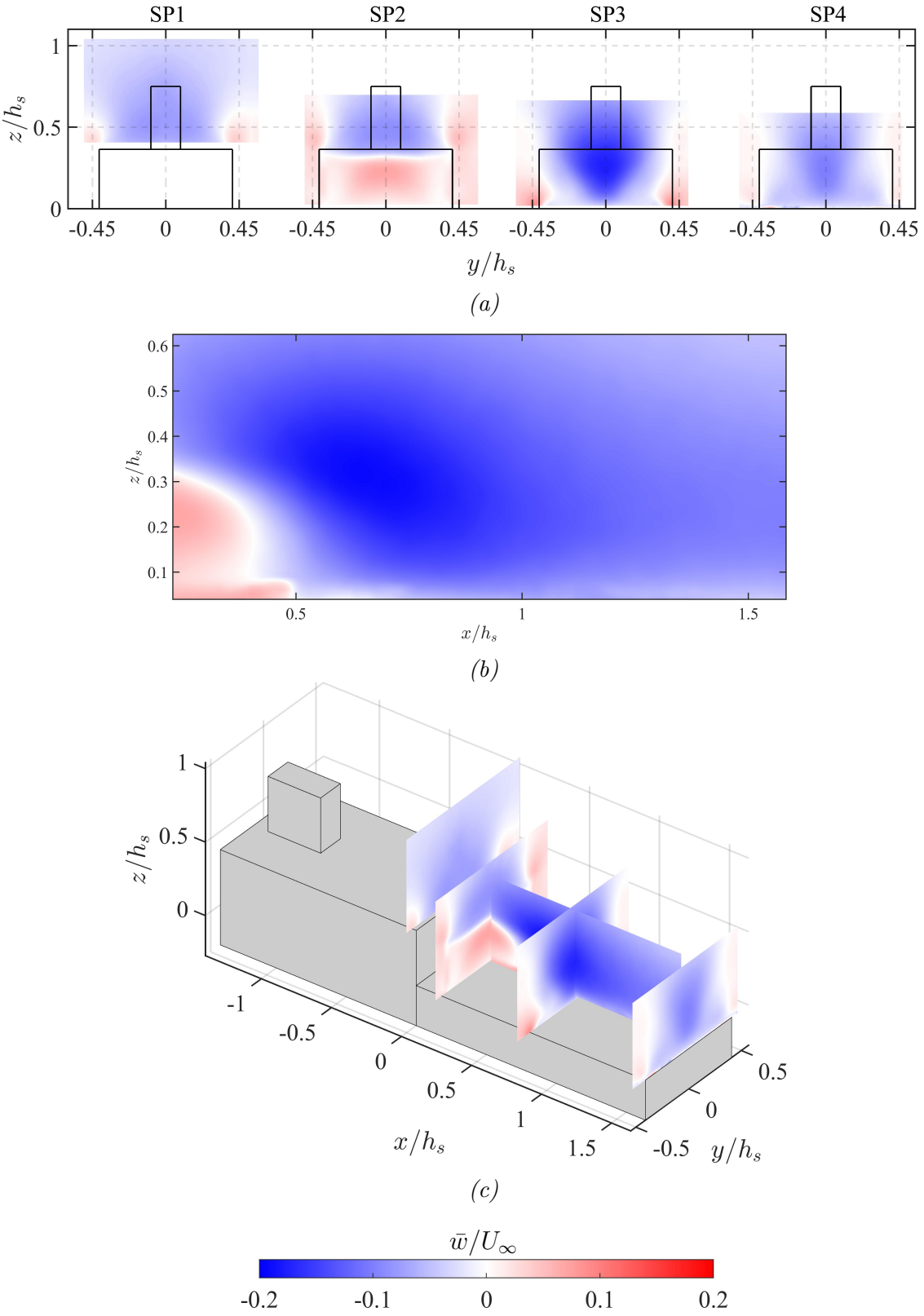

Figure B.5 Time-averaged wall-normal velocity under the influence of the sABL. (a) the four spanwise planes, (b) the streamwise plane, and (c) 3D perspective.

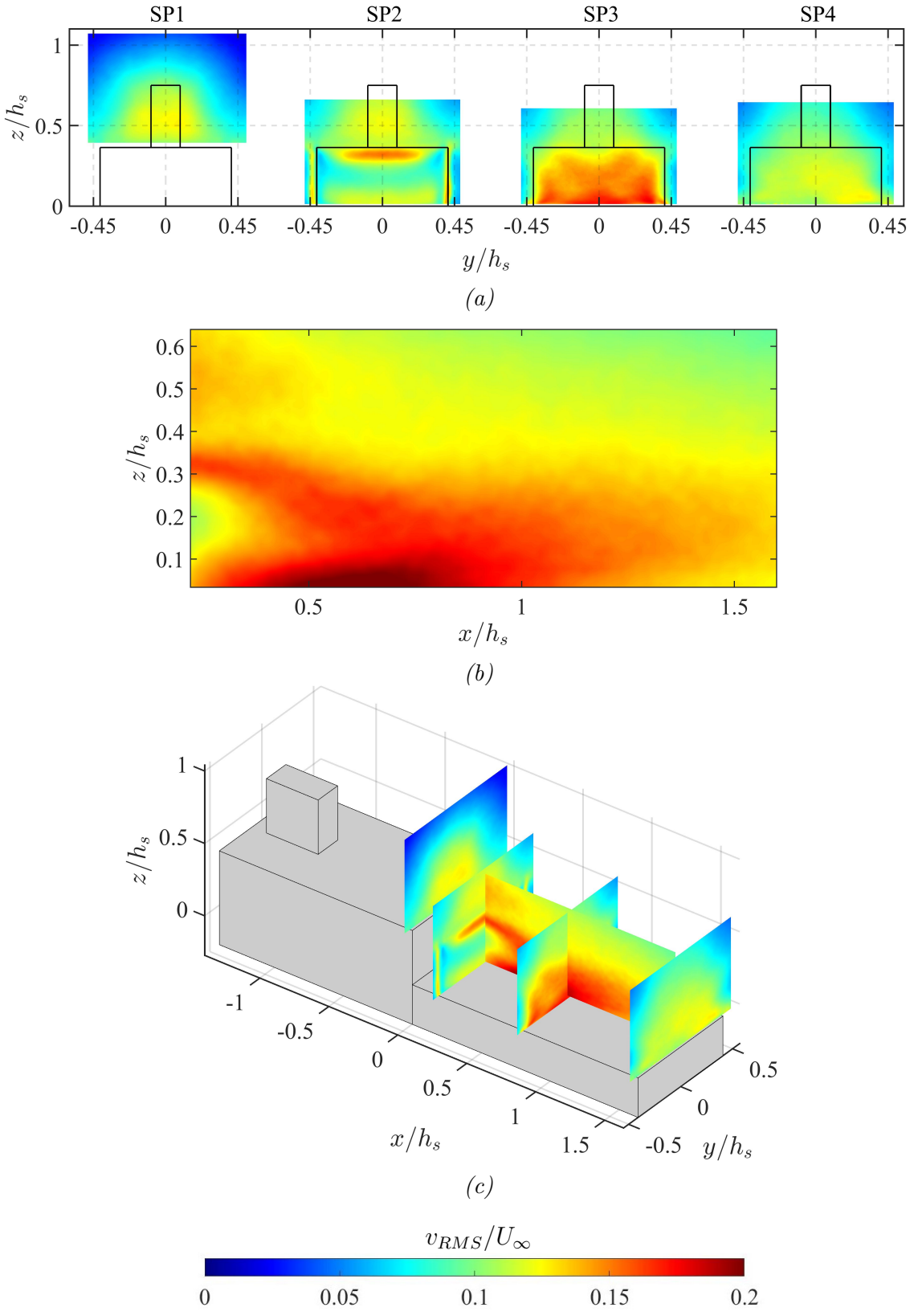

Figure B.6 Spanwise TI results for cases without the sABL. (a) the four spanwise planes, (b) the streamwise plane, and (c) 3D perspective.

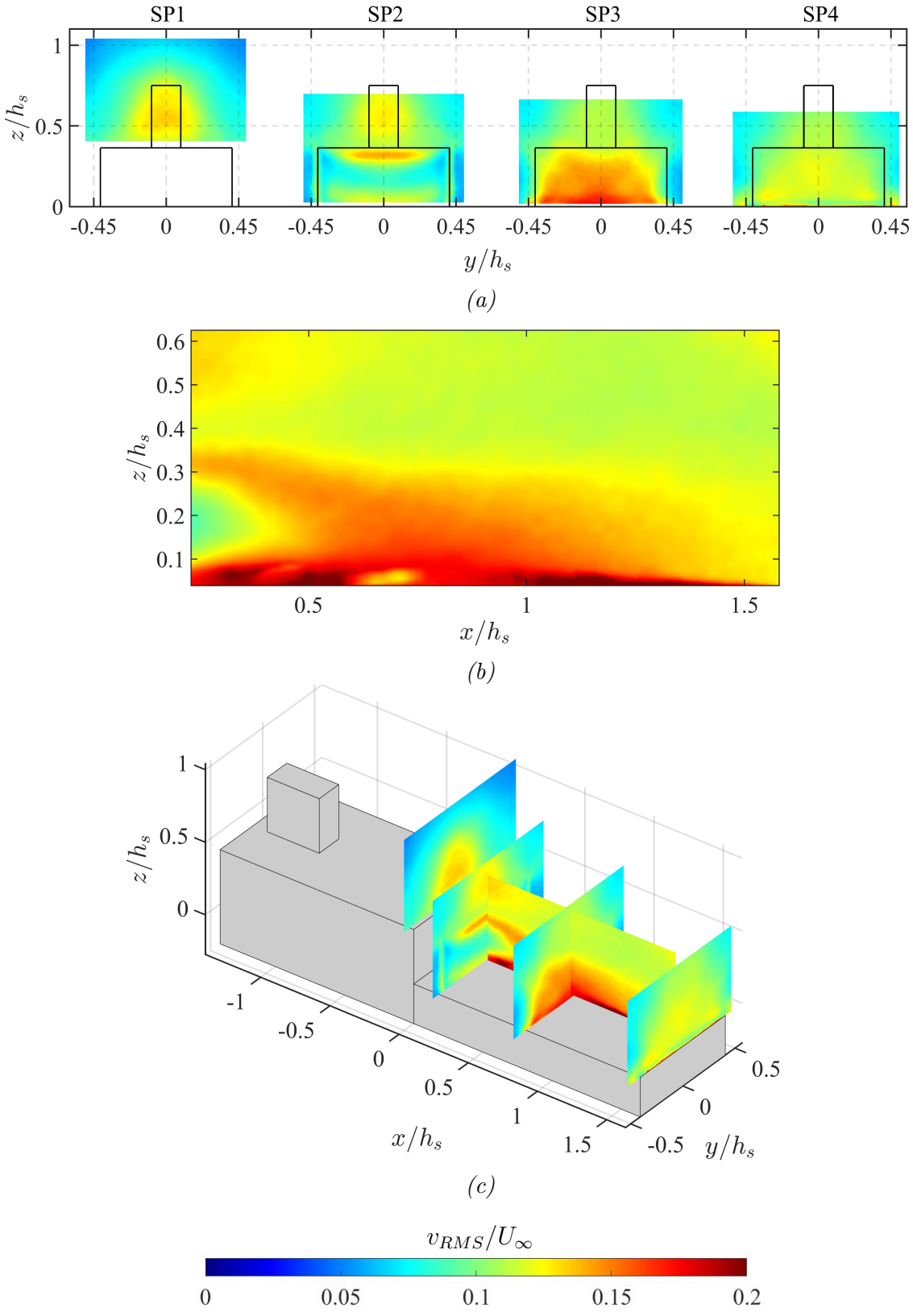

Figure B.7 Spanwise TI results under the influence of the sABL. (a) the four spanwise planes, (b) the streamwise plane, and (c) 3D perspective.

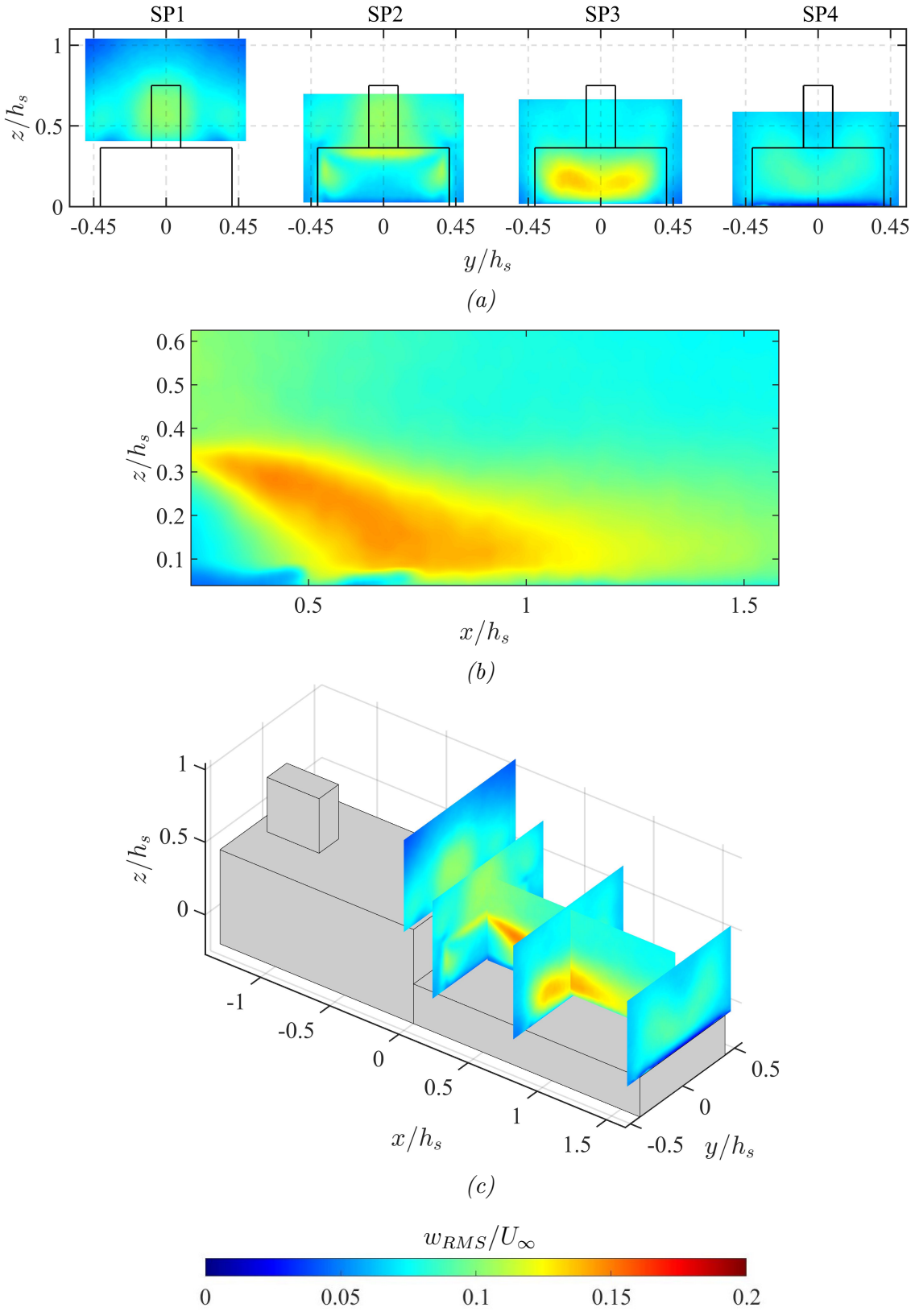

Figure B.8 Wall-normal TI results under the influence of the sABL. (a) the four spanwise planes, (b) the streamwise plane, and (c) 3D perspective.

C Conditionally Averaged Results

The conditional contours shown in Chapter 3 showed different isolated events of interest within the flow that are likely relevant to ship-rotorcraft operations. The two main events of interest studied were the vertical flow events in the shear layer and the bistable flow states of the hangar door wake. For the first event, cases without the sABL were shown in Chapter 3. This Appendix contains the corresponding analysis for cases with sABL. Similarly, the second event was analyzed using flow fields with the sABL. This appendix contains the results of the corresponding analysis for cases without the sABL.

C.1 Extreme Vertical Flow Fluctuations

The same condition criteria described in Section 3.2.1 was applied to the flow field under the influence of the sABL to observe possible differences in the resulting flow structures. The conditional velocity fields in the streamwise, spanwise, and wall-normal directions are presented below. Figures C.1, C.2, and C.3 show the flow when the shear layer induced positive vertical fluctuations in the conditional area while Figs. C.4, C.5, and C.6 show the flow conditioned to capture negative vertical fluctuations. The resulting conditional fields with the sABL were almost identical to those without the sABL. Similarly, the intensity of the large-scale regions remained unchanged in the cases with the sABL. Hence, it was concluded that the added turbulence upstream of the ship did not have any effect on the organized structures that were associated with the flapping motion of the shear layer.

C.2 Bistable Behavior of the Hangar Door Wake

The second event of interest discussed in Chapter 3 was the bistable behavior of the wake behind the hangar door. The bistable states shown in Section 3.2.2 were obtained using flow fields under the influence of the sABL. In addition, the corresponding analysis was carried out using measurements without the sABL. The results are presented in this section. Stable state 1 is shown in Fig. C.7 while stable state 2 is shown in Fig. C.8. Finally, the side-by-side comparison of each state is shown in Fig. C.9. Clearly, the same bistable effects were present without the influence of the sABL and the structures were comparable to the results with

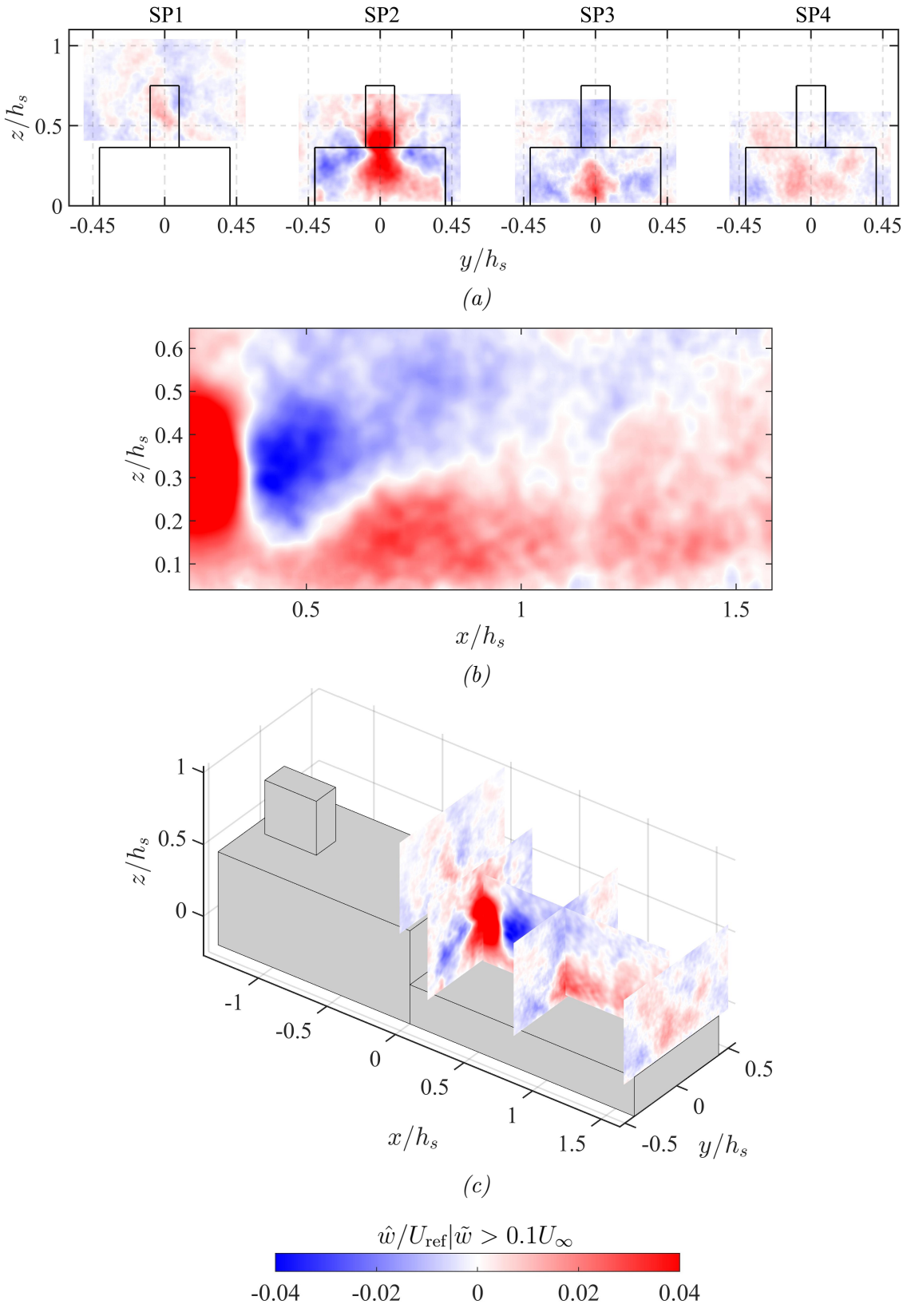

Figure C.1 Wall-normal conditional velocity field $\hat{w}/U_{\text{ref}}$ for positive fluctuations under the influence of the sABL. The same condition criteria described in Section 3.2.1 were used.

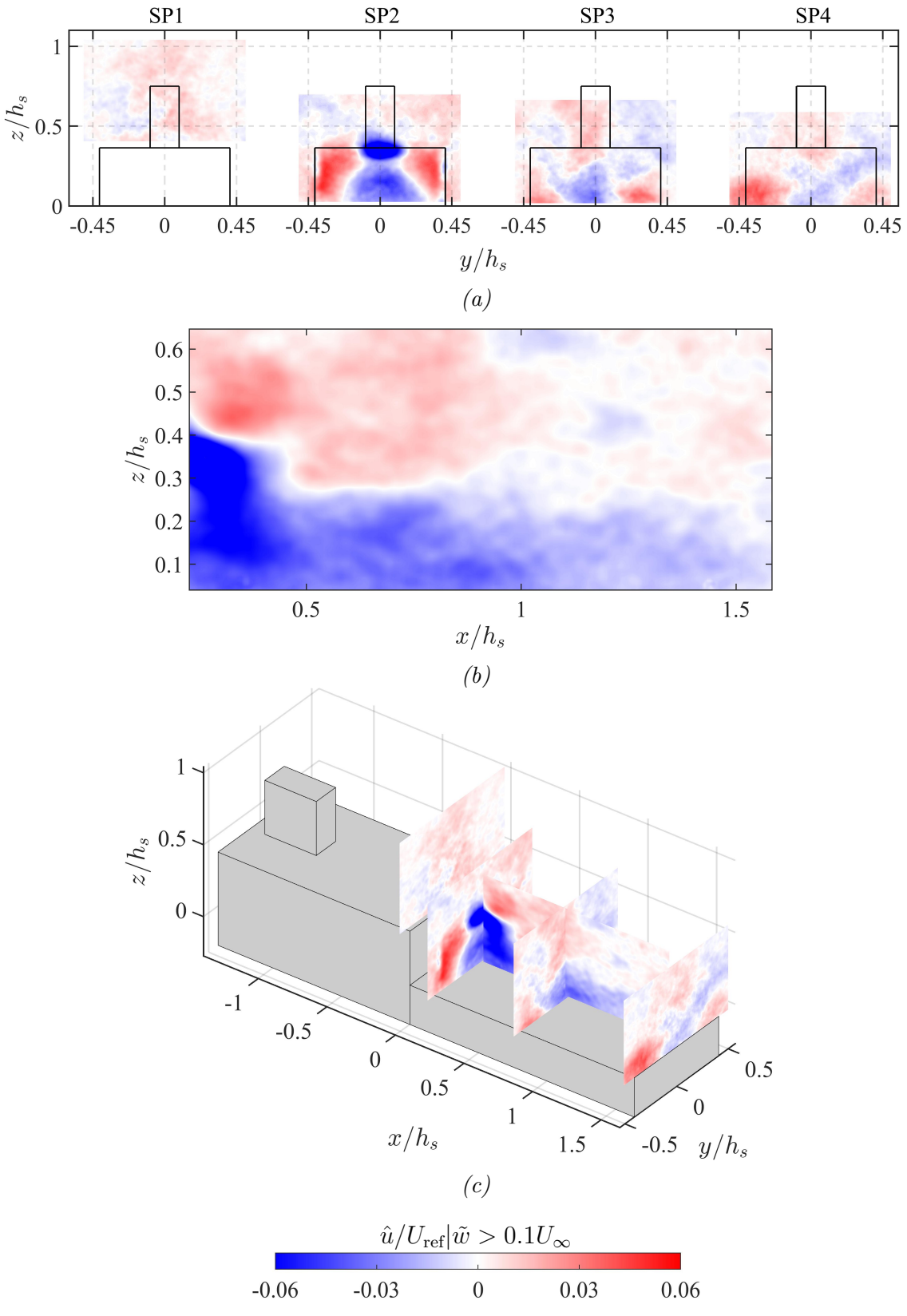

Figure C.2 Streamwise conditional velocity field $\hat{u}/U_{\text{ref}}$ for positive fluctuations under the influence of the sABL. The same condition criteria described in Section 3.2.1 were used.

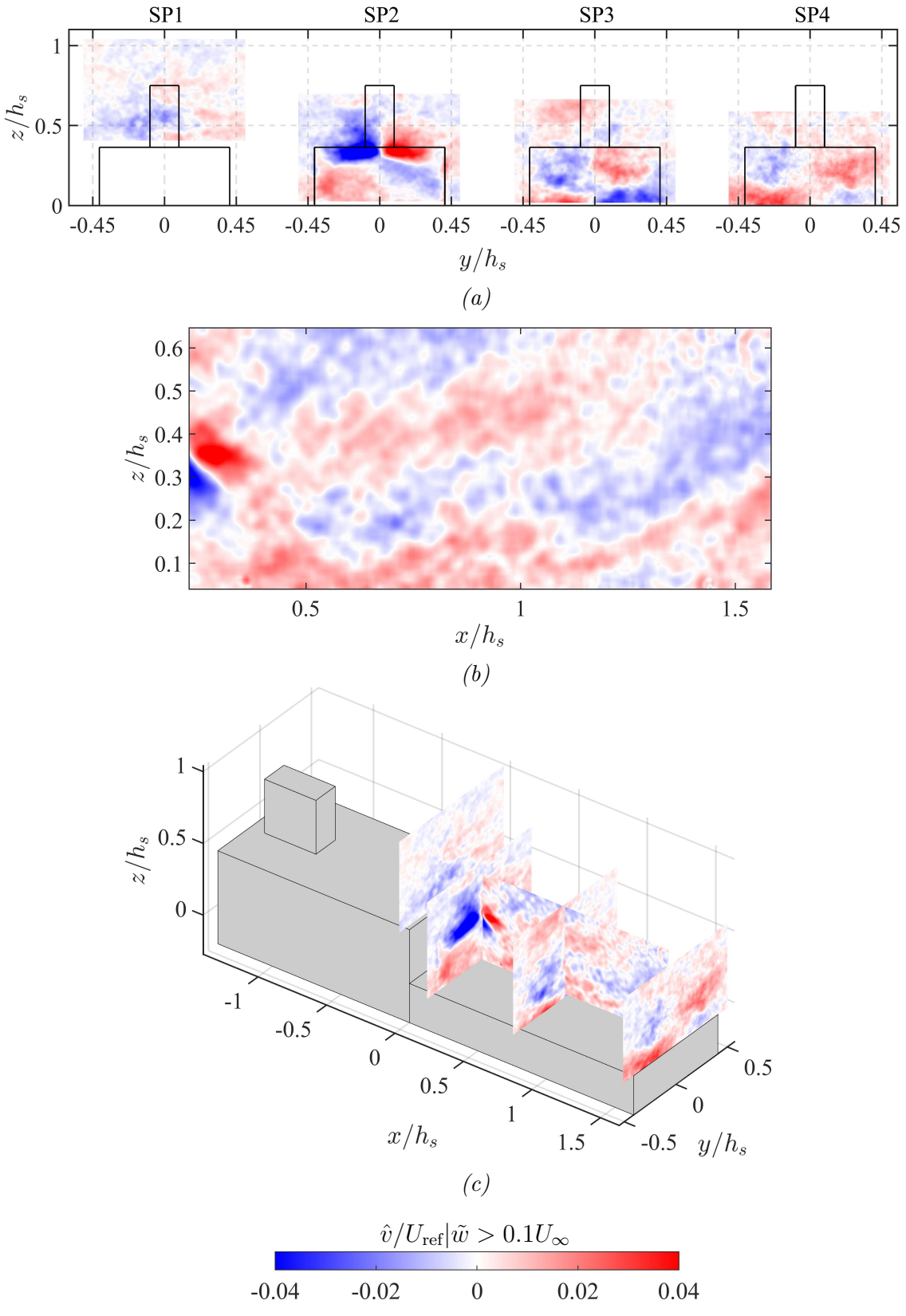

Figure C.3 Spanwise conditional velocity field $\hat{v}/U_{\text{ref}}$ for positive fluctuations under the influence of the sABL. The same condition criteria described in Section 3.2.1 were used.

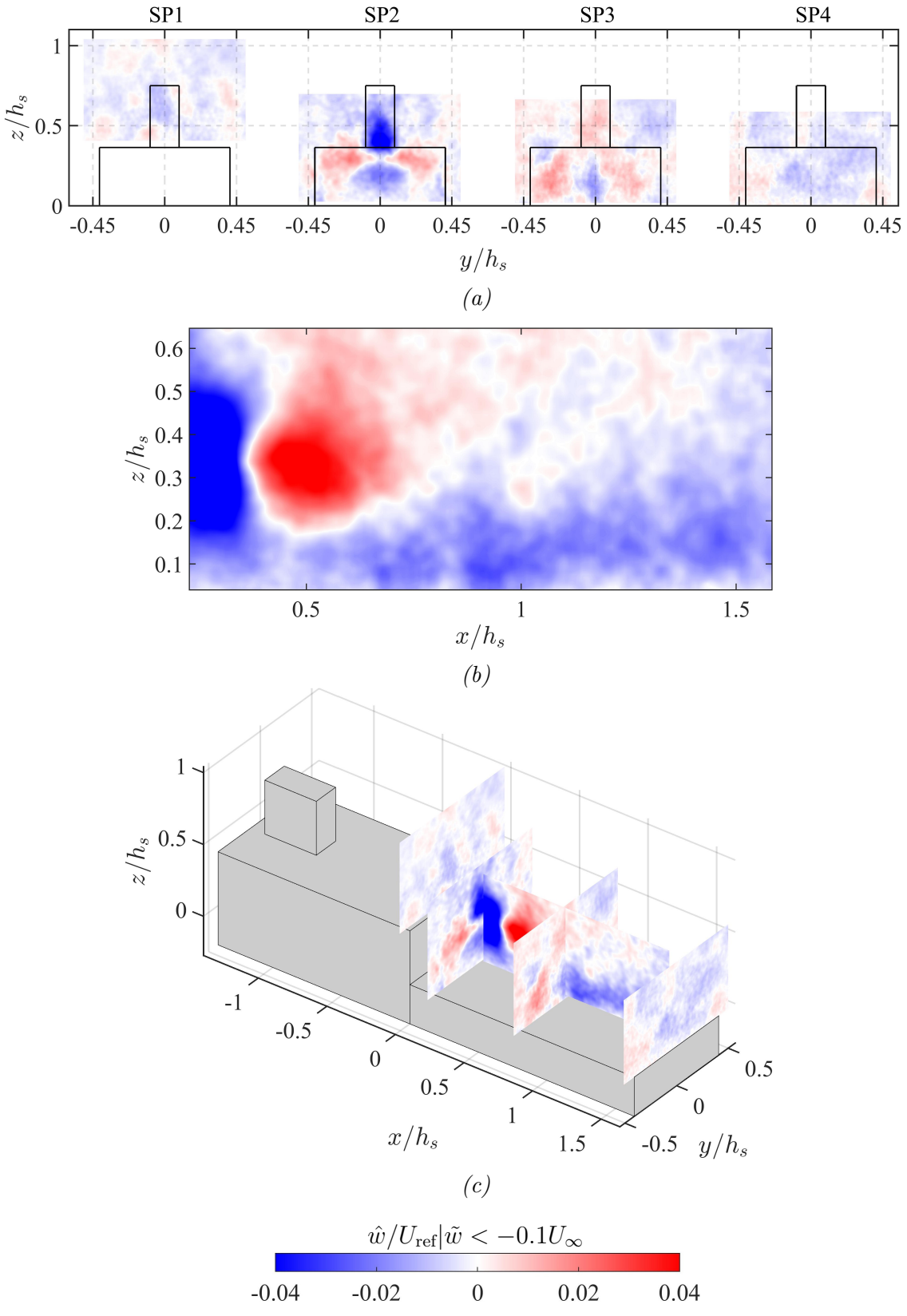

Figure C.4 Wall-normal conditional velocity field $\hat{w}/U_{\text{ref}}$ for negative fluctuations under the influence of the sABL. The same condition criteria described in Section 3.2.1 were used.

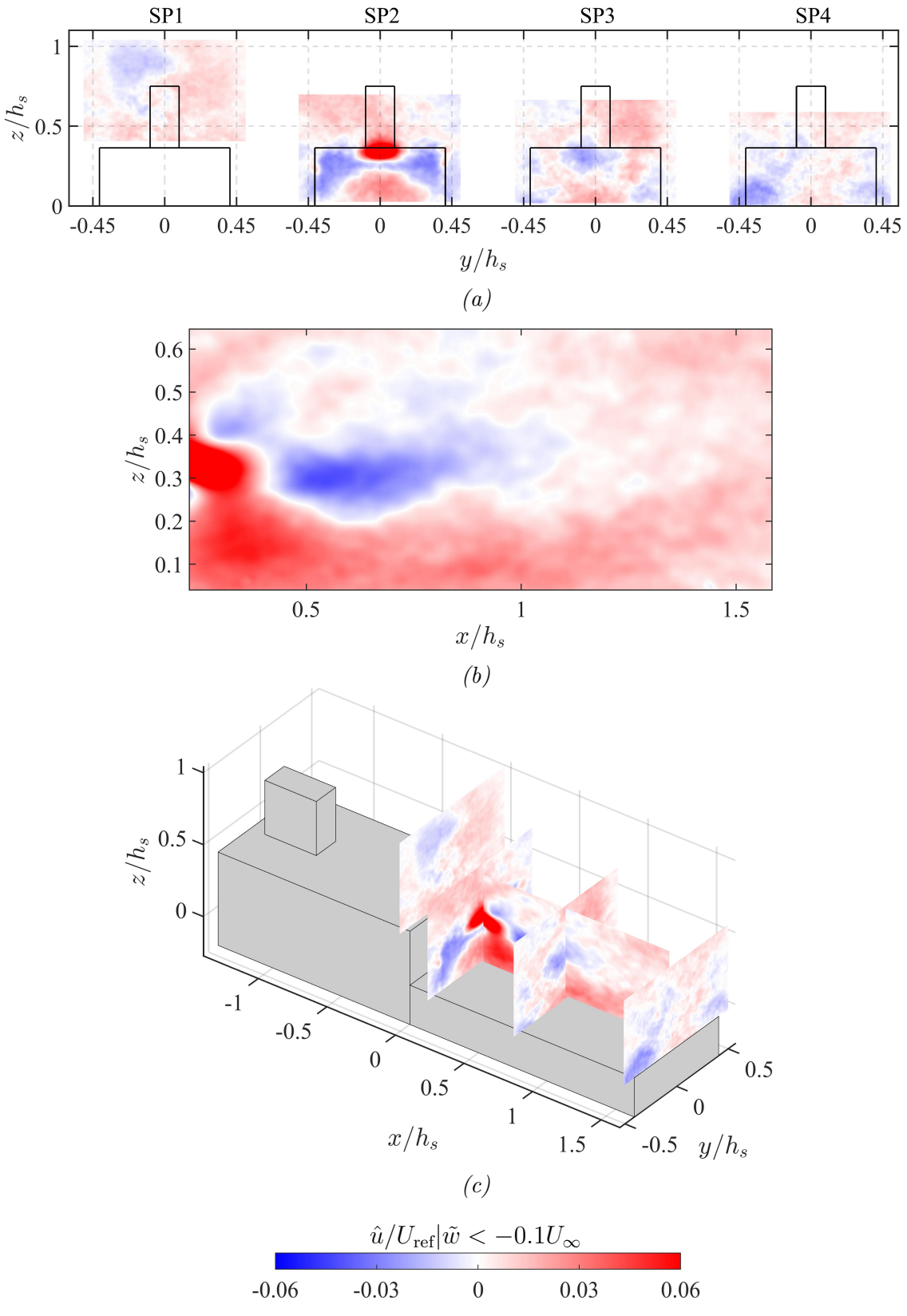

Figure C.5 Streamwise conditional velocity field $\hat{u}/U_{\text{ref}}$ for negative fluctuations under the influence of the sABL. The same condition criteria described in Section 3.2.1 were used.

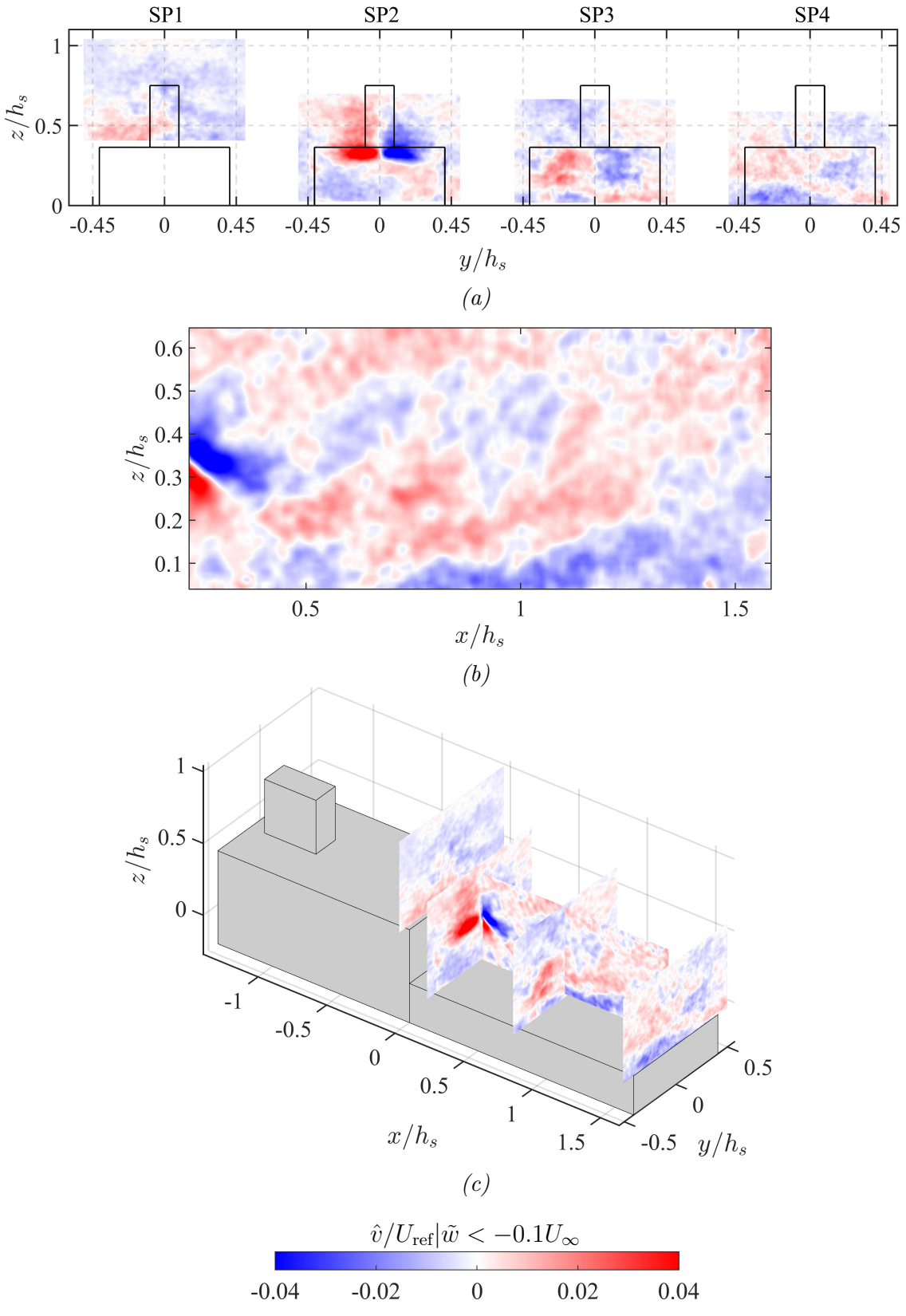

Figure C.6 Spanwise conditional velocity field $\hat{v}/U_{\text{ref}}$ for negative fluctuations under the influence of the sABL. The same condition criteria described in Section 3.2.1 were used.

the sABL. However, the downstream effects of each state appeared to be more pronounced without the sABL. For instance, in Fig. C.7, the streamlines in SP3 showed sharp velocity gradients on the port side while Fig. C.8 showed the same effect on the starboard side. These gradients closer to the flight deck surface appeared to be more distinct when compared to the conditional fields with the sABL, possibly due to the higher free-stream velocities, which is known to impact not only the development of the flight deck vortices but also the temporal behavior of the bistability phenomenon [2, 6, 30].

C.3 Transition Between Bistable States of the Hangar Door Wake

The transition between bistable states was analyzed following the procedure described in Section 3.2.3 for flow fields without the sABL. The PDF in Fig. C.10 shows that it was more likely to capture state 2 (e.g, $\tilde{v} > 0$) using flow fields without the sABL. This biased behavior was not seen in cases with the sABL. Since the states persisted in time for a longer period of time in the case without the sABL, the time period was adjusted to $t_0 \pm 20\Delta t$ to identify the transition in and out of each state.

A total of 106 transitions to state 1 were identified. Then, a temporal average at each time instance from $t_0 - 20\Delta t$ to $t_0 + 20\Delta t$ was obtained. For example, the time instance $t_0 - 20\Delta t$ of each one of the 106 transitions was used to obtain the mean flow structure at $t_0 - 20\Delta t$. This process was repeated for each time instance to study the time evolution of the transition.

Figure C.11 shows the conditional flow field at time instances in which its structure showed significant changes. Figure C.11a shows the time instance $t_0 - 10\Delta t$. At this time, the flow had not started transitioning to state 1 since the flow structure in all planes was symmetric. At $t_0 - 2\Delta t$, the flow within the recirculation region was no longer symmetric. The streamlines indicated the presence of a low-speed region on starboard side closer to the flight deck surface. Moving downstream, SP3 ans SP4 showed higher spanwise velocity closer to the flight deck, which showed agreement with the pattern seen in cases with the sABL in Section 3.2.3. At $t_0 - \Delta t$, the flow within the recirculation region moved from starboard to

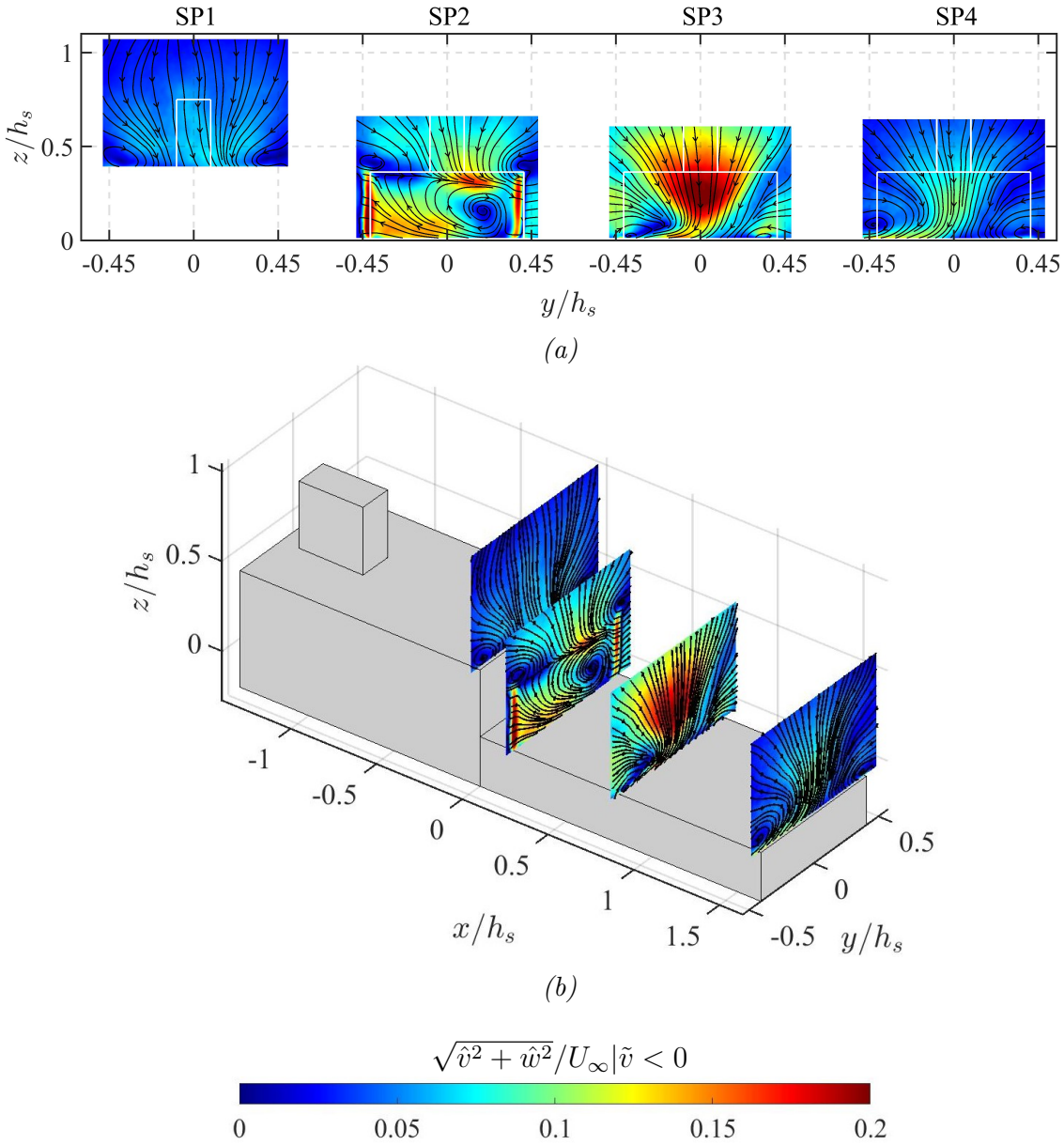

Figure C.7 Combined spanwise and wall-normal conditional fields for state 1 ($\tilde{v} < 0$) without the influence of the sABL.

port and a vortical structure started forming on the starboard side. However, at this point, the characteristic vortex had not been formed. Similarly, the flow structure downstream had not changed significantly. Finally, at t_0, the characteristic vortex was formed in the recirculation region. Additionally, the downstream flow structures within SP3 and SP4 showed that the flow closer to the deck surface slightly strengthened.

After the transition, the characteristic vortex persisted in time in between t_0 and $t_0 + 8\Delta t$

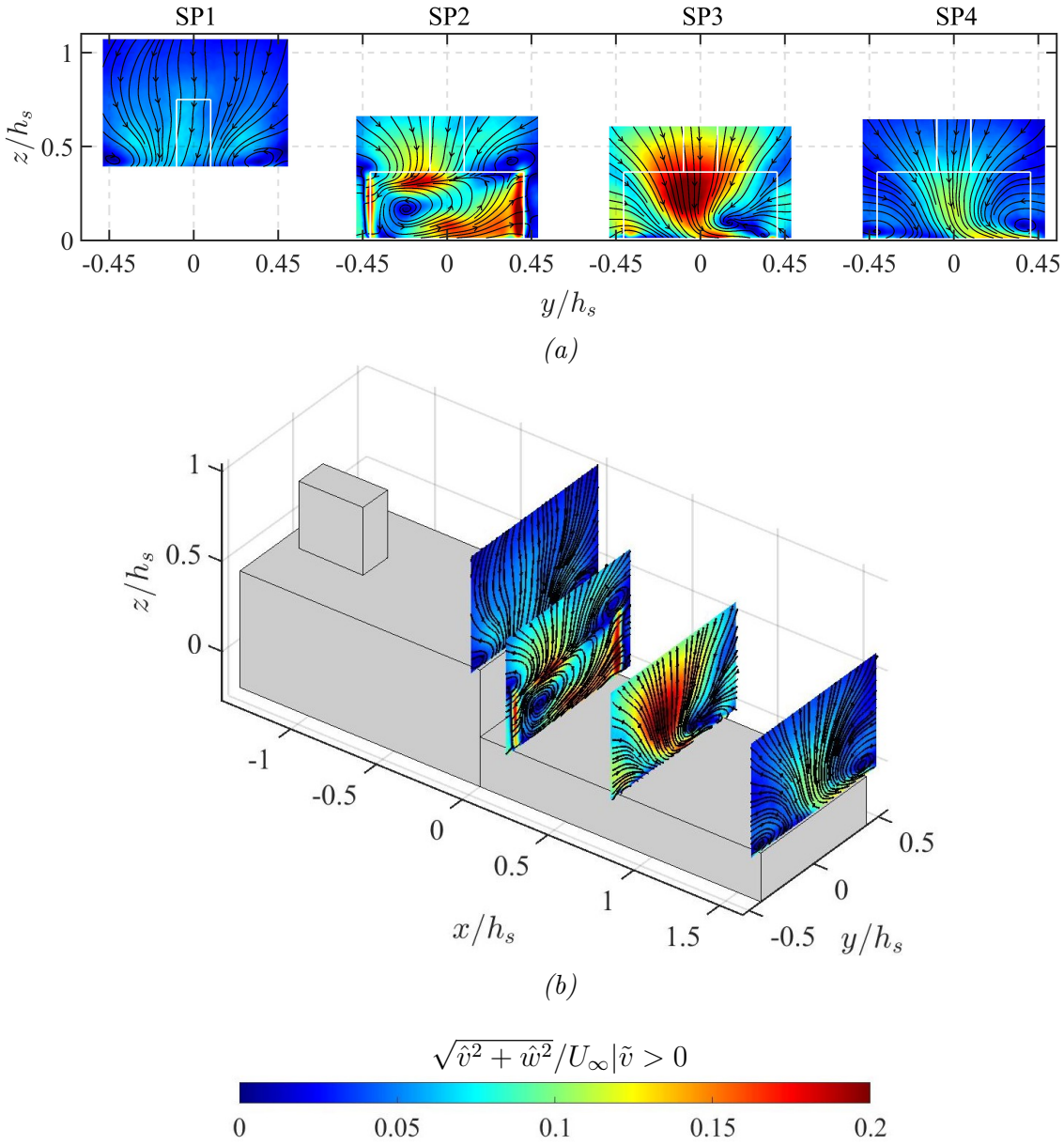

Figure C.8 Combined spanwise and wall-normal conditional fields for state 2 ($\tilde{v} > 0$) without the influence of the sABL.

as shown in Fig. C.12. At time $t_0 + 8\Delta t$, the characteristic vortex in the recirculating region weakened in comparison to the previously shown instance $t_0 + 6\Delta t$. This indicated the beginning of the transition out of state 1. Downstream, there were no major changes in flow structure at this point. At $t_0 + 20\Delta t$, the flow was symmetric with respect to the ship centerline again since the effects of the bistable configuration were no longer present neither upstream nor downstream of the hangar door.

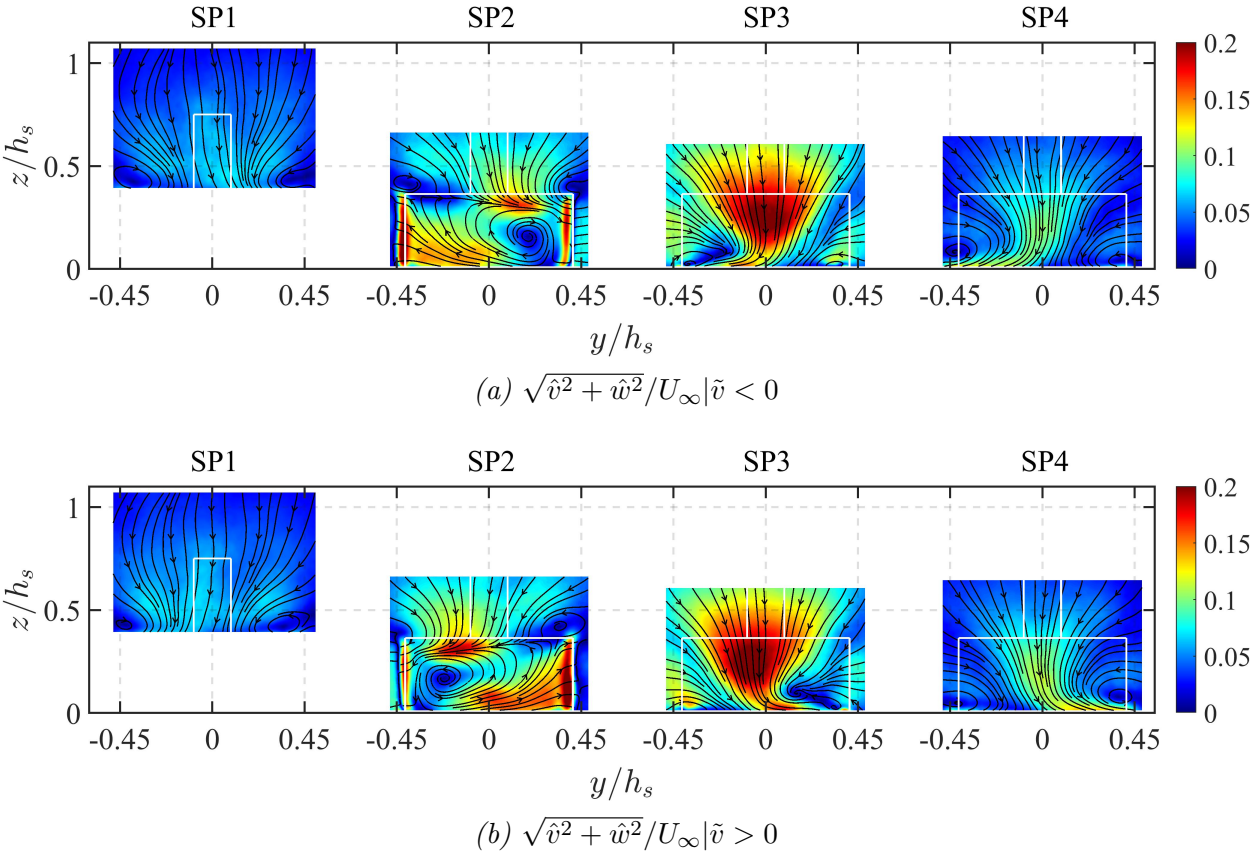

Figure C.9 A direct comparison of each state of the flow field without the sABL. The spanwise planes of state 1 and 2 are shown in the top and bottom figures, respectively.

Figure C.13 shows the average flow fields during the transition into state 2. First, the flow appeared to transition out of state 1 since the streamlines behind the hangar door indicated a flow bias that was characteristic of state 1. Downstream, the flow structures appeared symmetrical with respect to the ship centerline. At $t_0 - 2\Delta t$, the low speed region closer to the deck surface in SP2 was on the port side, which indicated the beginning of the vortex formation at this location. The flow structures in SP3 and SP4 also showed a slightly larger spanwise velocity on the flight deck, which showed agreement with the structures seen in cases with the sABL. At $t_0 - 2\Delta t$, the vortical structure was more defined. This appeared to have a greater influence on the downstream flow structure as the spanwise velocity was greater close to the deck surface. At the time of the transition t_0, the characteristic vortex was present and the gradients seen in SP3 appeared to strengthen, resulting in a larger vortex

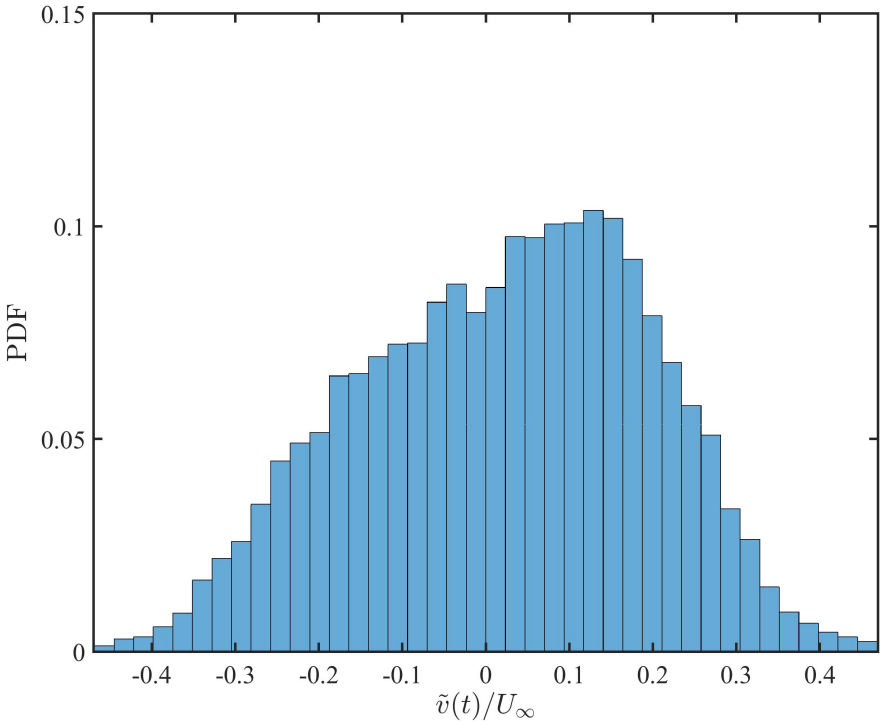

Figure C.10 PDF of $\tilde{v}(t)$ for cases without the sABL.

on the starboard side of the ship.

Figure C.14 shows the conditionally averaged flow fields during the transition out of state 2. In this case, however, the flow structure remained unchanged for a significantly longer time than state 1. This was expected since the PDF showed that the flow field was biased towards this state. There were no significant changes until $t_0 + 20\Delta t$, when the characteristic vortex was slightly weakened and the downstream flow structure appeared to be symmetric with respect to the ship centerline.

In summary, the flow structures without the sABL showed a similar pattern during the transition compared to the flow with the sABL. The main differences observed in this study were: (i) The flow without the sABL was biased towards state 2. Thus, 767 transitions to this state were identified while only 106 transitions to state 1 were isolated, (ii) this flow bias allowed state 2 to persist significantly longer in time compared to state 1, (iii) while state 2 persisted in time, the downstream flow structure in SP3 showed sharper velocity gradients and more deformed deck vortices when compared to state 1.

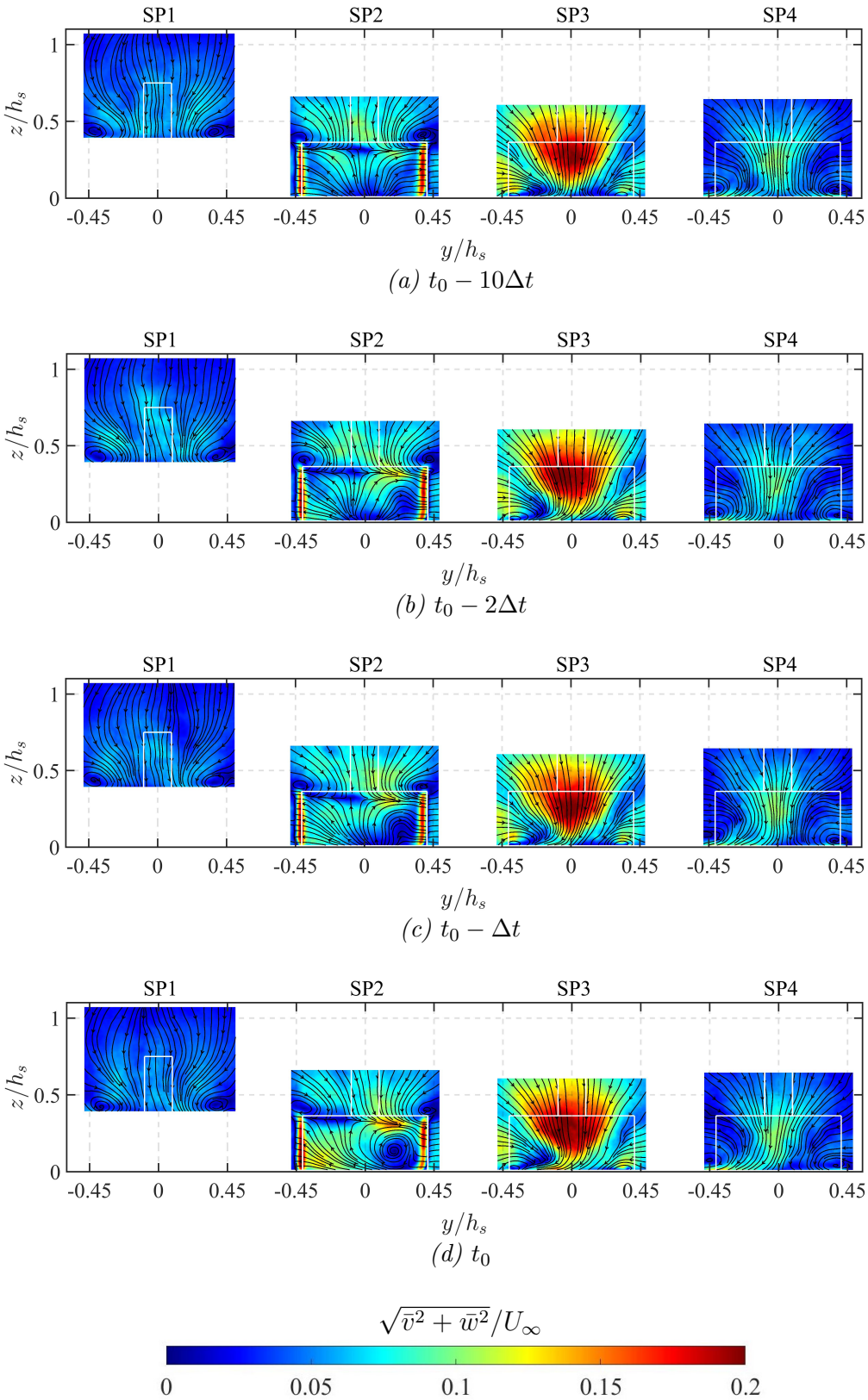

Figure C.11 Temporal average of the instances preceding the transition to state 1 in (a), (b), and (c) as well as the instance of the transition in (d). Case without the sABL.

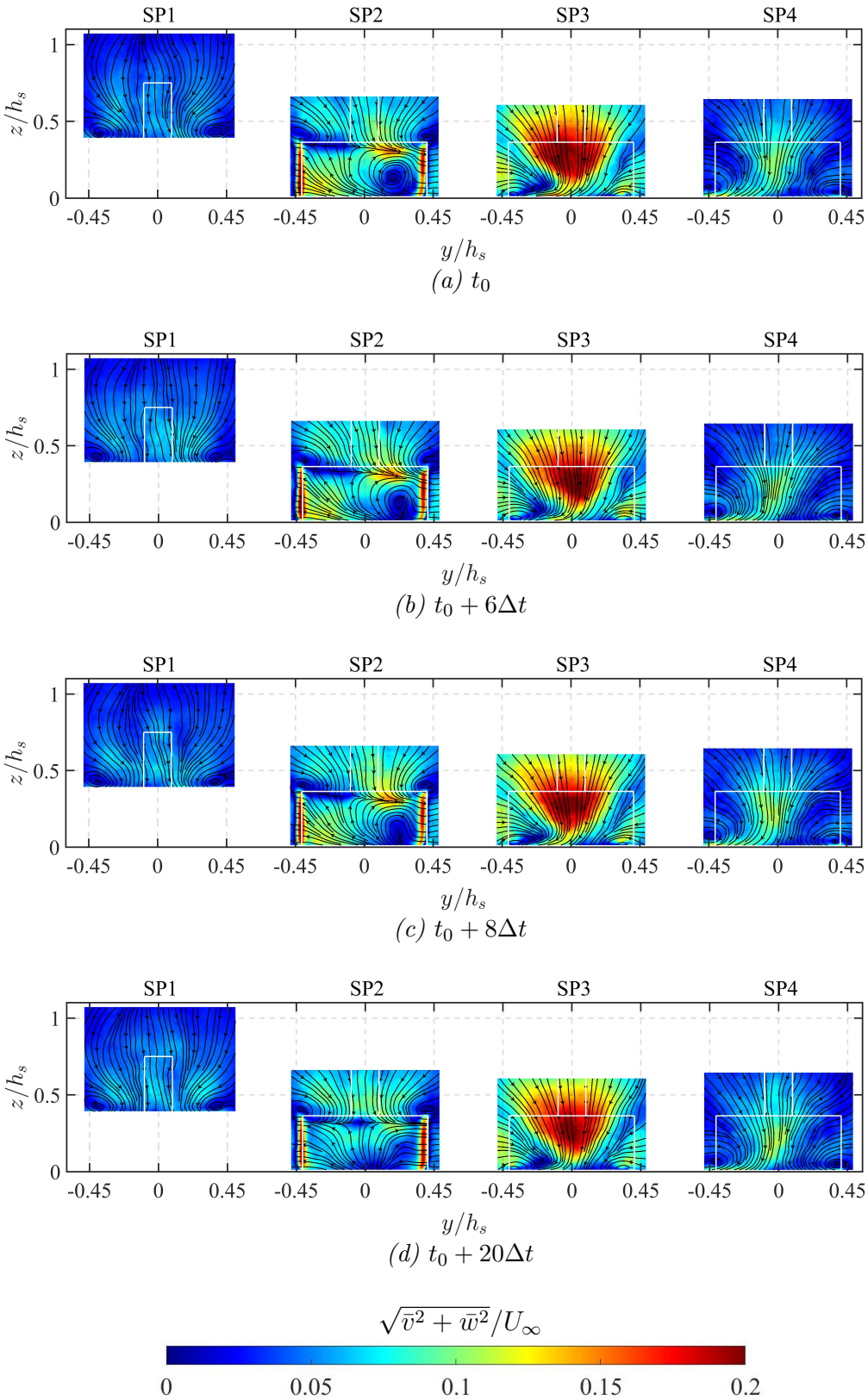

Figure C.12 Temporal average obtained using the instant of transition to state 1 in (a) and using the instants after the transition in (b), (c), and (d). Cases without the sABL.

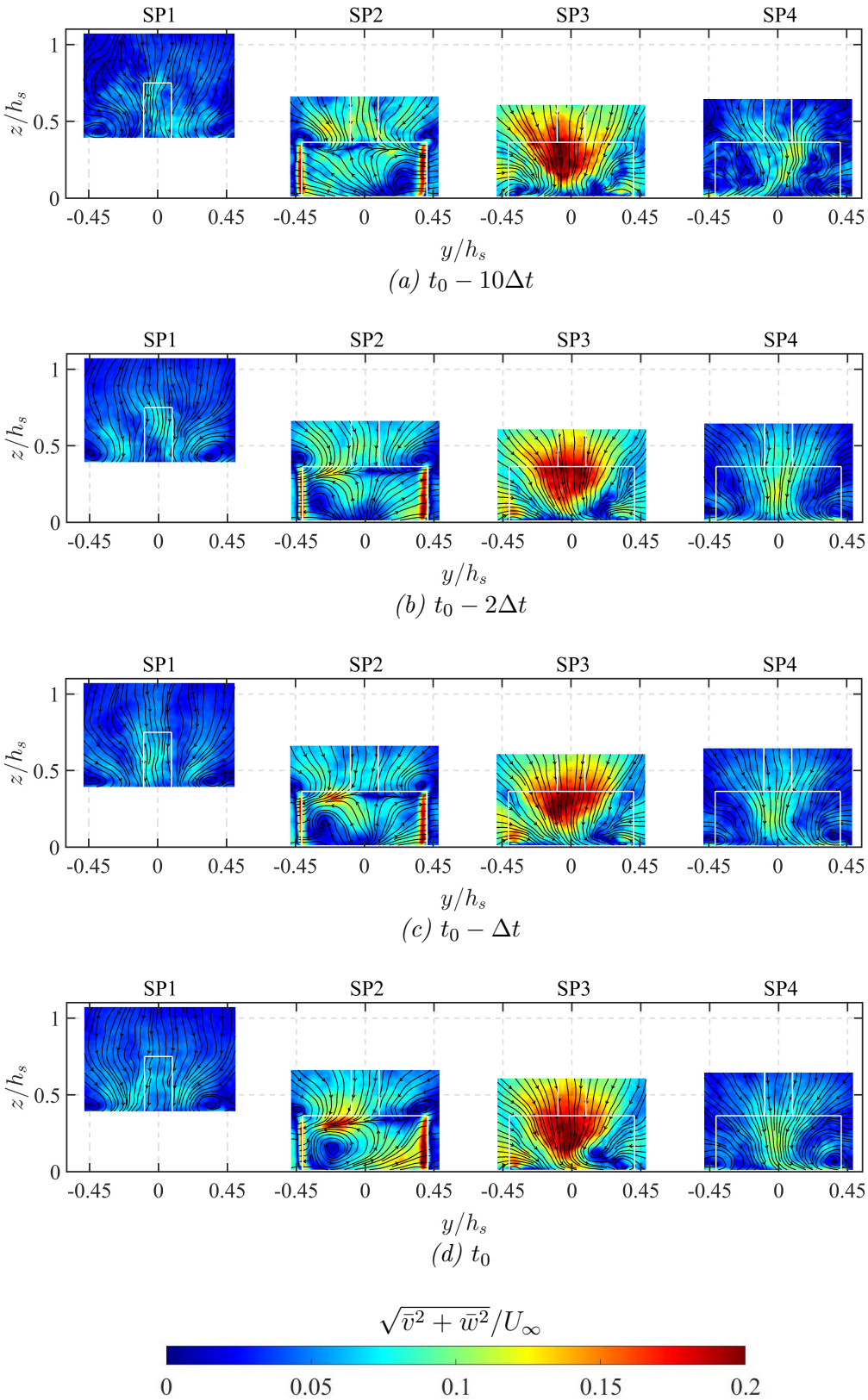

Figure C.13 Temporal average of the instances preceding the transition to state 2 in (a), (b), and (c) as well as the instance of the transition in (d). Case without the sABL.

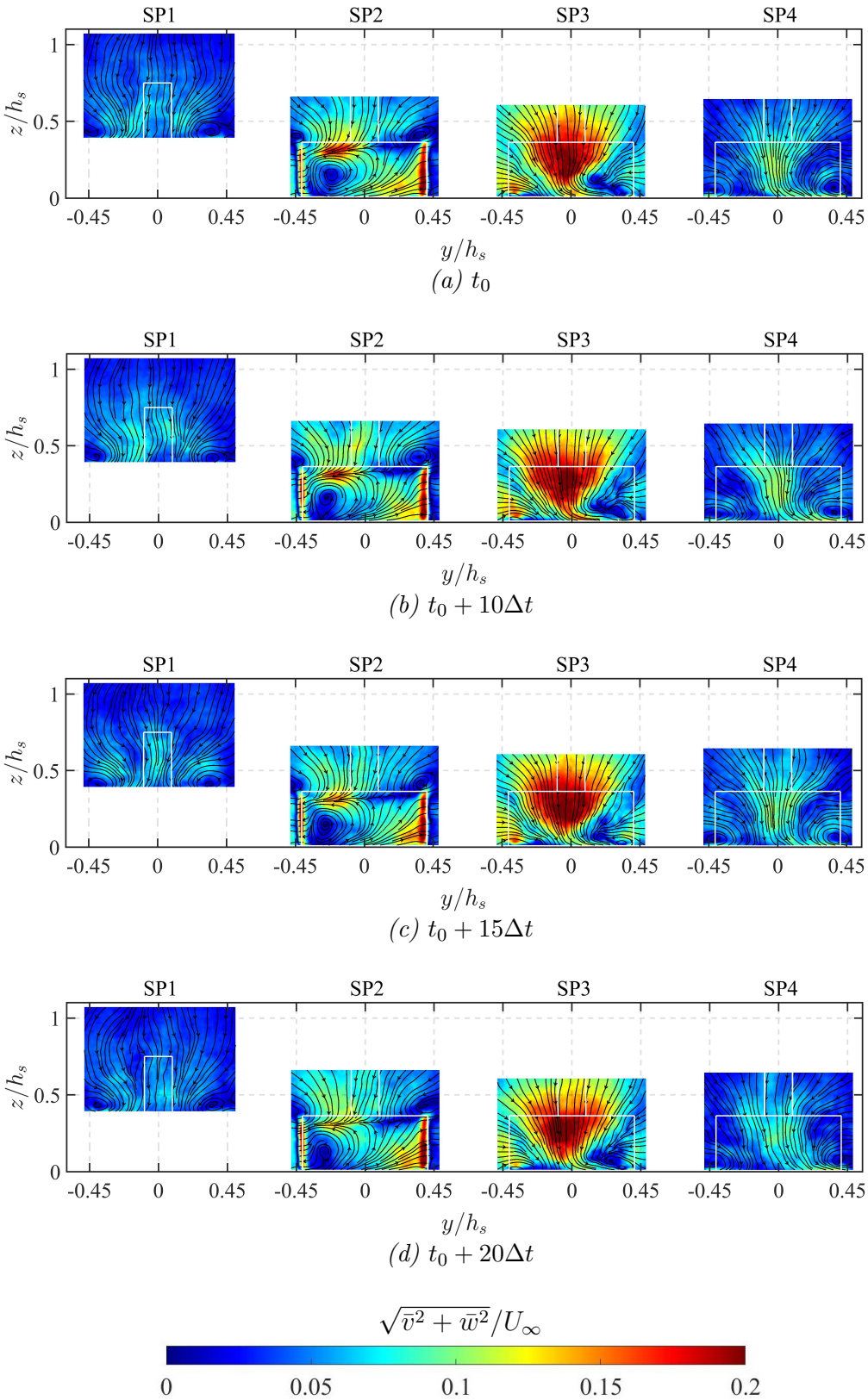

Figure C.14 Temporal average obtained using the instant of transition to state 2 in (a) and using the instants after the transition in (b), (c), and (d). Cases without the sABL.